LCH Laboratoire de Constructions Hydrauliques
Laboratory of Hydraulic Constructions

ÉCOLE POLYTECHNIQUE
FÉDÉRALE DE LAUSANNE

Communication 59

Influence of air entrainment on rock scour development and block stability in plunge pools

Rafael Duarte

Editeur : Prof. Dr A. Schleiss

Lausanne, 2014

Communications du Laboratoire de Constructions Hydrauliques ISSN 1661-1179
Ecole Polytechnique Fédérale de Lausanne
Editeur: Prof. Dr A. Schleiss

Preface

Rock scour occurring near dam foundations due to high-velocity jets of spillways impinging into the plunge pool is a major concern regarding dam safety. Scour in fractured rock resulting from high-velocity jet impact is a complex phenomenon, which involves the three phases: water, air and rock. Since 1998, the Laboratory of Hydraulic Constructions (LCH) of the Ecole Polytechnique Fédérale de Lausanne (EPFL) is conducting research in order to better understand the physical processes that contribute to rock scour. An innovative experimental facility, which can reproduce prototype jet velocities, was built and continuously improved. With the help of this experimental set-up, a new, completely physically based engineering model has been developed for the prediction of the ultimate scour depth of jointed rock, called Comprehensive Scour Method (CSM). The impact of high-velocity plunging jets produce highly dynamic pressures at the pool bottom, which are transferred into rock joints by transient flow governed by the propagation of pressure waves. The latter is strongly influenced by the air content in the plunge pool and the underlying rock fissures.

Dr. Rafael Duarte studied for the first time the effect of active jet aeration on the scour process in fractured rock. Systematic experiments allowed assessing the response of a block in a plunge pool impacted by high-velocity jets having different amount of active aeration. He could show that the air entrained by the jet influences the pressures on the bottom by two opposed effects. On one hand, the air-water mixture reduces the apparent density of the jet and thus its momentum. The kinetic energy per unit volume reaching the pool bottom is lower and consequently the pressures are also lower compared to similar clear-water jet. On the other hand, the air bubbles reduce the shear stress of the diffusing jet in the plunge pool. The velocity decay of aerated jets is therefore less resulting in higher velocities reaching the bottom, and thus higher pressures. Which of the two effects will be stronger depends above all on the pool depth.

Based on the experimental study and a comprehensive analysis of the results Dr. Duarte could enhance the Comprehensive Scour Method CSM in order to include active air entrainment at jet issuance.

We would like to thank the members of the jury Prof. Dr. Alain Nussbaumer, EPF Lausanne, Switzerland, Prof. Dr. Antonio Bento Franco, Instituto Superior Técnico, Lisbon, Portugal, Prof. Dr. Willi Hager, ETH Zurich, Switzerland and Dr. Erik Bollaert, AquaVision Engineering, Switzerland, for their helpful suggestions. Finally, we also thank gratefully the Portuguese Foundation for Science and Technology (FTC) for their financial support under Grant No SFPH/BD/51074/2010.

Prof. Dr. Anton Schleiss Prof. Dr. António Pinheiro

Abstract

Influence of air entrainment on rock scour development and block stability in plunge pools

The impingement of high-velocity water jets on plunge pools, such as it occurs downstream of spillways of high-head dams, may cause scour on the rock foundations. The scour process is the result of complex and consecutive physical phenomena. Turbulence plays a major role, especially in the jet development during the trajectory in the air, in the diffusion process in the pool, in the pressure fluctuations at the water-rock interface, and in the pressure propagation inside rock fissures.

These phenomena cannot be reproduced in Froude-based reduced-scale models without significant scale effects. Hence, observations on prototype-scale models and consideration of dynamic, fluctuating pressures are the only way to correctly assess the effect of jet impingement on the development of rock scour.

Air entrainment greatly influences the whole process. Air is entrained in the jet during the travel through the air and is also entrained in the plunge pool at impact. The air bubbles in the plunge pool influence energy dissipation. The bubbles may also enter rock fissures, where they change properties of pressure wave oscillation and amplification. The correct description of air bubbles behavior in plunge pools and their influence on the pressure fluctuations on the water-rock interface and inside underlying fissures under prototype conditions has never been achieved. Air has properties such as buoyancy, compressibility and solubility in water, which are difficult to evaluate and require a comprehensive research.

Since 1998, the Laboratory of Hydraulic Constructions (LCH) of the Ecole Polytechnique Fédérale de Lausanne (EPFL) develops a broad research to accurately describe the principles of rock scour due to high-velocity jets. An innovative experimental facility was built, which reproduces prototype jet velocities. Past developments were made to describe rock fissure break-up, block ejection, the influence of pool bottom geometry, amongst others topics.

The present research enhances the knowledge of air entrainment properties, air bubbles behavior and their influence in plunge pool bottom pressures, and tie the former work all together. Experiments were undertaken under near-prototype scale jets to measure air concentrations and air bubble velocities throughout different depths and radial distances in the jet diffusive layer, as well as dynamic pressures and displacements around a block embedded on the plunge pool bottom. Submerged jets, actively aerated at the nozzle, were reproduced to provide results with a known total aeration in the pool, whilst plunging jets, actively aerated as well, were tested to represent a more realistic scenario. Furthermore, the block was either fixed on the bottom or free to move, representing different degrees of opening and interlocking of the rock fissure network found in practice.

This study reveals that the air entrained by the jet influences the pressures on the bottom in two opposed ways. On one hand, the air-water mixture can be interpreted as a jet with a reduced apparent density, and thus with lower momentum. The consequence is

a reduced kinetic energy per unit volume reaching the bottom, which is converted into lower pressures than for a similar clear-water jet. On the other hand, the air bubbles reduce the shear stress of the diffusing jet. The velocity of aerated jets decreases along the pool at a lower rate, resulting in higher velocities reaching the bottom, and thus higher pressures. This second effect obviously depends on the pool depth. The overall influence of jet air entrainment is a balance of the two effects, but the experimental data show a general tendency of pressure reduction, both inside the fissures and on the water-rock interface, except at the jet centerline intersection with the pool bottom.

Air also clearly reduces the resonance frequencies of the pressure waves inside rock fissures. This is also the effect of a mobile block, when compared to a fixed one. Indeed, the celerity of the pressure waves propagating inside the fissures depends on the fluid properties and on the response of the flow boundaries. The fluid properties are the apparent density and the bulk modulus of elasticity of the air-water mixture. The vibrations of the block responding to a pressure excitation along the fissures correspond to a pseudo-elastic behavior of the boundaries, in a parallel to the water-hammer phenomenon in pressurized conduits. Hence, pressure wave celerities of approximately 70 m/s were observed for strongly aerated jets.

Two numerical models reproduce the dynamic ejection of rock blocks. The first model is derived from a thorough theoretical study of the phenomenon, and includes all the intervening forces into a differential equation. The block responds to the pressure field imposed by the jet, to its immerged weight, and to passive forces which tend to keep it inside its cavity. Of particular importance are the added mass of the block, which reflects the force needed to accelerate the fluid around an immerged moving body, and the resistance of the fluid in the fissure beneath the block to a change in volume. The computed added mass corresponded up to 10 times the mass of the block.

The second model corresponds to adaptations of a physically-based scour method developed previously in the framework of this research at the LCH, in order to consider the influence of air entrainment. It is a straightforward method for engineering practice, with a simplified representation of the forces acting on a rock block. Nevertheless, the forces considered are those relevant for block ejection after rock fissures are widened by a progressive joint break-up. Its application to the scour hole of Kariba dam shows good results, and allows validating the adapted model. The estimates of the scour hole give a bottom elevation at 306 m a.s.l., matching surveys performed in 1981 and 2001.

In conclusion, for the first time, the influence of jet air entrainment on rock scour development, from the air bubbles dissipation in the plunge pool to the dynamic ejection of an impacted block embedded in the rock mass, was investigated with systematic experiments of near-prototype jets. A numerical engineering method now predicts prototype rock scour with a sound reproduction of the physical-mechanical processes in water, rock and air.

Keywords: Air entrainment, rock scour, plunge pool, high-velocity jets, fluid-structure interactions, block stability, dynamic uplift, scour assessment, dam safety.

Résumé

Influence de l'entraînement d'air sur la stabilité des blocs et sur le développement de la fosse d'érosion du bassin de dissipation

L'impact de jets d'eau à haute vitesse sur un bassin de dissipation, tels qu'ils se produisent en aval de déversoirs de barrages à haute chute, peut engendrer l'affouillement des fondations rocheuses. Le processus d'érosion est le résultat de phénomènes physiques complexes qui se produisent successivement. La turbulence joue un rôle majeur, en particulier dans le développement du jet au cours de sa trajectoire dans l'air, mais aussi dans le processus de diffusion dans le bassin, tout comme dans les fluctuations de pression à l'interface eau - roche, et enfin dans la propagation de la pression à l'intérieur des fissures de la roche.

Ces phénomènes ne peuvent être reproduits en modèles réduits sans occasionner des effets d'échelle importants. Ainsi, l'utilisation de modèles à l'échelle du prototype et l'examen des fluctuations des pressions sont le seul moyen d'évaluer correctement l'impact des jets sur le développement de la fosse d'érosion.

L'entraînement d'air influe grandement sur l'ensemble du processus. De l'air est entraîné dans le jet au cours de sa chute et est également entraîné dans le bassin au moment de l'impact. Les bulles d'air dans le bassin influencent la dissipation de l'énergie. Les bulles peuvent également entrer dans les fissures de la roche, où elles changent complètement les propriétés d'oscillation et d'amplification des ondes de pression. La description du comportement des bulles d'air dans les bassins de dissipation et leur influence sur les fluctuations de pression sur l'interface eau-roche et à l'intérieur des fissures sous-jacentes dans des conditions de prototype, n'a jamais été réalisée. L'air possède des propriétés telles que la flottabilité, la compressibilité et la solubilité dans l'eau, qui sont difficiles à évaluer et nécessitent une recherche approfondie.

Depuis 1998, le Laboratoire de Constructions Hydrauliques (LCH) de l'Ecole Polytechnique Fédérale de Lausanne (EPFL) développe une large recherche pour décrire avec précision l'affouillement du rocher dû à des jets à haute vitesse. Ainsi, une installation expérimentale innovante, reproduisant des vitesses de jets prototypes, a permis de décrire l'évolution de la fissuration de la roche, l'éjection des blocs et l'influence de la géométrie du fond, entre autres sujets.

Cette étude améliore la connaissance de l'entraînement d'air, du comportement des bulles et de leur influence au fond de la fosse d'érosion et relie tous les travaux antérieurs. Des expériences employant des jets quasi-prototype ont mesuré les concentrations d'air et les vitesses des bulles dans différentes profondeurs et distances radiales de la couche de cisaillement du jet, ainsi que les pressions dynamiques et les déplacements d'un bloc placé au fond du bassin. Des jets immergés ont été reproduits, activement aérés au niveau de la buse, pour fournir des résultats avec une aération totale connue du bassin, tandis que des jets plongeants, également activement aérés, ont été testés pour représenter un scénario plus réaliste. En outre, le bloc était soit fixe au fond du bassin soit libre de se déplacer, représentant différents degrés d'ouverture et de verrouillage du réseau de fissures de la roche trouvés en pratique.

Cette recherche a révélé que l'air entraîné par le jet influe sur les pressions exercées sur le fond de deux manières opposées. D'une part, le mélange air-eau peut être interprété comme un jet ayant une densité apparente réduite, et donc avec une quantité de mouvement faible. La conséquence en est une diminution de l'énergie cinétique par unité de volume atteignant le fond, qui est convertie en pressions plus faibles que pour un jet similaire mais non aéré. D'autre part, les bulles d'air réduisent les tensions de cisaillement du jet. La vitesse des jets aérés diminue moins vite le long du bassin, ce qui engendre des pressions plus élevées au fond. Ce deuxième effet est dépendant de la profondeur du bassin. L'influence globale de l'aération d'un jet est un équilibre entre les deux, mais les données expérimentales montrent une tendance générale de réduction de la pression, à la fois à l'intérieur des fissures et sur l'interface eau-roche, sauf à l'intersection de l'axe du jet avec le fond du bassin.

L'air permet également de réduire nettement les fréquences de résonance des ondes de pression dans les fissures. C'est aussi l'effet d'un bloc mobile, par rapport à un fixe. En effet, la célérité des ondes de pression se propageant à l'intérieur des fissures est une fonction des propriétés du fluide et du comportement élastique des parois de l'écoulement. Les propriétés du fluide sont la densité apparente et le module d'élasticité du mélange air-eau. Les vibrations du bloc en réponse à une excitation de pression le long des fissures correspondent à un comportement pseudo-élastique des parois, en parallèle au phénomène de coup de bélier dans les conduites sous pression.

Deux modèles numériques reproduisent l'éjection de blocs rocheux. Le premier est dérivé d'une étude théorique du phénomène, et inclut toutes les forces qui interviennent dans une équation différentielle. Le bloc répond au champ de pressions imposé par le jet, à son poids immergé, et à des forces passives qui tendent à le maintenir dans sa cavité. La masse ajoutée du bloc, qui reflète la force nécessaire pour accélérer le fluide autour d'un corps mobile immergé, et la résistance du fluide à une variation de volume dans la fissure sous-jacente, sont d'une importance particulière.

Le deuxième modèle correspond à des adaptations d'une méthode d'affouillement basée physiquement, développée précédemment dans le cadre de cette recherche au LCH, afin d'examiner l'influence de l'entraînement d'air. C'est une méthode directe visant à la pratique de l'ingénierie, avec une représentation simplifiée des forces intervenant sur un bloc rocheux. Néanmoins, les forces considérées sont celles qui sont pertinentes pour l'éjection du bloc après que les fissures des roches soient élargies par leur rupture progressive. Une étude de cas est présentée sur la fosse d'érosion du barrage de Kariba pour valider le modèle, avec de bons résultats.

En conclusion, ce projet évalue l'influence de l'entraînement d'air sur le développement de la fosse d'érosion, depuis la dissipation des bulles d'air dans le bassin de dissipation jusqu'à l'éjection dynamique d'un bloc impacté au fond. Une méthode d'ingénierie est maintenant capable d'évaluer une fosse d'érosion réelle avec une reproduction fidèle des processus physico- mécaniques dans l'eau, la roche et l'air.

Mots-clés: Entraînement d'air, fosse d'érosion, bassin de dissipation, jets à haute vitesse, confinement de jet latéral, interactions fluide-structure, stabilité de bloc, soulèvement dynamique, évaluation de l'affouillement, sécurité des barrages.

Resumo

Influência da emulsão de ar na formação de fossas de erosão e na estabilidade de blocos de rocha em bacias de dissipação

O impacto de jatos d'água de alta velocidade em bacias de dissipação, como é o caso a jusante de vertedouros de grandes barragens, pode causar erosão no fundo rochoso. O processo erosivo é o resultado de fenômenos físicos complexos acontencendo em simultâneo. A turbulência tem um papel fundamental, em particular no desenvolvimento do jato em queda livre, na difusão no interior da bacia, nas flutuações de pressão no fundo e na propagação das pressões nas fissuras da rocha.

Esses fenômenos não podem ser representados em modelos reduzidos sem significantes efeitos de escala. Portanto, observações com escala semelhante ao protótipo combindasas com a consideração das flutuações de pressão são a única forma de avaliar corretamente o efeito do impacto de jatos na erosão do fundo rochoso.

A emulsão de ar influencia todo o processo. O ar é emulsionado pelo jato durante a queda livre e também no ponto de mergulho. As bolhas de ar na bacia influenciam a dissipação de energia. Estas podem igualmente penetrar nas fissuras da rocha, onde elas modificam as propriedades de oscilação e amplificação das ondas de pressão. A descrição, na escala do protótipo, do comportamento das bolhas de ar nas bacias de dissipação e a sua influência nas flutuações de pressão no fundo e nas fissuras da massa rochosa nunca foi estudada. O ar tem propriedades como compressibilidade, solução e empuxo em água, que são difíceis de avaliar e exigem uma investigação exaustiva.

Desde 1998, o Laboratório de Construções Hidráulicas (LCH) da Escola Politécnica Federal de Lausanne (EPFL) desenvolve uma ampla investigação para descrever corretamente os princípios da erosão do leito rochoso devido a jatos em alta velocidade. Uma instalação experimental inovadora foi construída, capaz de reproduzir jatos com velocidade de protótipo. Trabalhos passados descreveram o desenvolvimento de fissuras, a ejeção de blocos, a influência da geometria do fundo, entre outros.

Este projeto contribui para o melhor entendimento das propriedades de emulsão de ar, do comportamento das bolhas e sua influência nas pressões no fundo da bacia, em complementação aos trabalhos passados. Testes foram realizados com jatos em escala quasi-protótipo para medir as concentrações de ar e as velocidades das bolhas em diferentes profundidades e distâncias radiais dentro da camada de mistura do jato, bem como pressões dinâmicas e deslocamentos ao redor de um bloco no fundo da bacia. Jatos submersos foram reproduzidos, ativamente arejados no injetor, para proporcionar resultados com o arejamento total da bacia conhecido. Alternativamente, jatos mergulhando na bacia também foram testados, igualmente arejados ativamente, para representar uma configuração mais realista. Adicionalmente, o bloco foi simulado fixo no fundo ou livre, representando assim diferentes graus de abertura e intrincamento da rede de juntas encontrados na prática.

Esta investigação revela que o ar emulsionado pelo jato influencia as pressões no fundo de duas formas opostas. Por um lado, a mistura ar-água pode ser interpretada como um jato de densidade aparente reduzida, e portanto com menor quantidade de movimento.

A consequência é uma energia cinética por unidade de volume menor, que no fundo é convertida em pressões mais baixas do que seria o caso para jatos de água sem ar. Por outro lado, as bolhas de ar reduzem as tensões de cisalhamento do jato dissipando na bacia. A velocidade de jatos arejados decresce ao longo do tirante d'água numa taxa mais baixa, resultando em velocidades mais altas atingindo o fundo, e portanto maiores pressões. Este segundo efeito obviamente depende da altura d'água na bacia. A influência global do arejamento é um balanço dos dois efeitos, sendo que os dados experimentais mostram uma tendência geral de redução de pressões, tanto nas fissuras quanto na interface água-rocha, com exceção da interseção entre o eixo do jato e o fundo da bacia.

O ar também claramente reduz as frequências próprias das ondas de pressão no interior das fissuras. Esse é igualmente o efeito de blocos móveis, se comparados a blocos fixos. Com efeito, a celeridade das ondas de pressão em propagação nas fissuras é função das propriedades do fluido e do comportamento elástico das paredes do escoamento. As propriedades do fluido em questão são a densidade aparente e o módulo volumétrico da mistura ar-água. As vibrações do bloco reagindo à excitação exercida pelas pressões ao longo da fissura correpondem a um comportamento pseudo-elástico das fronteiras do escoamento, num paralelo com o fenômeno de golpe de aríete em condutas pressurizadas.

Dois modelos numéricos reproduzem a ejeção dinâmica de blocos de rocha. O primeiro é derivado de um estudo aprofundado do fenômeno, e inclui todas as força intervenientes numa equação diferencial. O bloco reage ao campo de pressões imposto pelo jato, ao seu peso submerso e a forças passivas que tendem a mantê-lo em sua cavidade. De particular interesse são a massa adicionada do bloco, que reflete a força necessária para acelerar o fluido no entorno de um corpo submerso em movimento, e a resistência do fluido presente na fissura sob o bloco a uma mudança de volume.

O segundo modelo corresponde a adaptações de um método fisicamente embasado de estimação da erosão, desenvolvido previamente no escopo desta investigação no LCH, de forma a considerar a influência do emulsionamento de ar. Trata-se de uma metodologia prática visada para a aplicações de engenharia, com uma representação simplificada das forças atuantes sobre o bloco de rocha. Contudo, as forças consideradas são aquelas relevantes na ejeção de blocos posterior ao alargamento das fissuras pela própria ação do jato. Um estudo de caso é apresentado sobre a fossa de erosão da barragem de Kariba, para validar o modelo, com bons resultados.

Em suma, a presente investigação estuda a influência do ar emulsionado por jatos no desenvolvimento da erosão no fundo rochoso, desde a dissipação das bolhas de ar na bacia à ejeção dinâmica de blocos da massa rochosa. Um modelo numérico de engenharia é agora capaz de avaliar o desenvolvimento de fossas de erosão em protótipos através de uma reprodução fiel dos processos físico-mecânicos da água, rocha e ar.

Palavras-chave: Emulsionamento de ar, erosão em rocha, bacia de dissipação, jatos de alta velocidade, interações fluido-estrutura, estabilidade de blocos, ejeção dinâmica de blocos, avaliação de erosão, segurança de barragens.

List of symbols and acronyms

Roman capitals

A	Threshold coefficient of Eq. 4.11	[-]
A'	Coefficient of Eq. 4.10	[-]
B	Arbitrary constant of integration	[m]
C	Air concentration (or void fraction) at any point in the plunge pool	[-]
C_a	Total entrained air concentration	[-]
C_{cl}	Air concentration in the jet centerline	[-]
C_I^{max}	Maximum dynamic impulsion coefficient	[-]
C_{max}	Maximum air concentration at the centerline of the uppermost profile	[-]
C_p	Time-averaged pressure coefficient	[-]
C_p^a	Aerated time-averaged pressure coefficient	[-]
$C_{p\,cl}$	Mean pressure coefficient in the jet centerline	[-]
C'_p	Pressure fluctuations coefficient	[-]
C^+_p	Extreme positive pressure coefficient	[-]
C^-_p	Extreme negative pressure coefficient	[-]
D	Pipe diameter	[m]
$D^{\#}$	Non-dimensional bubble diffusivity	[-]
D_p	Bubble penetration depth	[m]
E	Young's modulus of elasticity	[Pa]
E_k	Kinetic energy per unit volume	[Pa]
F	Force	[N]
F_d	Densimetric Froude number	[-]
F_h	Sum of the horizontal forces due to the jet	[N]
F_{hf}	Hydraulic friction forces	[N]
F_r	Froude number	[-]
F_{sf}	Solid friction forces	[N]
F_u	Resistance forces of the fluid to a change in volume	[N]
F_v	Sum of the vertical forces due to the jet	[N]
H	Difference between reservoir and tailwater levels	[m]
K	Coefficient of Eq. 4.16	[-]
K_1	Coefficient of Eq. 5.9	[-]
K_2	Coefficient for radian Gaussian decay of pressures on the pool bottom (Eq. 5.7)	[-]
K_{aw}	Bulk modulus of elasticity of the air-water mixture	[Pa]
L	Jet fall length	[m]
L_s	Turbulent length scale	[m]
P_{xx}	Power Spectral Densities of the pressure fluctuations	[Pa^2/Hz]
Q_a	Jet total entrained air discharge	[m^3/s]
Q_{a1}	Jet air discharge entrained into disturbances	[m^3/s]
Q_{a2}	Jet air discharge entrained at the plunge section	[m^3/s]
Q_{aa}	Jet air discharge at issuance	[m^3/s]
Q_{aw}	Jet total discharge at issuance	[m^3/s]
Q_w	Jet water discharge	[m^3/s]
$R_{C\,max}$	Position of r where C is at its maximum value	[m]

R_e	Reynolds number	[-]
R^2	Coefficient of determination	[-]
S	Area of influence of a pressure measurement position	[m^2]
T	Acquisition time	[s]
T_p	Period of the pressure waves	[s]
T_u	Turbulence intensity in the longitudinal direction	[-]
V	Flow velocity at any point in the plunge pool	[m/s]
V_a	Velocity of the air boundary layer at a given radius r	[m/s]
V_{aw}	Velocity of the jet at issuance	[m/s]
V_w'	Root-mean-square of the water jet velocity at issuance	[m/s]
V_b	Displacement velocity of the block	[m/s]
$\forall_b$	Volume of the block	[m^3]
V_e	Onset jet velocity for air entrainment at the plunge section	[m/s]
$\forall_f$	Volume of the fissure	[m^3]
V_i	Velocity of the jet at the plunge section	[m/s]
V_j	Velocity of the jet at issuance	[m/s]
W	Pool or channel width	[m]
W_e	Weber number	[-]
W_i	Immerged weight of the block	[N]
X_{xx}	Power Spectral Densities of the block position fluctuations	[m^2/Hz]
Y	Pool depth	[m]
Y'	Distance between the pressure transducer and the pool surface	[m]

Roman lower cases

b	Width of plane jets	[m]
b_p	Lateral spread coefficient for plunging jets (Eq. 4.16)	[-]
b_s	Lateral spread coefficient for submerged jets (Eq. 4.14)	[-]
c	Coefficient of Eq. 4.13	[-]
d_1	Distance between pressure transducers on the pool bottom and horizontal fissure	[m]
d_2	Distance between pressure transducers on the vertical fissure	[m]
d_{32}	Sauter diameter	[m]
d_c	Scour (or confinement) diameter	[m]
d_i	Jet diameter at the plunge section	[m]
d_j	Jet diameter at issuance	[m]
d_m	Mean sediment or rock length	[m]
d_{max}	Maximum block displacement	[m]
d_n	Nozzle diameter	[Pa]
e	Stiffness pressure of water	[Hz]
e_c	Conduit wall thickness	[m]
f	Frequency	[Hz]
f_{res}	Resonance frequency (fundamental)	[Hz]
f_{res1}	Resonance frequency for the entire fissure	[Hz]
f_{res2}	Resonance frequency due to partial reflections in the horizontal fissure	[Hz]
g	Gravitational acceleration	[m/s^2]
h	Pool depth above initial riverbed	[m]
h_{up}	Vertical displacement of the block (DI method)	[m]
k	Stiffness constant	[N/m]
k_1, k_2	Fit coefficients	[-]

l_f	Fissure distance	[m]
m_{add}	Added mass of the instrumented block	[kg]
m_b	Mass of the instrumented block	[kg]
p	Pressure	[Pa]
p_e	Perimeter of plane jets	[m]
p'	RMS of the pressure fluctuations	[Pa]
p_{mean}	Time-averaged pressure	[Pa]
$p_{mean\ cl}$	Time-averaged pressure in the jet centerline	[Pa]
p_{max}	Extreme maximum pressure	[Pa]
p_{min}	Extreme minimum pressure	[Pa]
q	Flow rate	[m^2/s]
q_a	Rate of air entrainment	[m^2/s]
r	Radial distance from jet centerline	[m]
r_0	Coefficient for lateral shift from jet centerline for double-Gaussian distribution	[m]
s	Side length of the cubic block	[m]
y	Depth below jet impingement	[m]
y_c	Core development length	[m]
y_i	Distance above the bottom where the impingement region begins	[m]
t	Time	[s]
Δt	Incremental time step	[s]
Δp	Pulse time	[s]
t_c	Scour detph	[m]
t_h	Fissure thickness around the block	[m]
x	Position of the lower face of the block	[m]
x_0	Arbitrary constant (Eq. 7.7)	[m]
z	Block height	[m]

Greek symbols

α	Kinetic energy correction factor	[-]
$\alpha_1, \ldots \alpha_5$	Exponential coefficients (Eq. 6.1)	[-]
β	Total jet aeration (or air-to-water ratio)	[-]
β_1	Jet aeration at issuance	[-]
δ	Boundary layer thickness	[m]
Δx	Distance between probe tips	[m]
μ	Coefficient for lateral shift from jet centerline for simple-Gaussian distribution	[m^2/s]
μ_a	Dynamic viscosity of air	[m^2/s]
μ_{aw}	Dynamic viscosity of the air-water mixture	[m^2/s]
μ_w	Dynamic viscosity of water	[m^2/s]
ρ_a	Density of air	[kg/m^3]
ρ_{aw}	Density of the air-water mixture	[kg/m^3]
ρ_b	Density of the block	[kg/m^3]
ρ_w	Density of water	[kg/m^3]
τ	Time lag of maximum correlation between tips signals	[s]
σ	Surface tension of water	[N/m]
τ_f	Shear stress of the moving block inside fissures	[Pa]
ν	Kinematic viscosity	[m^2/s]

υ	Dynamic solid friction coefficient	[-]
ψ	Term for conversion between kinetic energy and pressure	[-]

Acronyms

CFM	Comprehensive Fracture Mechanics method
CSM	Comprehensive Scour model
DI	Dynamic Impulsion method
EPFL	Ecole Polytechnique Fédérale de Lausanne
FCT	Fundação para a Ciência e a Tecnologia
FFT	Fast-Fourier Transform
HF	Horizontal fissure
IST	Instituto Superior Técnico
LCH	Laboratory of Hydraulic Constructions
PB	Pool bottom
PSD	Power spectral density
RMS	Root mean square
ULISBOA	Universidade de Lisboa
VF	Vertical fissure
ZRA	Zambezi River Authority

This work is dedicated

to my parents

and to my beloved wife Laurence

Table of Contents

List of Figures

List of Tables

1

Introduction

1.1 The rock scour phenomenon

Flood release structures are one of the most important safety devices of dams. They have to prevent uncontrolled overtopping of dams, guiding the excessive discharges during floods downstream in a safe manner. The design of high-head schemes often leads to the choice of high-velocity water jets plunging into a dissipation basin. These jets have approximately the same hydraulic head as the turbines of the powerhouse if it is located close to the dam toe, but several times more discharge. This shows the amount of energy that has to be dissipated at the plunge pool.

A precise assessment of the energy dissipation of impinging jets is, therefore, of crucial concern in the hydraulic design of high-head spillways. A careful design evaluates the need of a concrete-lined stilling basin instead of jet impingement directly in a natural plunge pool on the rock foundation of the original riverbed. Solutions are available to increase jet energy dissipation, such as:

- the implementation of a tailpond dam downstream of the jets which rises the level of the water cushion above the pool bottom;
- the maximization of the jet's trajectory in the air and the minimization of its dimensions (diameter in the case of cylindrical jets or thickness in the case of plane jets) in order to foster jet disintegration. This can be combined with different jet trajectories by the simultaneous use of a number of middle and bottom outlets with gated spillways, with different impact points in the receiving pool to distribute energy dissipation on a larger surface.

An example of the combined use of the above cited solutions is the Karun III dam in Iran (Figure 1.1). The multi-purpose hydraulic scheme has the objectives of flood control, discharge regulation and hydroelectric generation, with an installed capacity of 2'280 MW. The double-arch dam has a total height of 205 m. The flood release devices have a combined discharge capacity of 18'000 m^3/s, through chute, overfall and orifice spillways. The issuing jets plunge into a pool formed by a 60 m high tailpond dam. The 400 m long and 50 m wide pool is concrete-lined (Mahzari et al., 2002).

Figure 1.1. Spillage at Karun III dam in Iran, example of simultaneous use of different jet trajectories and tailpond dam (Photo Iran Water & Power Resources Development Co., 2010).

The distance of the dam foundation to the scour hole as well as the stability of the dam abutments will determine whether the rock can dissipate the jet's energy or if it is necessary to protect the pool bottom with concrete slabs. In both cases, a thorough knowledge of the dynamic pressures acting on the bottom is necessary in order to assess scours evolution or to design the lining.

This research considers the case of jets plunging into a pool with an unlined bottom. The jet energy is dissipated, partly by a hydraulic diffusion process of the jet along the pool, and partly by the rock mass. The energy of the plunging jet produces dynamic pressures on the pool bottom, which will act on the water-rock interface as well as inside underlying fissures of the cracked rock media.

These dynamic pressures have two consequences on the rock mass. They progressively break-up and enlarge rock fissures by hydraulic jacking and fatigue, thus creating and mobilizing rock blocks. Subsequently, the formed rock blocks are ejected from the rock mass into the pool by dynamic uplift. The pressure propagates inside the

rock fissures as pressure waves in pressurized flows, such as the case of water hammer in closed conduits. Resonance phenomena can therefore occur in rock joints, as the pressure waves are reflected at the fissure extremes and at the several intersections of the fissure network. Furthermore the pressure waves travelling back and forth in the fissured media can be superposed and amplified. Bollaert (2002) highlighted the importance of accounting for transient pressures when investigating rock scour, since dynamic uplift pressures acting in fissures around rock blocks up to 1.6 times the kinetic energy of the jet were observed, due to pressure fluctuations and wave amplifications in the fissures.

A scour hole is then progressively formed as a consequence of the number, duration and discharge of spilling events during a certain time, until an equilibrium condition is found at the ultimate scour depth (Schleiss, 2002). In this condition, the energy of the jet is dissipated along the pool and on the rock mass, so that further block ejection no longer takes place.

1.1.1 Air entrainment and rock scour

Plunging liquid jets can entrain air into the receiving pool. This phenomenon is of interest in many engineering domains, from industrial processes to environmental phenomena, and might be desired or not depending on the case. Air entrainment is influenced by the formation of disturbances on the jet's surface (Ervine, 1998; Zhu et al., 2000), which is strongly related to the turbulence intensity of the jets.

The jet, issued with input parameters such as discharge, velocity, characteristic dimension and initial turbulence intensity, travels form the releasing structure to the pool surface following ballistics theory. If the vertical component of velocity is predominant, the jet velocity in the air is increased and the transversal section is reduced by gravitational acceleration. Meanwhile, along this trajectory, disturbances are progressively formed on the jet surface as turbulence overcomes surface tension. These disturbances are a source of aeration to the outer region of the jet. They grow outwards, enlarging the jet total diameter, and also inwards, decreasing the undisturbed, non-aerated region of the jet, called the jet core. If the core is totally disintegrated in the air, the jet becomes a series of water packets before plunging into the pool (Ervine et al., 1997), and the erosion potential is consequently greatly reduced.

The jets considered in this study are turbulent and impact the pool surface with a solid core and high velocity. At the impact with the pool, independently from the formation of the aerated outer region of the plunging jet, a second aeration mechanism takes place. Additional air is entrained around the jet perimeter plunging into the water surface. Thus, a large amount of air is entrained by the jet into the plunge pool, which influences all phases of the scour process.

Contrary to water, air is a very compressible fluid. Air is also strongly affected by buoyancy forces inside water due to its density being 3 orders of magnitude lower. Buoyancy may influence the diffusive process of aerated jets in the pool, since the air bubbles tend to rise back to surface, thus counteracting the flow and intensifying energy dissipation. On the water-rock interface, Ervine and Falvey (1987) suggest that the mean

pressures due to the impact of aerated jets are reduced compared to similar non-aerated jets, as a consequence of a lower apparent density of the air-water mixture. In other words, aerated jets have a lower momentum compared to clear-water jets.

Inside rock fissures, air has a direct influence of pressure wave celerity and thus changes the behavior of pressure waves propagation. According to Bollaert (2002), air can be present inside the rock fissure network in three different ways, namely, free air bubbles, air pockets mainly located at local high points and dissolved air in water. Air dampens pressure fluctuations by consecutively compressing and decompressing. Additionally, air changes the resonance phenomena due to modifications it imposes on fluid properties, such as apparent density and bulk modulus of elasticity.

The influence of the jet air content on the equilibrium scour hole of loose granular material was studied experimentally by Canepa and Hager (2003). The results were expressed as a function of a modified Froude number which takes into account properties of air, water and sediments. They state that, if jets of the same water discharge and increasing air discharges are compared, the aerated jets produce deeper scour holes. On the other hand, if jets with the same total discharge and increasing air contents are considered, jet aeration results in lower scour depths.

In a discussion of their work, Manso et al. (2004) pointed out that adding air discharges to the same water discharge generates jets with increased kinetic energy, while jets of the same total discharge and increasing aeration have lower kinetic energy, which explains the results. The latter procedure makes it easier to transfer the results to prototype situations. This is because the velocity of the air-water mixture is maintained constant for the compared jets. Indeed, the energy input of the whole scour process is at the plunge section of the jet with the pool and, in real cases, the jet velocity is equal to the water velocity as far as the core of the jet persists at the impact point.

Summarizing, rock scour formation is a complex phenomenon involving the characteristics of three phases, namely water, air and rock. The turbulence of the impacting jet plays a major role, from air entrainment to the pressure fluctuations at the water-rock interface and transient pressures inside fissures. The phenomenon depends thus on Weber, Reynolds and Froude numbers, and all attempts of reproducing this process on a reduced-scale model would result in significant scale effects.

1.2 Background and purpose of the present research

This thesis research is performed in the scope of a long-term research topic at the Laboratory of Hydraulic Constructions (LCH) of the Ecole Polytechnique Fédérale de Lausanne (EPFL), where rock scour has been studied systematically since 1998 resulting in 3 previous PhD theses (Table 1.1).

Table 1.1. Conducted research investigations on rock scour at LCH-EPFL with indication of main focus

Bollaert (2002)	Manso (2006)	Federspiel (2011)	Current research
Joint fracturing and block uplift	Pool geometry	Block response	Influence of air entrainment
1D and 2D closed-end and open-end	1D closed-end	3D block geometry	3D block geometry
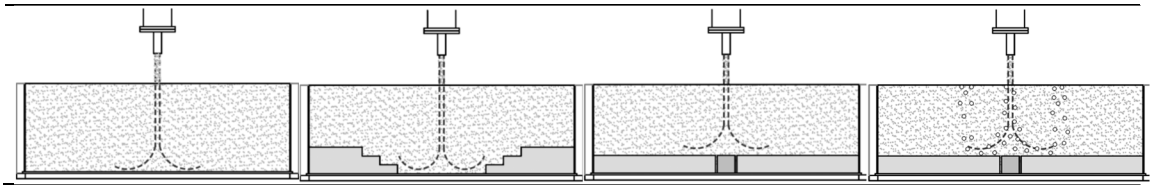			

The research on rock scour at LCH-EPFL relies on three basic principles. The first is the implementation of systematic **near-prototype experiments** of high-velocity jets impinging on a plunge pool. The objective is to minimize, and eventually rule out, scale effects related to the physical modeling of rock scour by reproducing near-prototype jet conditions of velocity and turbulence. The generated pressure signals at the bottom and inside fissures are thus representative of prototype pressure spectra.

The second principle is the consideration of **pressure fluctuations and transient pressures inside the fissures**. It has been shown that pressure fluctuations have to be taken into account for a correct assessment of the stability of concrete-lined stilling basins (Fiorotto and Rinaldo, 1992b) and the response of rock blocks at plunge pool bottoms (Bollaert, 2002). Furthermore, Bollaert (2002) concluded that the hydraulic fracturing of rock joints is the result of one of two possible mechanisms: brittle failure of rock joints, generated by short-duration pressure peaks, or fatigue resulting from cyclic loadings.

The third principle is a thorough **physical understanding of the reproduced phenomena**. Due to the complex nature of rock scour, empirical relationships are site-specific and can rarely be used in situations other than the one for which they were developed. Only a sound assessment of the physical processes results in numerical methods that can be transferred to different prototype conditions.

In this context, Bollaert (2002) developed the Comprehensive Scour Model (CSM), based on experiments with plunging high-velocity jets impinging on 4 closed-end and 1 open-end joint geometries at a flat pool bottom, where dynamic pressures were assessed. The CSM is a physically-based model that reproduces the scour process with three modules. The falling jet module reproduces the trajectory of the jet through the air, the plunge pool module represents jet dissipation in the plunge pool and the rock mass module represents the forces acting on the rock. The latter is divided into the Comprehensive Fracture Mechanics method, in which cracking propagation is modeled, and the Dynamic Impulsion method, where block uplift is reproduced.

Later, Manso (2006) studied the influence of the pool bottom geometry and consequent induced flow patterns on the dynamic pressures at the water-rock interface and inside closed-end joints. A lateral confinement of the plunging jet due to the pool

geometry is closer to reality after an initial scour hole is formed. Pool bottom confinement reduces the pressures on the rock due to an increase of energy dissipation. The jets are deflected upwards, creating additional shear with the impinging jet.

More recently, Federspiel (2011) improved the representation of the rock mass, in order to reproduce a 3D rock block embedded on the bottom of the plunge pool. He studied the response of rock blocks regarding high-velocity jet impact, including the added mass of the block in the formulation of block displacements. The added mass reflects the virtual force due to the inertia of the fluid that must be accelerated together with an immerged solid body.

The current reproduction of the scour phenomenon represents extensively the water and rock processes and considers only passive air entrainment. However, so far no systematic study has been performed regarding air entrainment of high-velocity jets and its influence on scour formation in fractured rock. The present research fills this lack of knowledge by testing plunging and submerged jets, actively aerated, impinging on a fixed or movable block embedded at the pool bottom. While submerged jets allow the assessment of the results with a known aeration of the pool, which is actively added to the jets, plunging jets represent a situation that is closer to reality.

1.3 Methodology and structure of the report

The research methodology is visualized in Figure 1.2. It addresses the three principles as mentioned in the previous section. It is composed of the following elements:

- A sound theoretical study of the physical-mechanical processes related to the effects of jet air entrainment on each process of the scour formation.
- Systematic experiments on a large facility, where aerated high-velocity jets are reproduced and impinge on a cubic block, whether on its center or directly on the fissure created on one of its sides. Air bubble parameters are measured in the shear layer of the jet in the plunge pool. Furthermore, dynamic pressures acting on the block and its displacements are observed. Fixed and mobile blocks are distinguished, reflecting rock joints that were completely or not yet previously fully opened by hydraulic jacking. Plunging and submerged jets are also compared. The experimental study addresses in detail jet and air dissipation across the pool depth, the resulting dynamic pressures around a block and its response.
- Adaptations to the CSM model are proposed in order to take into account the effect of air entrainment, considering the results of the theoretical and experimental studies. Finally the results are highlighted with a study case of the scour at Kariba dam.

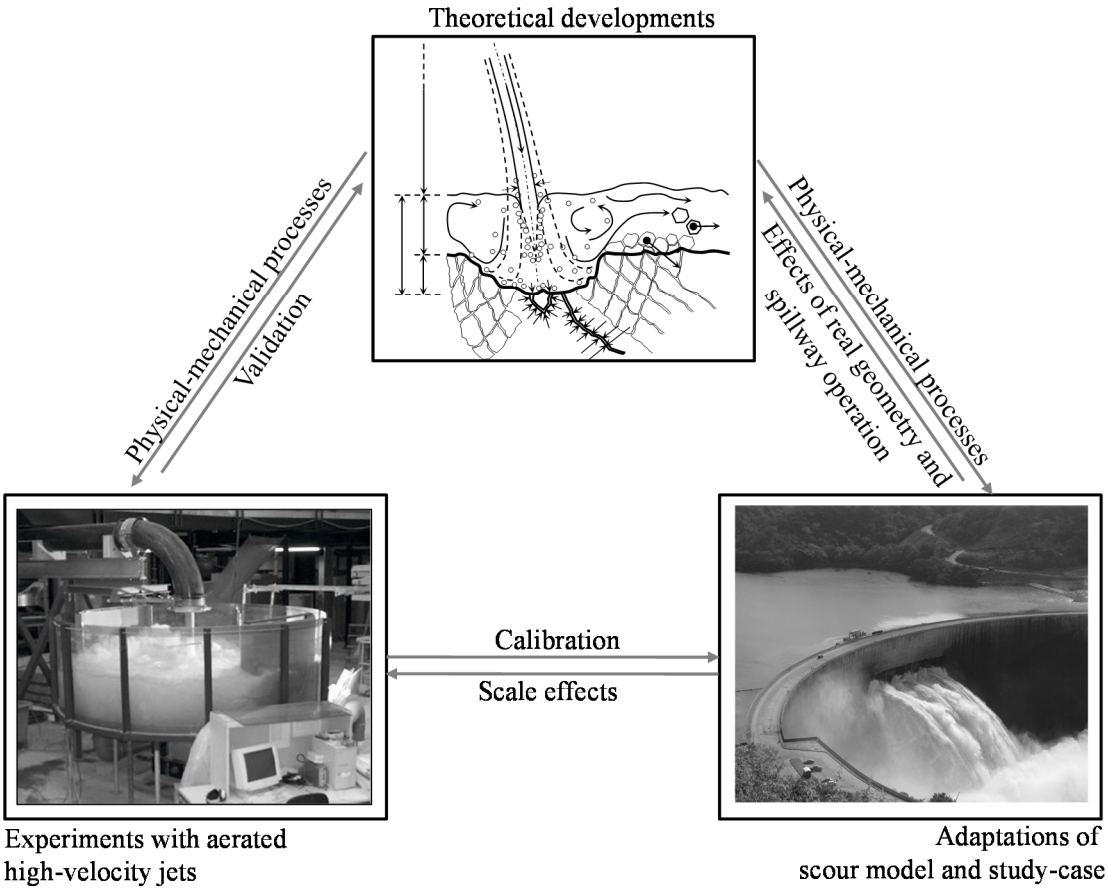

Figure 1.2. Research methodology.

This thesis report is organized in three parts with a total of nine chapters (Figure 1.3):

- In Part 1 the objectives and the experimental set-up used in this research are presented. It is composed of three chapters, as explained below:
  - ✓ Chapter 1 introduces the problematic involved in rock scour and the influence of air entrainment. It reveals the knowledge gap to be filled by the present study and presents the objectives and organization of the research.
  - ✓ Chapter 2 summarizes the state-of-the-art by a literature review of the physical phenomena involved in this study, especially covering in detail jet air entrainment, air bubble dissipation and rock scour processes, as well as the engineering methods available for scour assessment.
  - ✓ Chapter 3 outlines the experimental facility, measurement equipment and test program.

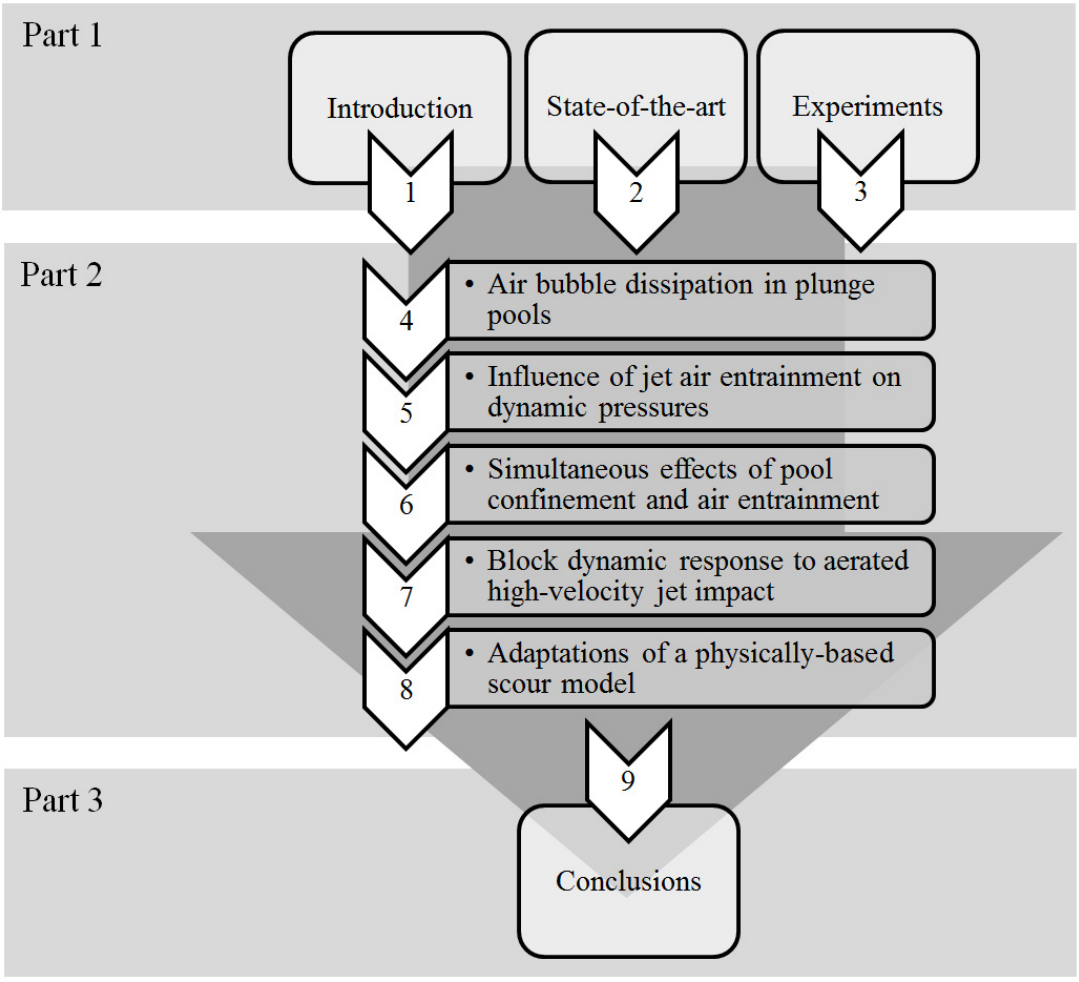

Figure 1.3. Outline of thesis research.

- Part 2 is the core of this research study. Five separate studies are presented, which cover the objective of describing the influence of jet air entrainment throughout the entire rock scour process. The individual studies are logically interconnected and form a consistent ensemble. However, they were conceived as journal papers and thus to stand alone. Therefore they contain some concise reminders of the experimental procedure and of the theoretical concepts relevant for each specific investigation. Part 2 is thus composed of the following five chapters:
  - ✓ Chapter 4 presents an experimental study of air bubbles dissipation in the pool. Air bubble velocities and air concentrations were measured in 33 positions in the experimental facility with state-of-the-art equipment, allowing a better understanding of the dissipation features of the flow and air. The dissipation of the air-water jets along the pool depth is important for scour formation. Hence, Chapter 4 provides the first essential input for the description of the phenomenon and explains under which conditions the jet impacts the pool bottom.
  - ✓ In Chapter 5, the dynamic pressures acting on the water-rock interface and inside underlying fissures due to aerated high-velocity jets are presented. The dynamic pressures were measured at 12 positions uniformly distributed

along one half of a cubic block embedded on the pool bottom, namely 4 on the top of the block and 8 inside the fissures around it. The results allow the pressure field around rock blocks, which lead to dynamic uplift and consequently to ejection from the rock mass, to be reproduced.

- ✓ In Chapter 6, dynamic pressures around a block resulting from the impingement of aerated high-velocity jets on laterally confined pool bottoms are presented. The dynamic pressures acting on the rock mass are deeply influenced by the geometry of the pool bottom, which may enhance jet energy dissipation along the pool depth. Additionally, in this chapter the differences between fixed and free blocks are highlighted. Fixed blocks represent fractures that are not fully intersected, while free blocks are a result of interconnected fissures and are thus available to be ejected from the rock mass.
- ✓ Chapter 7 presents the dynamic response of a block impacted by aerated high-velocity jets. The block displacements are related to simultaneous measurements of dynamic pressures resulting from jet impact and the other forces involved in block stability. A numerical model of the block vibrations was derived as a result of the theoretical analysis and validated with the experimental data.
- ✓ Finally, in Chapter 8, adaptations are proposed to a physically-based scour model in order to account for jet air entrainment. For this, the Comprehensive Scour Model originally developed by Bollaert (2002) and Bollaert and Schleiss (2005) is modified in view of the findings of the present research study. A case study with the prototype data of scour at Kariba dam was performed in order to validate the new model.

• Finally, in Part 3 conclusions of this research project and recommendations for future developments on rock scour assessment are given in Chapter 9.

The appendices at the end of the document provide graphical representation of selected results. The experimental data obtained in this research are available on request at the Laboratory of Hydraulic Constructions of the Ecole Polytechnique Fédérale de Lausanne (LCH-EPFL).

2

State-of-the-art on jet aeration and rock scour

This chapter provides a literature review focused on the physical phenomena involved in scour formation, downstream of aerated jets. Rock scour is the result of various consecutive processes, from jet development along the free-fall trajectory, passing through the two-phase flow of the dissipating air-water jet in the pool, to fluid-structure interactions in the rock mass. A scour hole forms progressively with the spillway operation in time, up to a point where energy dissipation is no longer capable of producing rock erosion. In the end of the Chapter, the engineering methods available for scour assessment are discussed.

2.1 Main processes and parameters of rock scour

The energy dissipation of jets created by dam spillways is an important concern in hydraulic engineering. This dissipation can occur in a lined stilling basin specially conceived for this purpose, or, if the local conditions allow, in a plunge pool which is created directly over the rock foundations. The energy to be dissipated is often higher than that of an eventual powerplant associated to the scheme. Scour holes of the order of 80 m are documented (Noret et al., 2013), which can compromise the safety of the structure.

Rock scour due to plunging water jets is a complex phenomenon, composed by a series of processes that occur consecutively. The evolution of the subsequent plunge pool geometry is the result of physical-mechanical interactions between three phases involved in the process, namely water, air and rock. Figure 2.1 shows a sketch of the physical processes that take place from jet issuance to the flow of water and segregated rocks downstream.

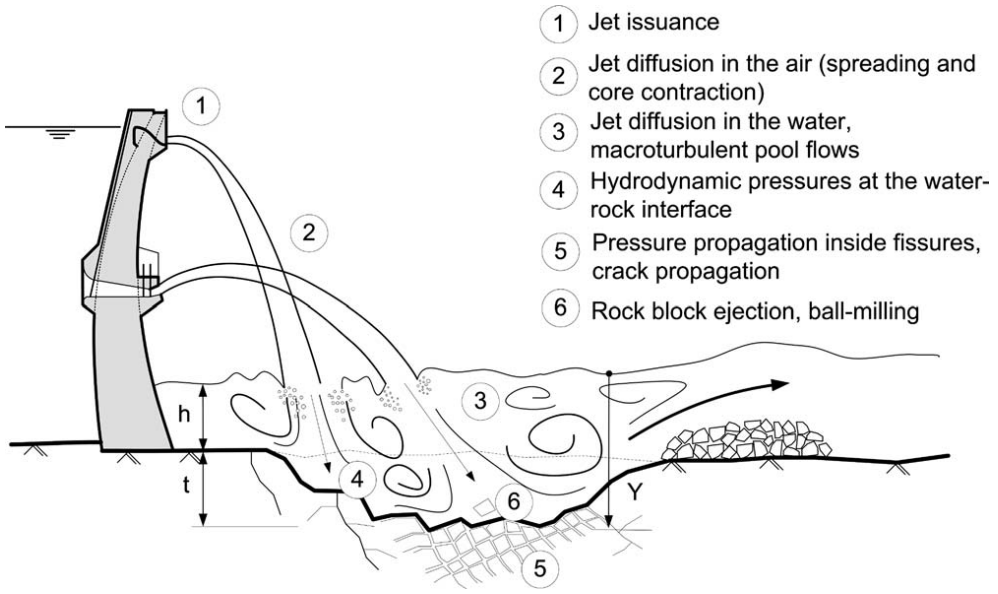

Figure 2.1. Main physical processes involved in rock scour; from Manso (2006).

The jet characteristics at issuance result from the hydraulic design of the structure. It sets the parameters that will be used to describe the jet, such as the water discharge Q_w, velocity V_j, jet diameter d_j (or thickness for plane jets), turbulence intensity T_u and the issuing angle θ_j. For a complete analysis of the jet, one should also add the water density ρ_w and kinematic viscosity ν.

Jet trajectory during the free-fall in the air is governed by ballistics. Thus, gravitational acceleration g and travel length L must be accounted for. The total jet diameter tends to increase, while disturbances in the outer layer are progressively created by the jet internal turbulence. In opposition, water surface tension σ contributes to keep

the core compact. Air is entrained inside the empty spaces between the disturbances and flows downstream with the jet.

The parameters and physical processes described above determine under what conditions the jet impacts the pool at the plunge section. The main parameters at the plunge section are the jet diameter d_i, jet velocity V_i, specific discharge q and the angle of impact θ. In addition to the air entrained upstream, a large amount of air enters the plunge pool at the moment of impact. The total air entrained into the pool is represented by the air-to-water ratio (or simply jet aeration), defined as:

$$\beta = \frac{Q_a}{Q_w} \tag{2.1}$$

where Q_a is the total air discharge entrained by the jet into the pool. The associated void fraction C_a determines the concentration of air over a characteristic cross-section of the jet entering the pool.

$$C_a = \frac{Q_a}{Q_a + Q_w} = \frac{\beta}{1 + \beta} \tag{2.2}$$

The conditions at the plunge section are of particular importance for scour analysis. The kinetic energy of the jet at this point determines the input of energy and governs the whole process.

Jet diffusion which takes place in the plunge pool is a function of the pool depth Y. Progressive formation of the scour hole confines the jet, which must be taken into account subsequently to the first year of spillage. Pool geometry might induce currents that contribute to energy dissipation and should also be considered (Manso, 2006). Confinement of the pool bottom may be characterized by a confinement diameter d_c and a scour depth t_c, so that $Y = h + t_c$ where h is the initial pool depth. Also, the air bubbles entrained at the plunge section tend to rise back to the surface, in opposition to the water flow and might contribute to energy dissipation (Manso, 2006).

Diffusion in the plunge pool dissipates a part of the jet energy. The remaining energy is responsible for the dynamic pressures applied on the pool bottom. The geomechanic characteristics of the rock foundations, the joint network patterns and fissures dimensions are of great importance to determine the scour development. Pressures applied on the bottom of the plunge pool propagate through the rock fissures. Bollaert (2002) showed that pressure wave propagation inside fissures may lead to pressure amplification. He revealed two different mechanisms of crack propagation: by brittle failure and by fatigue. The former is due to short duration peaks, while the latter depends on cyclic loadings. The actual influence of air inside rock fissures is not yet clear and is addressed in detail in the present research project.

Eventually, fissures will propagate until they are completely open. This means that they form rock blocks, which can be ejected from the rock mass as a result of the integration of the pressures on its top and through the fissures and of the resistance against the displacement (Federspiel, 2011). Both for the cracking of rock joints and for block

ejection, the work of Bollaert (2002) showed the importance of considering pressure fluctuations instead of only mean pressures. The free rock blocks will then be transported downstream by the flow, where they might form a deposition that contributes to elevate the water level in the pool. If the blocks are too heavy, they will remain in the scour hole, impacting one another and also against the pool bottom until, after their sizes are diminished by abrasion, they are small enough to be transported.

The scouring process will continue as a function of the spillage discharges and time duration until the pool depth and the rock mass are capable of dissipating the jet energy. In this situation, the equilibrium or ultimate scour depth is reached (Schleiss, 2002).

2.2 Free-falling jet

The free-falling jet is the first process of scour formation and determines the energy and turbulence conditions at the plunge section. These conditions dictate jet dissipation and air entrainment characteristics. The development of aerated water jets in the air has been extensively described (Ervine and Falvey, 1987; Pfister and Hager, 2010; Pfister et al., 2011).

Ervine et al. (1997) depicted two opposed properties that govern the flow of water jets in the air: stability and internal turbulence. Stability is obtained by surface tension and keeps the jet compact. On the other hand, internal turbulence creates lateral spread of the jet by the formation of disturbances on the jet surface, increasing with the distance from the issuance section. Jet surface disturbances increase the jet's outer diameter d_{out}, according to the following empirical expression (Ervine and Falvey, 1987):

$$\frac{d_{out}}{x_L} = 0.38T_u \tag{2.3}$$

where x_L is the distance from the issuance section. The turbulence intensity is obtained by dividing the RMS of the longitudinal velocity fluctuations V_j' by the mean longitudinal velocity V_j.

Simultaneously, the surface disturbances gradually reduce the undisturbed region in the center of the jet named the jet core. Hence, a typical cross-section of the falling jet is composed of a disturbed, aerated outer layer, which is the visible part, around a non-aerated, compact core. If the fall length is large enough, the disturbances reach the jet centerline and the core vanishes. In this case, the jet is said to be completely developed or broken and is formed by discrete droplets. The broken jet penetrates much less into the pool and its erosion capacity is deeply reduced.

The free-falling jet is accelerated and the equivalent cross-section is contracted by gravity, and reaches the plunge pool surface with velocity V_i and diameter d_i:

$$V_i = \sqrt{V_j^2 + 2gL} \tag{2.4}$$

$$d_i = d_j \sqrt{\frac{V_j}{V_i}} \tag{2.5}$$

Note, however, that gravitational acceleration is relevant for jets issued from a relatively high position above the pool surface, where the vertical component of velocity becomes significant. This differs, for instance, from jets issued from bottom outlets and some ski jumps that impact the receiving pool with a predominantly horizontal velocity. Schemes of typical spillways creating impinging jets are shown in Figure 2.2.

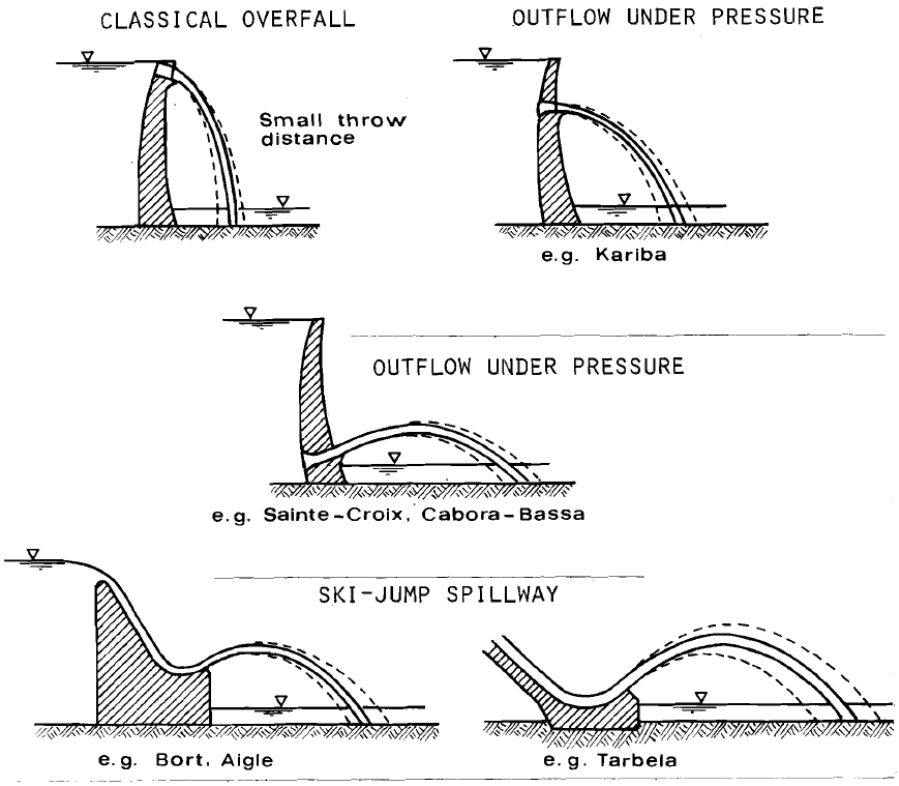

Figure 2.2. Types of spillways with jets according to Whittaker and Schleiss (1984).

2.3 Air entrainment mechanisms

The plunge section is also where the air content is transferred into the pool. Air entrainment by liquid jets is a phenomenon of interest not only for hydraulic engineers. As a matter of fact, plunging jet flows have wide applications such as mixing and stirring chemicals in industry, cooling systems of power plants, plunging breaking waves, amongst others (Brattberg and Chanson, 1998). Many researchers contributed to explain and quantify air entrainment of plunging jets. A non-exhaustive list includes Chanson and Toombes (2003), Cummings and Chanson (1997a), Davoust et al. (2002), Ervine et al. (1980), McKeogh and Elsawy (1980) and McKeogh and Ervine (1981).

Comprehensive reviews on the air entrainment processes were performed by Bin (1993), Ervine (1998) and, more recently, Kiger and Duncan (2012). Ervine (1998) focused on the air entrainment mechanisms of turbulent flows found in hydraulic structures. He outlined three mechanisms of plunge point aeration.

The *first mechanism* refers to the disturbances of the jet outer surface impacting the still water surface. Air is present in the disturbances in the outer layer of the falling jet, as explained before, and flows downstream with the jet. It is reasonable to state that this mechanism depends on jet velocity and turbulence. According to Ervine (1998) air is entrained into the pool within the jet disturbances, with a rate proportional to V_i^3. The following expression is proposed for the rate of air entrainment per unit jet width q_a:

$$q_{a1} = k_1 \left(\frac{V_i^3}{g}\right) T_u^2 \tag{2.6}$$

The *second mechanism* represents the air boundary layer which is entrained by the jet into the pool, independently from the existence of a disturbed outer region. The entrainment is caused by a discontinuity in the water meniscus between the perimeter of the jet and the pool. In this region, an induction trumpet is formed, from where outside air is entrained by the jet (Chanson, 1997). Ervine (1998) found the following expression for the air boundary layer entrainment:

$$q_{a2} = 1.73 \left(\frac{\nu}{2g}\right)^{\frac{1}{2}} V_i^{\frac{3}{2}} \tag{2.7}$$

which shows that this mechanism is proportional to $V_i^{3/2}$, in contrast with jet surface disturbance mechanism as mentioned before. A very similar result was found theoretically by Sene (1988):

$$q_{a2} = \frac{1}{3}\left(\frac{2\mu_a}{\rho_w g \sin\theta}\right)^{\frac{1}{2}} V_i^{\frac{3}{2}} \tag{2.8}$$

in which μ_a is the dynamic viscosity of air.

The *third mechanism* represents the aeration provided by the foamy surface of the pool, which contributes to the total aeration, particularly at high velocities. This entrainment process is caused by intense turbulence and vorticity in the impacted water surface, enabling additional air to enter the pool. Ervine (1998) derived the following relationship for jets plunging into impacted water inside conduits with diameter D:

$$q_{a3} = k_2 \frac{D - d_i}{\sin\theta} V_i \tag{2.9}$$

Summarizing plunging jet air entrainment, a simple relationship representing precisely the physical processes cannot be found. Different mechanisms exist, with relationships proportional to V_i^3, $V_i^{3/2}$ and V_i. This agrees with previous studies (Van de Sande and Smith, 1973, 1975, 1976), where air entrainment rates changed qualitatively

with certain thresholds of jet velocity and diameter. According to these studies, a high-velocity jet with regard to air entrainment is determined by a Weber number $W_e > 10$. Moreover, Sene (1988) found that the air entrainment rate, proportional to V_i^3, is predominant at low jet velocities, whilst for high jet velocities air entrainment is proportional to $V_i^{3/2}$.

The importance of the issuance characteristics was highlighted by Ohl et al. (2000) and Zhu et al. (2000). They designed particularly smooth nozzles and the onset of air entrainment was avoided for Reynolds numbers R_e beyond 10^5, which is far above the thresholds reported earlier. The inception conditions of air entrainment are usually taken as dependent on an onset jet velocity V_e (Kiger and Duncan, 2012), which ranges roughly between 0.5 to 2.0 m/s for most experimental tests (Bin, 1993; Chanson, 1997; Ervine et al., 1997). The present research, however, focuses on jet velocities well above this limit.

Although it is difficult to establish a physically-based formulation for air entrainment rates, empirical and semi-empirical formulations are available for the air-to-water ratio of turbulent jets. For plane jets, McKeogh and Ervine (1981) propose:

$$\beta = 0.26 \left(\frac{b}{p_e}\right) \left(\frac{L}{d_i}\right)^{0.446} \tag{2.10}$$

where b is the jet width and p_e is the jet perimeter. Accordingly, the air-to-water ratio was proposed for circular jets (Ervine et al., 1997):

$$\beta = K_1 \left(1 - \frac{V_e}{V_i}\right) \sqrt{\frac{L}{d_i}} \tag{2.11}$$

in which the parameter K_1 varies between 0.2 for smooth turbulent jets, and 0.4 for rough turbulent jets.

Brattberg and Chanson (1998) found the best correlation of the experimental data for plane jets in the expression below:

$$\beta = 2.9 \times 10^{-3} \left(\frac{L}{d_i} - 0.52\right) \left(\frac{V_i - V_e}{\sqrt{g d_i}}\right)^{1.8} \tag{2.12}$$

valid for $V_e < V_i < 4$ m/s, and

$$\beta = 5.75 \times 10^{-3} \left(\frac{L}{d_i} - 0.52\right) \left(\frac{V_i - V_e}{\sqrt{g d_i}} + 6.6\right) \tag{2.13}$$

valid for 4 m/s $< V_i <$ 8 m/s.

Although the applicability of these empirical formulas may be limited, it shows that the experimental results reflected the theoretical developments outlined before. It can be seen from Eqs. (2.12) and (2.13) that Brattberg and Chanson (1998) found an intermediate range of jet velocities where air entrainment is proportional to $V_i^{1.8}$ and a superior range where air entrainment varies linearly with V_i, in good agreement with the theory.

Moreover, the ratio L/d_i accounts for the degree of development of the jet, which is, in a certain extent, an indicator of the jet turbulence.

2.4 Jet dissipation in the pool

2.4.1 Single-phase dissipation processes

Turbulent jet flows and jet dissipation within a surrounding fluid are widely described in textbooks. For instance, Tennekes and Lumley (1972) and Pope (2000) cover the basis of turbulent flows, whilst Abramovich (1963) and Rajaratnam (1976) set the foundations of the theory of free jet diffusion. These references can be consulted for a detailed description of the phenomenon.

Albertson et al. (1948) performed extensive tests with air jets. The phenomenon is governed by the shear stresses between the incoming supercritical flow and the subcritical flow of the receiving fluid. The undisturbed jet core is then progressively disintegrated while the jet penetrates the receiving pool. Therefore, two distinct regions of the flow are defined.

The *zone of flow development* extends from the issuance section to the point where the jet core vanishes. This zone of the jet is characterized by almost inexistent velocity decay – the velocities along the jet centerline tend, in fact, to remain constant and keep the issuance velocity, as the jet core remains unaffected by the shear with the surrounding fluid. Also the velocity distribution along the cross-section of the jet is approximately uniform inside the core. The distance from the issuance section to the point where the jet core becomes extinct is named the core development length y_c.

The *zone of established flow* is the region of the jet downstream of core disintegration. In this zone, the centerline velocities decay as a function of the shear stresses with the receiving fluid, while a Gaussian distribution is found in a cross-section of the jet.

The conditions outlined above correspond to a *free jet*, meaning that the receiving fluid is semi-infinite and no boundary influences jet dissipation. This classification was developed by Albertson et al. (1948) for air jets, but corresponds well to water jets. The behavior of turbulent water jets was investigated by Ervine and Falvey (1987) both in the air and inside a water pool.

The influence of a downstream boundary of the pool, as shown in Figure 2.3, was studied by Cola (1965) for submerged water jets, and later by Beltaos and Rajaratnam (1974, 1977) for air jets.

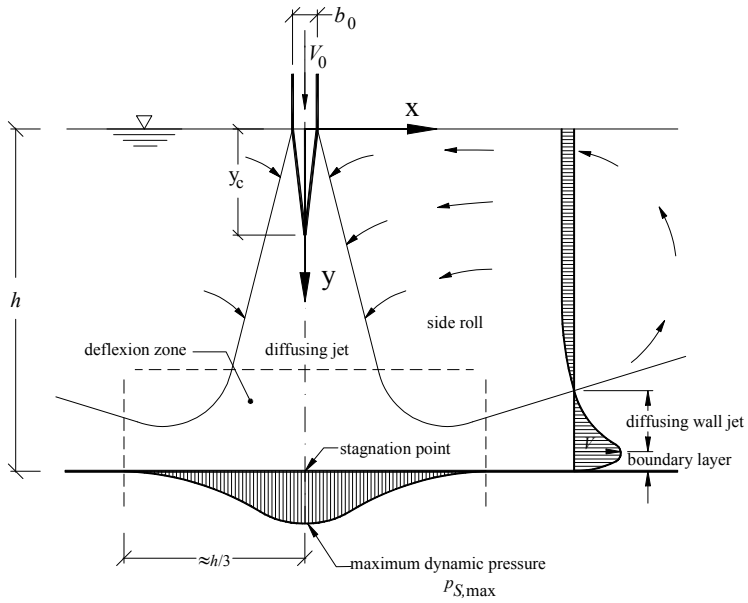

Figure 2.3. Schematic representation of diffusing jet in a pool (Melo, 2002).

Jets impinging on a flat surface are composed of 3 distinct regions:

1. The *free jet*, as explained before, where the jet is developing by shear with the surrounding fluid independently of the presence of the obstacle on the bottom.
2. The *impingement region*, created by the impact of the jet against the bottom. This results in a pressure build-up that decreases centerline velocities rapidly towards zero for a value of $y/d_i = Y/d_i$, and in jet deflection parallel to the obstacle plane.
3. The *wall jet region*, result of jet deflection creating a flow parallel to the bottom.

An analysis of impinging jet behavior is provided in the next section, where experimental data of the present research with water jets is compared to experimental and numerical results of air jets.

2.4.2 Comparison between water and air jets

This section compares experimental data of impinging water jets with CFD simulations and experimental benchmark data of air jets. By the analysis of centerline velocities, it was found that air and water jets behave similarly in the free jet region. On the other hand, results suggest that the *impingement region* has different limits for air jets in comparison to water jets. This section corresponds partially to a published scientific discussion (Duarte et al., 2014) on the paper "CFD analysis of the effect of nozzle stand-off distance on turbulent impinging jets" by Shademan et al. (2013) published in the Canadian Journal of Civil Engineering.

On their paper, Shademan et al. (2013) provide results of CFD simulation of turbulent circular jets impinging vertically on a flat plate. Three different numerical models were used, the realizable eddy viscosity model (k-ε), the shear stress transport model (k-ω SST) and the basic Reynolds stress model (RSM), and compared to experimental data from Rajaratnam et al. (2010) and Giralt et al. (1977). Many

characteristics of the impinging jet were reproduced in good agreement with the experimental data.

The CFD simulations and benchmark data are based on air jets. A comparison to experimental results from the present research on water jets provides some important additional conclusions. The experimental tests used in this comparison simulate submerged water jets issued at a relative distance from the bottom $Y/d_i = 9.58$, where Y is the pool depth and d_i is the jet diameter at issuance. Issuance velocities range from 4.9 to 22.1 m/s. More details on the experimental set up are presented in Chapter 2.

The results of Giralt et al. (1977) for the centerline velocity decay of air jets impinging on an aluminum plate illustrate well the regions of jet development. Figure 2.4 shows the normalized centerline velocities V/V_i as a function of the relative depth below issuance y/d_i. The core region is represented by an almost horizontal line at low depths, where the velocity of the jet remains almost the same as the issued velocity. Subsequently to the disintegration of the core, which takes place at approximately $y = 5.4d_i$, the centerline velocities reduce smoothly with the stresses with the surrounding fluid in the zone of established flow. Later, an abrupt reduction of velocities is observed in the impingement region. The velocities must be reduced to zero at $y/d_i = Y/d_i$, which represents the position of the obstacle.

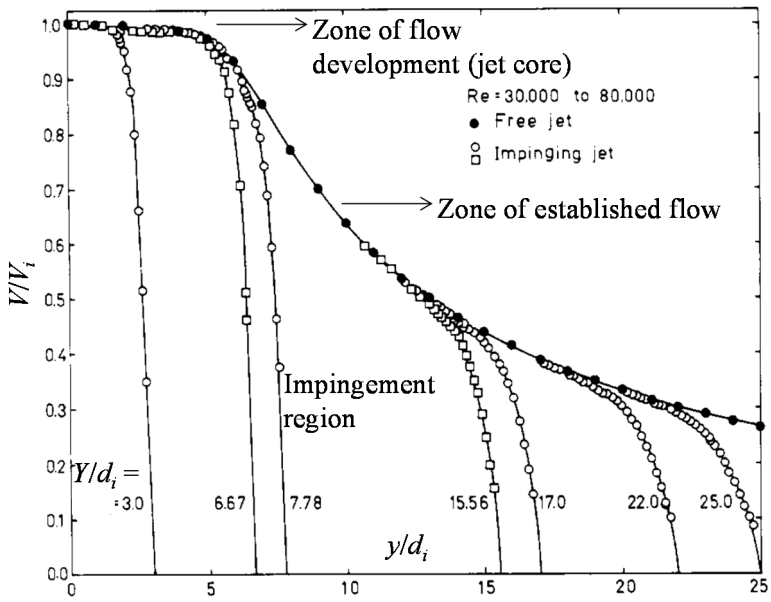

Figure 2.4. Centerline velocity decay of air jets, showing different behavior in the free jet region, divided into jet core and zone of established flow, and in the impingement region; adapted from Giralt et al. (1977).

Arguing that the RSM model is more accurate in the free jet region, Shademan et al. (2013) choose to adopt this model for further investigations. However, if compared to the data of the present research for water jets, the k-ω SST model gives a rather good agreement. Figure 2.5 shows the normalized centerline velocities V/V_i as a function of the relative depth y/d_i, for two jets of Reynolds number comparable to Shademan et al. (2013) who used $R_e = 10^5$ in their computations.

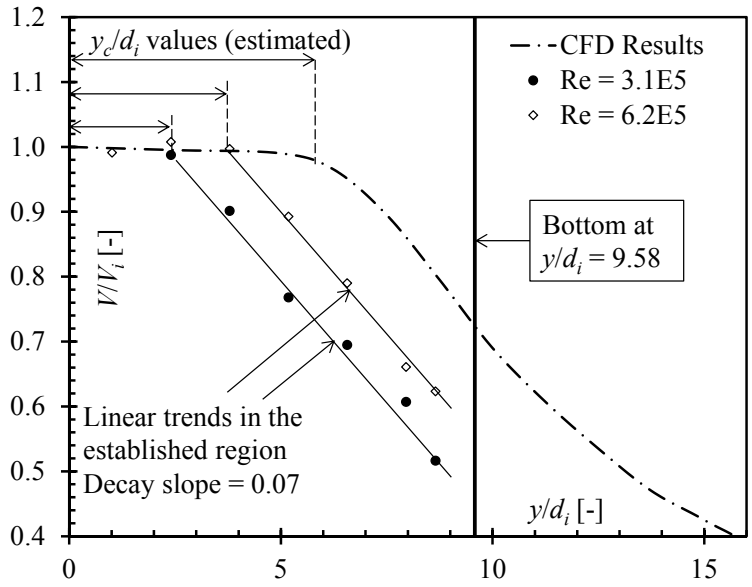

Figure 2.5. Centerline velocity. Comparison of CFD results and experimental data from the present research for water jets.

For each case, the normalized length of core decay y_c/d_i can be estimated as the point in the horizontal coordinate corresponding to the transition between constant and decaying velocities. It can be seen that jets with a different issuance velocity produce different lengths of core decay, which in turn are different from those obtained from Giralt et al. (1977) and from the CFD computations for air jets.

On the other hand, the decay slope in the zone of developed flow seems similar in all cases. If a linear trend is assumed in this region, a decay slope of 0.07 is found from the experimental results for water jets. This is in very good agreement with the CFD computations and with the work of Giralt et al. (1977), who proposed that this slope should be 0.077.

A closer analysis can be done if the results are plotted as a function of y-y_c/d_i, meaning that the *zone of established flow* begins at zero in the horizontal coordinate. This is shown in Figure 2.6, where experimental data for all submerged water jets are shown in the same plot and compared to a linear decay and CFD results. The CFD computations fit very well the data if a y_c/d_i value of 5.8 is used, very close to the analysis from Shademan et al. (2013) of a core development until y/d_i being around 6.

As a conclusion, CFD simulations are able to accurately reproduce centerline velocities for air and water jets in the free jet region. It has to be mentioned that, according to Shademan et al. (2013), computations were performed with incompressible RANS equations. Also in the free jet region, Shademan et al. (2013) call the attention to rather different behavior between the experimental data from Rajaratnam et al. (2010) and Giralt et al. (1977). They correctly suggest that this might be due to different nozzle designs that affect jet evolution. Indeed, different nozzle designs generate different turbulence intensities of the jet at the issuance section. This strongly influences the formation of

surface disturbances in the jet perimeter, and, as a consequence, the shear stresses with the surrounding fluid, as shown by Zhu et al. (2000).

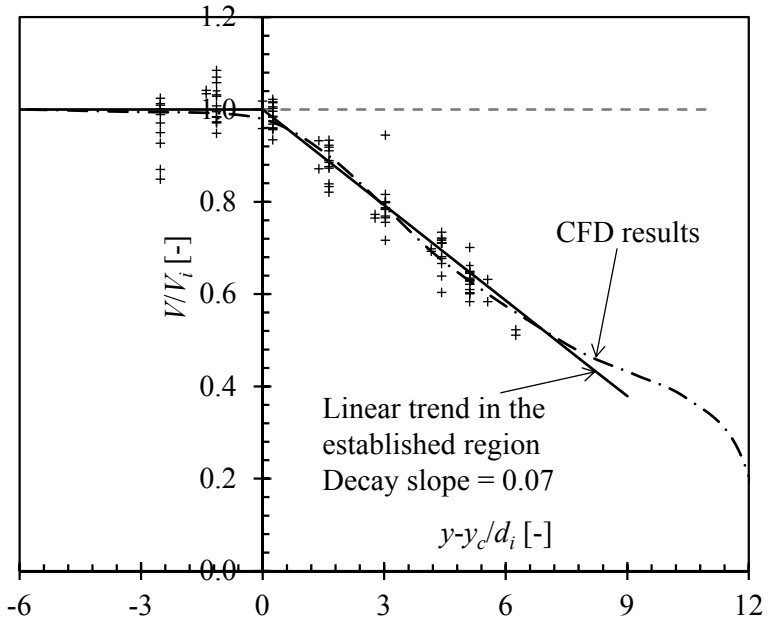

Figure 2.6. Convergence of results for U_c/U_j *versus* x-x_c/D for air and water jets. (+) experimental data from the present research.

Nevertheless, close to the downstream obstacle, in no case a steeper rate of velocity decay was found for the water jets in the positions measured in the present research. For air jets, Beltaos and Rajaratnam (1977) proposed that the impingement region starts at $y_i = 1.2d_i$ above the obstacle, while Giralt et al. (1977) suggested that this result is valid for nozzle heights of less than $Y/d_i = 6.8$, and for larger values

$$\frac{y_i}{d_i} = 0.153\left(1 + \frac{Y}{d_i}\right). \tag{2.14}$$

This suggests that the impingement region has different limits for air and water jets, certainly due to compressibility differences between these two fluids.

2.4.3 Air bubbles behavior in plunge pools

If air entrainment properties received attention of many researchers, fewer studies addressed the behavior of air bubbles in the plunge pool. The resulting two-phase flow is influenced by air properties, such as compressibility, solubility and buoyancy in water. Air bubbles are dragged by the turbulent eddies of the jet and flow downstream. At a certain point, buoyancy overcomes the turbulent drag and the bubbles are deflected laterally and then rise back to surface. If unbounded pools are considered, the flow is composed by a descending cone of small bubbles surrounded by ascending bubbles of larger size (Bin, 1993), as shown in Figure 2.7.

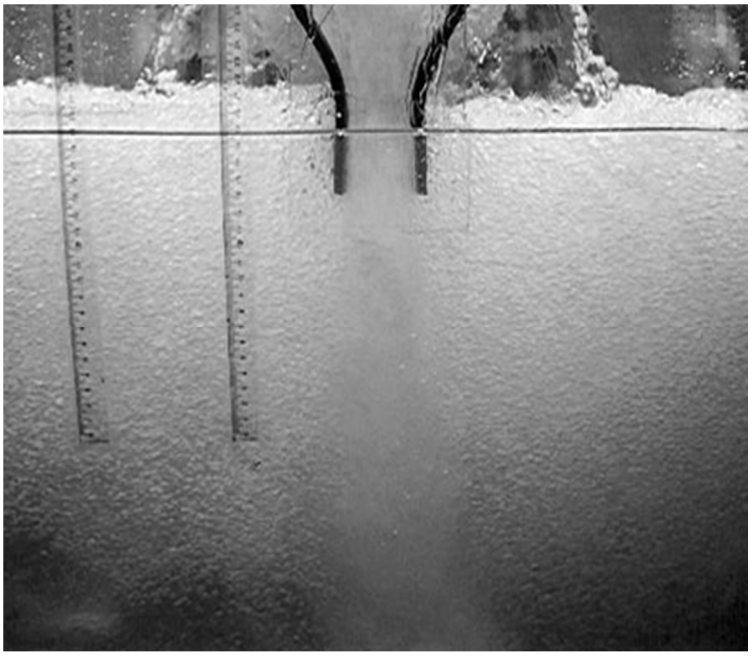

Figure 2.7. Photo of the flow formed by submerged water jets (Melo, 2002).

The buoyancy of air bubbles is often represented by a bubble rise velocity. Effectively, it represents the threshold velocity of the flow below which the bubbles will tend to rise, and hence determines the bubble penetration depth D_p (Qu et al., 2013; Qu et al., 2011). However, Ervine (1998) highlighted that the bubble rise velocity is known approximately for still water but is unknown for turbulent waters, where bubbles are trapped in vortices and rise at a lower velocity than in still water.

The effective bubble rise velocity is dependent on the turbulent drag and on bubbles size. Ervine (1998) stated that the typical size of entrained air bubbles range between 0.5 to 20 mm. Bin (1993) performed a review of several publications and pointed out bubble sizes from 0.13 to 7 mm. McKeogh and Ervine (1981) considered that the bubbles have a typical size of 2 mm, which results in a bubble rise velocity of 0.26 m/s.

McKeogh and Ervine (1981) proposed the following empirical formulation for the bubble penetration depth:

$$D_p = 2.6\left(V_j d_j\right)^{0.7}. \tag{2.15}$$

with dimensions in meters. Moreover, these authors used D_p as the scaling parameter of the aeration properties. They proposed the following expression for the centerline decay of air concentration C:

$$\frac{\mathrm{C}}{\mathrm{C_{max}}} = \frac{1}{1 + 3\left(\frac{y}{D_p}\right)^3} \tag{2.16}$$

where C_{max} is the maximum air concentration, found at the uppermost profile and corresponding approximately to 40%.

Furthermore, McKeogh and Ervine (1981) found that the air concentrations along the cross-section of the jet followed a Gaussian distribution inside the pool, similarly to jet velocities. However, the nature of air entrainment around the perimeter of plunging jets dictates that the radial function of air concentration is represented by a double-Gaussian distribution, with maximum values close to the induction trumpet formed on the jet perimeter. Van de Donk (1981) observed double-Gaussian distributions of air concentrations resulting from plunging jets close to the surface, which become simple-Gaussian distribution with increasing depth.

Maximum values of air concentration close to the induction trumpet of plunging jets were also observed experimentally by Chanson et al. (2004), who proposed, for the air concentration distribution of plunging water jets:

$$C = \frac{\beta}{4D^{\#}\frac{y}{R_{C_{max}}}} exp\left(-\frac{1}{4D^{\#}}\frac{\left(r/R_{C_{max}}\right)^2 + 1}{\frac{y}{R_{C_{max}}}}\right) \times I_0\left(\frac{1}{2D^{\#}}\frac{r/R_{C_{max}}}{\frac{y}{R_{C_{max}}}}\right) \tag{2.17}$$

where I_0 is the modified Bessel function of the first kind of order zero, R_{Cmax} is the position of r where C is at its maximum value and $D^{\#}$ is a non-dimensional bubble diffusivity that was determined from best fit of the experimental results and varied roughly from 3×10^{-3} to 9×10^{-3}.

2.5 Dynamic pressures on the pool bottom

The erosion on the pool bottom is caused by the direct action of dynamic pressures affecting either rock blocks or concrete slabs. A thorough review on scour related to energy dissipators of high-head structures is provided by Whittaker and Schleiss (1984).

Fiorotto and Rinaldo (1992a); Fiorotto and Rinaldo (1992b) investigated dynamic pressures caused by hydraulic jumps on the bottom of stilling basins. They set the standards of dynamic pressure analysis on pool floors by considering time-average pressures, the root-mean-square of the pressure fluctuations and extreme positive and negative pressure values using the kinetic energy of the jet as the scaling parameter for

the pressures, and by analyzing the pressure signals with further statistical moments such as skewness and kurtosis.

The dimensional analysis was used and adapted by other researchers. Federspiel (2011) used the following non-dimensional pressure coefficients to analyze dynamic pressures on the water-rock interface and inside underlying fissures:

$$C_p = \frac{(p_{mean} - p_{atm}) - Y}{\alpha \frac{V_i^2}{2g}} \tag{2.18}$$

$$C_p' = \frac{p'}{\alpha \frac{V_i^2}{2g}} \tag{2.19}$$

$$C_p^+ = \frac{p_{max} - p_{mean}}{\alpha \frac{V_i^2}{2g}} \tag{2.20}$$

$$C_p^- = \frac{p_{min} - p_{mean}}{\alpha \frac{V_i^2}{2g}} \tag{2.21}$$

$$C_p^{max} = \frac{p_{max}}{\alpha \frac{V_i^2}{2g}} \tag{2.22}$$

$$C_p^{min} = \frac{p_{min}}{\alpha \frac{V_i^2}{2g}} \tag{2.23}$$

where p_{mean} is the time-averaged absolute pressure, p_{atm} is the atmospheric pressure, p_{max} and p_{mean} are the maximum and minimum observed pressures, p' is the standard deviation of the pressures and α is the kinetic energy correction factor.

The pressures resulting from hydraulic jumps and affecting concrete slabs of stilling basins were investigated by other researchers, such as Bellin and Fiorotto (1995) and Pinheiro (1995). Although it represents a different situation from what is under investigation in the present study, the physical processes and the methods of analysis have important similarities. Furthermore, according to Rajaratnam (1976), hydraulic jumps are wall jets, as those created by the deflection of impinging jets considered in the present study.

Vertical jet impingement on concrete slabs were investigated by Melo et al. (2006), who focused the analysis on the joints width and location. They assessed dynamic pressures acting on the top and bottom of a net of concrete slabs, providing important results on dynamic uplift. They highlighted that the slabs have a tendency to be ejected

in groups, instead of individually. Pinheiro and Melo (2008) tested aerated submerged jets and proposed a buoyancy coefficient to account for the effect of jet aeration.

A milestone work on the pressure fluctuations on pool floors impacted by plunging jets was performed by Ervine et al. (1997). They tested vertical jets, with velocities ranging from 1.5 to 25 m/s, issued from nozzles with diameters between 25 to 78 mm, and plunging into pools which were 0.1 to 0.5 m deep. They also varied the fall length from 0.51 to 2.63 m.

They proposed that, for varying depths of the plunge pool, the time-averaged pressures at the intersection of the jet centerline with the bottom is composed of a constant value at low depths followed by a convex decrease for deeper pools. The constant region refers to the impact of the jet core which occurs at low depths, and corresponds to 86% of the kinetic energy of the incoming jet. The authors highlighted that, for submerged jets, this value is 100% and the difference is due to energy loss at the plunge section.

Their results indicate a jet core impacting the bottom for pools with depths less than 4 times the jet diameter. For deeper pools, a developed jet impact occurs at the bottom. Ervine et al. (1997) proposed the following relationship for the decreasing pressures:

$$C_p = 38.4(1 - C_a)\left(\frac{d_i}{Y}\right)^2 \tag{2.24}$$

Figure 2.8 shows results of the time-averaged pressure coefficient C_p at stagnation as a function of the relative pool depth Y/d_j from different authors gathered by Bollaert (2002). Submerged and plunging jets are compared, as well as circular and rectangular jets. The resemblance with the centerline velocity of air and water jets as a function of the depth below jet issuance shown in Figure 2.4 - Figure 2.6 is evident and recalls that these pressures are a direct consequence of the conversion of the kinetic energy of the jet reaching the bottom.

Inside rock fissures, pressures propagate as pressure waves in pressurized flows (Bollaert and Schleiss, 2003a). Hence, they are subject to resonance phenomena such as superposition and amplification. Bollaert and Schleiss (2003b) performed extensive experiments of high-velocity jets impinging on 4 closed-end and 1 open-end joint geometries, and examined the two process of rock erosion, namely, crack propagation and block uplift. They concluded that the rock fissures are submitted to two different failure modes: a brittle failure, due to short-duration pressure peaks, and failure by fatigue, consequence of cyclic loading.

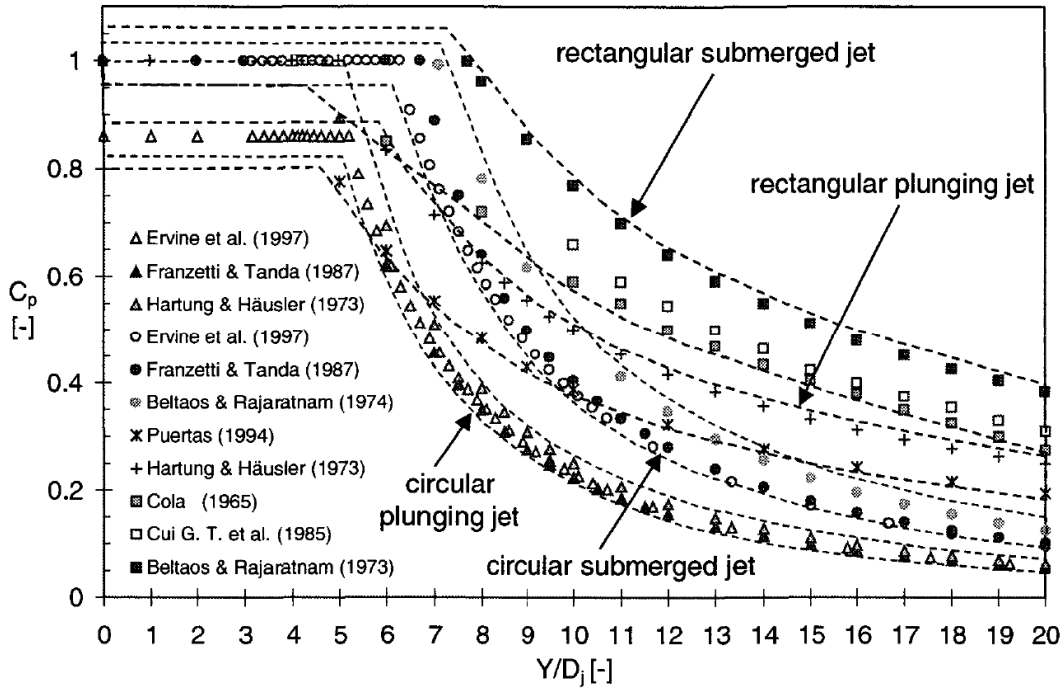

Figure 2.8. Time-averaged pressure coefficient C_p at stagnation as a function of the relative pool depth Y/d_j for various previous researches (Bollaert, 2002).

Yuditskii (1963) performed the first analysis of the block ejection process by considering pressure fluctuations and pressure differences acting on the upper and lower faces of rock blocks. His observation on block movements, as pointed out by Manso (2006), remains up-to-date and is worth mentioning:

"...the block is ejected, not by one pressure fluctuation of high amplitude nor by a succession of pressure fluctuations of high amplitude, but by one large average pressure that is established in the joint underneath the block following a small vertical displacement. The opening of the joint that allows this small vertical displacement is done by one pressure fluctuation of high amplitude."

Manso et al. (2009) investigated the influence of the pool geometry on the pressures generated by plunging jet impact, and compared to a flat bottom case (Manso et al., 2007). Eight laterally confined configurations were tested. They highlight that lateral pool confinement increases energy dissipation by deflecting the incoming jet towards the pool surface. This generates shear between the downward current of the main flow and the upward currents of the deflected flow.

Federspiel (2011) studied the response of a block impacted by plunging high-velocity jets embedded on the bottom of a pool. He emphasized the importance of accounting with the added mass of the block when describing the block movements. The added mass represents the virtual force necessary to accelerate the fluid around an immerged moving body, and is frequently used in naval engineering applications (Federspiel, 2011). Besides, he found that the block displacements are similar to a mass-spring-dashpot system with a forced vibration (Beatty, 2006). The same reasoning was

used by Bollaert et al. (2013a) and Bollaert (2013) to describe block vibrations impacted by water jets.

2.6 Rock scour assessment

2.6.1 Investigations with erodible beds

Experiments with jets impinging on loose granular material are the most direct way to assess scour development. Furthermore, this kind of tests provide information on the scour hole shape and evolution. Nevertheless, model tests with erodible beds have the disadvantage of not representing the degree of interlocking between rock blocks on the rock mass. In fact, it is easier to mobilize individual sediments on the model than ejecting rock blocks on prototype.

Mason and Arumugam (1985) proposed an expression that remains relevant due to the completeness of the data sets employed, originated from 47 physical models with erodible beds and 26 prototype cases:

$$Y = \alpha \frac{H^{\alpha_1} q^{\alpha_2} h^{\alpha_3}}{g^{\alpha_4}\, d_m^{\alpha_5}} \tag{2.25}$$

where H is the hydraulic head determined by the difference between the reservoir and tailwater levels, q is the discharge rate [m^2/s], d_m is the mean particle or rock size, $\alpha = 6.42 - 3.1H^{0.10}$, $\alpha_1 = 0.15 - H/200$, $\alpha_2 = 0.60 - H/300$, $\alpha_3 = 0.15$, $\alpha_4 = 0.30$ and $\alpha_5 = 0.10$. For this reason, Eq. (2.25) is considered the general equation for scour assessment in practical engineering (Bollaert, 2002). Despite its empiricism, it contains most of the parameters considered relevant in the scouring process.

Mason (1989) proposed an adaptation of Eq. (2.25) to represent the influence of air entrainment:

$$Y = \alpha \frac{(1+\beta)^{\alpha_1} q^{\alpha_2} h^{\alpha_3}}{g^{\alpha_4}\, d_m^{\alpha_5}} \tag{2.26}$$

where $\alpha = 3.39$, $\alpha_1 = 0.30$, $\alpha_2 = 0.60$, $\alpha_3 = 0.16$, $\alpha_4 = 0.30$ and $\alpha_5 = 0.06$. Nevertheless, the physical background of replacing the hydraulic head in Eq. (2.25) by the term $(1+\beta)$ in Eq. (2.26) is doubtful.

The geometrical characteristics of the scour hole created by plunging jets on granular sediments were investigated by Pagliara et al. (2008a), and its temporal evolution was described by Pagliara et al. (2008b). These authors used a modified Froude number which considers the properties of water and sediment to explain the results. A similar technique was used by Canepa and Hager (2003) to describe the influence of jet air entrainment in the formation of scour on an erodible bed. The modified Froude number considered properties of water, rock and air.

More recently, Mercier et al. (2014) studied experimentally and numerically the impact of water jets on cohesive soils. They conclude that the formation of a scour hole changes the flow regime in different ways, depending on whether the formed scour hole

is wide or narrow, due to its induced currents. Their conlusions are in agreement with previous findings by Manso et al. (2009) for jointed rigid bottoms.

2.6.2 Methods for rock scour estimation

Whittaker and Schleiss (1984), Schleiss (2002), Bollaert and Schleiss (2003a) and Annandale and Schleiss (2007a, b) provided state-of-the-art reviews on the scour mechanisms and prediction methods. Bollaert and Schleiss (2003a) classified the available engineering methods for scour assessment into 5 groups.

Empirical methods are simple and straightforward, but the lack of a sound theoretical basis might represent a limitation when transporting the results to different prototype situations. Experimental data are correlated to mathematical expressions using tools such as dimensional analysis. Notable examples are the expressions proposed by Mason and Arumugam (1985) and Mason (1989) explained before.

In the case of *semi-empirical methods*, some considerable degree of physical background is incorporated. The theoretical developments assimilated can consist of the jet diffusion theory, the initiation of motion concept applied to rock blocks, and the use of conservation equations. Spurr (1985) developed a method where the jet energy and spillage duration are compared to the erosion resistance of the rock mass. A rather similar approach was used by Annandale (1995), who established an erosion threshold relating the rate of energy dissipation to the material's resistance to erosion. For the latter, he developed the erodibility index, which is a non-dimensional value accounting for several geological parameters from 150 field observations and published data.

The third group includes methods considering *pressure fluctuations* on the pool bottom. It was pointed out that extreme pressures have the potential to cause brittle failure on rock fissures and also play an important role on block uplift, and their consideration is important for a correct description of the erosion process (Bollaert, 2002). Dynamic pressures are considered in works such as May and Willoughby (1991), Hartung and Häusler (1973), and Ervine et al. (1997).

The fourth group considers *pressure differences techniques* capable of imposing a dynamic uplift to the rock blocks. Fiorotto and Rinaldo (1992a) and Melo et al. (2006) employed pressure differences between the upper and lower faces to determine the uplift on concrete slabs.

Finally, the fifth group of methods accounts for *transient pressures* creating progressive opening of fissures by hydraulic jacking and dynamic uplift on rock blocks. At present, the Comprehensive Scour Model (Bollaert, 2002; Bollaert and Schleiss, 2005) is the only engineering model that is entirely physically-based and considers pressure fluctuations acting on the water-rock interface and inside rock fissures. It has the advantage of being conceived with the results of experiments with near-prototype jets.

The developments on scour assessment techniques can be divided into three coordinates, namely water, air and rock. In this context, Bollaert (2002) established a knowledge cube, where the advances on scour prediction are shown graphically. With the

present research, a considerable progress is made in the understanding of aeration effects, with consequent reproduction in an engineering model. The updated knowledge cube is shown in Figure 2.9. The current knowledge, with the contribution of the present work, encompasses jet, pool and rock aeration.

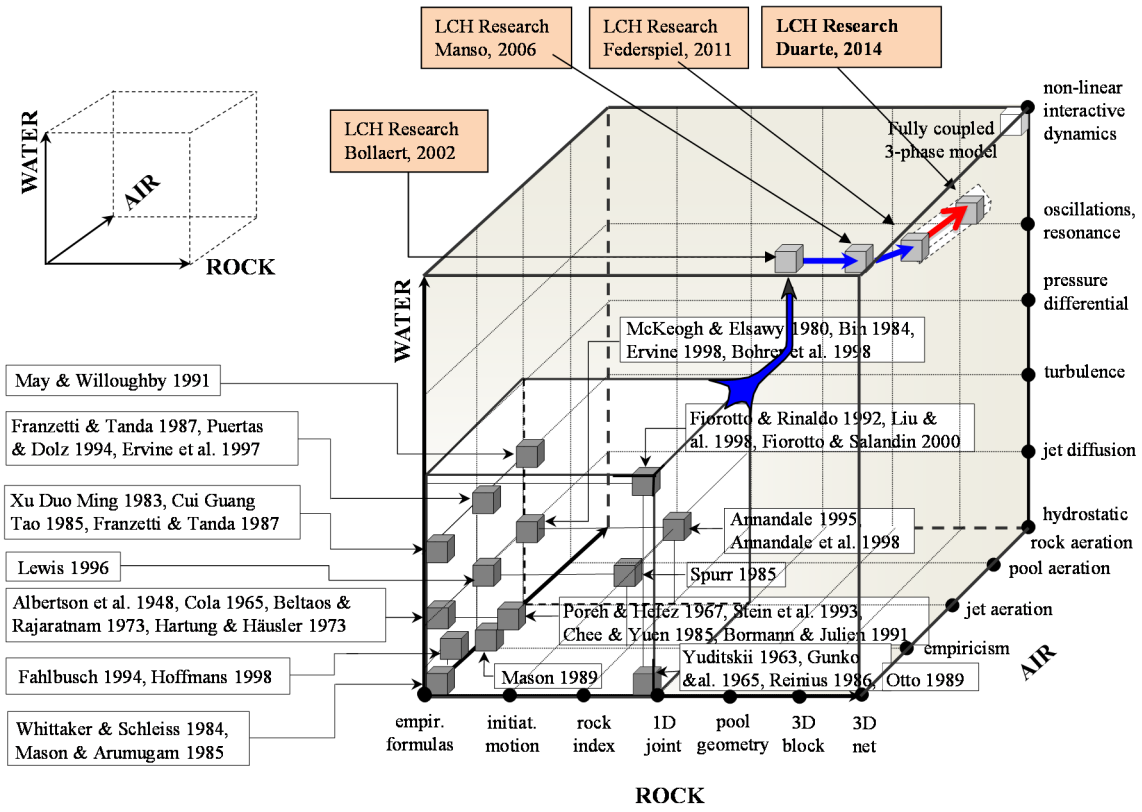

Figure 2.9. Knowledge cube, adapted from Bollaert (2002), Manso (2006) and Federspiel (2011) with the scope of the present research.

3

Experiments

The experimental tests of this research project reproduce aerated high-velocity jets, which dissipate in a receiving pool and impinge on a block embedded at the bottom. Dynamic pressures and displacements of the block are simultaneously assessed. Additionally, air bubble parameters are measured in the jet shear layer region, providing insight on the jet and air bubbles diffusion processes. In this chapter, the experimental facility, the measurement equipment and the undertaken test program are presented.

3.1 Experimental facility

The experimental facility at the Laboratory of Hydraulic Constructions (LCH) of the Ecole Polytechnique Fédérale de Lausanne (EPFL) has been modified and adapted several times since its first use by Bollaert (2002). The current set-up is presented in Figure 3.1. Currently, it consists of the undermentioned items:

- A 63.4 m-head pump which provides the required energy for the jet.
- A 300 mm diameter supply conduit. The conduit is supported by a rigid steel structure, and transports the pumped water from the laboratory's main reservoir to the facility. Due to the laboratory layout, the conduit approaches the experimental facility horizontally, and a 90° bend upstream of the outlet nozzle is necessary to generate the vertical jets. To reduce the flow disturbances created by the conduit bends from the reservoir to the nozzle outlet, a honeycomb grid and an air vent were placed upstream of the last bend, on the highest section of the supply system (Manso, 2006; Manso et al., 2008).

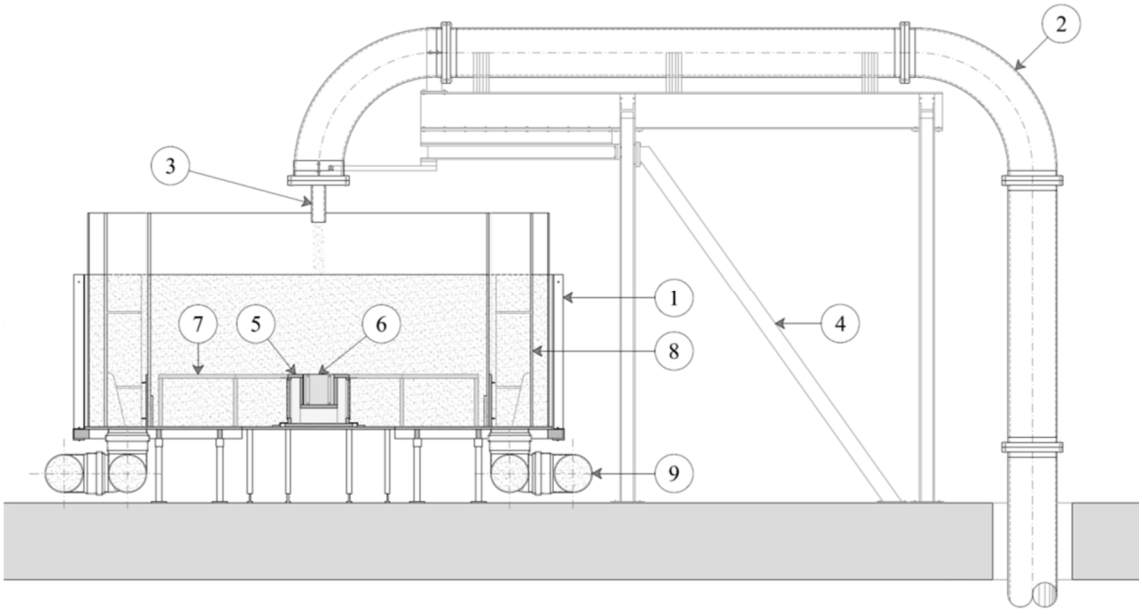

Figure 3.1. View of the experimental facility with (1) plunge pool; (2) supply conduit; (3) outlet nozzle; (4) supporting steel structure; (5) instrumented box; (6) instrumented block; (7) pool bottom; (8) overflow boxes and (9) restitution system; from Federspiel (2011).

- A 72 mm diameter cylindrical nozzle, mounted at the downstream end of the supply system, models and aerates the jet. The jet outlet systems with controlled aeration are the only elements of the experimental facility, which differ from the previous research performed by Federspiel (2011). Detailed information about the nozzle design is provided in §3.1.1.
- The plunge pool is represented by a 3 m diameter cylindrical basin made of Plexiglas walls reinforced with T-shaped steel profiles. The basin is 1.4 m high, supported by a steel table with four adjustable legs. The steel table surface is pre-

perforated to allow modifications in the position of the box/block structure which simulates the rock (Federspiel, 2011).

- The pool bottom is represented by thick, rigid wooden panels mounted 340 mm above the steel platform, and is coincident with the block and box upper surfaces, thus creating a flat pool bottom.
- At opposed sides of the basin, two overflow boxes made of Plexiglas adjust the water level by the insertion or removal of stop-logs.
- The overflow boxes discharge is transported back to the main reservoir by four restitution conduits.
- For the confined test configurations, lateral pool confinement is reproduced by a steel cylinder mounted on the pool bottom (not represented in Figure 3.1, more information can be found in Chapter 6). The cylinder is 0.2 m high and has a diameter of 0.8 m. This confinement corresponds to the "intermediate pool" used by Manso (2006).
- 3D open-end fissures are represented by the implementation of a 200 mm side cubic block which is inserted into a cavity embedded on the bottom. The formed fissure around the block is 1 mm thick, ensured by lateral guides on the vertical faces of the cube. Detailed information is provided in §3.1.2.

3.1.1 Jet issuance

The jets issued at the outlet nozzle are a mixture of controlled amounts of air and water (the tested jet series with air and water discharges is presented in Table 3.4). The water discharge is provided by the supply conduit at the upstream extremity of the nozzle, controlled by the pump operation and measured by an electromagnetic flowmeter type ABB FXE 4000 (COPA-XE). The air discharge is provided at the nozzle by means of 6 small aluminum tubes uniformly distributed along the nozzle transversal section (Figure 3.2). The design of these tubes included a small extension of their upper part inside the nozzle. This forms a depression in the water jet flowing inside the nozzle and thus facilitates the entrainment of outside air. At the same time, it avoids the flow of water through the tubes.

Federspiel (2011) performed passively, uncontrolled aerated tests with this kind of device. For the present research, the aluminum tubes are connected upstream to flexible tubes (Figure 3.3, left), then gathered into one larger tube by a coupling specially designed for this purpose. This larger tube was then connected to the laboratory compressed air system. The air discharge provided at the nozzle was controlled by a ball valve and measured by a flowmeter Wisag Type 2000 (Figure 3.3, right).

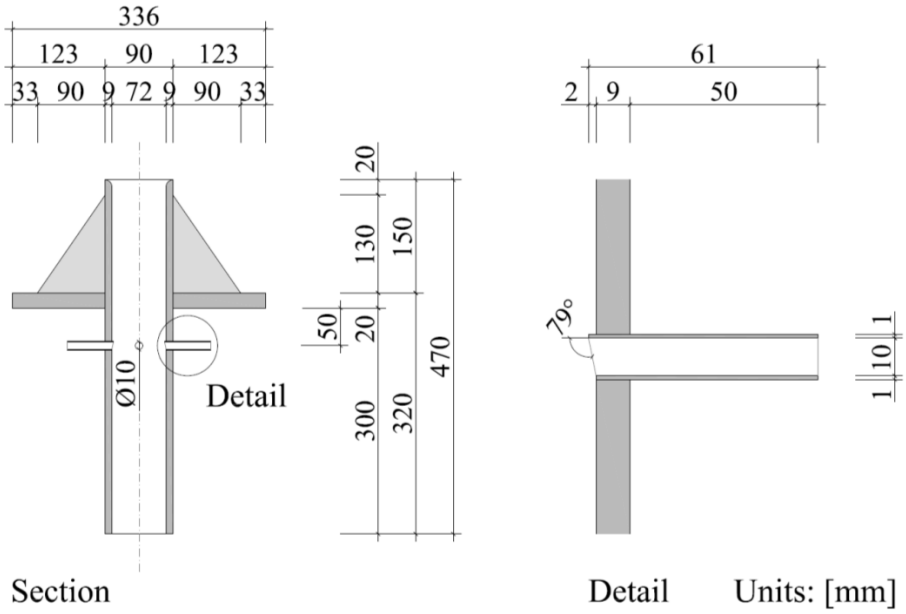

Figure 3.2. Dimensions of plunging jet nozzle; (left) longitudinal section; (right) detail of aeration inlet with depression for air suction.

The plunging jet nozzle dimensions are shown in Figure 3.2. The main body is a vertical cylinder with a 72 mm internal diameter and 9 mm thickness where the jet passes. The upstream extremity is rounded to minimize flow separation. The nozzle also contains structural elements for the connection with the supply conduit. The issuance section at the downstream extremity is located 1 m above the pool bottom.

For the reproduction of submerged jets, a similar but extended nozzle was built (Figure 3.4). The submerged nozzle is thus 300 mm longer than the plunging nozzle, and its downstream extremity is located 0.7 m above the pool bottom.

Figure 3.3. Photos of nozzle aeration devices; (left) aluminum tubes at the nozzle connected to flexible tubes; (right) air flowmeter.

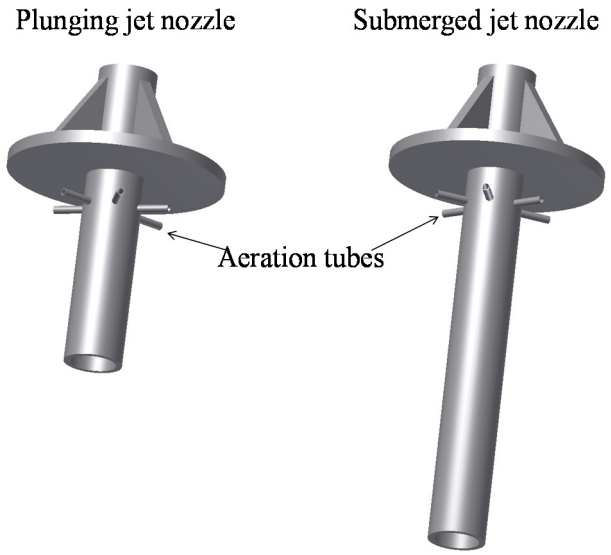

Figure 3.4. Perspective views of the (left) plunging jet nozzle and (right) submerged jet nozzle with aeration tubes.

Manso et al. (2008) measured the velocity distributions and computed the turbulence intensities T_u in the longitudinal direction, defined as the root-mean-square of the longitudinal velocity V_w' divided by the average jet longitudinal velocity V_w. The measurements were carried out on the plunging jet nozzle prior to the installation of the aeration tubes. They assessed the influence of the honeycomb grid and air vent previously installed upstream of the last bend of the supply conduit. For such, Manso et al. (2008) measured the dynamic pressures in different positions of the jet transversal section immediately downstream of the nozzle outlet with a micro pressure transducer. The velocity fluctuations V_w' were obtained from the measured pressure fluctuations p' using a relationship proposed by Arndt and Ippen (1970):

$$V_w' = \frac{\sqrt{\overline{p'^2}}}{\rho_w V_w} \tag{3.1}$$

where ρ_w is the water density. The use of a honeycomb grid and an air vent resulted in a better flow distribution across the transversal section of the jet. The velocity profiles tend to be uniform, especially for high jet velocities (V_w > 25 m/s). The resulting turbulence intensities are shown in Figure 3.5 and compared to the ones obtained by Bollaert (2002) without honeycomb and air vent. A gradual increase of the turbulence intensity is visible for jet velocities lower than approximately 15 m/s. Both studies indicate that, above this jet velocitiy threshold, stable compact jets are produced, and the turbulence intensities tend to values between 3 and 4%. These results are complementary to observations by previous authors for lower jet velocities shown in Table 3.1.

The kinetic energy correction factor α was 1.0 according to the velocity profiles measured by Manso et al. (2008) with honeycomb grid and air vent. For comparison, Bollaert (2002) obtained α values varying from 1.0 at low jet velocities and 1.05 at high jet velocites (up to 30 m/s).

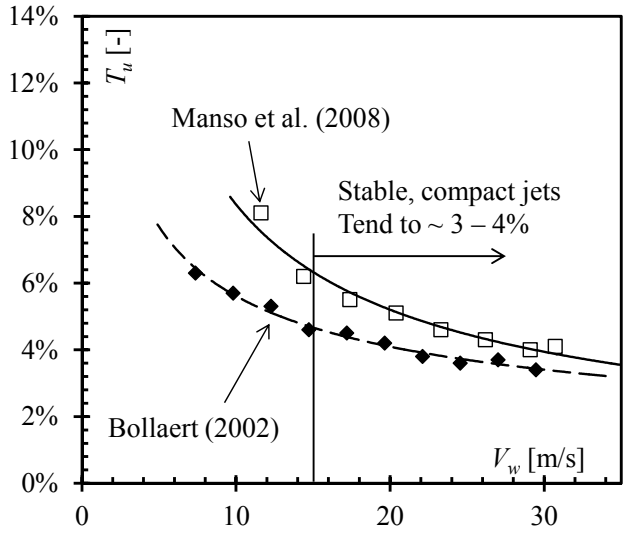

Figure 3.5. Turbulence intensities T_u in the longitudinal direction at issuance. Comparison of the results obtained by (♦) Bollaert (2002) and (□) Manso et al. (2008) and respective trend-lines for the plunging jet nozzle without aeration. The results from Manso et al. (2008) include the effect of a honeycomb grid and air vent upstream of the last conduit bend.

Table 3.1. Values of jet turbulence intensity observed by previous authors, according to Manso (2006)

Research	Jet velocities	Method	T_u [-]	Jet type
McKeogh and Elsawy (1980)	< 5 m/s	Pressure transducers	< 1%	laminar
			2%	turbulent
May and Willoughby (1991)	4.9 - 6.6 m/s	Pitot tube	5.5 - 5.8%	
Ervine and Falvey (1987)	3.3 - 29 m/s	Laser Doppler velocimeter	0.3%	almost laminar
			1.2%	smooth turbulent
			5%	rough turbulent

3.1.2 3D open-end fissure

The geometry of the pool bottom was modified by Federspiel (2011) to represent 3D open-end fissures. For this, a metallic system was implemented, composed of two components, as visualized in Figure 3.6 and Figure 3.7. The first is a box, which contains a cavity 201 mm deep and 202 × 202 mm wide. The second is a 200 mm side cubic block. A 1 mm thick fissure is thus formed between the block and the surrounding box, which was kept constant by 2 lateral guides on each vertical face of the block. Each lateral guide has eight contact points with the cavity walls. The construction tolerance was ± 0.01 mm, thus, small rotations of the block of up to ± 0.003° can occur (Federspiel, 2011).

The block is then able to move vertically inside the cavity as a response to the external solicitations. Alternatively, steel bars can be installed to fix the block to the box, preventing block displacements. The block has threaded holes on its top face, allowing to screw in the pressure transducers in different positions of the water-bottom interface. The

box also contains threaded holes to allow the installation of the pressure and displacement sensors in different positions in the fissures.

Federspiel (2011) obtained experimentally the natural frequency of the block by impacting different points of the block and box with a hammer. The spectral analysis shows that the natural frequency is situated in a range between 5 and 9 Hz, with a peak at 7 Hz.

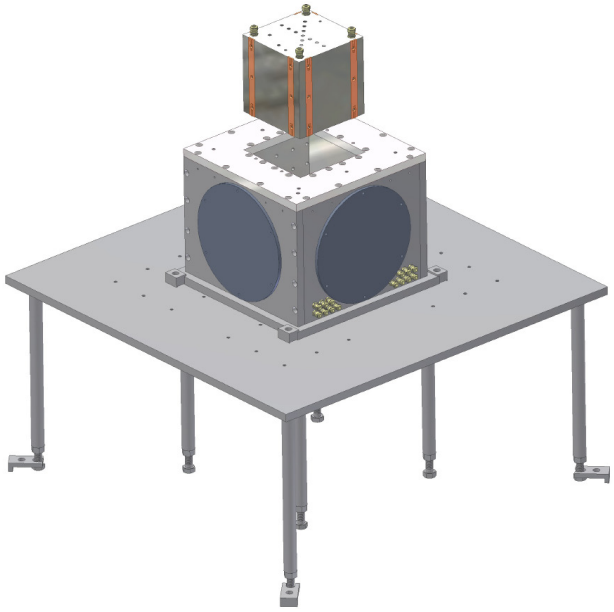

Figure 3.6. Axonometric view of the block/box system mounted on the steel table. The box can be moved to reproduce jet impingement in different positions on the block. Note that the table surface does not represent the pool bottom.

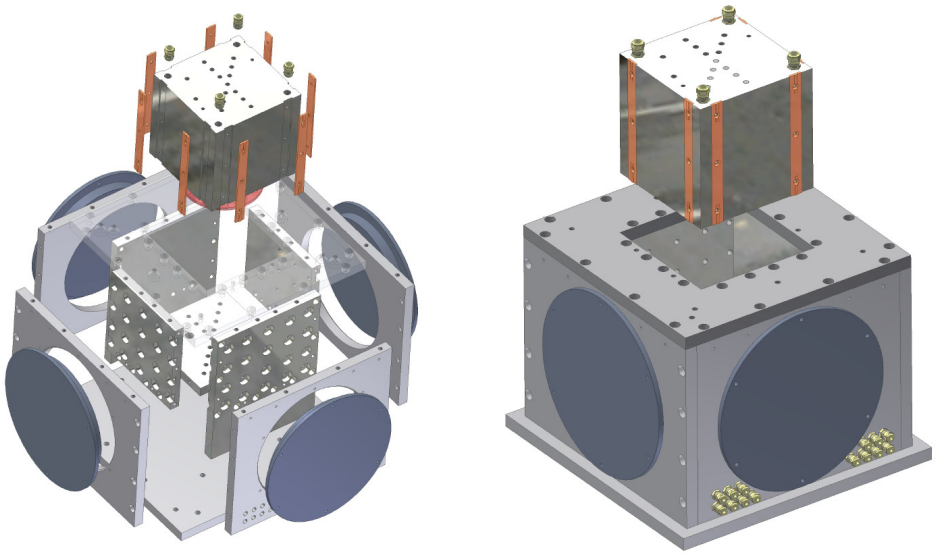

Figure 3.7. Exploded view (left) and axonometric view (right) of the block/box system (Federspiel, 2011).

The block is composed of an assembly of steel plates. The width of these plates was optimized to result in a mean density similar to the rock (2'400 – 2'500 kg/m^3). The block, fully equipped, has a mass of 21.7 kg.

3.2 Measurement equipment

3.2.1 Air bubble characteristics in the pool

A double fiber-optic probe (Figure 3.8) was used to measure air concentration and bubble velocity in 33 positions in the plunge pool (Figure 3.9). The positions are distributed along an axisymmetric plane in the jet shear layer region. The phase detection system developed by RBI Instrumentation (RBI, 2012) is composed of 3 elements:

- The double fiber-optic probe (Figure 3.8, left) has a work principle based on the difference of refraction coefficients of water and air. Light pulses emitted through the probe are thus refracted away from the sensitive tip surface when surrounded by water or reflected inwards when in presence of gas. The tips are cone-shaped with a minimum diameter of 20 μm.
- An optoelectronic apparatus (Figure 3.8, right) emits the light pulses to the tips with a very high frequency (1 MHz) and converts the reflected light into an electric signal. The resulting raw analog signal was set to 0 V when the tip is in the liquid phase and 5 V when the tip is in the gas phase. In a second step, the module converted the analog series into a digital Transistor-Transistor Logic (TTL) signal using a double threshold technique. The lower threshold was set to 1 V and the upper threshold was 3 V, resulting in a digital binary signal.
- The third element is the acquisition card and the software ISO v2.09, responsible for the acquisition and treatment routines.

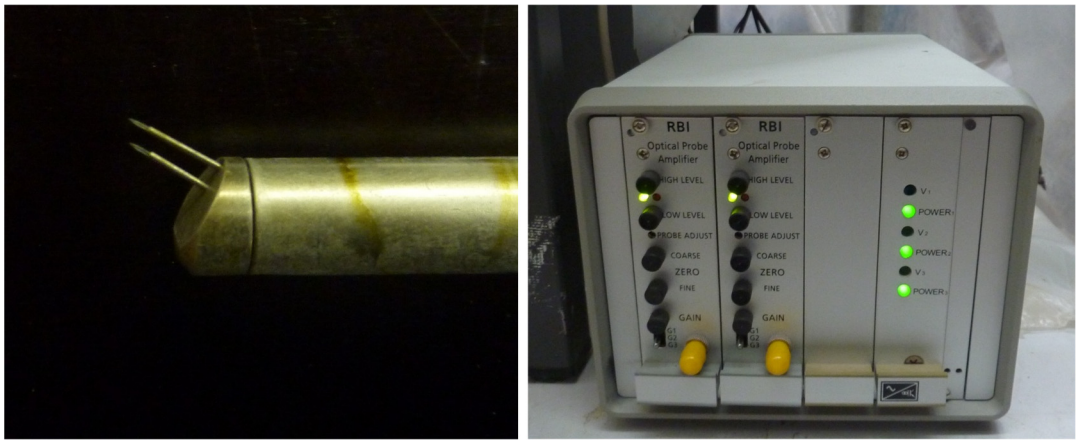

Figure 3.8. Detail of the double-fiber optic probe (left) and opto-electronic module (right), supplied by RBI instrumentation.

The air concentrations can be obtained from the treatment of the resulting binary signals as the relative amount of time the probe tip is in the air. The component of bubble velocities in the direction of the tips alignment are derived from the cross-correlation of the signals of the two probes, knowing that the distance between tips is 2.49 mm. The tips were aligned vertically during the experiments, hence, the measured velocities relate to the vertical components of the bubbles velocity.

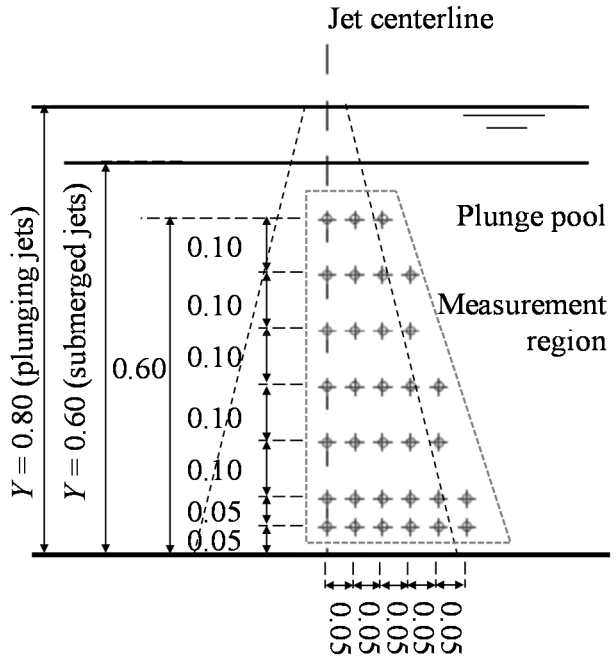

Figure 3.9. 33 Measurement positions for the acquisition of air concentration and air bubble velocity in the jet shear layer region in the pool (dimensions in m).

3.2.2 Block movement and pressure parameters

3.2.2.1 Dynamic pressures

Dynamic pressures were measured simultaneously at 12 positions uniformly distributed along one half of the block, being 4 on the top of the block, 4 on the side of the block (vertical fissure) and 4 underneath the block (horizontal fissure formed between the block lower face and the cavity bottom). Hence, starting on the center of the block, the measurement points are placed every 25 mm on both the top and bottom of the block, and every 50 mm on the side of the block.

Micro pressure transducers of type Kulite HKM-375M-17-BAR-A were used. The 8.1 mm diameter flush metal diaphragm was mounted on the measured surface (on the block for the water-bottom interface, on the box inside the created fissures). The transducers' sensitive sub-assembly is welded to a stainless steel body. These transducers exhibit high natural frequencies and were developed to measure highly dynamic phenomena such as pressure waves. A summary of their characteristics is presented in Table 3.2.

The pressure transducers were calibrated by Federspiel (2011) using a reference transducer, and calibration checks were performed three times on the experimental facility during the present study. In all occasions the pressure *versus* Volt relationships were the same and matched the supplier's calibration curves.

3.2.2.2 Block displacements

Two inductive sensors of the type Baumer IWRM 18U9704/S14 were employed to measure the block displacements. The sensors were mounted on the cavity bottom surface and made redundant measurements of the vertical position of the block lower face. The main characteristics of the displacement sensors are given in Table 3.2. Block displacement measurements were simultaneous to the pressure measurements.

Table 3.2. Characteristics of the block measurement equipment

Pressure transducer HKM-375M-17-BAR-A		Displacement sensor IWRM 18U9704/S14	
Pressure range	0 - 17 bar (absolute)	Distance range	0 - 8 mm
Linearity, hysteresis and repeatability	±0.1% FSO	Resolution	< 0.005 mm (static)
			< 0.01 mm (dynamic)
Full scale output (FSO)	100 mV	Repeat accuracy	< 0.015 mm
Natural frequency	750 kHz	Linearity error	±400 μm
Operating Temp.	-55 … +175°C	Operating Temp.	-10 … + 70°C
Temperature drift	±1% FSO/55°C	Temperature drift	± 5% (full scale)

The displacement sensors were calibrated on the experimental facility by Federspiel (2011). He performed acquisitions for different known positions of the block. Two calibration checks were performed during the present study.

3.2.2.3 Data acquisition

The data acquisition device is a National Instruments card type NI USB-6259 series M. The card is a multifunction module optimized for superior accuracy at fast sampling rates. It is operated by a laboratory-developed routine on LabVIEW© environment.

It has 32 single-ended analog inputs (SE) and 16 differential analog inputs (DI) working with a resolution of 16 bit and 1.25×10^6 samples/second per channel. The outputs are 4 analog channels (16 bit and 2.6×10^6 samples/second) and 48 digital I/O channels, of which 32 are clocked. It also contains two 32 bit counters with a maximum frequency of 80 MHz.

3.3 Test program

Table 3.3 summarizes the test program followed during this research project. For each configuration, the jet series presented in Table 3.4 was performed. The experiments were carried out in 4 phases.

During the *first phase*, the air parameters were measured at the 33 positions in the diffusing jet shear layer as indicated in Figure 3.9. The pool depth Y was set to the maximum value (80 cm). Note, however, that distance between the nozzle outlet and the pool bottom is Y = 70 cm for the submerged jet case. To ensure repeatability, three runs of 60 s were obtained at each measurement position with the phase detection probe. The total 6'138 acquisitions generated 11.3 GB of raw data.

During this phase, the jets impinged at the center of the block, the pool bottom was flat and the block was fixed. This allowed performing 6 runs of dynamic pressure acquisitions at different dates for these configurations, which are a reference scenario.

Table 3.3. Test program

Impact position	Impact type	Block movement	Bottom geometry	Pool depth Y [cm]
Centered jets	Plunging jets	Fixed	Flat	30, 50, 80
			Confined	
		Free	Flat	
			Confined	
	Submerged jets	Fixed	Flat	70
Sided Jets	Plunging jets	Fixed	Flat	30, 50, 80
		Free	Flat	30, 50, 80

The *second phase* completed the block measurements with centered jets and flat bottom. Block measurements are dynamic pressure and displacement acquisitions. For every test run, each sensor measured 65'536 samples at an acquisition frequency of 1 kHz. Each run was performed 3 times.

The *third phase* consisted of the confined bottom configurations. The confined bottom case was tested for plunging jets impinging on the center of the block.

Finally, for the *fourth phase* the box was moved in order to perform sided jets. This configuration corresponds to plunging jets impinging directly on a fissure formed on one of the sides of the block.

The lowest jet velocity (V_{aw} = 4.9 m/s) was only tested during the first phase, since the resulting pressures have little importance in the block response. The block measurements represented a total of 1'764 acquisitions which contain 15.4 GB of raw data.

Table 3.4. Summary of tested jet issuance conditions

Total disch.	Mixture velocity	Water disch.	Air disch.	Air - water ratio	Air conc.	Mean density	Kinetic energy / unit volume	Reduction of E_k due to aeration
Q_{aw}	V_{aw}	Q_w	Q_a	β_1	C_{aa}	ρ_{aw}	E_k	
[l/s]	[m/s]	[l/s]	[l/min]	[%]	[%]	[kg/m^3]	[kPa]	[%]
20	4.9	20.0	0	0	0	999	12.1	0
		17.4	158	15	13	868	10.5	13
		16.3	222	23	19	814	9.8	19
30	7.4	30.0	0	0	0	999	27.1	0
		27.9	127	8	7	929	25.2	7
		26.1	237	15	13	868	23.6	13
		24.4	333	23	19	814	22.1	19
40	9.8	40.0	0	0	0	999	48.2	0
		37.2	169	8	7	929	44.8	7
		34.7	316	15	13	868	41.9	13
		32.6	444	23	19	814	39.3	19
50	12.3	50.0	0	0	0	999	75.3	0
		46.5	211	8	7	929	70.0	7
		43.4	395	15	13	868	65.4	13
		40.7	556	23	19	814	61.4	19
60	14.7	60.0	0	0	0	999	108.5	0
		55.8	254	8	7	929	100.9	7
		52.1	474	15	13	868	94.2	13
		48.9	667	23	19	814	88.4	19
70	17.2	70.0	0	0	0	999	147.7	0
		65.1	296	8	7	929	137.3	7
		60.8	553	15	13	868	128.3	13
		57.0	778	23	19	814	120.3	19
80	19.6	80.0	0	0	0	999	192.9	0
		74.4	338	8	7	929	179.3	7
		69.5	632	15	13	868	167.5	13
		65.2	889	23	19	814	157.2	19
90	22.1	90.0	0	0	0	999	244.1	0
		83.7	380	8	7	929	226.9	7
		78.2	711	15	13	868	212.0	13
		73.3	1000	23	19	814	198.9	19

3.4 Scale effects

The phenomena under study are highly complex and difficult to reproduce without substantial scale effects. Air entrainment and air bubble dissipation depend on Weber, Reynolds and Froude numbers. Moreover, the fluid-structure interactions on the rock mass follow Strouhal similitude. Strictly speaking, experimental results of block ejection due to the impact of aerated jets obtained on a reduced-scale model cannot be directly extrapolated to prototype conditions.

Chanson (2009) studied dynamic similarity and scale effects of plunging jet flows regarding air entrainment and the transport of air bubbles. His dimensional analysis provided the following expression:

$$C, \frac{V}{\sqrt{g d_i}}, \frac{F d_i}{V_i}, \frac{u'}{V_i}, \frac{d_{ab}}{d_i} \ldots = f\left(\frac{x}{d_i}, \frac{y}{d_i}, \frac{z}{d_i}, T_u, F_r, R_e, W_e, \frac{L}{d_i}, \frac{\delta}{d_i}, \frac{W}{d_i}, \text{Salinity}, \ldots\right) \quad (3.2)$$

In which F is the bubble count rate, d_{ab} is a typical bubble size, u' is a characteristic turbulent velocity, δ is the boundary layer length (in the case of supported plane jets) and W is the pool or channel width.

However, measures were used to minimize these scale effects. For experiments considering air entrainment and air bubble dissipation of plunging jets, Chanson (2009) and Heller (2011) recommend that the Weber number of the jet should be above 10^3, whilst the Reynolds number should be greater than 10^5. These limits were met for all the tested jets.

Furthermore, scale effects related to fluid-structure interaction on the block are minimized by performing near-prototype jet velocities. The objective is to reproduce properly the pressure signals acting on the water-rock interface and inside underlying fissures, and these pressures are a direct result of the kinetic energy of the jet reaching the bottom. Only with appropriate jet velocities and turbulence intensities it is possible to generate pressures fluctuations on the bottom which reproduce prototype pressure values. Moreover, the equipped block is representative of a real block in a fissured network due to its density and realistic joint thickness (1 mm).

Nevertheless, the experimental facility has reduced dimensions and scale effects might arise from this fact. Realistic ratios between jet diameter and pool depth were tested and should provide a fair representation of jet development in the plunge pool. Another limitation is that a real fissure network is composed of sets of joints in three directions where partial pressure wave reflections can take place nearly anywhere. Considering this aspect, the experimental facility reproduces a simplified 3D joint geometry. It is due to this simplification, however, that it is possible to assess important resonance properties and to draw conclusions based on the fluid and joint properties.

4

Air concentration and velocity patterns in plunge pools due to impinging high-velocity aerated jets

This study presents an experimental research on the dispersion of air bubbles in plunge pools resulting from turbulent impinging high-velocity vertical water jets with different initial air contents. A comparison is made between submerged and plunging jets. A forced aeration of the issued water jets is performed in the nozzle using a compressed air supply system, resulting in air-to-water ratios from 0 to 23%. The air concentration and the interfacial velocity were measured at 33 positions in the shear layer region of the jet with a double-fiber optic probe. The experimental data for the centerline velocity can be expressed by one general relationship with a constant value in the zone of flow development and a subsequent linear decay. Also, empirical equations that allow for the description of the centerline decay of the air concentration for both the submerged and plunging jets are derived. Furthermore, it can be observed that the air bubble lateral spread follows a Gaussian distribution for aerated submerged jets. Nevertheless, plunging jets show a double-Gaussian distribution as a consequence of the air entrainment mechanism in the jet perimeter at the plunge section.

Keywords: Air entrainment, air-water interactions, plunging jets, submerged jets, bubble dispersion, plunge pool

4.1 Introduction

4.1.1 Background

The diffusion of aerated liquid jets into a receiving pool is a subject of interest in many engineering fields, from industrial applications to environmental phenomena. The case of high-velocity turbulent water jets can be found, for example, in flood release structures of high-head dams. In this case, significant scour may occur at the bottom of the plunge pool due to the conversion of kinetic energy into dynamic pressures (Schleiss, 2002).

The entrainment of air bubbles and subsequent dispersion into the water pool is a highly complex phenomenon. Even if the general features of air entrainment are currently known, there is still a lack of general approaches and appropriate scaling laws. Broad reviews on the jet air entrainment processes were conducted by Bin (1993) and more recently by Kiger and Duncan (2012). The earlier works of McKeogh and Ervine (1981), Ervine and Falvey (1987), Ervine et al. (1997), Ervine (1998) and Chanson (1997) provide a general understanding about jet development in the atmosphere, air entrainment and diffusion in the plunge pool and resulting dynamic pressures at the bottom.

Nevertheless, appropriate knowledge of air bubble dispersion features in the case of high-velocity jets is lacking. The objective of this study is to assess the dispersion patterns of the air bubbles that are produced by turbulent high-velocity jets, using a systematic test procedure. Figure 4.1 illustrates the main physical processes and defines parameters used in this study.

4.1.2 Jet air entrainment

The total entrained air discharge Q_a of a turbulent water jet with discharge Q_w plunging into a water pool is the sum of the air entrainment during the trajectory through the atmosphere, Q_{a1}, and the air entrainment at impact with the plunge pool, Q_{a2}. The resulting air-to-water ratio β and its corresponding concentration C_a are defined as

$$\beta = \frac{Q_a}{Q_w} \tag{4.1}$$

$$C_a = \frac{Q_a}{Q_a + Q_w} = \frac{\beta}{1 + \beta} \tag{4.2}$$

Q_{a1} is related to the disturbances occurring at the jet perimeter during the travel in the air. It is a result of the turbulence of the jet and progressively disintegrates the internal jet core. Air is entrained by the jet surface roughness and is carried downstream with the jet. If the jet core vanishes completely, then the jet is said to be broken and is formed of discrete droplets.

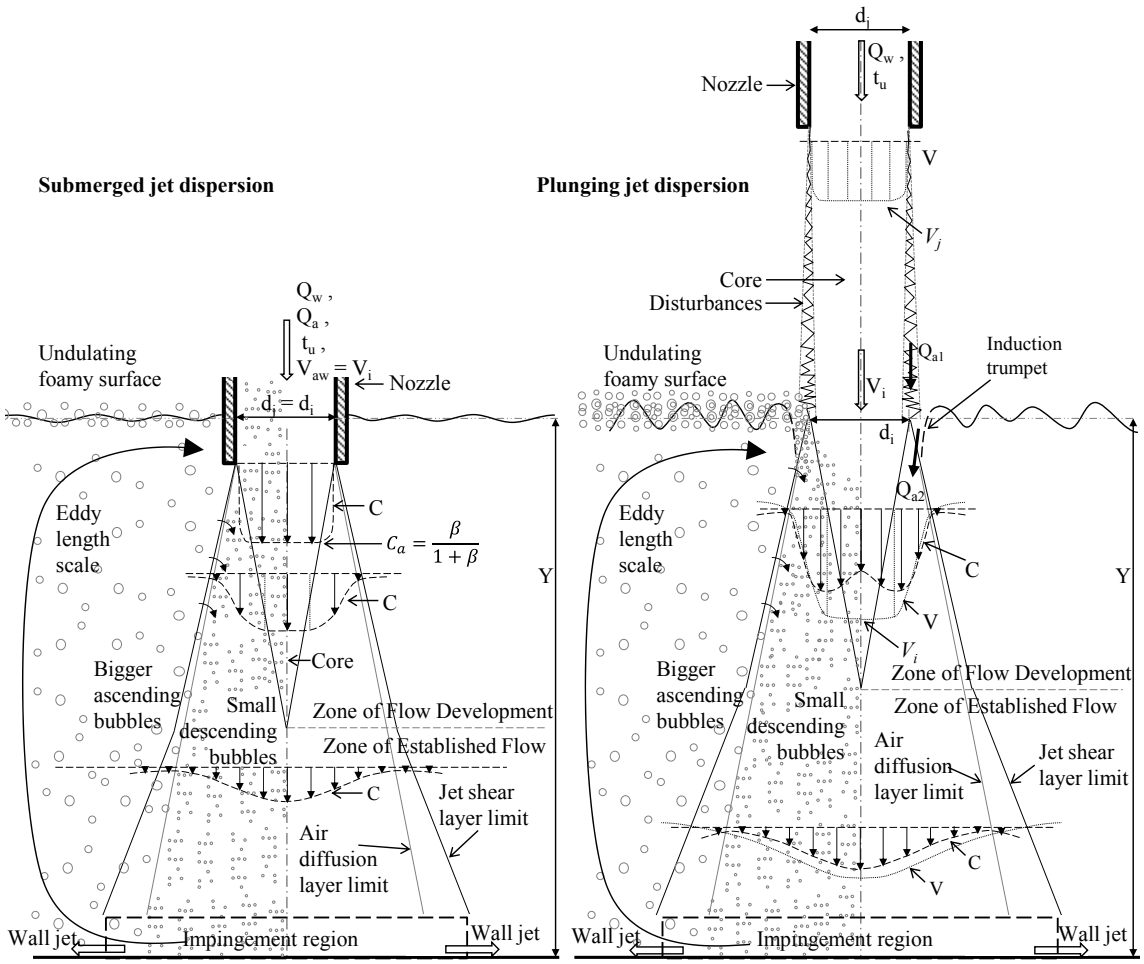

Figure 4.1. Physical processes and parameters for air entrainment and bubble diffusion patterns of aerated submerged jets (left) and plunging jets (right).

As a consequence, at the plunge section with the pool, a turbulent jet has some degree of development, with an inner "solid" core surrounded by a disturbed perimeter, or is fully broken. A vertical cylindrical jet with an issuance velocity V_j and diameter d_j impacts the pool at the plunge section, with a mean impact velocity V_i and a diameter d_i based on gravitational acceleration (Figure 4.1).

Q_{a2} corresponds to the air that is entrained when the jet plunges into the pool. Air is entrained into the pool by the air boundary layer that forms on the jet perimeter. According to Bin (1993), Q_{a2} is given by

$$Q_{a2} = \int_{d_i/2}^{\infty} V_a 2\pi r \, dr \tag{4.3}$$

where V_a is the local air velocity of the air boundary layer at a given radius r. According to Ervine and Falvey (1987), conventional shear layers of the jet dispersion in the pool cannot exist in the case of plunging jets. The real instantaneous jet diameter at the plunge section varies rapidly from the jet core to the outer limit of the jet surface and is also influenced by the pool surface undulations. Thus, the edge of the incoming jet is not clearly defined as it is in the case of submerged jets.

The entrainment process is produced by a discontinuity in the meniscus between the jet and the pool (Kiger and Duncan, 2012). An induction trumpet is formed, from where the outside air is entrained by the jet (Chanson, 1997).

Ervine (1998) describes in detail the different mechanisms of air entrainment at the plunge section. Van de Sande and Smith (1973) had already observed that air entrainment rates changed qualitatively with certain thresholds of jet velocity and diameter. According to them, a high-velocity jet with regard to air entrainment is determined by a Weber number $W_e > 10$. Sene (1988) performed a theoretical study and suggested that, at low velocities, the rate of air entrainment is $q_a \sim V_i^3$, while, for high-velocity jets, $q_a \sim V_i^{3/2}$.

4.1.3 Air bubble diffusion features

The outer layer of the jet is the source of the air bubbles that enter into the pool and is also a source of vorticity. According to Chanson (2009), a double diffusion process takes place due to different diffusion rates of momentum and air bubbles.

The entrained air bubbles are trapped within the shear layer of the jet and transported downstream. If the pool is deep enough, then this process continues until buoyancy effects counteract the flow. The bubbles are then deflected laterally and rise back to surface. A biphasic cone of small descending bubbles is then surrounded by a region of bigger rising bubbles (Bin, 1993). In the case of a pool of limited depth, the jet and the bubbles are deflected laterally by the bottom of the pool.

To the author' knowledge, no study has quantitatively addressed the air bubble dissipation features of high-velocity jets dissipating in bounded pools. Qu et al. (2011) experimentally and numerically studied jet flow and entrained air bubble patterns in deep pools and provided conclusions about the jet penetration depth. McKeogh and Ervine (1981) proposed an empirical solution for the decay of air concentration C at the jet center line in deep pools:

$$\frac{\mathrm{C}}{\mathrm{C_{max}}} = \frac{1}{1 + 3\left(\frac{y}{D_p}\right)^3} \tag{4.4}$$

where D_p is the bubble penetration depth and C_{max} is the maximum air concentration. According to the authors, the maximum air concentration is found at the centerline of the uppermost profile and corresponds to a value of approximately 40%.

The radial function of C has a double-Gaussian distribution close to the plunge section, given its origin between the jet perimeter and the pool surface. With increasing depth, the distribution essentially becomes Gaussian, developing a similarity with the velocity profiles (Bin, 1993; Van de Donk, 1981). Chanson et al. (2004) obtained an analytical solution of the advective diffusion equation for impinging circular jets in the development region:

$$C = \frac{\beta}{4D^{\#}\frac{y}{R_{C_{max}}}} exp\left(-\frac{1}{4D^{\#}}\frac{\left(r/R_{C_{max}}\right)^2 + 1}{\frac{y}{R_{C_{max}}}}\right) \times I_0\left(\frac{1}{2D^{\#}}\frac{r/R_{C_{max}}}{\frac{y}{R_{C_{max}}}}\right) \quad (4.5)$$

where I_0 is the modified Bessel function of the first kind of order zero, R_{Cmax} is the position of r where C is at its maximum value and $D^{\#}$ is a non-dimensional bubble diffusivity that was determined from best fit of the experimental results and varied roughly from 3×10^{-3} to 9×10^{-3}.

The air bubbles begin moving upwards when the descending flow velocity is below a given threshold. According to McKeogh and Ervine (1981), the diameter of the descending bubbles is approximately 2 mm. In this case, 0.26 m/s would be a critical downward velocity below which buoyancy makes the bubbles rise to surface. In the present experimental study, the jets hit the pool bottom with a velocity far above this limit. The measured velocities close to the bottom varied from 1.6 to 16.8 m/s. In this case, the pool bottom acts as an obstacle, resulting in a pressure build-up in the impingement region (Beltaos and Rajaratnam, 1974, 1977) and a lateral deflection of the jet and air bubbles in the wall jet.

4.2 Experiments

4.2.1 Experimental set up

The experiments were carried out at the Laboratory of Hydraulic Constructions (LCH) of the Ecole Polytechnique Fédérale de Lausanne (EPFL). The facility comprises a 3 m diameter cylindrical pool composed of steel reinforced plastic walls and an above installed vertical circular jet (Duarte et al., 2013).

Figure 4.2 shows the experimental set up with definitions of the main parameters. Two different nozzle lengths were used to produce submerged and plunging jets. In both cases, the nozzle diameter d_n was 72 mm. Compressed air was injected into the nozzle through 6 small orifices.

4.2.2 Instrumentation and data treatment

A double-fiber optic-probe was used for air-water phase detection in each position in the measurement region (Duarte, 2013). The working principle of phase detection probes was described by Cartellier and Achard (1991). This principle is based on the difference in the refraction indices of the two phases. In the present case, light signals emitted with a frequency of 1 MHz are refracted outwards when water surrounds the probe tip, and reflected inwards when the tip is in air.

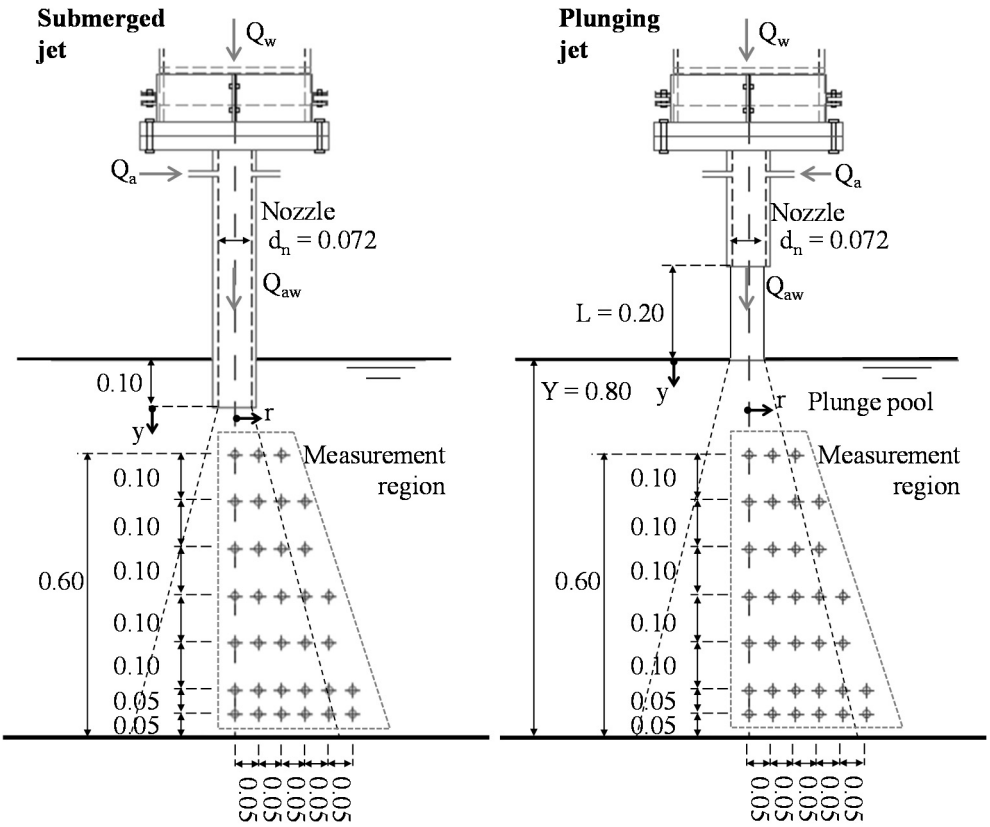

Figure 4.2. Experimental set up and definition of parameters for submerged and plunging jets. Dimensions are in m.

A double threshold technique was used to convert the analog signal into a binary digital signal. The probe tips are cone-shaped diamonds with a minimum diameter of 20 μm. The structural design of the probe was reinforced to resist to high-velocity jets.

The air concentration C can be measured relative to the amount of time the probe tip is in the air. If each bubble duration is Δt during the acquisition time T, then C can be defined as the fraction of air in the flow:

$$C = \frac{1}{T}\sum_{i=1}^{N} \Delta t_i \tag{4.6}$$

The tips are parallel, with a distance Δx = 2.49 mm between them. The tips were aligned perpendicular to the vertical jet axis, allowing the estimation of vertical velocities at each point. The two obtained signals were assumed to be very similar but shifted of a time lag τ. The interfacial velocities were estimated by

$$V = \frac{\Delta x}{\tau} \tag{4.7}$$

where τ is determined by the time lag corresponding to a maximum cross-correlation between the signals from the leading tip and the trailing tip. In practice, this is an invasive method, and the leading tip may affect how bubbles arrive in the trailing tip (Cartellier

and Achard, 1991; Vejražka et al., 2010). However, cross-correlation analyses in the jet axis showed very good results. Furthermore, the measurement of vertical velocity components in positions not along the jet centerline also showed quite good results. According to Manso (2006), the correlation process constitutes a mathematical tool that replaces physical evidence. Coherent velocity measurements in directions that differ from the flow streamlines are most likely due to correlated spectra of the signals. In other words, the air flow as a function of time at a certain control volume in the pool is formed by groups of bubbles with dominant frequencies that are correlated in two points very close to each other even if not aligned with the flow.

4.2.3 Test program

Tested discharges with the jet characteristics are shown in Table 4.1. The pool depth Y was set to 0.8 m. Relative depth Y/d_n was 11.1, corresponding to a developed jet impact on the bottom.

Turbulent intensities $T_u = \text{RMS}(V_{aw})/V_{aw}$ of the plunging water jets were determined by Manso et al. (2008) in the longitudinal direction and varied from values of approximately 8% for the lower velocities, to converge towards values between 4% and 5% for jet velocities above 20 m/s, with a rather uniform velocity distribution in the section.

Table 4.1. Jet characteristics at issuance from the nozzle

Total jet discharge	Total jet velocity	Reynolds number	Froude number	Weber number
Q_{aw} [l/s]	V_{aw} [m/s]	R_e [-]	F_r [-]	W_e [-]
20	4.9	3.10×10^5	5.8	2.36×10^4
30	7.4	4.65×10^5	8.8	5.31×10^4
40	9.8	6.20×10^5	11.7	9.45×10^4
50	12.3	7.76×10^5	14.6	1.48×10^5
60	14.7	9.31×10^5	17.5	2.13×10^5
70	17.2	1.09×10^6	20.5	2.89×10^5
80	19.6	1.24×10^6	23.4	3.78×10^5
90	22.1	1.40×10^6	26.3	4.78×10^5

At the issuance section at the nozzle outlet, the total jet discharge Q_{aw} is the sum of the water discharge Q_w and the active air discharge Q_{aa}. An upstream active jet aeration is therefore defined as $\beta_1 = Q_{aa}/Q_w$. The corresponding air concentration at the issuance section is $C_{aa} = Q_{aa}/Q_{aw} = \beta_1 /(1+ \beta_1)$. Each jet discharge was tested with 4 values of upstream jet aeration: $\beta_1 = 0$, 8%, 15% and 23%.

Both submerged and plunging jets were tested. Thus, $\beta = \beta_1$ for the submerged jet case and the total aeration was known, allowing for relevant conclusions on dispersion patterns.

For each measurement position, 3 runs with $T = 60$ s each were performed to ensure repeatability of the results. A total of 6'138 acquisitions were obtained.

For simplicity, it may be assumed that the resulting jet was uniformly aerated. If ρ_w is the water density and ρ_a is the air density, the density of the incoming jet can be derived:

$$\rho_{aw} = \frac{1}{1+\beta_1}\rho_w + \frac{\beta_1}{1+\beta_1}\rho_a \tag{4.8}$$

Considering that ρ_w is 3 orders of magnitude greater than ρ_a, for practical reasons, the second term in the sum of Eq. (4.8) can be neglected. For each total jet discharge in Table 4.1, the four tested values of upstream aeration produce jets of similar velocity but different mean densities.

4.2.4 Scale effects

Air-water turbulent flows are Froude, Reynolds and Weber dependent phenomena. In a strict sense, dynamic similarity of air entrainment and diffusion for impinging jets in such a case is not possible (Chanson, 2009). Nevertheless, with the assumption of Froude similarity, acceptable limits of R_e and W_e, above which relevant scale effects are minimized, can be defined. For the case of vertical plunging circular jets, recommended values of W_e are above 1×10^3, while R_e should be larger than 1×10^5 (Chanson, 2009; Heller, 2011). Table 4.1 shows that these ranges are met in the present study.

The governing parameters are:

- The aeration provided by the jet: β and C_a.
- The jet properties: V_w, d_i and the turbulence intensity T_u.
- Fluid properties: ρ_a, ρ_w, air and water kinematic viscosities μ_a and μ_w and surface tension σ.
- Other properties: Y, L, g, bubbles Sauter diameter d_{32}, etc.

If the diameter d_i is taken as the scaling length, then the following non-dimensional parameters can be found according to Chanson (2009) but applied to the parameters investigated in this study:

$$\frac{C}{C_a}, \frac{V}{V_i} = f\left(\frac{y}{d_i}, \frac{r}{d_i}, T_u, F_r, R_e, W_e\right) \tag{4.9}$$

4.3 Results

4.3.1 Vertical velocity pattern of the dispersing jet

Contour plots in the measurement region of the vertical interfacial velocity measurements for an incoming jet of V_{aw} = 4.9 m/s and β_1 = 23% for a submerged and a plunging jet are shown in Figure 4.3. The scale distinguishes between downwards (positive) and upwards (negative) velocities. The air diffusion layer is thus fairly visible. Note that the measurement region starts 20 cm below the water surface and ends 5 cm above the pool bottom (as shown in Figure 4.2).

The centerline velocities are analyzed in Figure 4.4 and Figure 4.5. The centerline interfacial velocities are considered to be representative of the flow velocities. Indeed, in this region, the buoyancy forces are negligible when compared to the turbulent drag. The bubbles are trapped and transported with the jet into the water body.

The velocities are normalized by the impact velocity V_i and plotted as a function of y/d_i. The upstream jet aerations provided at the nozzle have minimum influence on the centerline velocities, especially for the submerged jets. For plunging high-velocity jets, aerated jets produce slightly higher centerline velocities in the *zone of established flow*, showing that shear stresses might be reduced due to large entrained air quantities.

The velocity pattern indicates 2 distinct regions, namely one region where the velocities are mostly constant, corresponding to the jet core, followed by a deeper, second region where the velocities decay linearly, corresponding to the *zone of established flow*.

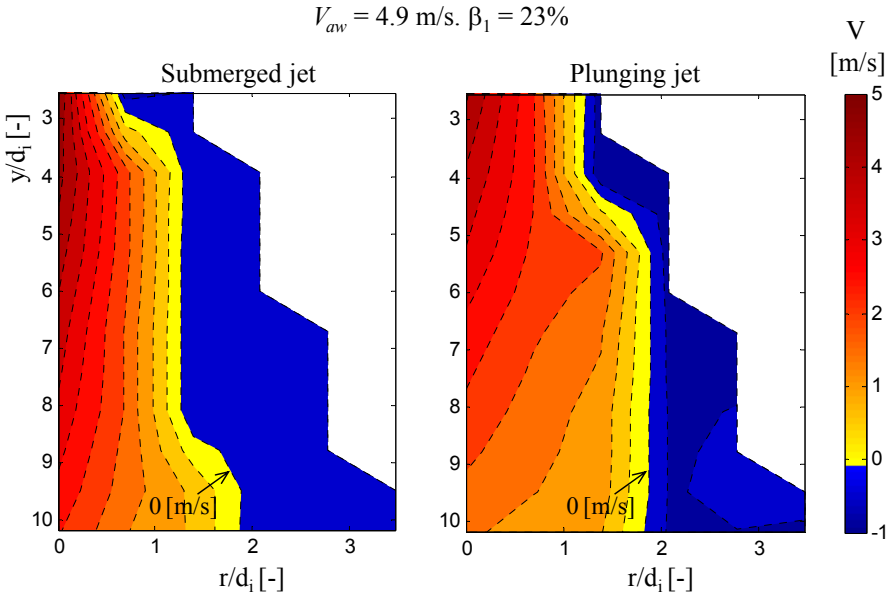

Figure 4.3. General view of vertical velocities in the measurement region. Comparison of the submerged and plunging jets for a jet velocity of 4.9 m/s and active aeration of 23%. Contour lines are shown at each 0.5 m/s.

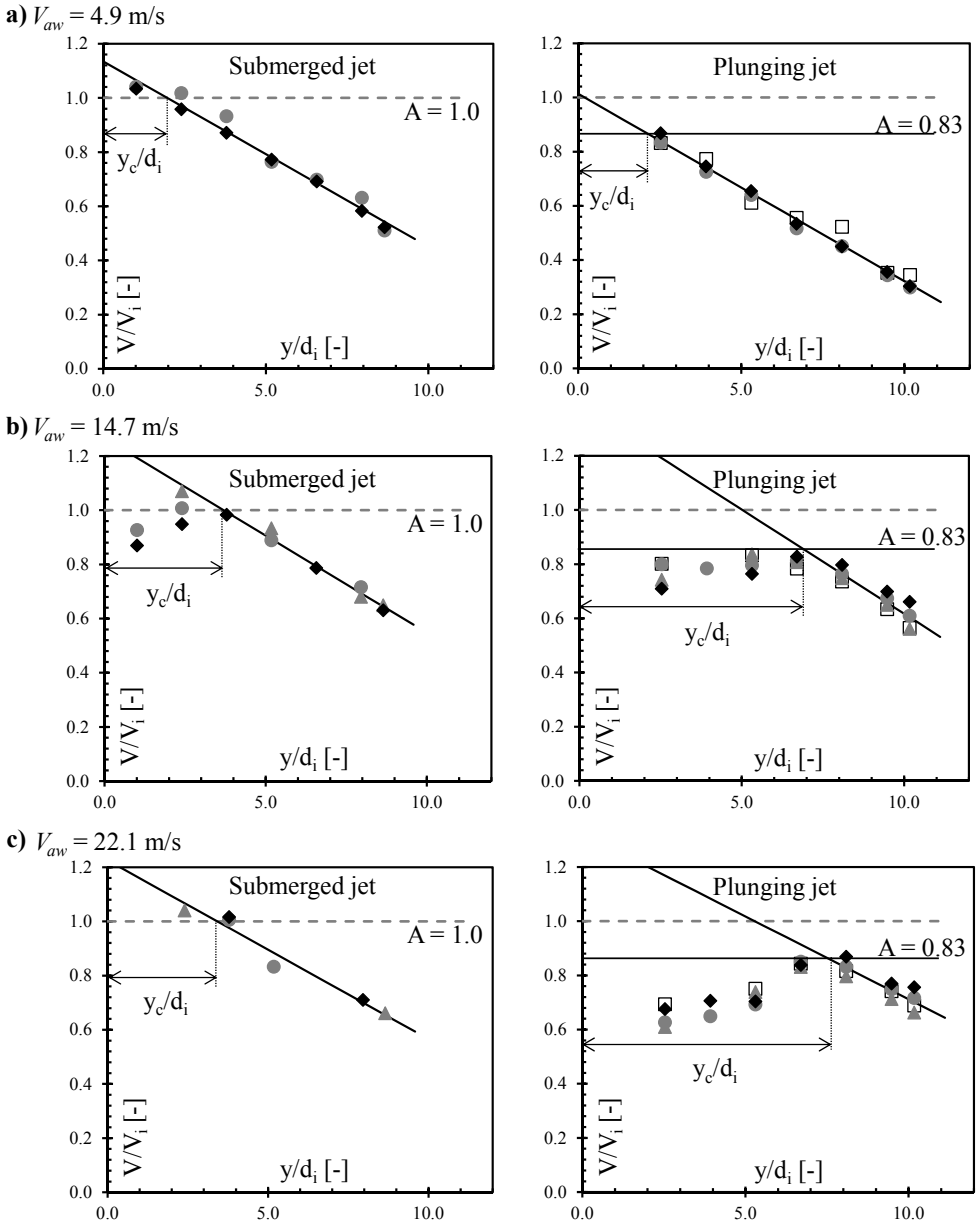

Figure 4.4. Normalized centerline velocity plotted as a function of y/d_i, comparison of submerged and plunging jets, and a linear fit of the data in the *zone of established flow*; (□) β_1 = 0%; (▲) β_1 = 8%: (●) β_1 = 15%; (♦) β_1 = 23%.

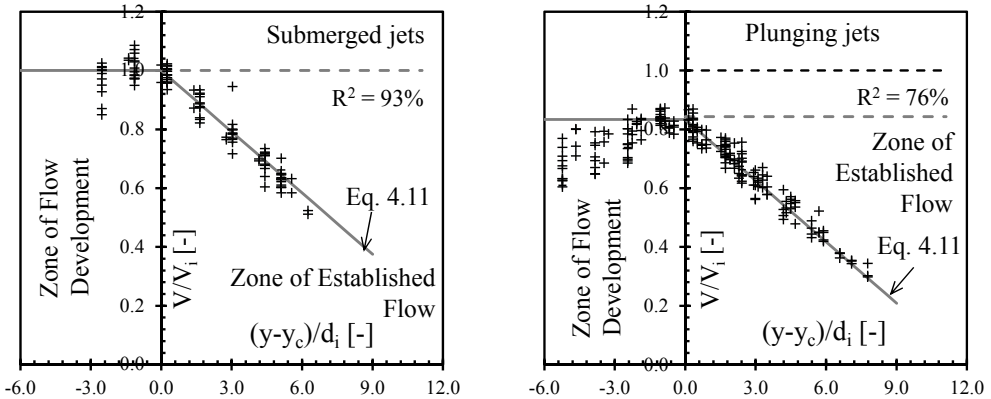

Figure 4.5. Experimental data for all tested jet velocities as a function of y-y_c/d_i, compared to Eq. (4.11).

For submerged jets, the upper threshold value of V/V_i is 1. For plunging jets, the value of V/V_i has a limit in the *zone of flow development* of approximately 0.83. This feature corresponds to the energy that is lost upon impact and results in the spreading of the plunging jet at the plunge section, as observed in Figure 4.3. This result is in agreement with the study of Ervine et al. (1997), who found that normalized mean pressures acting on the bottom for pool depths Y below the core development length y_c have a constant value of 0.86, followed by a curve proportional to $(d_i/Y)^2$. These pressures are a result of the remaining kinetic energy of the jet on the pool bottom.

The relative core lengths y_c/d_i were estimated by considering the horizontal coordinate of the point corresponding to the intersection between the upper threshold and the decaying velocities (Figure 4.4). The relative core length varies linearly with the impacting jet velocity until a constant value is reached for high-velocity jets.

The experimental data of centerline velocity suggest:

$$\begin{cases} \dfrac{y_c}{d_i} = 7.74 \times 10^{-6}\, \dfrac{V_i d_i}{\nu} & if \quad \dfrac{y_c}{d_i} \le A' \\ \dfrac{y_c}{d_i} = A' & if \quad \dfrac{y_c}{d_i} > A' \end{cases} \tag{4.10}$$

where A' is 7.8 for plunging jets and 3.5 for submerged jets.

If the experimental results are plotted as a function of $(y\text{-}y_c)/d_i$, then all data fit on the same curve (Figure 4.5). By doing so, the *zone of flow development* and the *zone of established flow* respectively correspond to the negative and positive values in the horizontal coordinate. The following relationship is obtained:

$$\begin{cases} \dfrac{V}{V_i} = A & if \quad y \le y_c \\ \dfrac{V}{V_i} = A - 0.07\dfrac{y - y_c}{d_i} & if \quad y > y_c \end{cases} \tag{4.11}$$

where A is 1 for submerged jets and 0.83 for plunging jets. The linear relationship proposed in Eq. (4.11) for the *zone of established flow*, with a decay slope of 0.07, is in good agreement with centerline velocity decay for air jets found experimentally by Giralt et al. (1977), who suggested a decay slope of 0.077 in the free jet region.

As shown in Figure 4.4 and Figure 4.5, some normalized velocities do not have the value of the threshold A in the *zone of flow development* but instead have lower values. This was observed especially for high-velocity jets. This result may be explained by the induction trumpet that is formed around the jet perimeter that entrains a large quantity of air. These bubbles are certainly entrained very close to the measurement position and are not fully accelerated by the jet velocity. Thus, the interfacial velocities measured in this region for high-velocity jets most likely do not correctly represent the vertical flow velocity.

4.3.2 Air concentrations in the plunge pool

4.3.2.1 General behavior

An overview of the air concentration as a function of r/d_i and y/d_i in the measurement region is given in Figure 4.6. The air concentration in the dispersing region of the aerated submerged jet (Figure 4.6a) follows a distribution with a maximum in the jet centerline. On the other hand, the plunging jets result in much higher air concentrations, with maximum values observed close to the pool surface at r/d_i slightly higher than 0.5 (Figure 4.6b). This is coherent with air entrainment at the perimeter of the jet. Then the maximum of the radial distribution progressively becomes centered as the jet develops into the pool. This shift could be clearly measured for low-velocity jets (see Figure 4.6c).

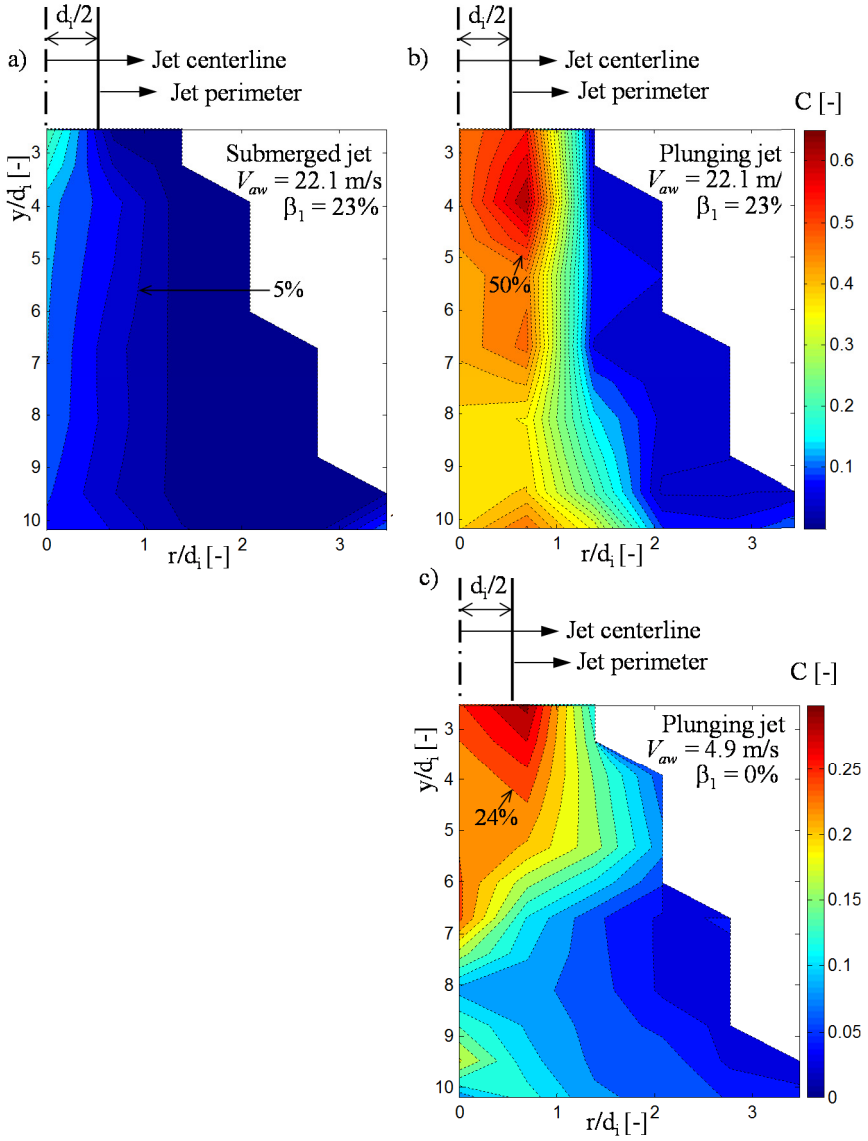

Figure 4.6. Contour plots of air concentration measurements as a function of r/d_i and y/d_i. a) and b) Comparison of actively aerated high-velocity submerged and plunging jets. Contour lines each 2.5%. c) Non-aerated low-velocity plunging jet. Contour lines each 2%.

In Figure 4.6b it can also be seen that extremely high values occur close to the jet perimeter in the impingement region. The highest recorded concentration is 62.6%. It is evident that this region is in direct influence of the induction trumpet, which is highly undefined in the case of turbulent plunging jets.

4.3.2.2 Air concentration along the jet centerline

Normalized air concentrations along the jet centerline as a function of y/d_i are shown in Figure 4.7 for submerged jets and in Figure 4.8 for plunging jets.

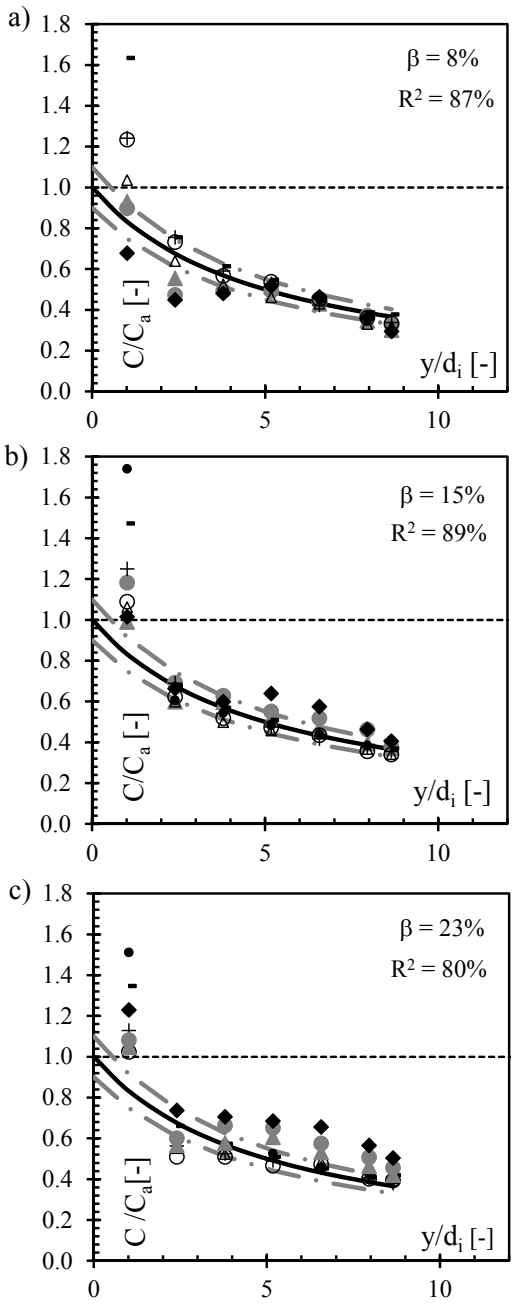

Figure 4.7. Normalized centerline air concentration for submerged jets *versus* y/d_i for the three different jet aerations. a) $\beta = 8\%$; b) $\beta = 15\%$; c) $\beta = 23\%$. (●) V_{aw} = 4.9 m/s; (-) V_{aw} = 7.4 m/s; (+) V_{aw} = 9.8 m/s; (○) V_{aw} = 12.3 m/s; (Δ) V_{aw} = 14.7 m/s; (▲) V_{aw} = 17.2 m/s; (●) V_{aw} = 19.6 m/s; (♦) V_{aw} = 22.1 m/s; (continuous line) Eq. (4.12); (grey dashed lines) 10% confidence interval; (black dashed line) $C = C_a$.

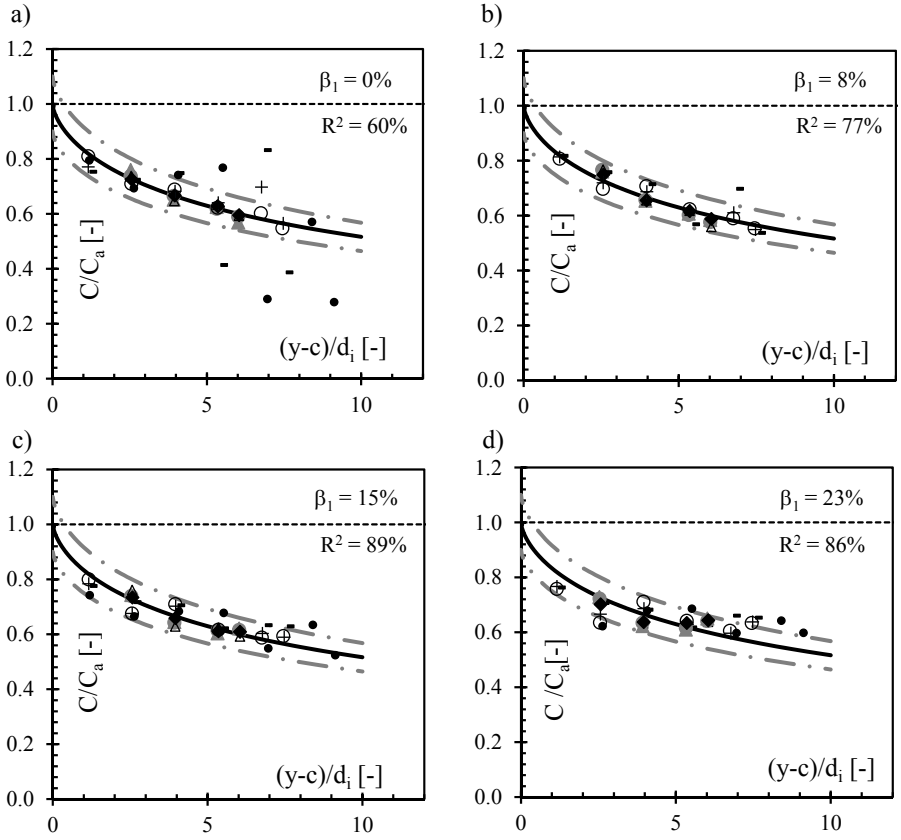

Figure 4.8. Normalized centerline air concentration for the plunging jet *versus* $(y\text{-}c)/d_i$ for the different nozzle jet aerations. a) β_l = 0%; b) β_l = 8%; c) β_l = 15%; d) β_l = 23%. (●) V_{aw} = 4.9 m/s; (-) V_{aw} = 7.4 m/s; (+) V_{aw} = 9.8 m/s; (○) V_{aw} = 12.3 m/s; (Δ) V_{aw} = 14.7 m/s; (▲) V_{aw} = 17.2 m/s; (●) V_{aw} = 19.6 m/s; (♦) V_{aw} = 22.1 m/s; (continuous line) Eq. (4.13); (grey dashed lines) 10% confidence interval; (black dashed line) $C = C_a$.

In the case of submerged jets, where the total incoming air concentration C_a is precisely known, the results can be described by the following expression:

$$\frac{C}{C_a} = \frac{1}{1 + 0.2\frac{y}{d_i}} \tag{4.12}$$

Eq. (4.12) describes the air concentration decay for a given air concentration C_a as shown in Figure 4.7. This equation agrees well with the experimental data, with coefficients of determination R^2 ranging from 60% to 89%. The agreement is better for the low-velocity jets and low aerations. For increasing jet velocity and aeration, the experimental data have a slight tendency to increase compared to Eq. (4.12). This can be explained by the re-circulating bubbles in the pool that contribute to an additional aeration of the jet.

Experimental values of C/C_a above 1 close to the issuance point indicate that the air is not perfectly uniformly distributed in the cross section of the issuing jet. This behavior is more pronounced for the low-velocity jets and less for high jet velocities.

For the experimental results of the plunging jets, the results can be described by the following expression:

$$\frac{C}{C_a} = \frac{1}{1 + 0.2\left(\frac{y-c}{d_i}\right)^{2/3}} \tag{4.13}$$

Because the total incoming air concentration C_a is unknown for plunging jets, it was estimated by fitting Eq. (4.13) to the experimental data. The coherence of the results was ensured by comparing the estimations with the air concentration values measured at positions closest to the surface of the pool.

The parameter c in Eq. (4.13) corresponds to a shift in the y axis. The use of c is necessary because, as mentioned before, the induction trumpet can penetrate rather deep into the pool. This means that the process of air entrainment is completed only at a certain distance below the plunge section. The parameter c varied from 10 cm for the low-velocity jets to 30 cm for the high-velocity jets.

4.3.2.3 Radial distribution of air concentration

The air concentration data follows a simple Gaussian distribution in the radial direction for submerged jets, with a maximum value in the centerline C_{cl} (Figure 4.9). The experimental data can be fitted by the following expression:

$$\frac{C}{C_{cl}} = exp\left\{\left(\frac{-\left(\frac{r}{d_i} - \mu\right)}{b_s}\right)^2\right\} \tag{4.14}$$

On one hand, the parameter μ in Eq. (4.14) is a consequence of the transformation of a rather uniform distribution in the issued jet towards a full Gaussian distribution, so that $C/C_{cl} = 1$ for values of $r/d_i < \mu$. Eq. (4.14) is thus valid for r/di > μ. Near the issuance section, μ is 0.5 and rapidly tends towards zero, following a sigmoid function with asymptotes in these limit values. Nevertheless, μ has little influence in the overall description of the radial distribution of air concentration.

On the other hand, b_s describes the lateral spread of the submerged jets and is of great importance. Figure 4.10 shows the parameter b_s obtained by the experimental results fitted with Eq. (4.14), as a function of the normalized depth y/d_i. It can be observed that b_s grows logarithmically and then tends toward infinity when approaching the pool bottom. This behavior is represented by

$$b_s = k_1 \ln\left(k_2 \frac{y}{d_i}\right) + \frac{0.3}{((Y-y)/d_i)} \tag{4.15}$$

where k_1 and k_2 are fit parameters whose results are presented in Table 4.2. The parameters k_1 and k_2 are linear and quadratic functions of the incoming jet velocity, respectively.

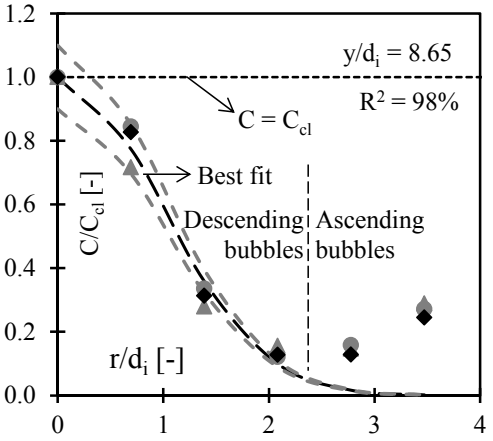

Figure 4.9. Normalized air concentration radial distribution for submerged jets as a function of r/d_i for a jet velocity V_{aw} = 17.2 m/s and different jet aerations; (▲) Jet aeration = 8%: (●) Jet aeration = 15%; (♦) Jet aeration = 23%; (dashed lines) best fit and 10% confidence interval.

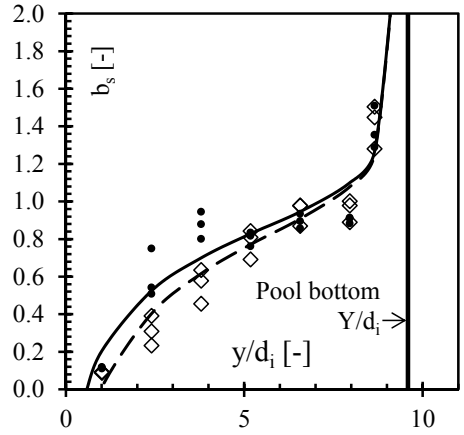

Figure 4.10. Parameter b_s as a function of the normalized depth y/d_i for different jet velocities; (◊) V_{aw} = 7.4 m/s; (●)V_{aw} = 19.6 m/s; and best fit according to Eq. (4.15) for V_{aw} = 7.4 m/s (dashed line) and V_{aw} = 19.6 m/s (continuous line).

Table 4.2. Parameters k_1 and k_2 of Eq. (4.15) and C_a of Eq. (4.13) obtained by best fit

Total jet velocity	Fit parameters of Eq. (4.15)		Values of C_a obtained by best fit for plunging jets			
V_{aw}	k_1	k_2	β_1 = 0%	β_1 = 8%	β_1 = 15%	β_1 = 23%
[m/s]	[-]	[-]	[-]	[-]	[-]	[-]
4.9	0.68	0.92	0.32		0.27	0.31
7.4	0.44	0.94	0.33	0.21	0.22	0.26
9.8	0.43	1.01	0.29	0.22	0.25	0.31
12.3	0.41	1.17	0.24	0.22	0.28	0.35
14.7	0.39	1.24	0.23	0.23	0.31	0.42
17.2	0.37	1.42	0.24	0.25	0.36	0.49
19.7	0.36	1.58	0.25	0.27	0.41	0.55
22.1	0.36	1.98	0.27	0.30	0.45	0.62

In the case of plunging jets, the radial distribution of the air concentration followed the expression (Figure 4.11):

$$\frac{C}{C_{cl}} = K\left[exp\left\{\left(\frac{-\left(\frac{r}{d_i} - r_0\right)}{b_p}\right)^2\right\} + exp\left\{\left(\frac{-\left(\frac{r}{d_i} + r_0\right)}{b_p}\right)^2\right\}\right] + \frac{C_{(sub)}}{C_{cl}} \quad (4.16)$$

C/C_{cl} in Eq. (4.16) is composed of a double-Gaussian distribution resulting from plunge section aeration in the jet perimeter and the simple Gaussian distribution found for the submerged case. The parameter r_0 represents an axial translation of the maximum value from the jet centerline. The parameter K indicates how much higher the maximum value is than C_{cl}, and b_p corresponds to a lateral spread. $C_{(sub)}$ is the air concentration for submerged jets for the similar position and jet configuration, as obtained by Eq. (4.14).

$C_{(sub)}$ is used to represent the upstream nozzle aeration. Although this method might induce some error because the diffusion of the nozzle aeration might not be exactly the same for submerged and plunging jets, it was used to find parameters in the double-Gaussian expression, in the left part of the sum in Eq. (4.16), which have a physical meaning. Coherence of the results is ensured by verifying that the obtained parameters are similar for aerated and non-aerated plunging jets. Figure 4.11 illustrates an example of the experimental results fitted with Eq. (4.16).

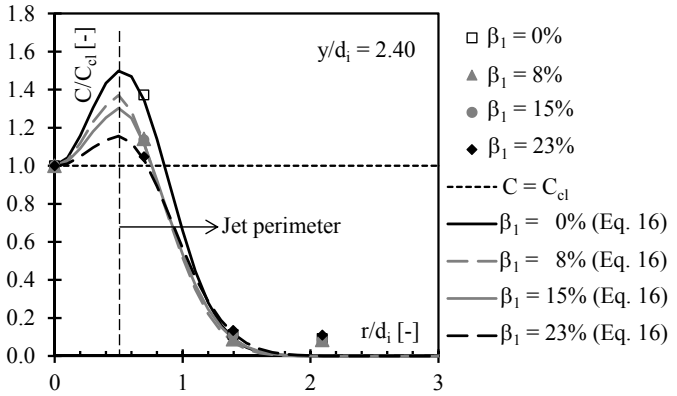

Figure 4.11. Normalized air concentration radial distribution for plunging jets as a function of r/d_i for a jet velocity V_{aw} = 14.7 m/s.

The parameters r_0, b_p and K obtained from best fit for the case of β_1 = 8% are presented in Figure 4.12 as a function of the relative depth y/d_i. The results of r_0, b_p and K are very similar for the different values of β_1. Although the scatter in Figure 4.12 is not negligible, the results show some important features, which are outlined below.

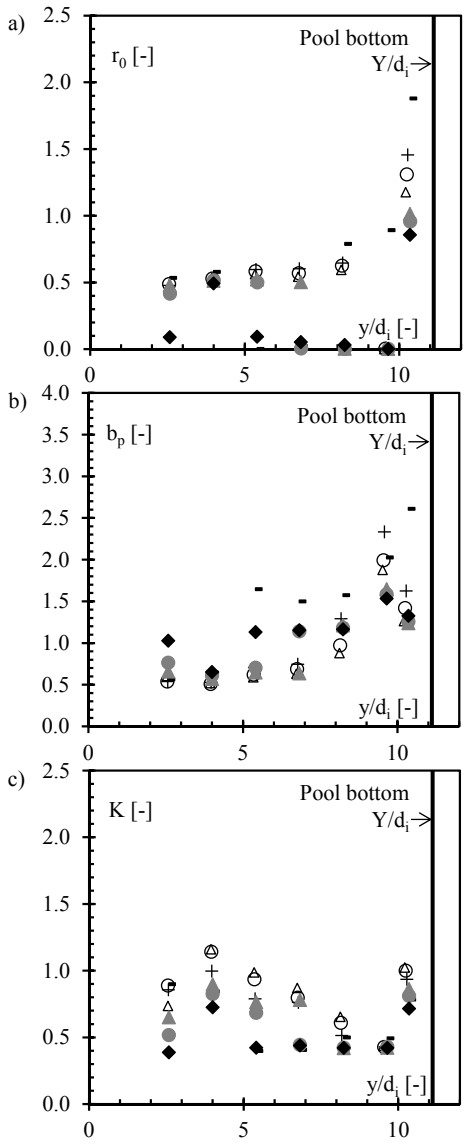

Figure 4.12. Parameters of Eq. (4.16) as a function of the normalized depth y/d_i for β_1 = 8% for different jet velocities; a) r_0; b) b_p; c) K.

The parameter r_0 has a value of approximately 0.5 close to the pool surface. This is in good agreement with the results obtained by Brattberg and Chanson (1998) for a two-dimensional jet and by Chanson et al. (2004) for circular jets. Both studies examined the near-flow field below jet impingement. After a slow increase, r_0 tends to decrease toward zero for y/d_i between 5 and 8. This reduction towards a simple Gaussian distribution did not take place in all cases.

The parameter K often reaches a maximum 30 cm below the pool surface (for y/d_i near 4). Then, K tends towards 0.4. The behavior of b_p seems somewhat similar to b_s for submerged jets.

Close to the pool bottom, the three parameters r_0, b_p and K showed an increase. This is explained by a pressure build up in the impingement region (see Figure 4.1) on the pool

bottom. Transformation of kinetic energy into pressures pushes air bubbles away from the jet centerline at stagnation.

4.4 Discussion

Overall, Eqs. (4.14) and (4.16) represented well the experimental data of the radial distributions for submerged and plunging jets. The minimum values of R^2 in the measurement region were 93% for submerged jets and 96% for plunging jets. The same can be stated on Eqs. (4.12) and (4.13), which reproduce air concentrations in the jet centerline for submerged and plunging jets, with R^2 values between 60% and 89%.

Manso (2006) assessed air concentrations in the same facility, in three positions of the impinging jets. The first was close to stagnation (in the jet centerline, 2 cm above the bottom). The second was in the wall jet (radial distance of 10 cm from the first point) and the third was in the jet centerline, 10 cm above the bottom. He tested plunging jets without active aeration, and pool depths Y of 67, 40, 30 and 20 cm.

The third position is comparable to the measurement region in the present study, even if the pool depths are different. Manso (2006) indicates, for Y = 67cm, air concentration values between 4 and 12%. In the present study, plunging jets without active aeration generated air concentrations 5 cm above the bottom ranging from 9 to 18%, which are close to the range obtained previously. However, very close to the bottom (2 cm), Manso (2006) measured air concentrations ranging between 2 and 7% for Y = 67cm. This is a strong reduction comparing to the free jet region (10 cm above the bottom), confirming that the impingement region formed around the stagnation point reduces air concentrations due to a rise of the pressures.

4.5 Conclusions

The dispersion features of air bubbles entrained by turbulent high-velocity jets in a plunge pool were assessed with systematic experiments. Aerated submerged jets were tested to analyze the bubble dispersion features for known jet aerations. Aerated and non-aerated plunging jets were also tested, representing a configuration that is more similar to prototype conditions for free-falling jets.

Interfacial velocities and air concentrations in the dispersing region of the jet were analyzed by means of non-dimensional parameters issued from dimensional analysis. The results obtained in this manner were similar for different jet velocities and aerations. The physical meaning of the obtained parameters and of the proposed expressions could be highlighted. Additionally, the experimental results allowed for the assessment of the influence of important flow features, such as the induction trumpet and the impingement region.

The centerline flow velocity is formed by a constant region in the *zone of flow development*, followed by a linear decay in the *zone of established flow*. Empirical formulations are proposed that describe the core length of the jets and the centerline velocity decay.

The air concentrations at any point in the air diffusion layer are described in terms of the centerline decay and radial distribution. It could be shown that for submerged jets, the radial function of air concentration follows a Gaussian distribution with a maximum value in the jet centerline. However, a double-Gaussian distribution is observed for plunging jets, with a maximum value originated in the induction trumpet, which is formed between the jet perimeter and the plunge pool.

Finally, it was found that the pool bottom has a direct influence on the radial distribution parameters. The pressure build-up in the impingement region pushes the air bubbles away from the jet centerline.

5

Influence of jet aeration on pressures around a block embedded in a plunge pool bottom

The influence of the air entrained by water jets on the dynamic pressures applied on the bottom of a plunge pool and inside underlying fissures was analyzed with systematic experiments. The large experimental facility reproduced aerated high-velocity jets up to 22.1 m/s impinging on a pool and impacting on an instrumented cubic block embedded on the bottom. Plunging and submerged jets are compared, as well as jet impingement on the center or on the side of the block. A relationship is proposed to describe the time-averaged pressures at stagnation as a function of the relative pool depth, considering pressure measurements in this position as well as recent experimental evidence on the jet centerline velocity decay. Air bubbles influence the dynamic pressures on the rock bottom by reducing jet momentum, but also by reducing the jet dissipation rates in the water pool. These two processes are opposed. The reduction of momentum, consequence of a jet with a lower apparent density, results in lower pressures, while lower jet dissipation in the pool results in higher kinetic energy of the jet impacting the bottom and higher pressures. Finally, the spectral contents show that the resonance frequencies of aerated jets are shifted as a consequence of wave celerity reduction caused by lower mean densities inside the fissures, which is an evidence of the presence of air bubbles.

Keywords: Air entrainment, plunging jets, submerged jets, rock scour, plunge pool, high-velocity jets

5.1 Introduction

5.1.1 Background

Ultimately, dynamic pressures applied on the bottom of a plunge pool and inside rock fissures by high-velocity water jets are responsible for block uplift and, as a consequence, for the formation of scour holes on the river bed. If the case of jets issued from flood release structures of high-head dams is considered, the whole process is composed by a water jet that plunges into the pool, entraining large air quantities. Subsequently, a diffusion process takes place by shear of the jet penetrating the pool. The energy of the jet that is not dissipated in the pool acts on the rock bottom, being transmitted to the rock joints in the form of dynamic pressures (Bollaert and Schleiss, 2003a). Rock joint fracturing and block uplift are a direct consequence of these pressure fluctuations.

Ervine et al. (1997) performed a theoretical and experimental research and provided the basis for the analysis of pressure fluctuations in plunge pool floors impacted by plunging jets. The rather similar case of pressure fluctuations caused by hydraulic jumps on the bottom of stilling basins was studied by Fiorotto and Rinaldo (1992b), while Bellin and Fiorotto (1995) assessed uplift forces on concrete slabs subjected to hydraulic jumps. Melo et al. (2006) investigated pressure fluctuations on concrete slabs due to impacting jets and Pinheiro and Melo (2008) propose a buoyancy coefficient to account for the effect of jet aeration on the pressures applied on concrete slabs.

Bollaert (2002) and Bollaert and Schleiss (2003b) conducted the first study to systematically assess pressure fluctuations in joints due to high-velocity jets. The large experimental facility produced near-prototype jet velocities up to approximately 30 m/s, and pressures were assessed in 4 closed-end joints and 1 open-end joint. He stated that rock joints are subject to either a brittle failure, generated by short-duration pressure peaks or to failure by fatigue generated by cyclic loadings. Hence, Bollaert (2002) showed that the consideration of the transient characteristics of the pressure waves inside rock joints is essential for rock scour assessment, as resonance phenomena might amplify peak pressures and influence joint failure.

Later, Federspiel (2011) modified the representation of the pool bottom by using an instrumented metallic cubic block, which created an open 3D fissure. He assessed block displacements and the corresponding pressure fields around the block impacted by plunging high-velocity water jets impinging on different positions of the block.

Bollaert and Schleiss (2003a) performed a state-of-the-art review of existing methods for rock scour assessment, and classified the past developments into the three main axes: water, rock and air. Currently, even if gaps still exist, the hydraulic features are rather well understood, considering jet development in the air and the hydraulic shear layer in the pool, pressure fluctuations on the water-rock interface and transient pressures inside underlying fissures. Fewer studies, such as the ones cited above, investigated fluid-

structure interactions between water and rock, which take into consideration the rock properties.

To the Author's knowledge, no study has ever assessed systematically the influence of air entrainment on the dynamic pressures on the water-rock interface and underlying fissures impacted by high-velocity jets. This study intends to fill this gap by assessing the influence of the incoming jet aeration on the dynamic pressures around a block embedded on the bottom of a plunge pool.

5.1.2 Theoretical aspects

Detailed descriptions of air entrainment features and of the development of aerated jets in plunge pools are provided in Chapters 2 and 4. On the water-rock interface, the remaining kinetic energy of the turbulent jet is converted into dynamic pressures. Difference is made if the pool depth Y is smaller or larger than the core development length y_c required for the jet core to vanish. If $Y < y_c$, a core jet impact is observed on the pool bottom. The jet hits the water-rock interface with almost the same kinetic energy it entered the pool at the plunge section. The core of the jet generates on the bottom high mean pressures with relatively low fluctuations. On the other hand, if $Y > y_c$, a developed jet impact occurs at the bottom. In this case, time-averaged pressures decrease with increasing pool depth.

On the bottom, the radial function of time-averaged pressures follows a simple Gaussian distribution (Beltaos and Rajaratnam, 1977; Ervine et al., 1997), similarly to the transversal velocity distribution of a vertical jet in the pool. The intersection of the jet centerline with the pool bottom is called stagnation. At this point, the pressures are at a maximum value and velocity is zero. The region in the vicinity of the stagnation point is the impingement region, where the jet is slowed by the bottom, resulting in a pressure build-up (Beltaos and Rajaratnam, 1974, 1977; Duarte et al., 2014). The jet is deflected outwards the impingement region, creating a wall jet, with velocity parallel to the bottom and increasing with radial distance from the jet axis (Figure 5.1).

The energy fluctuations at the rock joints entrance in the water-rock interface provide the excitation signal for the pressures waves that propagate inside the fissures, which can be analyzed as closed-conduits subjected to transient phenomena (Bollaert and Schleiss, 2005). Two distinct cases are of interest to this study: a vertical jet impinging on the block center, designated as a centered jet, or directly on a fissure, designated as a sided jet.

Considering a centered jet and neglecting transient phenomena inside the fissures, symmetry dictates that the flow inside the fissures is zero, and that the time-averaged pressures due to the jet are constant. These pressures are lower compared to the ones on the upper side of the block. Hence, the net force applied on the block pulls it further down and no dynamic uplift occurs.

On the contrary, considering a sided jet, a relatively high fraction of the energy is transmitted into the fissures. A flow occurs due to energy differences between the fissure

extremes and time-averaged pressures decay linearly with the distance from the fissure entrance. A net dynamic uplift pressure may occur in this case.

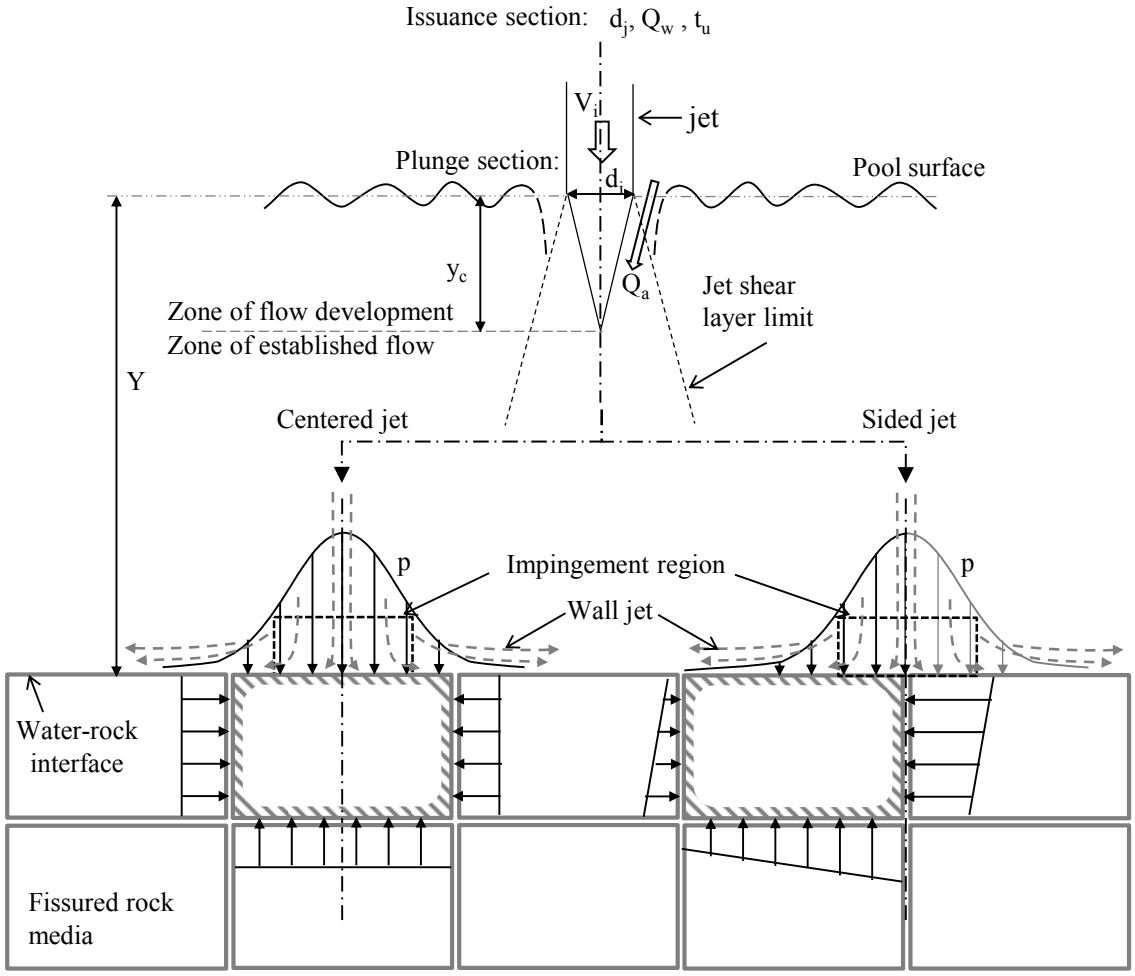

Figure 5.1. Sketch of time-averaged pressure field around a block embedded in a flat rock bottom and main parameters for centered jets (left) and sided jets (right).

Nevertheless, if transient phenomena inside rock fissures are considered, pressure wave superposition and amplification occur, with resonance properties strongly influenced by the air content inside the joints. Significant oscillatory and resonance pressures have been observed by Bollaert and Schleiss (2003b) in closed-end 1D joints.

5.2 Experiments

5.2.1 Experimental arrangement

The large facility was built at the Laboratory of Hydraulic Constructions of the Ecole Polytechnique Fédérale de Lausanne (Bollaert and Schleiss, 2003b; Duarte, 2013; Duarte et al., 2013).

The vertical jets were issued from a 72 mm diameter outlet nozzle. The velocity distribution at the issuance section is uniform, due to the use of a honeycomb grid and air

vent (Manso, 2006; Manso et al., 2008). Turbulence intensities T_u close to the issuance section were assessed experimentally by Manso et al. (2008) in the longitudinal direction and are approximately 8% for the lower jet velocities, reducing asymptotically towards values between 4 and 5% for higher jet velocities.

Aeration of the issued water jets was obtained by adding compressed air into the nozzle. The jets impinged into a 3 m diameter cylindrical basin composed of steel reinforced plastic walls, either on the center or on the fissure entrance on the side of the block.

Plunging jets were tested for pool depths Y of 30, 50 or 80 cm, resulting in relative pool depths Y/d_j of 4.2, 6.9 and 11.1. The plunging jet nozzle outlet was 1 m above the pool bottom. Additionally, submerged jets were tested with an extended nozzle whose outlet was 70 cm above the pool bottom (Y/d_j = 9.7). Table 5.1 shows the studied test configurations.

On the bottom of the pool, Federspiel (2011) implemented a metallic box with a cavity 201 mm deep and 202 x 202 mm wide, where a 200 mm side cubic block is inserted (Figure 5.2). Therefore, a 1 mm thick fissure exists between the block and the box, representing fully open 3D fissures on the rock mass. Lateral guides were used on the block to maintain the 1 mm thickness and to ensure a 1 degree of freedom vertical displacement, minimizing block rotations. For the analysis performed in this Chapter, the block was fixed inside the cavity by steel plates specially conceived to this purpose.

Table 5.1. Tested configurations

Impingement position	Impingement type	Pool depth	Total jet discharge	Jet aeration at issuance
		Y	Q_{aw}	β_I
		[cm]	[l/s]	[%]
Centered jets	Plunging jets	30, 50, 80	30, 40, 50, 60, 70, 80, 90	0, 8, 15, 23
	Submerged jets	70		
Sided Jets	Plunging jets	30, 50, 80		

Dynamic pressures were measured at 12 positions uniformly distributed along one half of the block (Figure 5.2), being 4 on the pool bottom ("PB1" to "PB4"), 4 on the vertical fissure ("VF1" to "VF4") and 4 on the horizontal fissure ("HF1" to "HF4"). The pressure transducers were of type Kulite HKM-375M-17-BAR-A. These sensors measure absolute pressures in the range between 0 and 17 bars with a precision of ± 0.1% of the full-scale output and have a resonance frequency of 750 kHz. The acquisition card is a National Instruments type USB-6259 series M, driven with laboratory developed routine.

The pressure transducers were calibrated by Federspiel (2011) using a reference transducer and calibration checks were performed 3 times on the model during this study. In all cases, the manufacturer calibration curves were confirmed.

Each test configuration was performed at least 3 times to check the repeatability of the results. Plunging and submerged centered jets with fixed block and respectively 80 or 70 cm deep pools were repeated 6 times per configuration in different dates. In each test run 65'536 samples were measured with an acquisition frequency of 1 kHz. Bollaert (2002) and Manso (2006) performed sensitivity analysis and concluded that this frequency is adequate to evaluate the relevant pressure fluctuations and the spectral contents of the pressure signals.

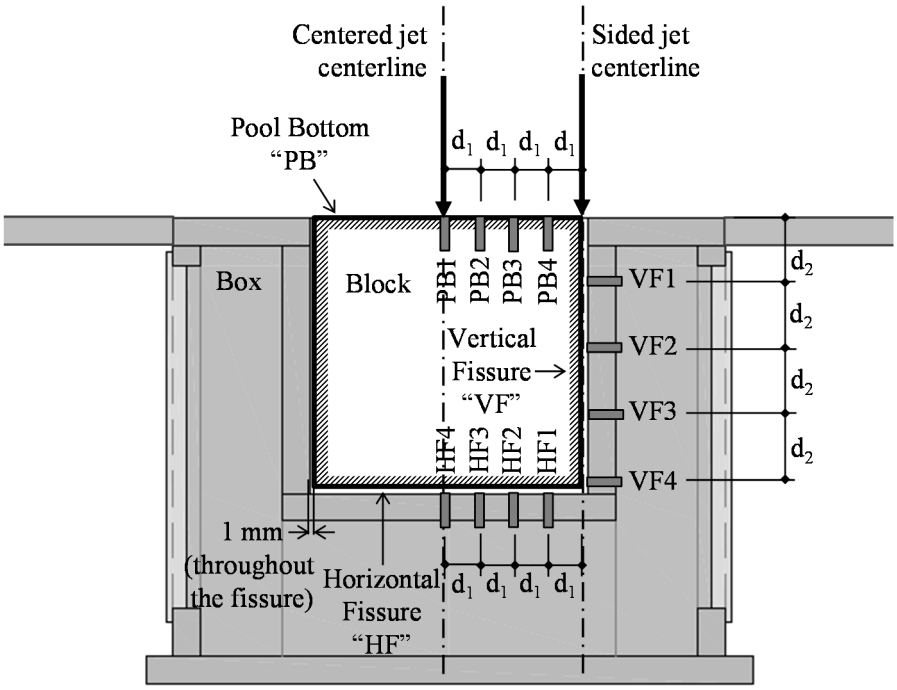

Figure 5.2. Schematic detail of the instrumented box and block and jet impingement positions; d_1 = 25 mm and d_2 = 50 mm; PB1-4: pressure transducers positions on the pool bottom; VF1-4: pressure transducers positions on the vertical fissure; HF1-4: pressure transducers positions on the horizontal fissure.

5.2.2 Data analysis procedure

5.2.2.1 Issuance parameters

The total issued jet discharge Q_{aw} at the nozzle outlet is the sum of the incoming water discharge Q_w and the air discharge Q_{aa} pumped into the nozzle (Table 5.1). The corresponding total issued jet velocities V_{aw} ranged from 7.4 to 22.1 m/s. The jet aeration at the nozzle is $\beta_I = Q_{aa}/Q_w$ and the related air concentration at issuance is $C_{aa} = \beta_I/(1+\beta_I)$.

For the plunging jet case, a relevant additional amount of air is entrained at the plunge section (Chapter 4 and Figure 5.1). However, in the case of submerged jets, Q_{aa} can be considered equal to the total air discharge Q_a entrained into the pool, since the influence of recirculating bubbles and air entrainment in the undulating pool surface can be neglected. Both effects increase with the jet discharge, but remain small compared to

Q_{aa} (Chapter 4). Hence, $\beta_I = \beta$ for submerged jets, where $\beta = Q_a/Q_w$ is the total jet aeration (or alternatively air-to-water ratio). The related total entrained air concentration is $C_a = Q_a/Q_{aw} = \beta/(1+\beta)$.

For each total jet discharge, 4 values of issuance aeration β_I were tested (Table 5.1). It may be assumed that the jets are uniformly aerated. Thus, jets of similar issuance velocity but different mean density ρ_{aw} are obtained. If ρ_w is the water density and ρ_a is the air density, the mean issued jet density is given by:

$$\rho_{aw} = \frac{1}{1+\beta_1}\rho_w + \frac{\beta_1}{1+\beta_1}\rho_a \tag{5.1}$$

5.2.2.2 Plunge section parameters

After a free-fall through the air, plunging jets impact the pool surface with total velocity V_i and diameter d_i influenced by gravitational acceleration, whereas for submerged jets, issuance and impact sections are the same, and so $d_i = d_j = 72$ mm and $V_i = V_{aw}$.

The kinetic energy per unit volume of the jets impacting in the pool surface can thus be derived:

$$E_k = \frac{1}{2}\rho_{aw}V_i^2 \tag{5.2}$$

5.2.2.3 Block parameters

The dynamic pressures around the block are analyzed by means of non-dimensional pressure coefficients and the spectral contents of the pressure fluctuations. The dynamic pressure coefficients are obtained using the following expressions:

$$C_p = \frac{p_{mean} - \rho_w g Y'}{\frac{1}{2}\rho_{aw}V_i^2} \tag{5.3}$$

$$C_p' = \frac{p'}{\frac{1}{2}\rho_{aw}V_i^2} \tag{5.4}$$

$$C_p^+ = \frac{p_{max} - \rho_w g Y'}{\frac{1}{2}\rho_{aw}V_i^2} \tag{5.5}$$

$$C_p^- = \frac{p_{min} - \rho_w g Y'}{\frac{1}{2}\rho_{aw}V_i^2} \tag{5.6}$$

where g is the gravitational acceleration, Y' is the distance between the pressure transducer and the pool surface and p_{mean}, p', p_{max} and p_{min} are, respectively, the average

pressure, the RMS value of the pressure fluctuations, and the extreme maximum and minimum observed pressures. Only relative pressures regarding atmospheric pressure are considered.

C_p represents non-dimensional time-averaged pressure values. It can also be interpreted as the fraction of the incoming jet kinetic energy that has not been previously dissipated in the pool. Similarly, C_p', C_p^+ and C_p^- represent the pressure fluctuations and extreme pressure values compared to the energy of the jet.

Power Spectral Densities (PSD) of the pressure fluctuations were obtained using a Welch periodogram-based Fast Fourier Transform (FFT). The pressure fluctuation signals, composed of 2^{16} samples, are divided into 64 segments sampled by a Hamming window with 50% overlapping.

5.2.3 Scale effects

Pressure fluctuations on a plunge pool bottom and inside underlying fissures due to turbulent aerated high-velocity jets result from a series of complex phenomena. These phenomena are related to the aerated jet development through the air and along the pool (Chanson, 2009; Chanson et al., 2004), conversion of kinetic energy into turbulent dynamic pressures and transient phenomena of the pressure waves inside fissures.

Heller (2011) and Chanson (2009) propose that the Reynolds R_e and Weber W_e numbers of the jets should be larger than 10^5 and 10^3 respectively, to minimize the scale effects on a Froude F_r similarity model. These limits are respected in this study, since the minimum values of R_e and W_e were 4.7×10^5 and 5.3×10^4 respectively.

With the objective of minimizing scale effects related to the dynamic pressures around a rock block, near-prototype jet velocities up to 22.1 m/s are reproduced. Prototype conditions studied by Ervine et al. (1997), Bollaert (2002) and Manso et al. (2008) lead to jet velocities and turbulence intensities close to the ones used in this study.

Thus, the non-dimensional pressure coefficients, as well as the spectral ranges of the pressure signals are considered to correspond well to prototype conditions. However, it is acknowledged that the experimental facility is a geometrically reduced scale representation of prototype structures. For instance, scale effects might arise from the ratios between jet diameter and block side length or fissure thickness.

Additionally, the 3D open-fissure model is a simplified representation of a highly complex three-dimensional jointed rock network, where pressure wave partial reflections can occur nearly anywhere. Nevertheless, the simplified model allows a better understanding of the influence of air entrainment on dynamic pressures around a block, and adds knowledge to recent developments on rock scour assessment.

5.3 Results and discussion

5.3.1 Time domain analysis

5.3.1.1 General behavior of pressures around the block

An overview of the time-averaged pressure coefficients around the block for non-aerated jets is shown in Figure 5.3 for a total jet velocity V_{aw} = 22.1 m/s plunging into a relatively deep pool (Y/d_j = 11.1). A comparison is made between a centered jet and a sided jet.

The behavior is similar on the water-rock interface, where a radial Gaussian decay is observed. For the mean pressures, Ervine et al. (1997) proposed:

$$\frac{C_p}{C_{p\,cl}} = exp\left\{-K_2\left(\frac{r}{Y}\right)^2\right\} \tag{5.7}$$

where C_{pcl} is the mean pressure coefficient in the jet centerline and K_2 is a parameter that determines the decay rate. According to Ervine et al. (1997), K_2 ranged from 30 for shallow pools, to 50 for deeper pools. In this study, K_2 was found to vary roughly between 25 for Y/d_j = 4.2 and 250 for Y/d_j = 11.1. Additionally, in a general way, all the non-dimensional pressure coefficients were found to decay exponentially as a function of the radial distance from the jet centerline in the pool bottom.

Inside fissures, the behaviors of centered and sided jets are different. For centered jets, the pressures inside the fissures are small because of the distance from the jet centerline. Then, mean pressures, pressure fluctuations and extreme pressures slightly increase towards the center of the fissure, as it can be seen more clearly in the unfolded view in Figure 5.4. A symmetric behavior is assumed for centered jets. Sided jets produce higher pressures at the fissures entrance, which decay almost linearly with the fissure length.

5.3.1.2 Pressures at stagnation

To describe the decay of the time-averaged pressure coefficient at stagnation due to plunging water jets as a function of the relative pool depth, Ervine et al. (1997) proposed:

$$C_p = 38.4(1 - C_a)\left(\frac{d_i}{Y}\right)^2 \tag{5.8}$$

where the entrained air concentration C_a was derived from the air-to-water ratio β using the following empirical expression (Ervine et al., 1997):

$$\beta = K_1\left(1 - \frac{V_e}{V_i}\right)\sqrt{\frac{L}{d_i}} \tag{5.9}$$

where V_e is the onset jet impact velocity at the plunge section above which the air entrainment process takes place, considered about 1 m/s, L is the jet fall length between the issuance and plunge sections and K_1 is a parameter that varies between 0.2 for smooth jets to 0.4 for very rough turbulent jets.

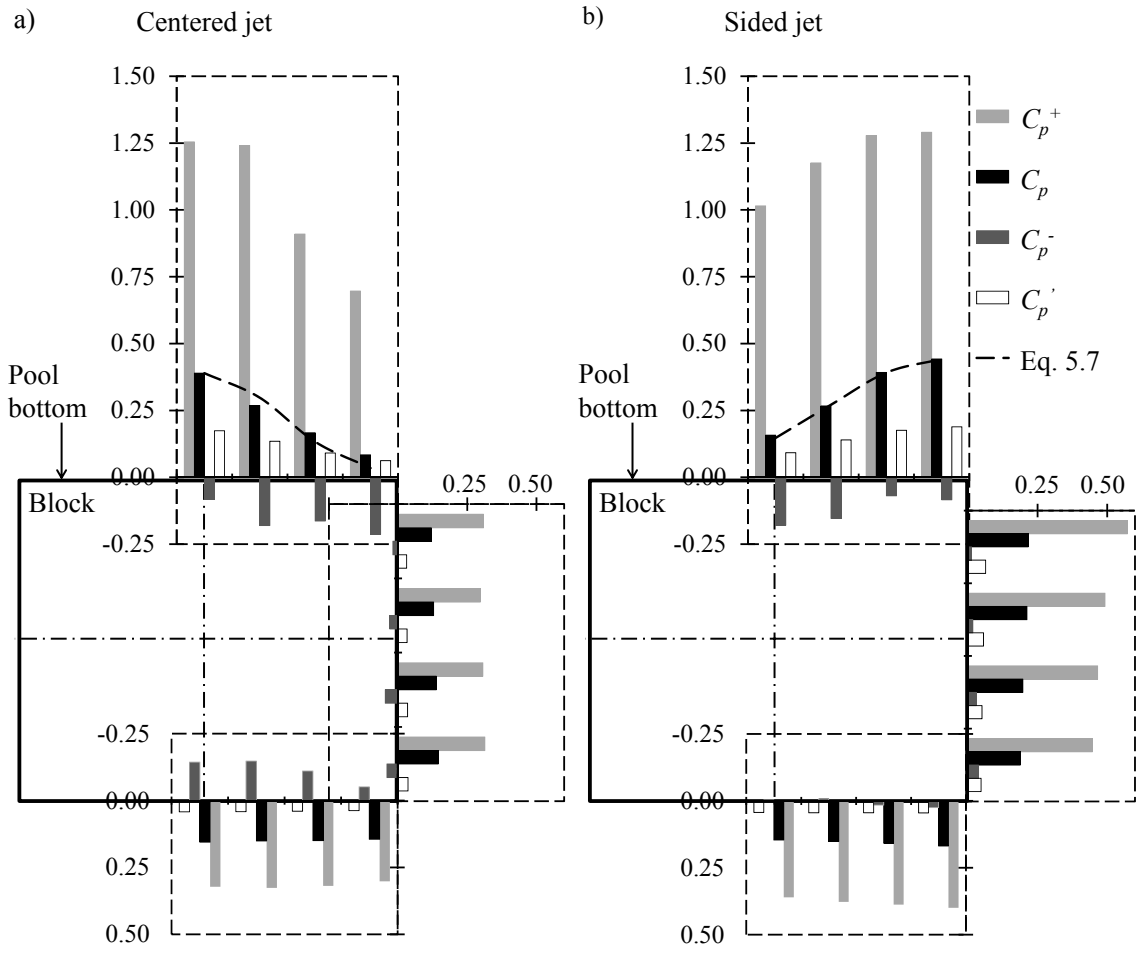

Figure 5.3. Pressure coefficients around the block. Non-aerated jet (β_1 = 0 %), V_{aw} = 22.1 m/s, block free, Y/d_j = 11.1; (light grey bars) C_p^+; (black bars) C_p; (dark grey bars) C_p^-; (white bars) C_p'; (dashed line) Eq. (5.7); a) Centered jet; b) Sided jet.

Direct measurements of the jet velocities in the pool performed in Chapter 4 showed that the time-averaged jet centerline velocity V is constant along the *zone of flow development*, where the core of the jet still persists, followed by a linear decay in the *zone of established flow*. The following expression could be derived:

$$\frac{V}{V_i} = A - 0.07\frac{y - y_c}{d_i} \quad if \quad y > y_c \tag{5.10}$$

where A is a threshold constant value for the jet centerline velocity in the jet core. For submerged jets, A = 1, meaning that the jet impact velocity remains the same while the core persists, and for plunging jets, A = 0.83 as a result of energy loss at the plunge section.

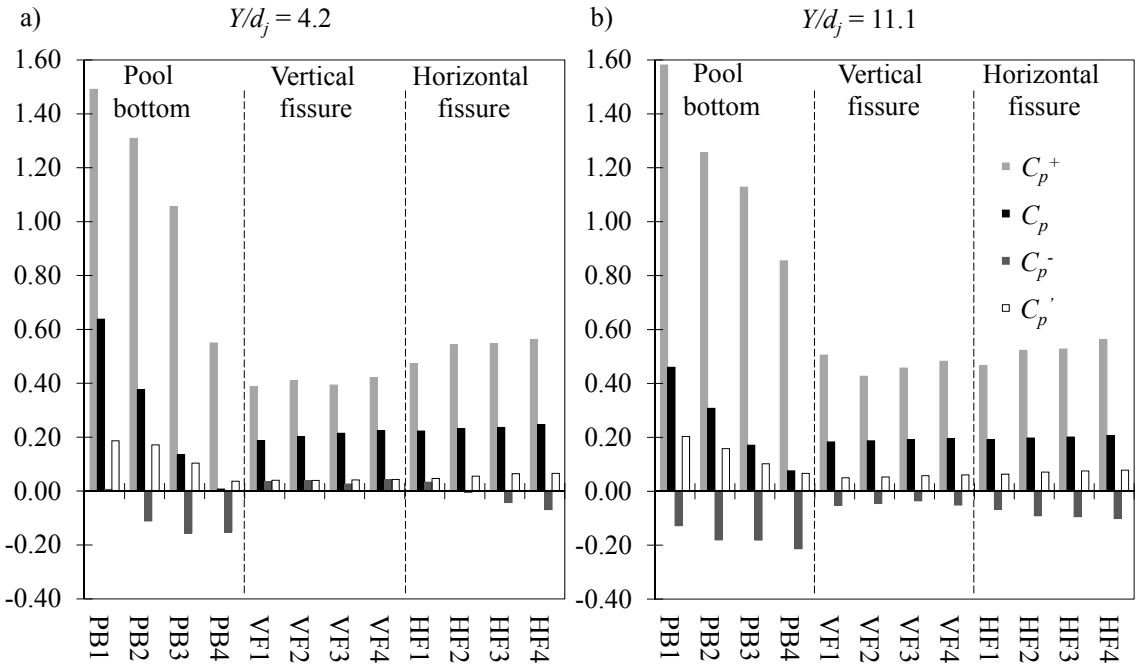

Figure 5.4. Detailed view of pressure coefficients around the block. Centered non-aerated jet (β_I = 0 %), V_{aw} = 22.1 m/s, block fixed; (light grey bars) C_p^+; (black bars) C_p; (dark grey bars) C_p^-; (white bars) C_p'; a) Y/d_j = 4.2; b) Y/d_j = 11.1.

The length of core decay y_c could also be obtained empirically:

$$\begin{cases} \dfrac{y_c}{d_i} = 7.74 \times 10^{-6} \dfrac{V_i d_i}{\nu} & if \quad \dfrac{y_c}{d_i} \le A' \\ \dfrac{y_c}{d_i} = A' & if \quad \dfrac{y_c}{d_i} > A' \end{cases} \tag{5.11}$$

where ν is the kinematic viscosity of the fluid. The parameter *A'* is 3.5 for submerged jets and 7.8 for plunging jets. The term $V_i d_i/\nu$ corresponds to the Reynolds number of the jet at the plunge section.

The kinetic energy per unit volume of the jet is converted into dynamic pressures at the water-rock interface. For this reason, the time-averaged pressure coefficient may be derived from the mean jet velocities. Taking into consideration Eqs. (5.2), (5.3) and (5.10) for the kinetic energy, C_p and the centerline velocity, an expression of the following form could be obtained theoretically for the time-averaged pressure coefficient:

$$C_p = \psi \left(A - 0.07 \frac{Y - y_c}{d_i} \right)^2 \quad if \quad y > y_c \tag{5.12}$$

where the term ψ reflects the loss of kinetic energy in the impingement region.

The analysis of the experimental results showed that ψ strongly depends on the incoming jet velocity, differently from the jet development in the free jet region above. The best fit of the experimental data for non-aerated plunging jets yields:

$$C_p = \psi\left(0.926 - 0.0779\frac{Y - y_c}{d_i}\right)^2 \quad if \quad y > y_c \tag{5.13}$$

$$\psi = \frac{1}{1 + exp\left\{-5.37 \times 10^{-6}\left(\frac{V_i d_i}{\nu} - 6.63 \times 10^5\right)\right\}} \tag{5.14}$$

Figure 5.5 shows the experimental results of C_p at stagnation as a function of the relative pool depth, compared to Eq. (5.13) for the different incoming jet velocities of non-aerated plunging and submerged jets.

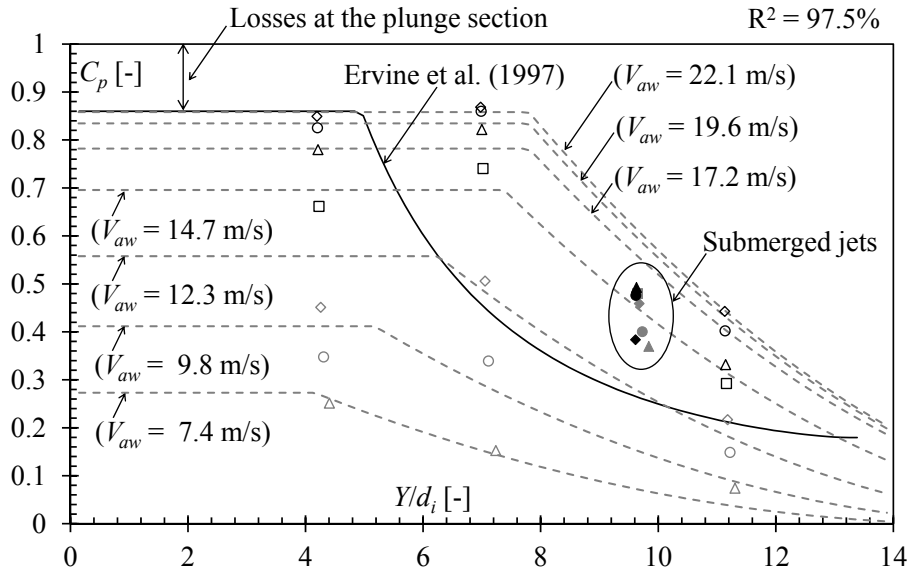

Figure 5.5. Mean pressure coefficient C_p *versus* the relative pool depth Y/d_i for non-aerated jets; (continuous line) Ervine et al. (1997); (dashed line) Eq. (5.13) for different values of jet velocity V_{aw}; experimental data for plunging jets: (△) V_{aw} = 7.4 m/s; (○) V_{aw} = 9.8 m/s; (◊) V_{aw} = 12.3 m/s; (□) V_{aw} = 14.7 m/s; (Δ) V_{aw} = 17.2 m/s; (○) V_{aw} = 19.6 m/s; (◊) V_{aw} = 22.1 m/s; experimental data for submerged jets. (▲) V_{aw} = 7.4 m/s; (●) V_{aw} = 9.8 m/s; (♦) V_{aw} = 12.3 m/s; (■) V_{aw} = 14.7 m/s; (▲) V_{aw} = 17.2 m/s; (●) V_{aw} = 19.6 m/s; (♦) V_{aw} = 22.1 m/s

Time-averaged pressure coefficient can be fairly well derived from jet centerline velocity decay in the pool. The empirical Eq. (5.13) is rather similar to the theoretical Eq. (5.12). It provides physical evidence that low C_p values for lower jet velocities are a result of kinetic energy dissipation in the impingement region rather than in the *zone of established flow*, where jets of different velocities dissipate similarly. The term ψ is a logistic function of the impact velocity, asymptotically reaching the value 1 for high-velocity jets.

Figure 5.5 shows that C_p values for a core jet at stagnation ($y < y_c$) have an upper limit that corresponds to the one proposed by Ervine et al. (1997) of approximately 0.86. This limit is asymptotically reached for the high-velocity jets. Higher C_p values cannot be observed due to energy loss at the plunge section.

The C_p results for submerged jets, which were tested for 1 pool depth only, are grouped together in a narrow zone, showing that they are much less dependent on the jet velocity.

5.3.1.3 Influence of jet aeration

Mean pressures

Ervine and Falvey (1987) stated that the entrainment of air bubbles in the diffusing shear layer in the plunge pool reduces the mean dynamic pressures on the bottom. Their reasoning is based on the reduction of momentum, consequence of a void fraction of the incoming jet, and yields:

$$\frac{p_{mean\ (aerated\ jet)}}{\frac{1}{2}\rho_w V_i^2} = \frac{\frac{1}{2}\rho_w (1 - C_a) V_i^2}{\frac{1}{2}\rho_w V_i^2} = (1 - C_a) \tag{5.15}$$

Eq. (5.15) compares the mean pressures of an aerated jet with the kinetic energy of a clear-water jet of the same velocity. Although its simplicity, Eq. (5.15) is useful because it shows that, if the dissipation in the pool is neglected – or similar to that of a clear-water jet, an aerated jet produces mean pressures that are lower than those of a water jet, proportionally to its water fraction (1 - C_a). The same reasoning would lead to similar C_p results for different jet aerations considering Eq. (5.3), if the dissipation conditions in the pool are the same. Indeed, the non-dimensional dynamic pressure coefficients are computed relatively to the kinetic energy per unit volume of the jet, which already accounts for the apparent density of the air-water mixture and, consequently, for the lower momentum of aerated jets.

In this study, the total jet aeration is known for the submerged jets. Figure 5.6 shows mean pressures around the block generated by submerged and plunging jets. The mean pressure coefficients for submerged jets (Figure 5.6a) are rather similar for different jet aerations, especially inside the fissures. A slight increase indicates that jet diffusion in the pool is different for jets with different air content. Nevertheless, the reduction in the jet momentum remains the main process of pressure reduction on the pool bottom.

However, for plunging jets (Figure 5.6b and d) on the pool bottom at stagnation (PB1), an inversion occurs and even the absolute pressures increase with jet aeration. This is a consequence of the reduction of kinetic energy dissipation due to shear stress and consequent increase of velocity in the *zone of established flow* caused by the large air quantities entrained by plunging jets.

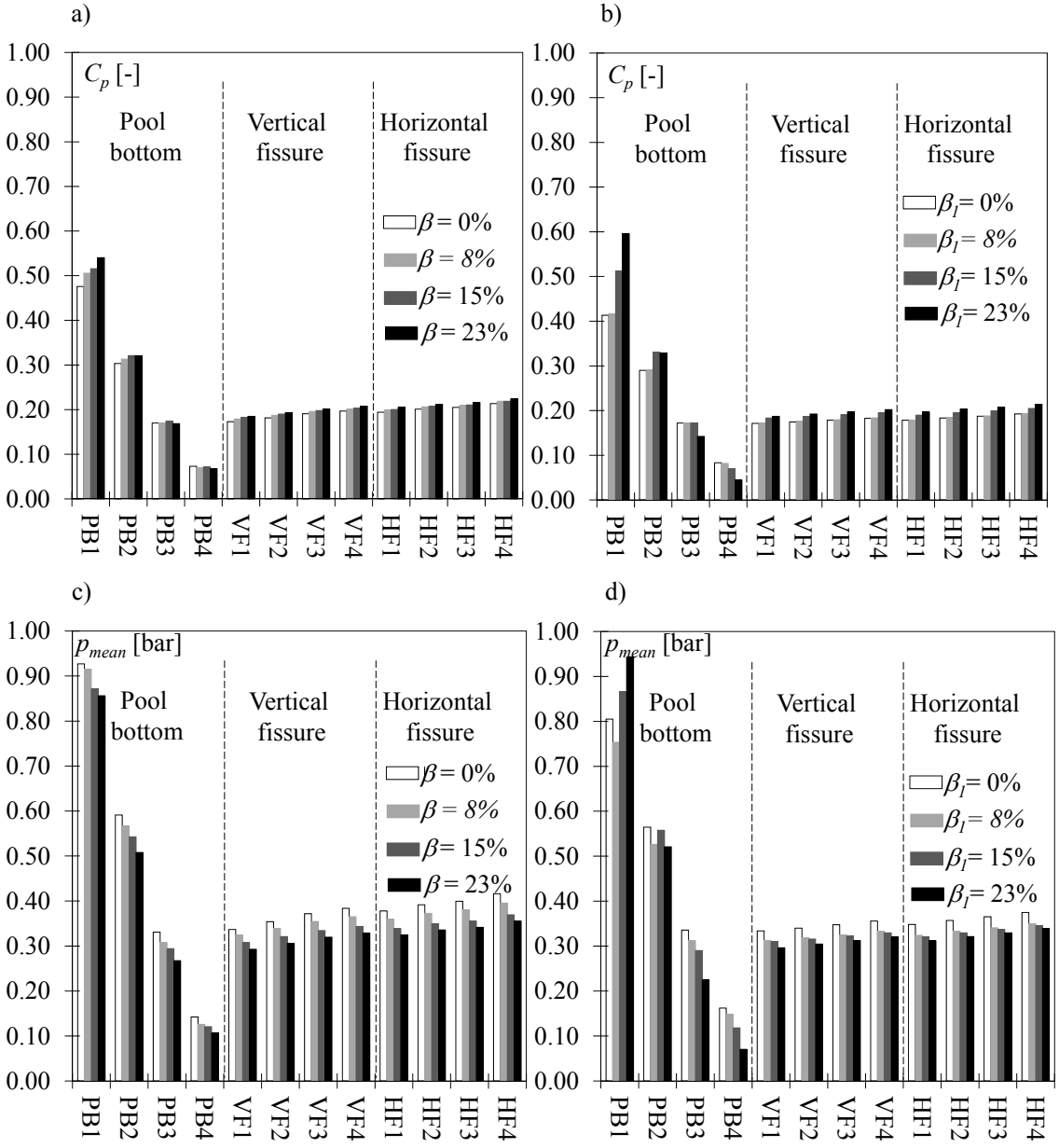

Figure 5.6. Influence of the incoming jet aeration β_1 on the time-averaged pressures p_{mean} and pressure coefficients C_p around the block; centered jets, fixed block, V_{aw} = 19.6 m/s; a) and c) submerged jet; Y/d_j = 9.7; b) and d) plunging jet; Y/d_j = 11.1.

This phenomenon is without doubt the reason of higher C_p values observed for both aerated submerged and plunging jets at stagnation. An increase in centerline velocities for aerated jets in the *zone of established flow* was certainly too small and could not be measured for submerged jets (in Chapter 4) due to relatively low air quantities. Nevertheless, a slight increase tendency was observed for plunging jets, indicating that shear stresses are reduced by the presence of air bubbles. This is confirmed by the pressure measurements in this study.

A direct assessment of the influence of jet aeration on the mean pressures may be obtained by dividing the time-averaged pressures of the aerated jets by the time-averaged pressures at the same position of a clear-water jet, which will be called as relative aerated

pressure for clarity in the following. It can be precisely computed for submerged jets (Figure 5.7a at stagnation – PB1; and Figure 5.7b at the fissure entrance, VF1). For the plunging jets, even if the test configurations with $\beta_1 = 0$ still entrain a considerable amount of air at the plunge region, the same procedure of dividing the time-averaged pressures of an aerated jet by the time-averaged pressures of the similar non-aerated jet was used (Figure 5.7c at stagnation – PB1; and Figure 5.7d at the fissure entrance, VF1).

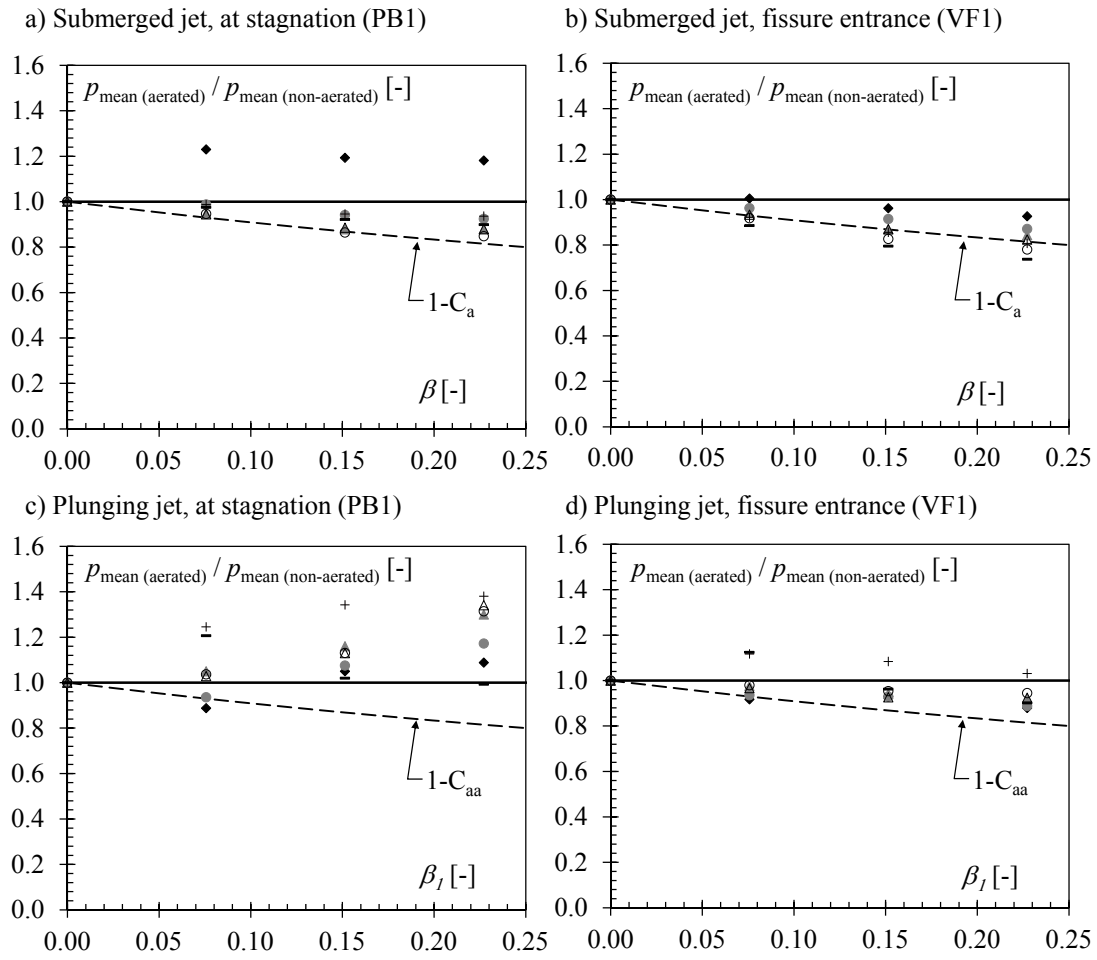

Figure 5.7. Time-averaged pressures for an aerated jets divided by the time-averaged pressures of the similar non-aerated jet *versus* the incoming jet aeration, centered jets, fixed block; a) and b) submerged jets, $Y/d_j = 9.7$; c and d) plunging jets, $Y/d_j = 11.1$; a) and c) stagnation (PB1); b) and d) fissure entrance (VF1); (-) $V_{aw} = 7.4$ m/s; (+) $V_{aw} = 9.8$ m/s; (○) $V_{aw} = 12.3$ m/s; (Δ) $V_{aw} = 14.7$ m/s; (▲) $V_{aw} = 17.2$ m/s; (●) $V_{aw} = 19.6$ m/s; (♦) $V_{aw} = 22.1$ m/s; (dashed line) 1-C_{aa}.

For the submerged jets, it can be seen in Figure 5.7 that the incoming jet aeration mainly causes a reduction of the relative aerated pressures, both at stagnation and inside fissures, with the exception of V_{aw} = 22.1 m/s at stagnation. At the fissure entrance (Figure 5.7b) the momentum reduction ($1 - C_a$) gives the general trend of the pressure reduction, which is lower as the jet velocities are higher.

For the plunging jets, it is evident that the incoming jet aeration produces higher relative aerated pressures at stagnation as a result of higher velocities in the jet centerline. This may be relevant for the block stability in the case of jets impinging directly over a fissure. Nevertheless, for the centered jet presented in Figure 5.7d, the incoming jet aeration mostly diminishes relative aerated pressures inside the fissures, even if less than the reduction of momentum would lead to. In Figure 5.7c and d, note that a curve for 1-C_a taking into account the whole entrained air concentration would result in a curve lower than 1-C_{aa} shown for plunging jets.

The effects of the incoming jet velocity and pool depth on the mean pressures for incoming plunging aerated jets (β_1 = 23%) are compared to non-aerated jets in Figure 5.8, at stagnation and fissure entrance. It can be confirmed that the aerated centered plunging jets produce more often higher mean pressures at stagnation (Figure 5.8a) and lower mean pressures inside fissures (Figure 5.8b).

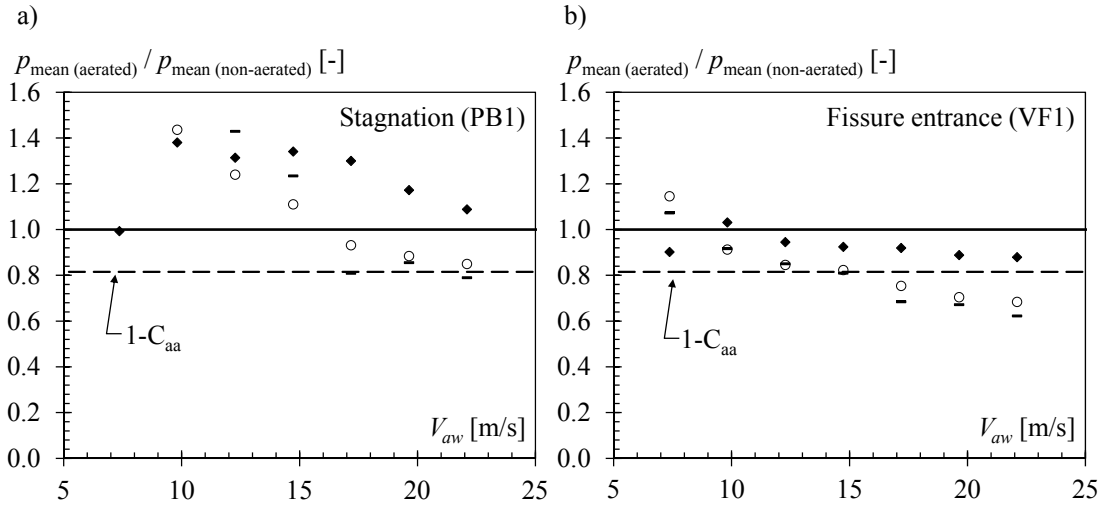

Figure 5.8. Time-averaged pressures for aerated jets (β_1 = 23%) divided by the time-averaged pressures of the similar non-aerated jet *versus* the incoming jet velocity V_{aw} for different relative pool depths, centered plunging jets, fixed block; a) stagnation (PB1) b) fissure entrance (VF1), (-)Y/d_j = 4.2; (○)Y/d_j = 6.9; (♦) Y/d_j = 11.1; (dashed line) 1-C_{aa}.

In general, deeper pools generated higher relative aerated pressures compared to shallow pools, both at stagnation and inside fissures. This confirms again that aerated jets reach the bottom with higher velocities by dissipating less energy along the pool trajectory.

Hence, the balance between two physical processes determines the influence of jet aeration. Aerated jets have less momentum due to a lower mean apparent density, which diminishes the pressures around the block. Nevertheless, the entrainment of air bubbles also reduces the shear stresses in the dissipating jet, and jet velocities for aerated jets become higher. This results in a pressure rise, especially close to the jet centerline.

On one hand, pressure rise due to the reduction of jet dissipation is influenced by the entrained air concentration and pool depth. On the other hand, the pressure reduction due to the loss of momentum is influenced by air concentration only, as described in Eq. (5.15). With increasing jet velocity, the relative importance of jet dissipation reduction in the pool depth decreases and so the relative aerated pressures reduce (Figure 5.8a and b).

Pressure fluctuations

The RMS values of the pressure fluctuations are shown for submerged and plunging jets in Figure 5.9. It can be seen that plunging jets produce higher pressure fluctuations than submerged jets, due to an increase in turbulence at the plunge region. Also, submerged aerated jets produce higher pressure fluctuations at the pool bottom as well as inside the fissures.

The pressure fluctuations around the block for plunging jets have a different behavior. The aeration of plunging jets increases pressure fluctuations at the pool bottom, but reduces pressure fluctuations inside the fissures.

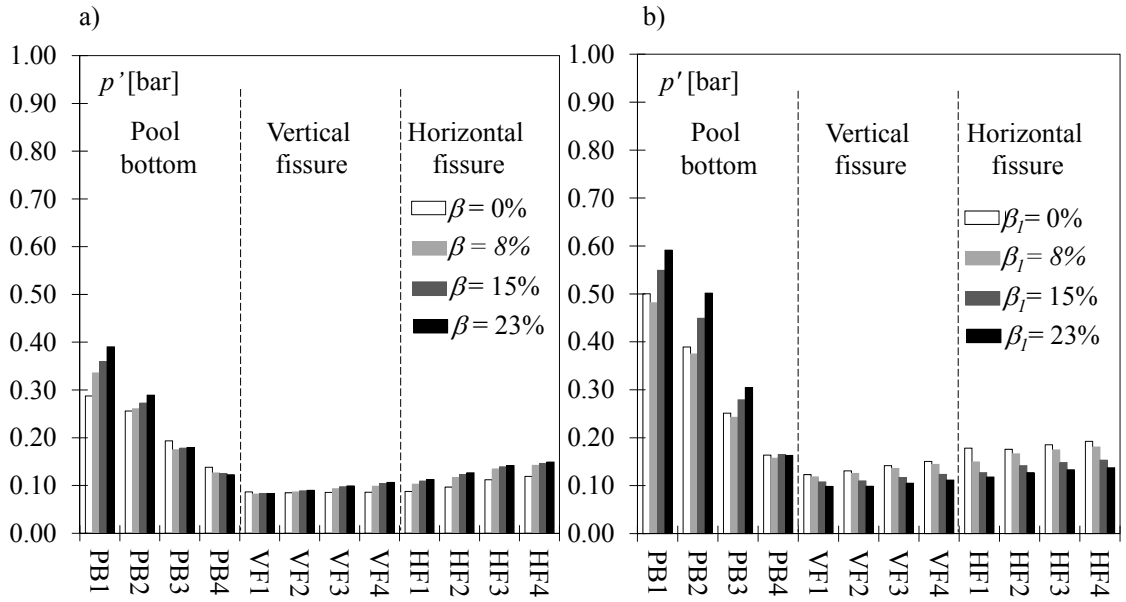

Figure 5.9. Influence of the incoming jet aeration on the RMS of pressures fluctuations around the block; centered jets, fixed block, V_{aw} = 22.1 m/s; a) submerged jet; Y/d_j = 9.7; b) plunging jet; Y/d_j = 11.1.

To analyze the influence of jet aeration in the RMS of the pressure fluctuations, these values are divided by the RMS of the pressure fluctuations for similar non-aerated jets, which will be called relative aerated RMS for clarity in the following, similarly to what was done for the time-averaged pressures.

Figure 5.10 shows relative aerated RMS in the same configurations shown in Figure 5.7 for relative aerated pressures. At stagnation, relative aerated RMS grows

exponentially with jet aeration while, at the fissure entrance, a reduction is observed. Note that, in Figure 5.9a, for submerged jets, the position VF1 was the only pressure sensor inside the fissure where the RMS of the aerated jets is lower than the one of the non-aerated jet.

Figure 5.11 shows the effect of the incoming jet velocity and of the pool depth on the relative aerated RMS, for plunging centered jets. At stagnation, the deep pool (Y/d_j = 11.1) produces much higher relative aerated RMS than the shallower pools. The differences between the relative aerated RMS for Y/d_j = 11.1 and for Y/d_j = 4.2 and 6.9 are maximal for jet velocities of approximately V_{aw} = 15 m/s and begin to converge toward approximately 1.2 for jets of higher velocities. At the fissure entrance, aerated plunging jets produce lower pressure fluctuations. The relative aerated RMS has a slight tendency to reduce with increasing jet velocities.

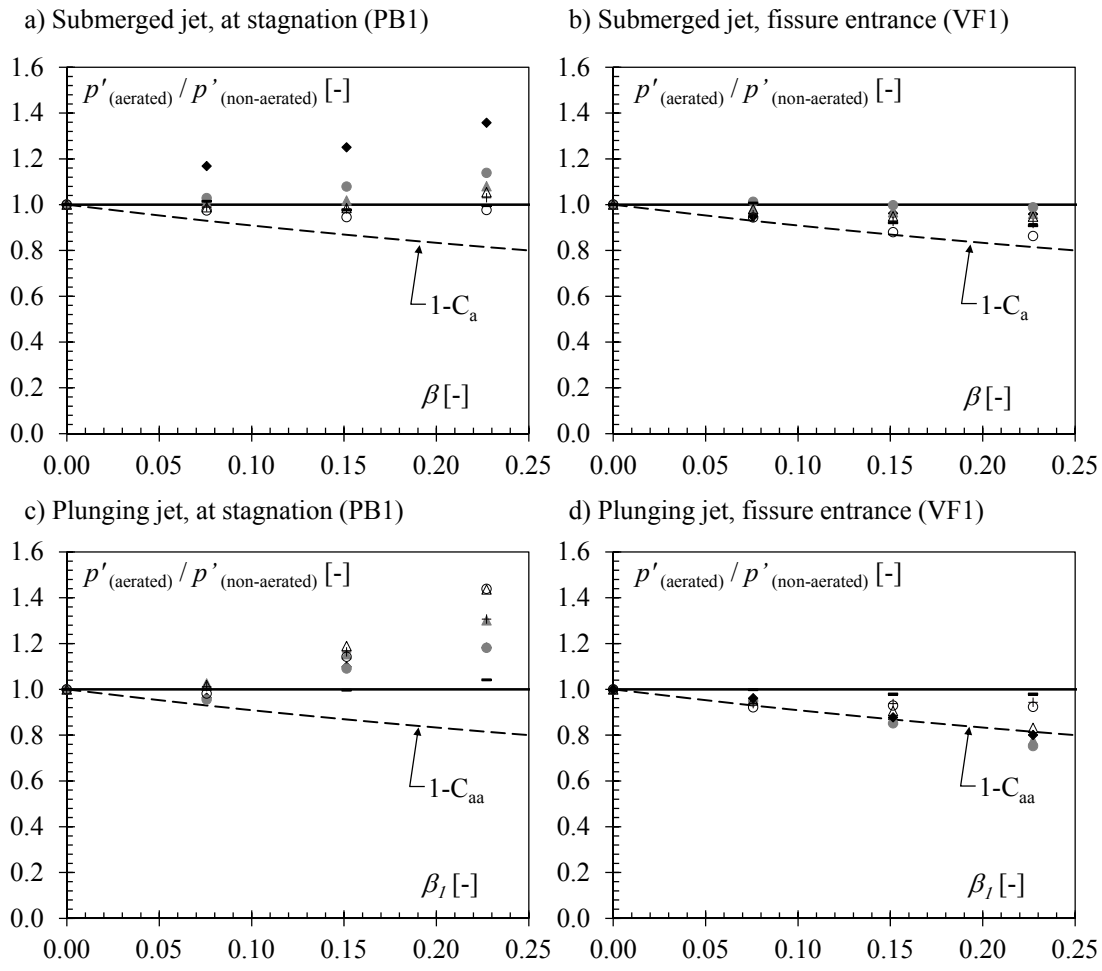

Figure 5.10. Relative aerated RMS *versus* the incoming jet aeration, centered jets, fixed block; a) and b) submerged jets, Y/d_j = 9.7; c and d) plunging jets, Y/d_j = 11.1; a) and c) stagnation (PB1); b) and d) fissure entrance (VF1); (-) V_{aw} = 7.4 m/s; (+) V_{aw} = 9.8 m/s; (○) V_{aw} = 12.3 m/s; (Δ) V_{aw} = 14.7 m/s; (▲) V_{aw} = 17.2 m/s; (●) V_{aw} = 19.6 m/s; (♦) V_{aw} = 22.1 m/s; (dashed line) 1-C_{aa}.

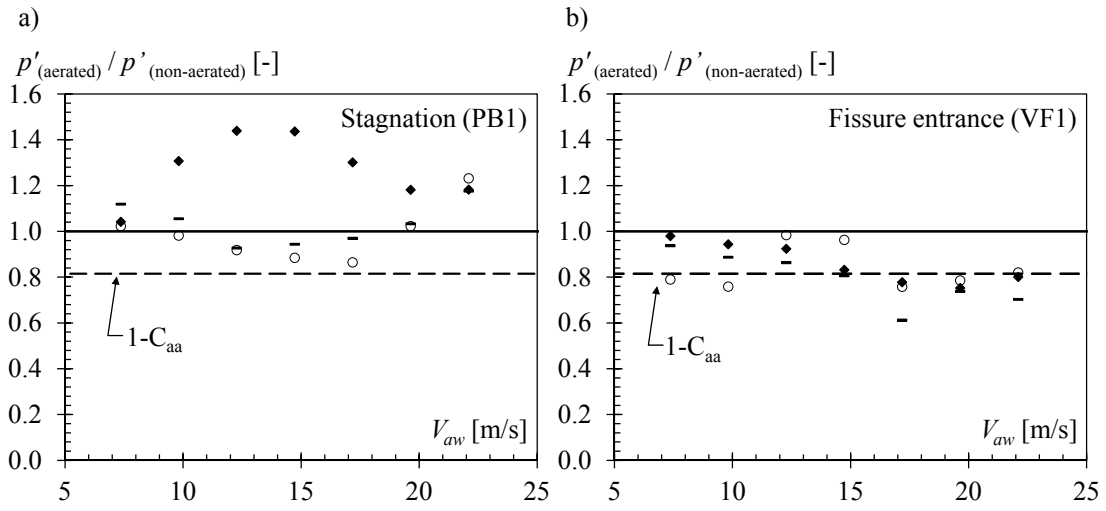

Figure 5.11. Relative aerated RMS for aerated jets (β_1 = 23 %) divided by the Relative aerated RMS of the similar non-aerated jet *versus* V_{aw} for different relative pool depths, centered plunging jets, fixed block; a) stagnation (PB1) b) fissure entrance (VF1), (-)Y/d_j = 4.2; (○)Y/d_j = 6.9; (♦) Y/d_j = 11.1; (dashed line) 1-C_{aa}.

5.3.2 Frequency domain analysis

The entrained air bubbles influence not only the dynamic pressure coefficients, but also the structure of the turbulent flow. Especially inside fissures, the air bubbles influence transient phenomena by changing properties of the fluid, such as the apparent fluid density, fluid compressibility and pressure wave celerity. Bollaert (2002) stated that air may be present inside rock joints in three manners: dispersed free air bubbles, air bubble cavities and dissolved air.

Figure 5.12 shows the Power Spectral Densities P_{xx} of the pressure fluctuations computed for high-velocity plunging centered jets, for selected positions around the fixed block. The positions on the pool bottom have a higher spectral energy, and are clearly distinguishable from the positions inside the fissure. At low frequencies, the spectral contents follow the "unfolded" distance from the jet centerline, and the positions inside the fissures are packed in a narrow band (see Figure 5.12a).

In his milestone work on the turbulence structure of incompressible fluid flows, Kolmogoroff (1941) stated that the turbulence energy is transferred as a power function of the eddies frequency. A core jet impacts the bottom when the relative pool depth is small. That means that the shear layer is not large and the turbulent eddies are of reduced size. Thus, the core jet impact produces turbulent energy at a large range of frequencies, including high frequencies, resulting in a steady decay slope of -1 (Figure 5.12a and c).

On the other hand, a developed jet impact on the bottom takes place when the pool is relatively deep. The shear layer of the diffusing jet is larger and the turbulent energy is produced at lower frequencies, limited by the turbulence length scale which is limited by the largest eddy size. Then, the spectral content decays at a slope of -5/3 (Figure 5.12b and d), in the inertial range of scales where no turbulent energy is produced, towards viscous energy dissipation in the form of heat in the smallest scales.

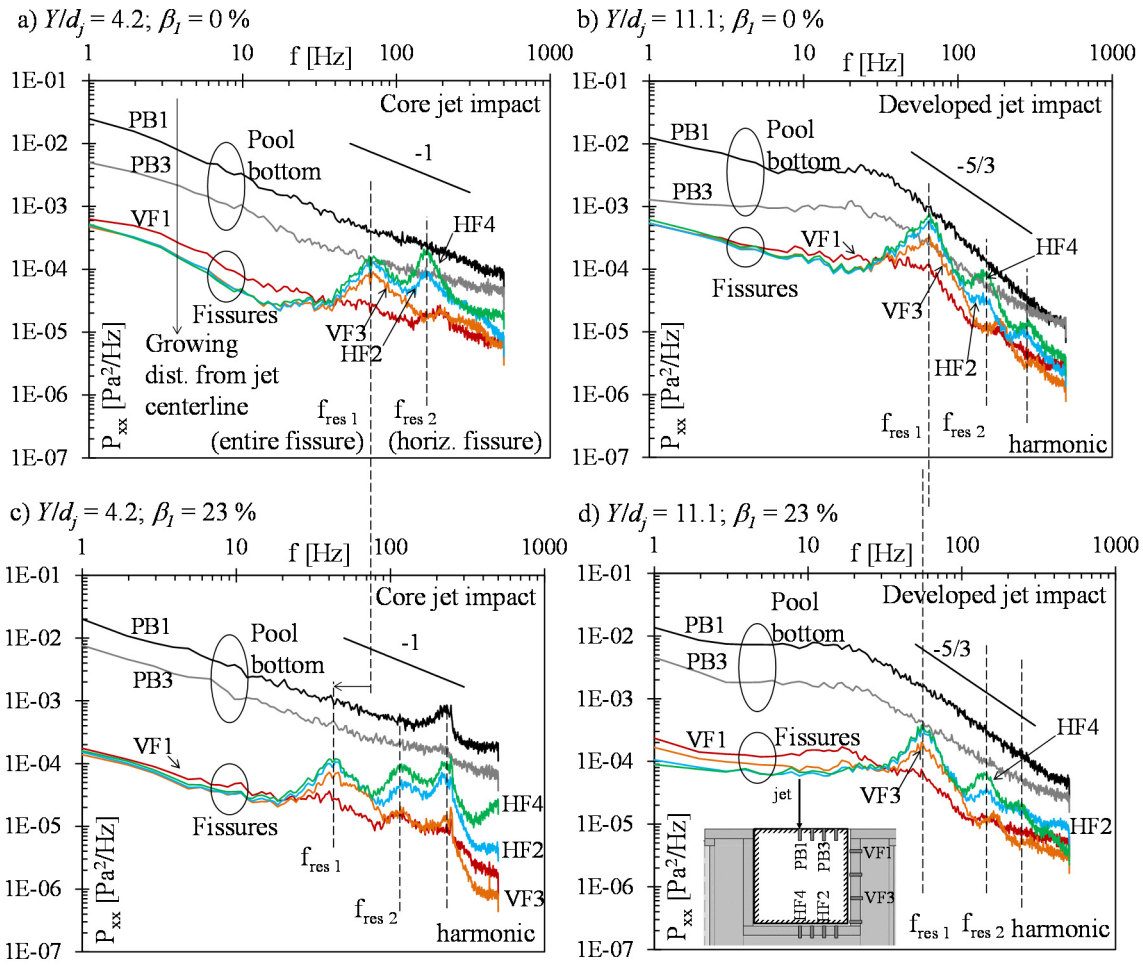

Figure 5.12. PSD of the dynamic pressure signals at selected positions around the fixed block; centered plunging jets, V_{aw} = 22.1 m/s, above: non-aerated jets a) Y/d_j = 4.2; β_1 = 0 %; b) Y/d_j = 11.1; β_1 = 0 %; below: aerated jets c) Y/d_j = 4.2; β_1 = 23 %; d) Y/d_j = 11.1; β_1 = 23 %.

The turbulence length scale L_s is determined by the frequency where the slope change towards a -5/3 decay is observed. Although the exact frequency is difficult to determine, the analysis of Figure 5.12b; and d suggest that, for the non-aerated jet, f = 30 Hz, while, for the aerated jet with β_1 = 23 %, f = 20 Hz. On the pool bottom, the turbulence length scale L_s can then be calculated with $L_s = V/f$.

Using the measured mean pressures as the kinetic energy per unit volume at stagnation and Eq. (5.2), the jets issued with a velocity of V_{aw} = 22.1 m/s reach the bottom with 15.1 m/s (β_1 = 0 %) and 17.4 m/s (β_1 = 23 %). This leads to length scales of approximately 0.50 m (β_1 = 0 %) and 0.87 m (β_1 = 23 %). This is an approximation since it is difficult to determine the exact frequencies. Nevertheless, it clearly shows that the aeration of the jet changes the structure of the diffusing jet by enlarging its shear layer.

The transient effects inside the fissures are certainly the most evident feature in Figure 5.12. If the spectral energy decreases with the distance from the jet centerline at low frequencies, an inversion occurs as a consequence of wave superposition at higher

frequencies. The symmetric layout dictates that the highest resonance peaks are observed for the position HF4. The peaks observed at lower frequencies, denoted as f_{res1}, correspond to resonance frequencies of pressure waves travelling the entire fissure around the block, while the second peaks, denoted as f_{res2}, are a consequence of partial wave reflections in the horizontal fissure.

The aerated jets produced lower resonance peaks compared to the non-aerated jets. In the case of core jet impact, the aerated jet produced a relevant shift of the resonance frequency f_{res1} towards a lower value. The PSD estimates show f_{res1} = 65 Hz approximately for the non-aerated jet and f_{res1} = 40 Hz approximately for the jet with β_1 = 23 %. Although difficult to visualize, a small shift also took place for the developed jet impact, where again f_{res1} = 65 Hz approximately for the non-aerated jet and f_{res1} = 55 Hz approximately for the jet with β_1 = 23 %.

A lower resonance frequency is related to a reduction in wave celerity due to the presence of air bubbles. This provides experimental evidence that the air bubbles were capable of entering the fissures and of modifying resonance properties. The influence of the total jet aeration on the resonance phenomena is analyzed for the submerged jet case in Figure 5.13. The spectral densities of the pressure fluctuations at the center of the fissure (HF4) are compared for jets with different air contents. The resonance frequencies are highlighted and are directly influenced by the jet aeration.

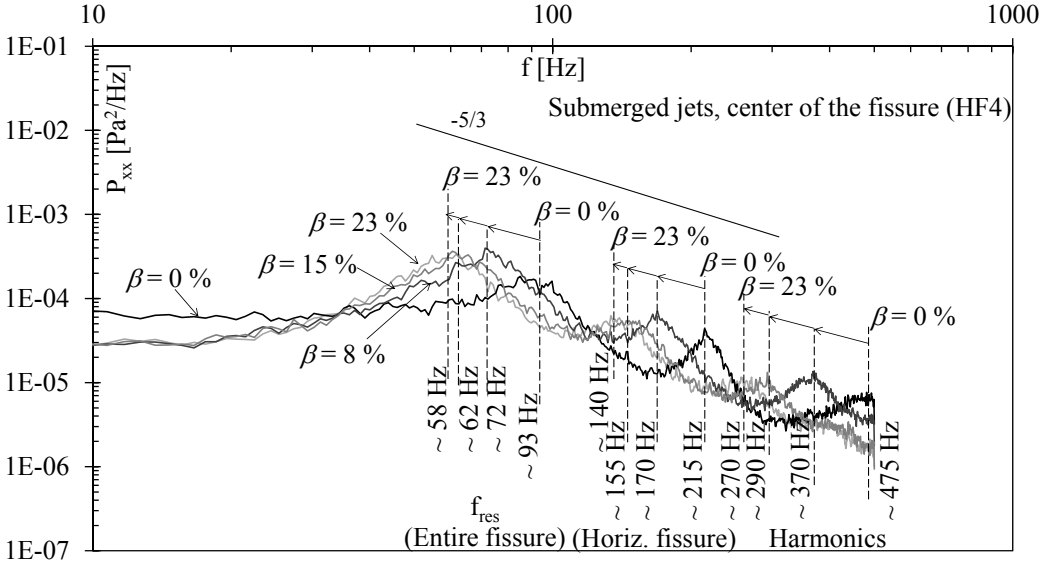

Figure 5.13. PSD of the dynamic pressure signals at the center of the fissure (position HF4) for submerged jets; V_{aw} = 22.1 m/s, above: non-aerated jets (black line) β = 0 %; (dark grey line) β = 8 %; (grey line) β = 15 %; (light grey line) β = 23 %.

The pressure wave celerity inside the open-ended fissure is calculated using $c = f_{res} \times 2L_f$, where L_f is the fissure length. The experimental results of wave celerity versus jet aeration β for submerged jets with different velocities are shown in Figure 5.14. The

celerity decreases with jet aeration following a power-law. The celerity average is approximately 104 m/s for the non-aerated jets and approaches 70 m/s for high jet aerations.

These values of pressure wave celerity are much lower than the celerity values for unbounded clear-water media (1'465 m/s at 15°C) and air media (340 m/s at 15°C) (Blevins, 1984). Pressure waves propagating inside fissures are influenced by the fluid-structure interactions with the flow boundaries. Analogy is made with the water-hammer phenomenon in closed-conduits, where pressure wave celerity is known to be dampened by the elastic behavior of the conduit (Hachem and Schleiss, 2011). In this study, although the block was fixed inside the cavity, it vibrated when impacted by the jets. These block vibrations act as a pseudo-elasticity of the flow boundaries, which explains the low celerity results.

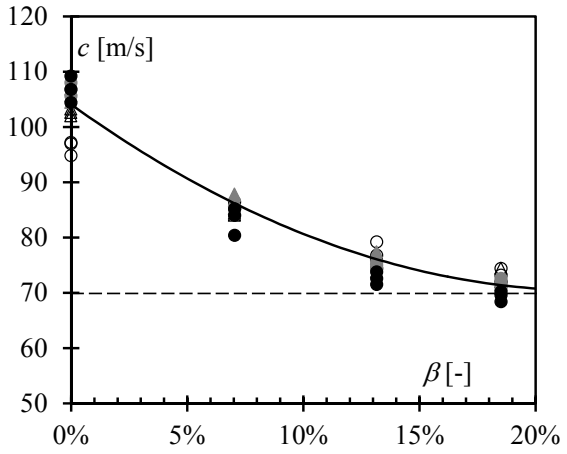

Figure 5.14. Celerity of the pressure waves for submerged jets *versus* jet aeration β; fixed block, (○) V_{aw} = 12.3 m/s; (Δ) V_{aw} = 14.7 m/s; (▲) V_{aw} = 17.2 m/s; (●) V_{aw} = 19.6 m/s; (●) V_{aw} = 22.1 m/s, (black line) general trend; (dashed line) asymptotic value at 70 m/s.

5.4 Conclusion

A systematic experimental study was carried out to assess the influence air entrained by high-velocity jets on the dynamic pressures applied on the bottom of a plunge pool and inside underlying fissures. Vertical water jets with different issuance velocities and aerations impinged into a water pool and the resulting dynamic pressures were measured on 12 different positions uniformly distributed along one half of a cubic block embedded on the bottom.

The different test configurations also compared plunging and submerged jets and jet impingement on the center or on the side of the block. The time-averaged pressures, pressure fluctuations, extreme pressure values and the spectral energy of the pressure fluctuations around the block were analyzed.

A relationship is suggested to describe the time-averaged pressures on the pool bottom at the jet centerline as a function of the relative pool depth by coupling pressure

measurements at stagnation with velocity measurements in the jet centerline performed in recent study (Chapter 4).

It was found that the entrainment of air bubbles produces two opposed effects. First, an aerated jet, due to its lower apparent density, has less momentum than a similar clear-water jet. This effect contributes to lower pressures on the pool bottom. Second, the entrained air bubbles reduce the shear stresses of the dissipating jet in the pool, allowing the aerated jets to flow with higher velocity. This effect contributes to a pressure rise, mainly close to the jet centerline. The influence of air entrainment is a balance of these two effects. However, inside the fissures, most often, the aerated jets produce lower mean pressures and oscillations, tendency that is enhanced for high-velocity jets. For rock scour assessment, this indicates that jet air entrainment contributes to decrease the formation of a scour hole at the pool bottom.

Additionally, the spectral densities of the pressure fluctuations show that the air bubbles are able to enter the fissures and to modify the resonance properties of the pressure waves by reducing their celerity.

6

Effect of pool confinement on dynamic pressures acting on a block impacted by plunging aerated jets

The erosion caused by jets issued from hydraulic structures progressively develops a confined scour hole on the original riverbed. A realistic scour assessment has to take into account the influence of the entrained air bubbles as well as the flow patterns induced by the bottom geometry on the jet diffusion in the plunge pool. This Chapter analyses the combined influence of jet aeration and lateral pool confinement on the dynamic pressures affecting the water-rock interface and inside 3D open-end fissures. The lateral confinement of a plunge pool reduces time-average pressures and pressure fluctuations on the water-rock interface and inside fissures. The confinement also changes the structure of the turbulent flow, concentrating turbulent energy production at the lower frequencies of the periodogram. Additionally, when a block is mobile in the rock mass, it generates a pressure release inside the surrounding joints consequently to its augmented vibrations in opposition to a fixed block. It also reduces the celerity of pressure waves propagating inside the fissures.

Keywords: Air entrainment, plunging jets, flow pattern, rock scour, plunge pool, high-velocity jets, lateral jet confinement

6.1 Introduction

High-velocity jets issued from high-head hydraulic schemes have the potential to generate erosion when impacting the rocky riverbed, where a confined scour hole progressively develops (Schleiss, 2002). This modification of the riverbed bottom geometry has a significant effect on the jet dissipation features and therefore on the dynamic pressures acting on the water-rock interface and underlying fissures of the rock mass (Manso, 2006). The equilibrium or ultimate scour is established when the incoming energy of the jet is dissipated to an extent where further rock fissure break-up and rock block ejection no longer take place.

Compared to the simpler flat bottom case, the impingement of a jet into a plunge pool with ideal confinement can be characterized by a confinement diameter d_c and a pool depth Y comprising the sum of the initial pool depth h relatively to the original riverbed and the scour depth t_c (Figure 6.1). An empirical formula proposed by Mason and Arumugam (1985) is of particular interest due to exhaustive data sets used from 26 prototype cases and 47 physical models with erodible beds:

$$Y = \alpha \frac{H^{\alpha_1} q^{\alpha_2} h^{\alpha_3}}{g^{\alpha_4} d_m^{\alpha_5}} \tag{6.1}$$

where H is the hydraulic head determined by the difference between the reservoir and tailwater levels, q is the discharge rate [m^2/s], g is the gravitational acceleration, d_m is the mean particle or rock size, $\alpha = 6.42 - 3.1H^{0.10}$, $\alpha_1 = 0.15 - H/200$, $\alpha_2 = 0.60 - H/300$, $\alpha_3 = 0.15$, $\alpha_4 = 0.30$ and $\alpha_5 = 0.10$. The variable parameters were a consequence of the analysis of the prototype data. If only model tests are analyzed, the result of the fitting process gives $\alpha = 3.27$, $\alpha_1 = 0.05$, $\alpha_2 = 0.60$, $\alpha_3 = 0.15$, $\alpha_4 = 0.30$ and $\alpha_5 = 0.10$.

Later, to account for the effect of air entrainment, Mason (1989) proposed a modification to Eq. (6.1), this time only considering model tests on erodible beds formed with loose granular sediments:

$$Y = \alpha \frac{(1+\beta)^{\alpha_1} q^{\alpha_2} h^{\alpha_3}}{g^{\alpha_4} d_m^{\alpha_5}} \tag{6.2}$$

where β is the jet aeration provided at the plunge section, or air-to-water ratio, defined as the entrained air discharge Q_a divided by the jet water discharge Q_w. The fitting process, for model results only, led to constant parameters, $\alpha = 3.39$, $\alpha_1 = 0.30$, $\alpha_2 = 0.60$, $\alpha_3 = 0.16$, $\alpha_4 = 0.30$ and $\alpha_5 = 0.06$. Although the physical background of replacing the hydraulic head H by the jet aeration β as a parameter for scour assessment is questionable, it gives a reasonable upper bound for the scour depth (Bollaert, 2002).

The geometrical features of the scour hole in granular, loose material were investigated by Pagliara et al. (2008a). Experiments were performed with inclined jets impinging on erodible beds, and the resulting geometric parameters of the scour hole were described in terms of a densimetric Froude number F_d that takes into account water and sediment densities. A similar approach was used by Canepa and Hager (2003) who

studied the influence of air entrainment in the scour hole formation. The scour depth results were drawn in terms of a modified densimetric Froude number that considers the three relevant phases in the scouring process, namely water, air and sediments.

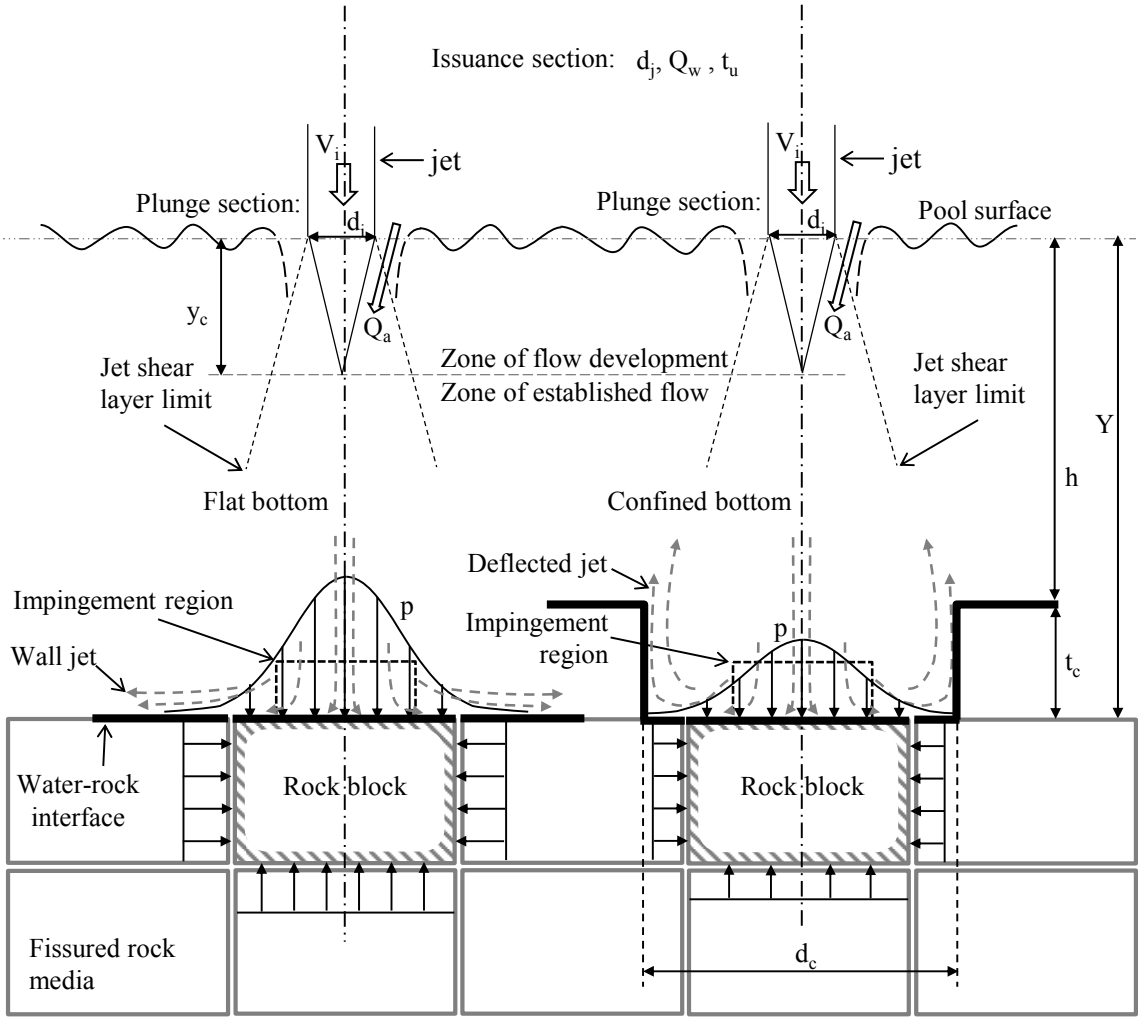

Figure 6.1. Definition sketch of plunging jets showing jet flow streamlines and time-averaged pressure distribution around a block embedded on a flat bottom (left) and a confined bottom (right).

To evaluate the dynamic pressures acting on a rock mass, a solid but fissured media has to be considered. Systematic experiments using high-velocity jets on a large facility were performed by Bollaert and Schleiss (2003b), Manso et al. (2007) and Federspiel (2011) for pools with a flat bottom and by Manso (2006) and Manso et al. (2009) for confined pool bottoms.

Manso (2006) assessed dynamic pressures acting on the water-rock interface and inside a closed-end fissure on the bottom of a plunge pool with 9 different geometries, including 1 flat bottom case and 8 laterally confined configurations. He pointed out that the pool bottom geometry induces coherent flow patterns (Figure 6.1), which strongly influence jet dissipation and air bubble penetration. The confined pool deflects the jet back towards the pool surface, creating intermittent jet ejections, oscillations inside the confined region, pool surface oscillations and ring vortexes. The upward currents accentuate jet development and jet velocity decay, resulting in less energy reaching the

pool bottom. Nevertheless, a narrow lateral confinement may enhance pressure transmission to the rock and pressure amplification inside closed-end fissures (Manso et al., 2009).

In this Chapter, the influence of a laterally confined pool on the dynamic pressures acting in a 3D open-end fissure around a rock block impacted by aerated high-velocity jets is assessed experimentally. This allows a more complete understanding of the combined influences of jet aeration and pool geometry, taking into account the recent developments of Manso (2006) and Manso et al. (2009) on the influence of pool confinement on closed-end fissures, as well as the work of Federspiel (2011) on a 3D open-end fissure in a flat bottom case and the findings of Chapter 5 on jet aeration.

6.2 Physical model tests

The experiments were carried out in a large facility (Figure 6.2) built at the Laboratory of Hydraulic Constructions (LCH) of the Ecole Polytechnique Fédérale de Lausanne (EPFL). The circular jets were issued vertically from a d_j = 72 mm diameter cylindrical nozzle. Air was pumped into the nozzle through 6 small orifices to produce aerated water jets at the issuance section (Duarte, 2013).

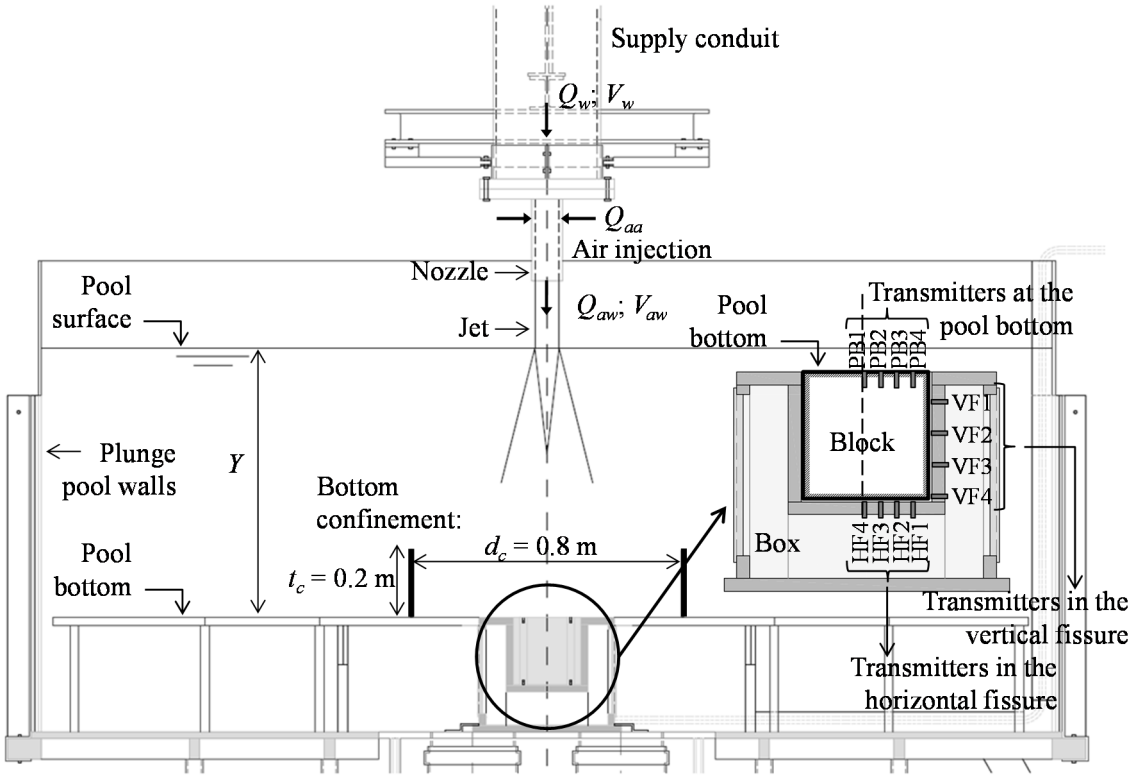

Figure 6.2. View of the experimental facility with confined bottom and detail of the instrumented block with the position of the pressure transmitters; adapted from Federspiel (2011).

The generated air-water jets discharges Q_{aw} varied from 30 to 90 l/s. The corresponding velocities of the air-water jets at the issuance section V_{aw} varied from 7.4 to 22.1 m/s. Four different values of jet aeration at the nozzle outlet $\beta_1 = Q_{aa}/Q_w$ were

tested: 0, 8, 15 and 23 %. In addition, there is relevant air entrainment at the plunge section, as illustrated in Figure 6.1.

The turbulence intensities T_u of the water jets immediately downstream of the issuance section were measured in the longitudinal direction by Manso et al. (2008). T_u values of approximately 8 % for the lower jet velocities, reducing asymptotically to values between 4 and 5 % for high jet velocities, were observed. Hence, the experimental jets present near-prototype velocities and turbulence characteristics. Scale effects are thus minimized and the spectral content of the pressure signals are accurately reproduced (Bollaert and Schleiss, 2003b).

The pool depth Y was either 30, 50 or 80 cm, corresponding to relative pool depths Y/d_j of 4.2, 6.9 and 11.1 respectively. Lateral confinement was simulated by a 0.8 m diameter steel cylinder (d_c/d_j = 11.1, Figure 6.3b) and compared to a reference flat bottom case. This confinement corresponds to the "intermediate pool" tested by Manso et al. (2009). A rock block embedded on the pool bottom was represented by a metallic system composed of a box and a block (Figure 6.3a). The 20 cm side cubic block was inserted into a box, whose dimensions provided a1 mm thick 3D fissure between the block and the cavity, which was kept constant by lateral guides. The center of the block was aligned with the jet centerline reproducing an axisymmetric configuration. Comparison was made between the block fixed inside the cavity or free to move in the vertical direction.

12 pressure transducers of type Kulite HKM-375M-17-BAR-A were uniformly flush-mounted along one half of the block (Figure 6.2). The dynamic pressures were measured with an acquisition frequency of 1 kHz. 65'536 samples were obtained for each test run. To ensure repeatability, each test run was performed 3 times (Duarte et al., 2013).

6.3 Results and discussion

6.3.1 General behavior of the jet and induced flow patterns

According to Beltaos and Rajaratnam (1977), the impingement of a jet on a flat obstacle perpendicular to its centerline is composed of three distinct regions, namely i) the free jet region, where the jet dissipates by shear with the surrounding fluid independently from the obstacle; ii) the impingement region, where the jet is slowed abruptly by the presence of the obstacle causing a pressure build-up around the stagnation point, which is the intersection between the jet centerline and the pool bottom and iii) the wall jet region, consequence of mass conservation at stagnation. Hence, the vertical jet is deflected creating a flow parallel to the obstacle.

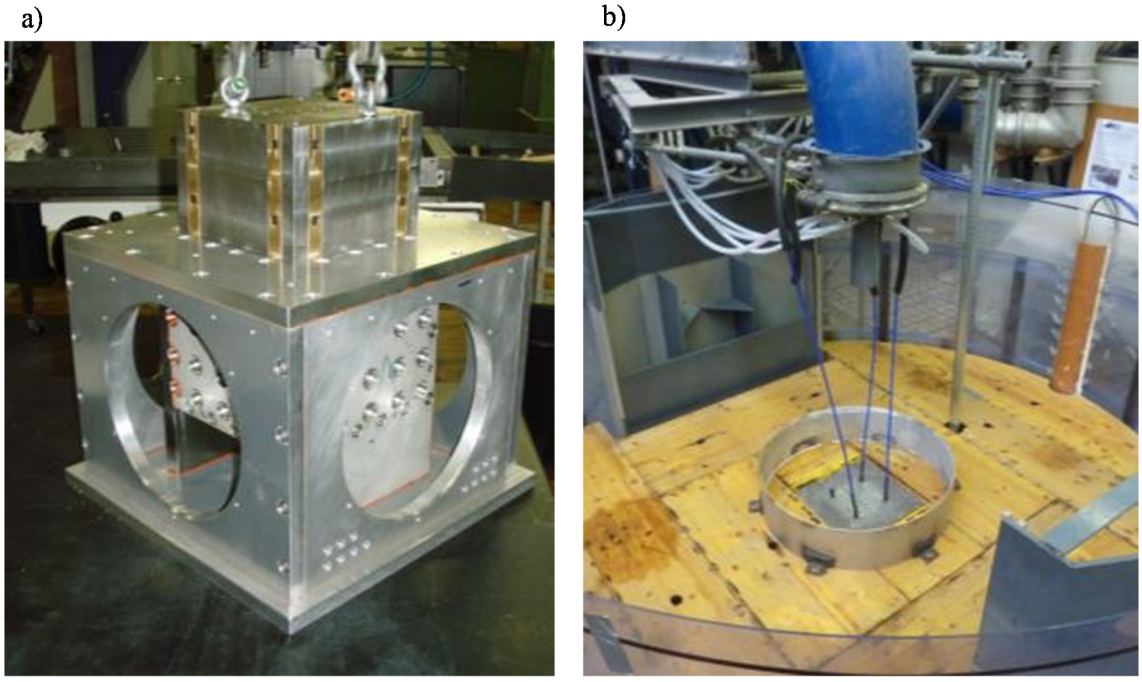

Figure 6.3. Photos of a) detail of the instrumented block being inserted into the cavity and b) experimental facility with confinement cylinder and instrumented block installed on the bottom.

The wall jet pulls the flow further from the diffusive shear layer. After a while, when the energy of the wall jet is also dissipated, the recirculating currents in the pool make the flow rise slowly towards the surface. A laterally confined pool alters this behavior by deflecting the wall jet upwards before its energy is dissipated. This might induce shear between the downward and upward currents and contribute to jet dissipation.

In Figure 6.4a an upward deflection of the wall jet as a consequence of pool bottom confinement is clearly visible due to the flow of the entrained air bubbles. In Figure 6.4b jet ejections from the pool surface can be seen. The latter is more pronounced for relatively shallow pools and high jet velocities. Low frequency pool surface oscillations, which do not occur for the flat bottom case, were also observed.

6.3.2 Dynamic pressures around the block

The pressure time-averaged values and the pressure fluctuations around the block were analyzed. By considering the issued jet as a homogeneous mixture of air and water, the mean density of the jet at issuance is:

$$\rho_{aw} = \frac{1}{1+\beta_1}\rho_w + \frac{\beta_1}{1+\beta_1}\rho_a \tag{6.3}$$

where ρ_w and ρ_a are respectively the water and air densities.

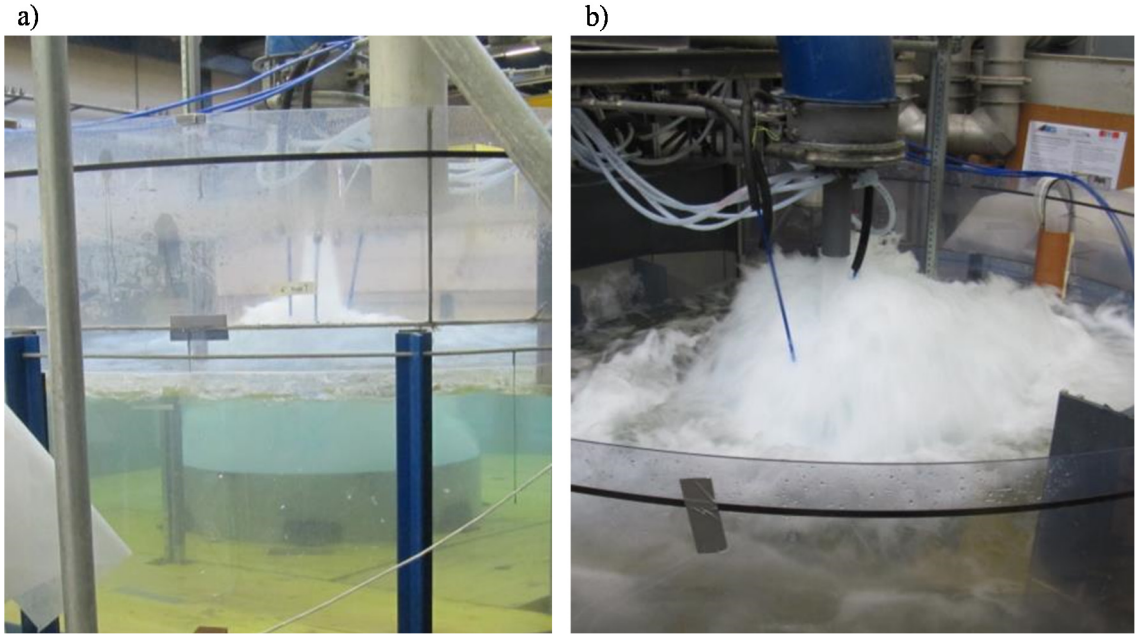

Figure 6.4. Photos of a) detail of the jet flow induced patterns in the plunge pool (V_{aw} = 7.4 m/s, β_I = 0 %), and b) jet geyser-like flow ejections (V_{aw} = 22.1 m/s, β_I = 0 %).

Non-dimensional pressure coefficients for the time-averaged pressures C_p and for the pressure fluctuations C'_p were computed at each transducer position on the block using the kinetic energy per unit volume of the jet at the plunge section as the scaling parameter.

$$C_p = \frac{p_{mean} - \rho_w g Y'}{\frac{1}{2}\rho_{aw} V_i^2} \tag{6.4}$$

$$C'_p = \frac{p'}{\frac{1}{2}\rho_{aw} V_i^2} \tag{6.5}$$

where p_{mean} and p' are, respectively, the time-averaged pressure and the RMS of the pressure fluctuations, g is the gravitational acceleration, Y' is the vertical distance between the pool surface and the pressure transducer and V_i is the velocity of the jet at the plunge section, considering acceleration of gravity during the fall distance.

6.3.2.1 Dynamic pressures for fixed block

C_p and C'_p values for the highest tested jet velocity (V_{aw} = 22.1 m/s) and for the three tested relative pool depths are represented in Figure 6.5 and Figure 6.6. The flat and the confined bottom configurations and non-aerated (β_I = 0 %) and aerated jets (β_I = 23 %) are compared.

The general trend for both C_p and C'_p distributions throughout the block have been explained in Chapter 5. Both parameters present Gaussian distributions on the pool bottom (top of the block), similarly to the velocity distribution in a cross section of a jet impinging in the pool. Inside the fissures, the time-averaged pressure and pressure fluctuation coefficients slowly increase toward the center of the joint (HF4). In such a symmetric case, this increase of the pressure coefficients inside the fissure is caused by the superposition of the pressure waves, and reaches its maximum in the central position of the fissure.

In Figure 6.5 and Figure 6.6 it can be seen that the influences of the jet aeration and of the confined bottom are strongly dependent on the relative pool depth. The influence of the entrained air was discussed in detail in Chapter 5. It was highlighted that the air bubbles have two opposed effects on the resulting pressures. On one hand, the pressures are reduced as a consequence of a lower momentum of the aerated jets, due to its lower density. On the other hand, jet velocity decay along the pool depth is reduced by the entrained air bubbles, which increases the pressures on the bottom, especially close to stagnation. The latter effect is evidently stronger in relatively deep pools.

The reduction of the time-averaged pressure coefficient C_p (Figure 6.5) due to pool confinement is stronger for a deep pool (Y/d_j = 11.1) while it is almost inexistent for a shallow pool (Y/d_j = 4.2). This may be explained by the effect of the shear between upward and downward currents on the resulting pressures, which are dependent on the pool depth. The pool depth determines the length along which the shear stress dissipates the jet energy.

A similar behavior is observed for the pressure fluctuations coefficient C'_p (Figure 6.6). The deeper the pool, the stronger the pressure fluctuations are reduced for the confined bottom case. For the flat bottom case, C'_p values are higher for the deep pool (Y/d_j = 11.1), in agreement with Bollaert and Schleiss (2005) and Manso et al. (2007), who found that a developed jet impact on the bottom produces higher pressure fluctuations.

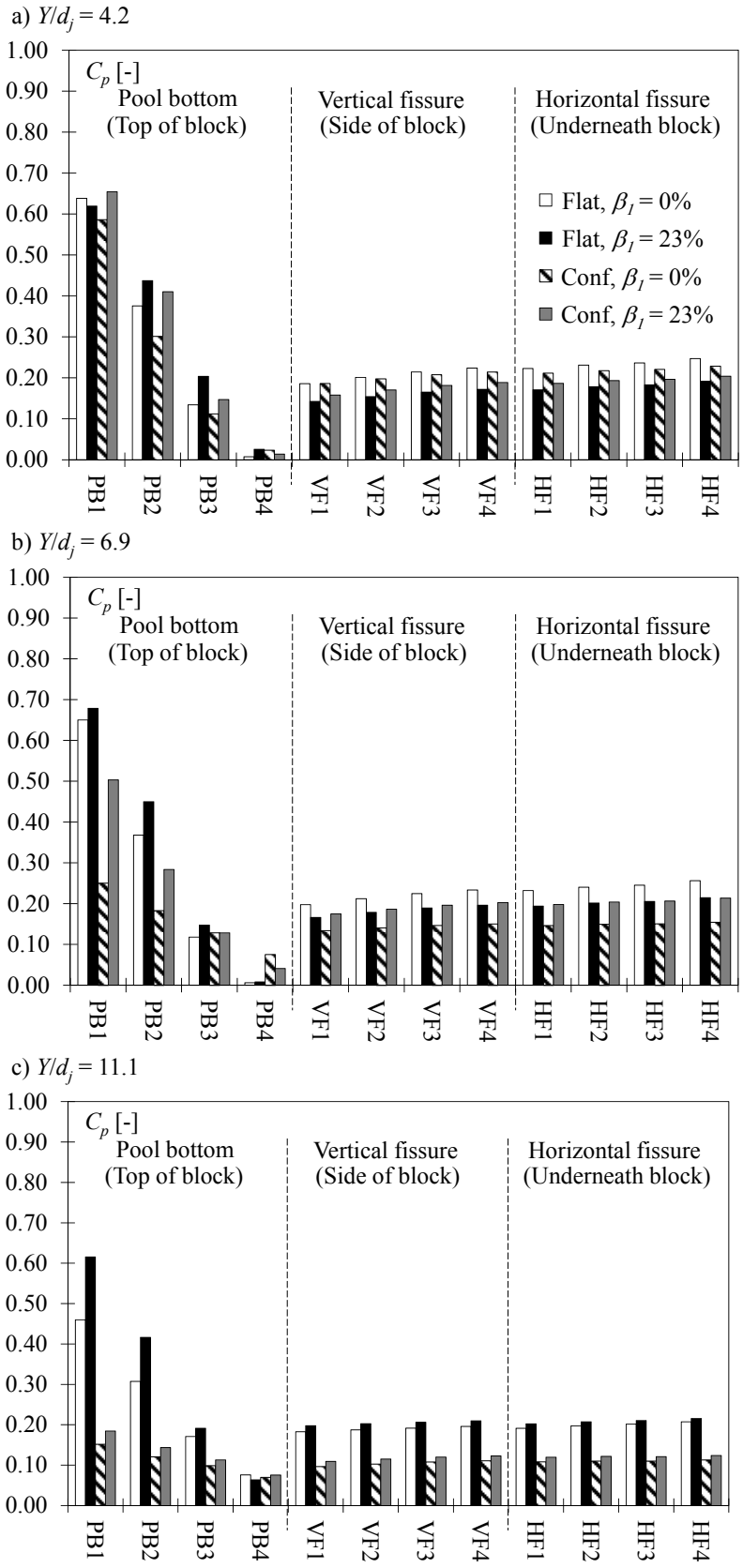

Figure 6.5. Time-averaged pressure coefficient C_p around the fixed block for an issuance jet velocity V_{aw} = 22.1 m/s and different relative pool depths; a) Y/d_j = 4.2; b) Y/d_j = 6.9; c) Y/d_j = 11.1; for flat bottom with β_1 = 0 % (white bars) and β_1 = 23 % (black bars); as well as for confined bottom with β_1 = 0 % (hatched bars) and β_1 = 23 % (grey bars).

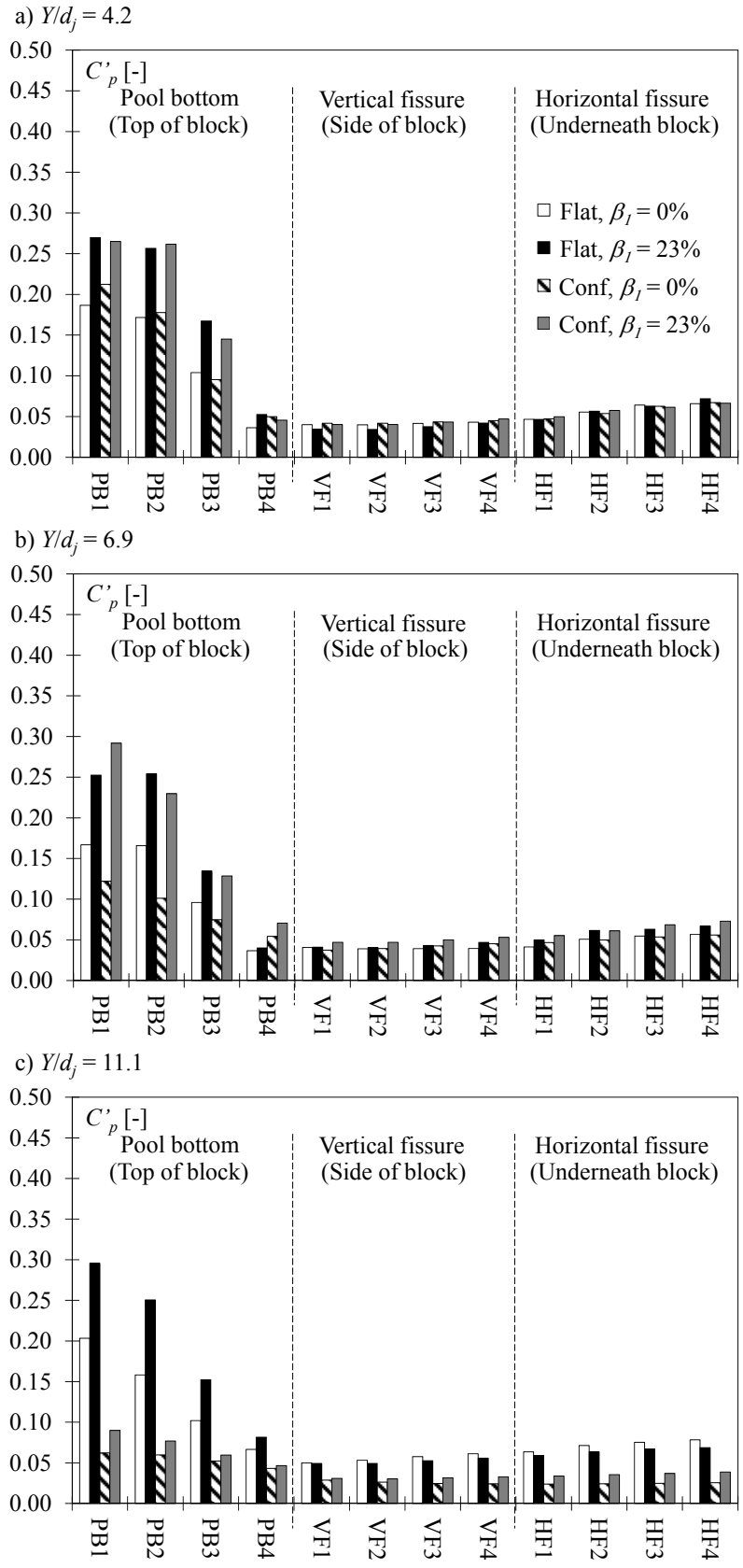

Figure 6.6. Pressure fluctuations coefficient C'_p around the fixed block for an issuance jet velocity V_{aw} = 22.1 m/s and different relative pool depths; a) Y/d_j = 4.2; b) Y/d_j = 6.9; c) Y/d_j = 11.1; for flat bottom with β_1 = 0 % (white bars) and β_1 = 23 % (black bars); as well as for confined bottom with β_1 = 0 % (hatched bars) and β_1 = 23 % (grey bars).

The influences of pool confinement and jet aeration on the time-averaged pressure coefficient C_p for the whole set of tested jet velocities and pool depths are shown in Figure 6.7 at the intersection of the jet centerline with the water-rock interface (stagnation point, PB1). Two different regions can be clearly distinguished, corresponding to a developed jet impact or a core jet impact on the bottom.

A core jet impact on the bottom occurs when the required core development length y_c is greater than the existing pool depth Y. The consequence is a jet compact core impacting directly on the bottom, which results in high time-averaged pressures and relatively low pressure fluctuations. On the other hand, a developed jet impact is observed when $y_c < Y$ (Figure 6.1 is an example). The resulting time-averaged pressures are lower due to the dissipation of the jet along its centerline.

It was pointed out in Chapter 5 that the limit between a core jet impact and a developed jet impact depends both on pool depth and on jet velocity. Figure 6.7 (all cases) shows that, for relatively low velocities, C_p increases with a concave function of the jet velocity. This corresponds to a developed jet impact on the bottom, where the core of the jet was previously disintegrated on the shear layer. For a deep pool (Y/d_j = 11.1), only developed jet impact is observed since the jet core never reaches the bottom (Figure 6.7c). Indeed, in Chapter 4, the maximum core length found for high jet velocities was $y_c = 7.8d_i$ for plunging jets, which is coherent with the current pressure results.

For the remaining shallower pool depths (Y/d_j = 4.2 and 6.9, Figure 6.7a and b), a change is noted for V_{aw} = 15 m/s approximately, from an increasing function at lower jet velocities to a convex decreasing function at higher jet velocities, corresponding to core impacts on the bottom. The maximum C_p values are observed in the intersection of the two regions. This means that the transitional jets where $y_c = Y$ are the most efficient in terms of converting the kinetic energy of the jet into time-averaged pressures acting on the bottom at stagnation. However, it has to be noted that the outer bounds in Figure 6.7 are only indicative of the behavior of the time-averaged pressure coefficient evolution with increasing jet velocity. They correspond only approximately to the zones for core and developed jet impact and its transition.

The influences of pool bottom confinement and jet aeration are very clear and confirm the assumptions made previously. A confined bottom resulted in lower C_p values at stagnation for jets of similar velocity and aeration. The deeper the pool, the stronger the reduction of the confined case compared to the flat one. Reductions of C_p due to pool bottom confinement were none or barely noticed for the shallow pool (Y/d_j = 4.2, Figure 6.7a). If similar jets with different aerations are compared, the most aerated jets produced higher C_p values. The differences increase with the pool depth. Hence, both the effects of pressure reduction due to jet confinement and pressure rise due to lower jet dissipation rate of aerated jets close to stagnation are exacerbated by an increasing pool depth.

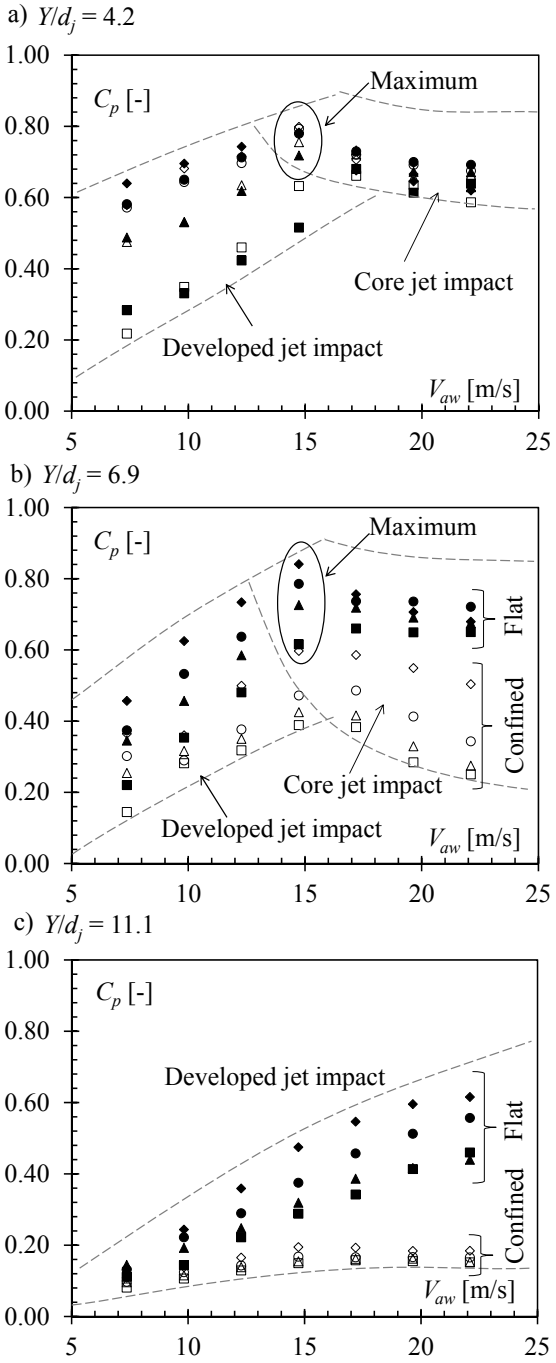

Figure 6.7. Time-averaged pressure coefficients C_p at stagnation *versus* the issuance jet velocity V_{aw} for different relative pools depths; a) Y/d_j = 4.2; b) Y/d_j = 6.9; c) Y/d_j = 11.1; flat bottom with β_l = 0 % (■), β_l = 8 % (▲);β_l = 15 % (●) and β_l = 23 %(♦); confined bottom with β_l = 0 % (□), β_l = 8 % (Δ), β_l = 15 % (○) and β_l = 23 %(◊); and indicative outer bounds (dashed lines).

6.3.2.2 Differences between fixed and free block

When the block is free to move in the vertical direction inside the cavity, pressure releases inside the fissures due to block vibrations. The pressures acting inside the fissures are the result of the excitation provided by the energy signals at the fissure entrances at the water-rock interface and by the pressure wave propagation inside the 3D joint. Hence, the dynamic pressures inside the fissures will be analyzed at the position VF1 close to the fissure entrance.

Figure 6.5 shows that the jets impinging on the center of the block produce time-averaged pressure coefficients C_p close to the fissure entrance which are always higher inside the fissure (VF1) than on the pool bottom (PB4), where a wall jet is formed. This confirms that the fissure is excited by a combination of both dynamic pressures and wall jet.

Then, the increase of mean pressures, pressure fluctuations and extreme pressure values towards the center of the fissure (HF4) is a result of the superposition of pressure waves, even though this increase is too small to produce a positive dynamic uplift force. Bollaert and Schleiss (2003a) stated that the differences in the persistence-time over the block, where the macro-turbulent velocities range is 10^0 – 10^1 m/s, and underneath the block, where pressure-wave celerities are of the order of 10^3 m/s, dampen out transient oscillations inside the fissures.

Figure 6.8 shows the time-averaged pressure coefficient C_p at the fissure entrance (VF1) for non-aerated jets impinging on a flat and a confined bottom with different relative pool depths. Comparison is made between fixed and free blocks.

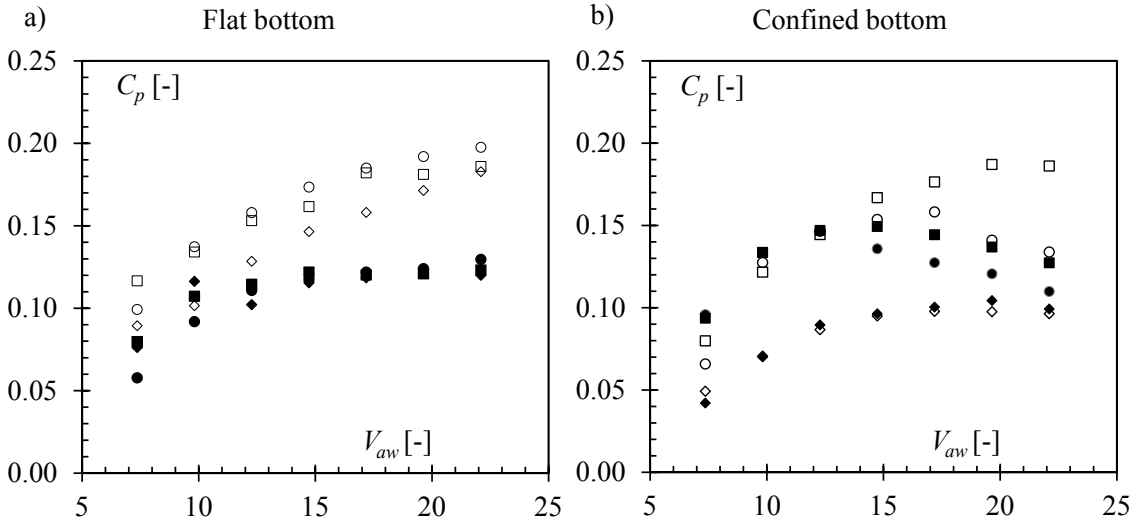

Figure 6.8. Time-averaged pressure coefficient C_p at the fissure entrance (VF1) *versus* jet velocity V_{aw}; non-aerated jets (β_1 = 0 %); for a fixed block with Y/d_j = 11.1 (◊);Y/d_j = 6.9 (○) or Y/d_j = 4.2 (□); and for a free block with Y/d_j = 11.1 (♦); Y/d_j = 6.9 (●) or Y/d_j = 4.2 (■); a) flat bottom; b) confined bottom.

For the flat bottom case (Figure 6.8a), the differences between the time-averaged pressure coefficients C_p for fixed and free blocks become significant for jet velocities V_{aw} > 11 m/s. It is likely that above this limit the block vibrations for the flat case are relevant.

While the C_p values for a fixed block continues to increase, for a free block they reach a limit at approximately 0.12. For the confined case (Figure 6.8b), the behavior of C_p is strongly dependent on the relative pool depth, for the reasons stated before. For a relatively shallow pool ($Y/d_j = 4.2$), a fixed block generates C_p values very similar to those for a flat bottom. A pressure release is observed for jet velocities approximately above 14 m/s. On the other hand, for the deep pool ($Y/d_j = 11.1$), fixed and free block result in similar C_p values, because block vibrations are insignificant in this case.

The pressure fluctuation coefficients C'_p close to the fissure entrance, at VF1, are analyzed in Figure 6.9, under the same configurations used for C_p. For the flat bottom case, C'_p decreases when jet velocity increases for the deeper pools ($Y/d_j = 6.9$ and $Y/d_j = 11.1$), while C'_p increases slightly as a function of the jet velocity for the shallow pool ($Y/d_j = 4.2$). The free block results in a small reduction of the C'_p values. For the confined bottom case, the C'_p results are concentrated in a narrow range, between 2 and 5 %, for all the tested jet velocities. The higher fluctuations observed for lower jet velocities and deep pools, for the flat bottom, were reduced. As the block almost does not move, the differences between fixed and free blocks are minimal.

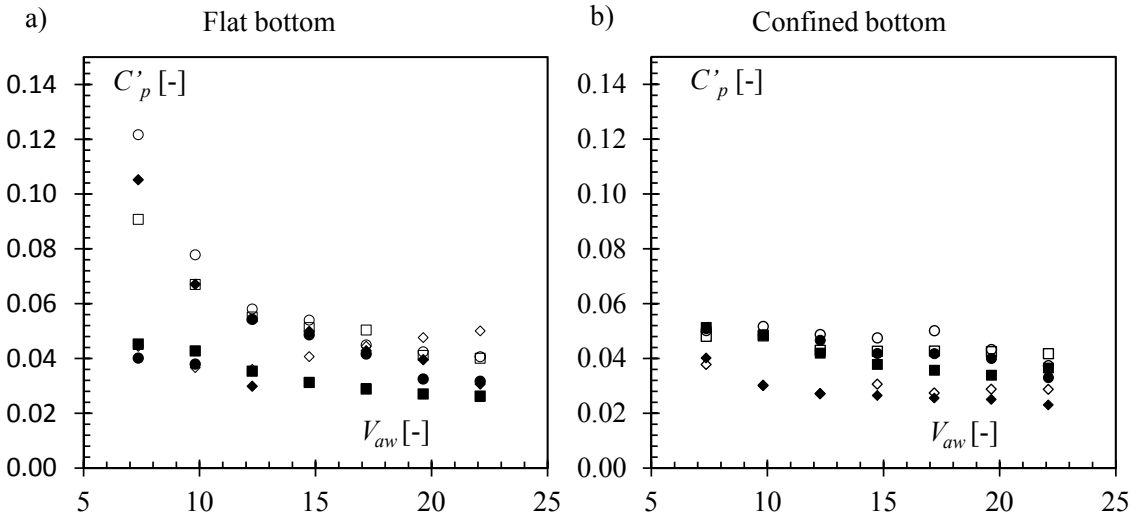

Figure 6.9. Pressure fluctuation coefficient C'_p at the fissure entrance (VF1) *versus* jet velocity V_{aw}; non-aerated jets ($\beta_1 = 0$ %); for a fixed block with $Y/d_j = 11.1$ (◊); $Y/d_j = 6.9$ (○) or $Y/d_j = 4.2$ (□); and for a free block with $Y/d_j = 11.1$ (♦); $Y/d_j = 6.9$ (●) or $Y/d_j = 4.2$ (■); a) flat bottom; b) confined bottom.

6.3.3 Spectral contents of the pressure signals

The Power Spectral Densities (PSD) of the pressure signals P_{xx} were computed using a Welch-periodogram based Fast Fourier Transform (FFT). The signals, composed each of 65'536 samples, were segmented into 64 blocks using a Hamming window and a 50 % overlapping.

The spectral content of the signals represents the energy of each frequency range and provide information about the flow features. In turbulent flows, each frequency is related to turbulent eddies of corresponding length (Chassaing, 2000). In the case of

impinging jets, the energy associated to each eddy size decays as a power function of the frequency (Bollaert and Schleiss, 2003b).

6.3.3.1 Influence of pool confinement and jet aeration

Figure 6.10 shows the obtained spectral contents around the fixed block for a high-velocity jet (V_{aw} = 22.1 m/s), comparing the flat and the confined cases for the shallow pool (Y/d_j = 4.2) and the deep pool (Y/d_j = 11.1).

In general, the developed jet impact occurring in deep pools is characterized by a relatively large shear layer where the turbulent energy is produced. This corresponds, for example, to the almost horizontal spectral content at low frequencies as shown in Figure 6.10c. The limit between horizontal and inclined zones is representative of the largest length of the eddies in the shear layer of the jet. Smaller eddies practically do not produce turbulent energy and this is represented by an inertial range of scales with a -5/3 decay slope in the spectral content (at the right side of the slope change in Figure 6.10c).

On the other hand, a core jet impact occurs in a relatively shallow pool and is characterized by a relatively thinner shear layer, compared to developed jets. The turbulent energy is thus produced at the whole range of frequencies, which is represented by a -1 decay slope (Figure 6.10a). In both developed and core jet impacts, relevant resonance phenomena are observed inside the fissures. Due to symmetry, the amplification of the pressure waves is maximal at the center of the fissure (position HF4). The fundamental frequency $f_{res} = c/(2L_f)$ of the whole open-end fissure around the block is represented as f_{res1}. Due to important partial reflections in the horizontal part of the 3D fissure, a second fundamental frequency is also observed at positions HF2 and HF4 and is denoted as f_{res2}.

The confined bottom configuration changes the structure of the turbulent flows. The comparison of Figure 6.10a with Figure 6.10b shows that the original core jet spectrum, with a constant -1 decay, changed to a typical developed jet spectrum. A concentration of the turbulent energy production at lower frequencies can be observed for the confined case, followed by typical inertial scales with a -5/3 slope decay.

A concentration of turbulent energy production at lower frequencies can also be seen when comparing the developed jet impinging on a flat bottom in Figure 6.10c with the similar confined configuration in Figure 6.10d. There is a significant shift of the slope change towards lower frequencies for the confined case. Additionally, for the confined case, the energy is transferred with a -7/3 decay slope in the inertial range of scales, instead of -5/3 observed in the flat bottom case.

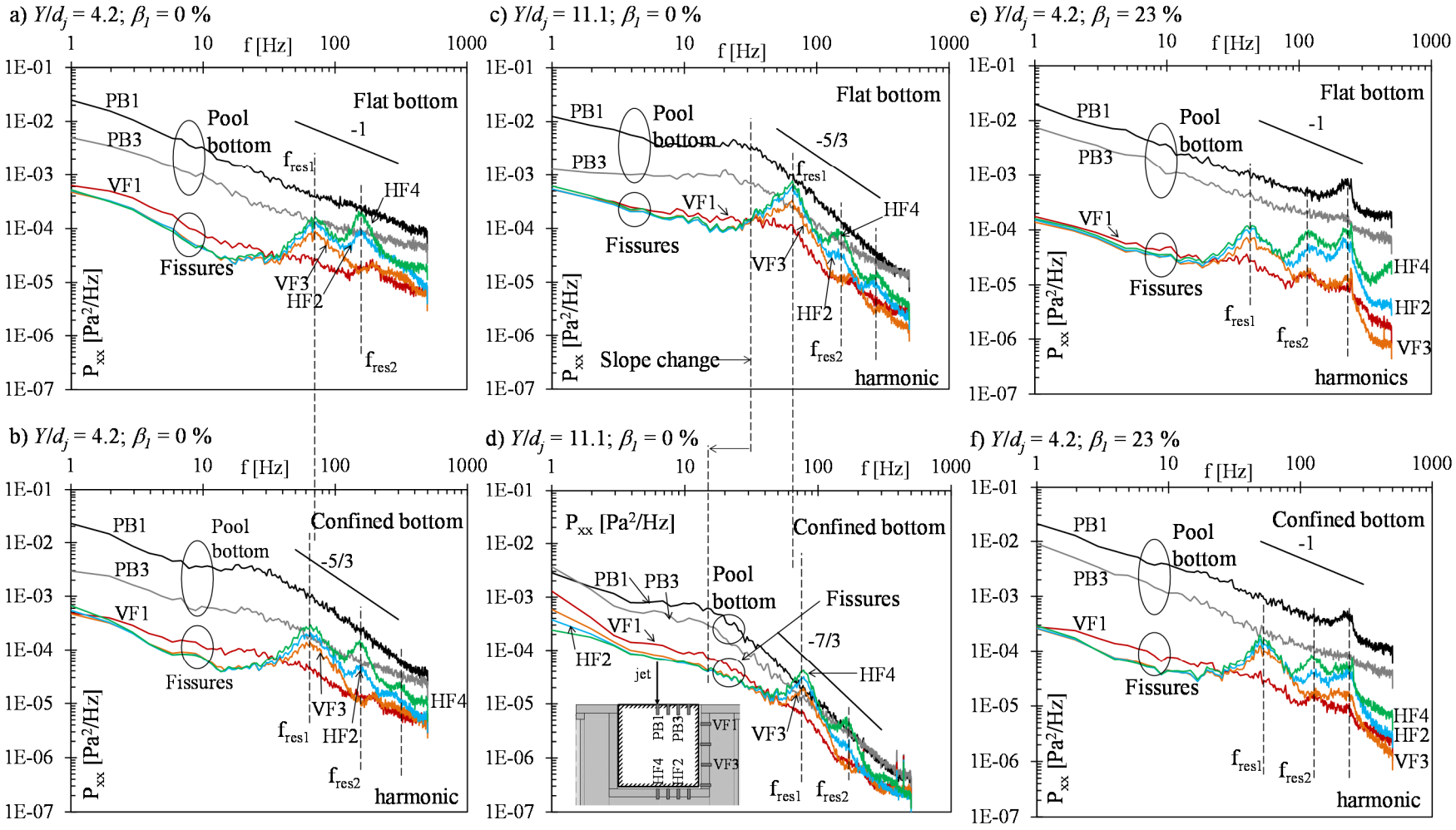

Figure 6.10. PSD of the pressure fluctuations at selected positions on the fixed block; V_{aw} = 22.1 m/s; for a shallow pool (Y/d_j = 4.2), non-aerated (β_1 = 0 %), with flat (a) and confined bottom (b), as well as for a deep pool (Y/d_j = 11.1), non-aerated (β_1 = 0 %) with flat (c) and confined bottom (d), and for a shallow pool (Y/d_j = 4.2), aerated (β_1 = 23 %) with flat (e) and confined bottom (f).

The pool bottom confinement has negligible influence on the resonance frequencies inside the fissures, differently from the case of jet aeration (Chapter 5). The resonance frequency inside the fissures is a function only of the pressure waves celerity and varies with the air concentration of the air-water flow and fluid-structure interactions with the flow boundaries.

However, when aerated jets (β_I = 23 %) impinge on the confined bottom, the previously observed concentration of spectral energy on lower frequencies is neutralized. This is shown by comparing aerated high-velocity jets impinging on a flat bottom (Figure 6.10e) or a confined bottom (Figure 6.10f), which have similar spectral contents.

6.3.3.2 Differences between fixed and free block

Compared to a fixed block, a free block has two effects on the spectral content of the pressure fluctuations. The overall spectral energy inside the fissures is lower due to the pressure release taking place for free blocks. Additionally, a free block has significant influence on the resonance frequencies, hence on the wave celerity of the pressure waves inside the joints.

Figure 6.11 shows the power spectral density estimates for fixed and free blocks and for either shallow or deep pools. The resonance peaks inside the fissures observed for the fixed blocks are strongly dampened and shifted toward lower frequencies if the blocks are free to move. This results from the fluid-structure interactions between the dynamic pressures propagating inside the joints and the moving boundaries of the flow, which are the block faces.

The celerity of the pressure waves propagating on closed conduits depends on the elastic properties of the fluid and of the flow boundaries. This has been extensively studied for the water-hammer phenomenon inside pressure tunnels (Ghidaoui et al., 2005; Hachem and Schleiss, 2011; Halliwell, 1963) and a parallel can be done with the case of pressure waves inside rock joints (Bollaert, 2002). The pressure wave celerity is presented as a function of the fluid density ρ_{aw} and bulk modulus of elasticity K_{aw}, both hereby representing apparent properties of the air-water mixture, Young's modulus of elasticity of the pipe walls E as well as the ratio between the conduit wall thickness e_c and diameter D. According to Ghidaoui et al. (2005), the celerity of the water-hammer propagating inside closed-conduits is defined by:

$$c = \sqrt{\frac{K_{aw}}{\rho_{aw}\left(1 + \frac{K_{aw} \cdot D}{E \cdot e_c}\right)}} \tag{6.6}$$

Comparisons with pressure waves propagating inside open-ended rock joints surrounding free or moderately interlocked rock blocks demonstrate that the wave celerity inside the fissures is reduced by both jet air entrainment and block vibrations. Nevertheless, this phenomenon will not be reproduced correctly by Eq. (6.6), as an important part of the rock vibrations are not due to elastic deformations of the rock material but due to displacement of the whole block as a solid body.

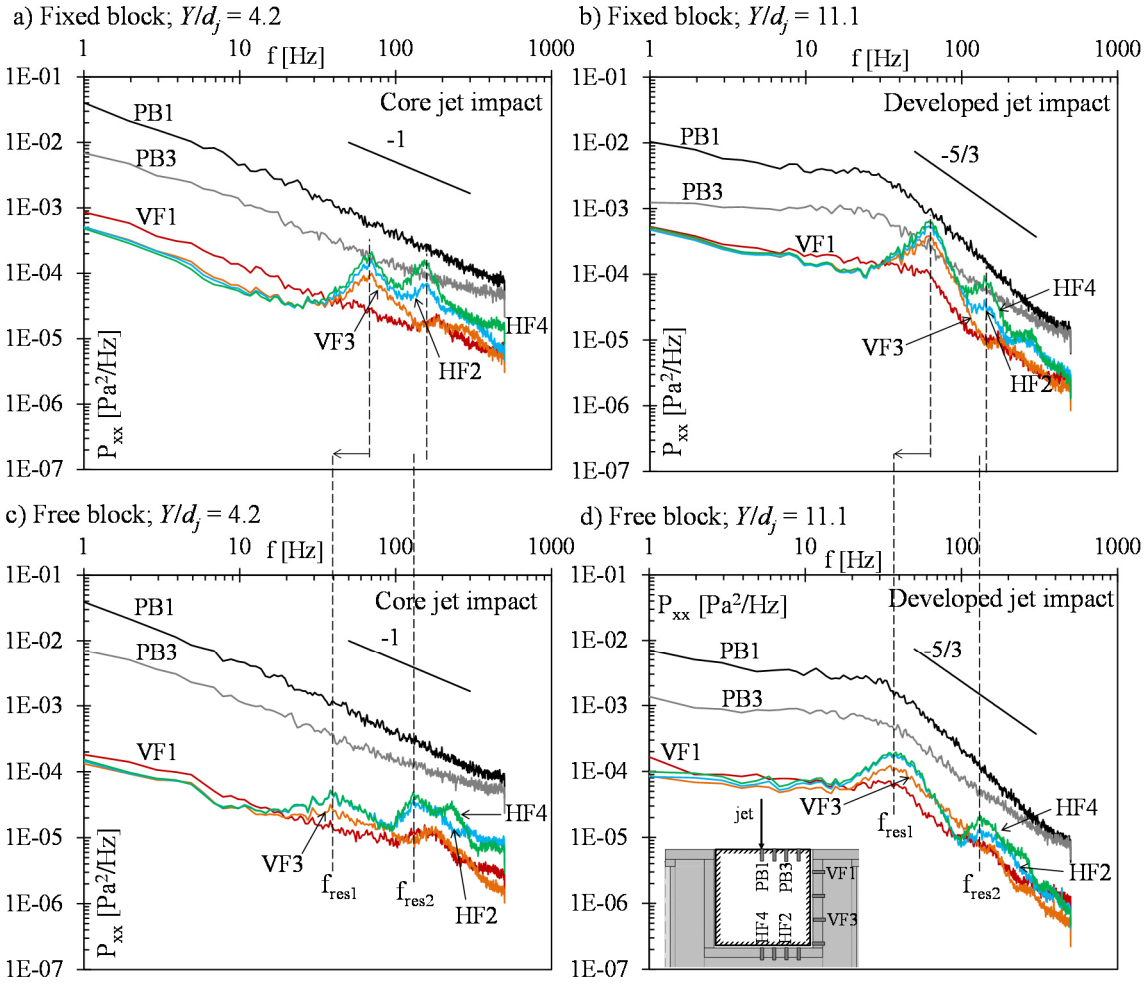

Figure 6.11. PSD of the pressure fluctuations at selected positions around the block for a flat bottom with β_I = 8 %; V_{aw} = 22.1 m/s; for a fixed block with a) shallow pool (Y/d_j = 4.2) or b) deep pool (Y/d_j = 11.1); as well as for a free block with c) shallow pool (Y/d_j = 4.2) or d) deep pool (Y/d_j = 11.1).

6.4 Conclusions

The combined influences of pool bottom confinement and jet aeration on the pressures acting on a 3D open-end fissure on a plunge pool bottom were assessed experimentally using near-prototype jet velocities. This enables a better understanding of the physical mechanisms acting on the scour process, and complements recent experimental researches on the isolated effects of jet aeration (Chapter 5), pool geometry with closed-end fissures (Manso et al., 2009; Manso, 2006) and open-end fissures on a flat bottom (Federspiel, 2011).

The pool bottom confinement produces lower time-averaged pressures and pressure fluctuations on the water-rock interface and inside fissures, due to the shear between the downward current of the incoming jet and the upward current of the deflected wall jet. This is superposed with the effect of the entrained air bubbles, which reduces pressures due to a lower momentum of the jet, but also increases pressures due to a reduction of velocity decay in the pool. The influence of aerated jets impinging on a confined bottom is a superposition of the 3 effects, and is strongly dependent on the relative pool depth.

The pool bottom confinement also changes the structure of the spectral content of the turbulent flow. Turbulent energy production is concentrated at lower frequencies for the laterally confined bottom case, due to a more developed jet in the shear layer.

At the intersection of the jet centerline with the water-rock interface, the time-averaged pressure coefficient C_p follows an increasing function of the incoming jet velocity in the developed jet impact zone, where $y_c < Y$. For relatively shallow pools and high jet velocities, a change takes place and C_p evolves following a convex downward function of the jet velocity in the core jet impact zone. The maximum C_p values are observed in the transition between these two zones, where $y_c = Y$. This transition is located where the conversion of the kinetic energy of the incoming jet into pressure at stagnation is maximum for a given pool depth.

If the block embedded in the pool bottom is free to move vertically, a pressure release inside the fissures occurs, when compared to a fixed one, due to the block vibrations. It also has an important effect on the resonance phenomena inside the fissures, as it reduces significantly the celerity of the pressure waves propagating in the rock joints.

7

Dynamic response of an embedded block impacted by aerated high-velocity jets

Uplift of blocks from the rock mass at the bottom of plunge pools is the main physical process of the scouring phenomenon under a high-velocity plunging jet impact. It depends on the properties of the three phases involved, water, rock and air. However, if the influences of water and rock properties on dynamic block ejection have been investigated in the past, no systematic research has ever assessed the influence of jet air entrainment. This study presents theoretical developments and experimental investigations on the vertical displacements of a block embedded in the pool bottom impacted by aerated plunging jets. The theoretical model reproduces reasonably well the measured block vibrations, especially for high-velocity jets where the physical properties of the air-water mixture inside the fissures are steadier. It could be observed that the block displacements are smaller with increasing jet aeration for shallow pools, but inversely, higher with increasing jet aeration for deeper pools. This agrees with the findings of Chapter 5, showing that jet aeration reduces jet momentum due to a lower apparent density, but also increases bottom pressures due to lower velocity decay along the plunge pool depth.

Keywords: Air entrainment, fluid-structure interactions, rock scour, plunge pool, high-velocity jets, block stability

7.1 Introduction

Even though dynamic block uplift is the most important mechanism of scour formation in plunge pools with rock bottom and concrete-lined stilling basins, systematic

researches on this topic have seldom been performed. Most works studied the dynamic pressures on plunge pool floors (Ervine et al., 1997) and stilling basins (Fiorotto and Rinaldo, 1992b) or around concrete slabs (Bellin and Fiorotto, 1995; Melo et al., 2006; Pinheiro and Melo, 2008), providing recommendations for engineering design with failure criteria based on uplift forces resulting from dynamic pressures. Fewer studies investigated systematically the behavior of dynamic pressures propagating inside closed-end and open-end fissures at the bottom of plunge pools (Bollaert and Schleiss, 2003b; Manso et al., 2007).

With a different approach, Pagliara et al. (2006), Pagliara et al. (2008a) and Pagliara et al. (2008b) investigated the formation of scour on erodible beds of granular materials impacted by plunging inclined jets. The 3D scour hole features were described in terms of a densimetric Froude number F_d that takes into account the sediment characteristics. Using a similar approach, Canepa and Hager (2003) studied the influence of the incoming jet aeration. A modified densimetric Froude number was proposed that combines the three phases involved, namely air, water and sediments.

They highlighted that, if jets with the same water discharge are compared, the scour hole depth increases when adding air discharge to the jet. However, if the total air-water discharge is constant and different air concentrations are considered, relevant reduction of the scour hole depths are observed for increasing jet aeration. Manso et al. (2004) pointed out that jets with the same water discharge but with increasing air content have higher kinetic energy, which explains the increase of the scour hole depth in this case. They stated that comparing jets with constant air-water discharge is preferable when transferring the results to prototype conditions. In this case, the aerated jets have a lower kinetic energy and thus produce less scour.

More recent researches based on a large experimental facility (Asadollahi et al., 2011; Bollaert, 2013; Bollaert et al., 2013a; Federspiel, 2011) gave a better insight in the modeling of block uplift due to high-velocity plunging jets.

In the present study, the influence of jet air entrainment on the movements of a block embedded in the bottom of a plunge pool was investigated systematically. Simultaneous measurements of dynamic pressures and vertical displacements of the block were performed for different high-velocity jet impact and aeration conditions. A theoretical study of the phenomena involved is presented and a physically-based numerical model for the block movements has been implemented, which shows good correspondence with the experimental data. Additionally, the block vibration signals are analyzed by means of their spectral densities.

7.2 Experimental facility

The experimental facility shown in Figure 7.1, built at the Laboratory of Hydraulic Constructions (LCH) of the Ecole Polytechnique Fédérale de Lausanne (EPFL), produces vertical high-velocity jets issued from a d_j = 72 mm diameter nozzle (Duarte, 2013; Duarte et al., 2013). Air is pumped into the nozzle to produce aerated jets at the issuance

section. The tested velocities of the issued air-water mixture V_{aw} vary from 12.3 to 22.1 m/s. For each value of the jet velocity at issuance, 4 different jet aerations at the nozzle outlet β_1 are tested: 0, 8, 15 and 23 %. Note that the parameter β_1 accounts only for jet aeration at the issuance section and is given by $\beta_1 = Q_{aa}/Q_w$, where Q_w is the jet water discharge and Q_{aa} is the jet air discharge that is pumped into the nozzle. β_1 does not consider relevant amounts of air entrained into the pool at the plunge section. This topic was addressed in detail in Chapter 4.

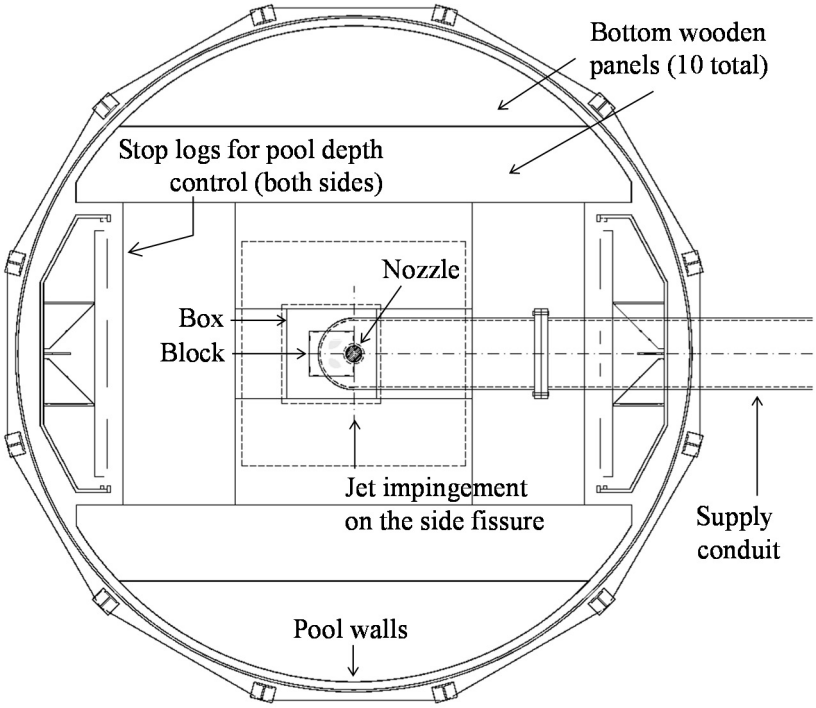

Figure 7.1. Plan view of the experimental facility.

The jets plunge into a 3 m diameter basin, where the water depth Y is 30, 50 or 80 cm. This results in relative pool depths Y/d_j of 4.2, 6.9 and 11.1 respectively. The distance between the nozzle outlet and the pool bottom is 1 m.

A metallic system is installed on the bottom to represent a block in the rock media (Federspiel, 2011). It is composed by a cubic block with side s = 200 mm inserted into a box containing a cavity 201 mm deep and 202 × 202 mm wide. An open 3D fissure with thickness t_h = 1 mm is formed around the block. 8 lateral guides (2 on each vertical side) are used to keep this thickness and to minimize block rotations during the vertical displacements. Each lateral guide has 8 contact points with the metallic cavity. Moreover, during the tests the block was either fixed into the cavity or left free to move.

Dynamic pressures and vertical displacements of the block are measured simultaneously (Figure 7.2). The dynamic pressures are measured on 12 positions uniformly distributed along one half of the block (Chapter 5). In the plan views of Figure 7.2, the 4 positions on the top of the block (Figure 7.2a, positions PB1 to PB4) and underneath the block (Figure 7.2b, positions HF1 to HF4) are shown. The pressure transducers are of type Kulite HKM-375M-17-BAR-A (Chapter 5).

For the measurement of vertical displacements, 2 inductive sensors of type Baumer IWRM 18U9704/S14 are used. The sensors are calibrated on the model by Federspiel (2011) and re-calibrated for this study. They are placed on 2 different positions on the bottom of the cavity (Figure 7.2b, sensor D1D and D2D) and measure the vertical position of the lower face of the block at the corresponding vertical axis. Hence, both measurements are supposed to be redundant and the only differences between them are related to block rotational vibrations.

The data acquisition device consists of a NI card type USB-6259 series M and is operated with laboratory-developed routine. During each test run 65'536 samples are acquired with a frequency of 1MHz. 3 runs are performed for each test configuration to ensure repeatability of the results.

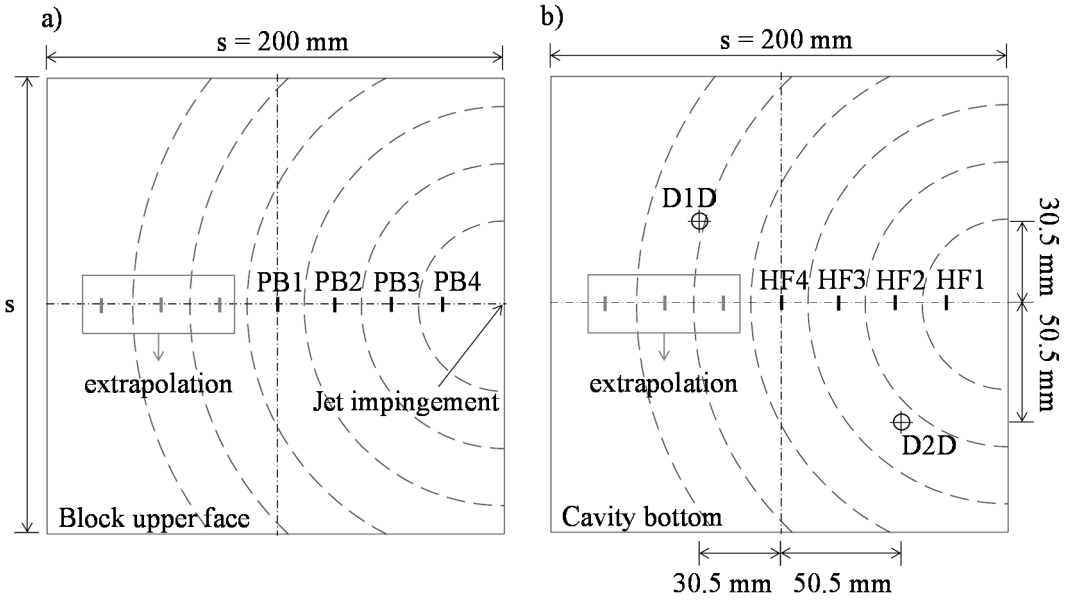

Figure 7.2. Detailed plan view of the block surface with instrumentation positions and respective areas of influence; a) upper face of the block with pressure transducers PB1 to PB4; b) cavity bottom below block with pressure transducers HF1 to HF4 and displacement sensors D1D and D2D.

7.3 Theoretical developments

The full physical phenomenon involves complex processes concerning the three relevant phases involved, namely air, water and rock, and their properties (Figure 7.3). The plunging jet travels through the air and impacts the water pool at the plunge section,

entraining large quantities of air. Then, part of the jet kinetic energy will dissipate due to shear forces along the pool. A detailed description of jet and air dissipation features in the water pool is provided in Chapter 4.

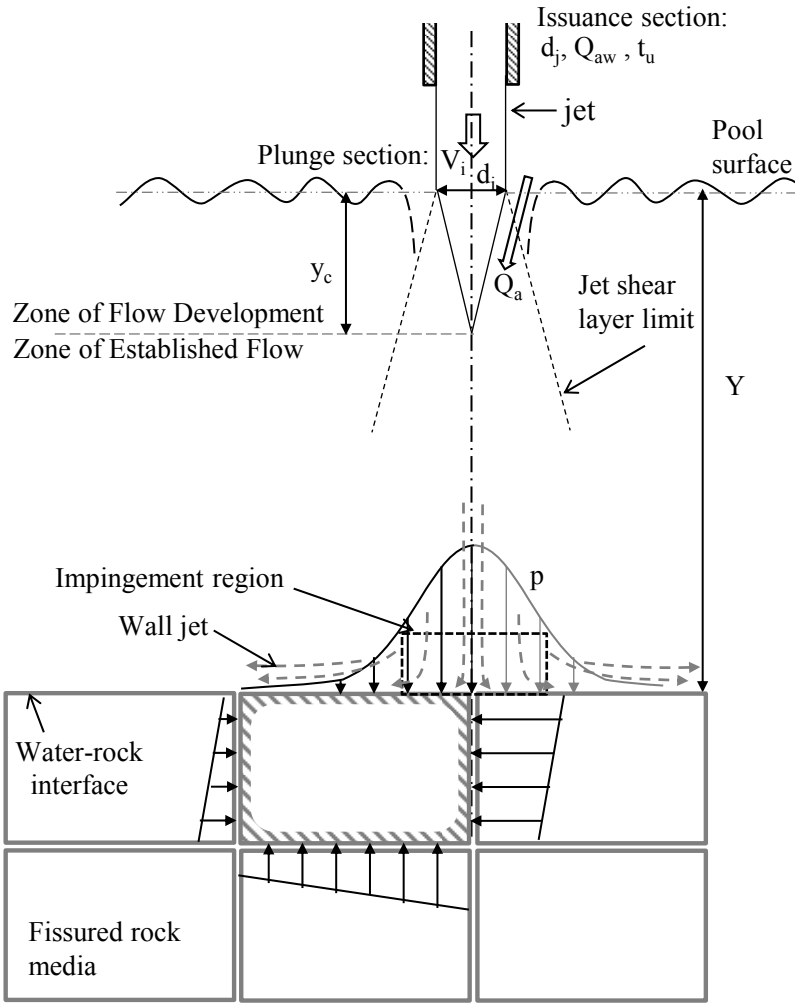

Figure 7.3. Sketch of the time-averaged pressure field around a block embedded in a flat rock bottom due to a circular jet impacting on one of its sides and main parameters (based on Chapter 5).Pressure field around the block

Subsequently, the fraction of the kinetic energy of the jet which is not dissipated in the pool is transferred to the water-rock interface and underlying fissures as dynamic pressures. Dynamic pressures for jets impinging on the center or on the side of a block were analyzed in Chapter 5.

The behavior of sided plunging jets is of particular interest for block uplift analysis (Figure 7.3). Chapter 5 indicated that sided jets generate significant uplift forces on a block, due to the transfer of a higher fraction of the kinetic energy inside the fissures. A pressurized flow is established inside the rock joint due to the differences of energy in its extremities. The time-averaged pressures have an approximately linear decay with increasing distance from the fissure entrance. The resulting pressure field reveals that the

block can be vertically ejected from its cavity. The block is also subjected to some degree of rotation due to asymmetrical lateral pressures. In the following, only vertical forces will be considered.

A sketch of the instantaneous vertical pressure forces acting on the block is presented in Figure 7.4. These forces can be classified into active forces (black triangular-shaped arrows) and passive forces (grey elements). The active forces are composed by the pressure field p acting on the block surface resulting from jet impingement and the block immerged weight W_i. The passive forces are the dumping effect created by the shear stress in the vertical fissures τ_f, the water "stiffness" F_u in the horizontal fissure and the virtual force resulting from the added mass of the block. The passive forces depend on the block response and occur only during displacements.

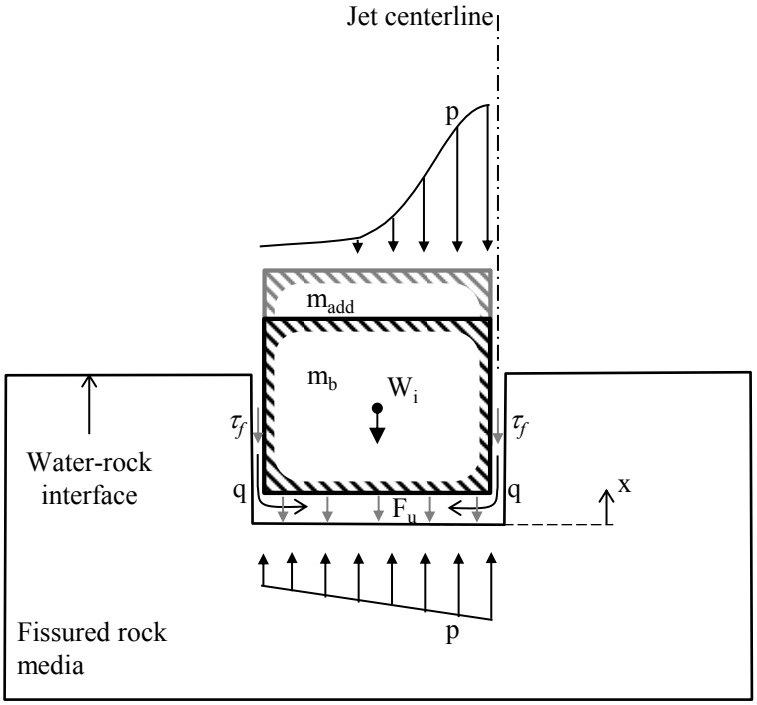

Figure 7.4. Representation of the instantaneous forces in the vertical direction acting on a block impacted by a sided jet during an upwards displacement.

7.3.1 Pressure field around the block

The instantaneous pressures acting on the upper and lower faces of the block are the only pressures that can produce a resulting uplift force. All the remaining forces tend to keep the block inside the cavity. The sum of the vertical forces arising from the cylindrical impacting jet F_v is determined by the expression:

$$F_v = \sum_{i=1}^{14} p_i S_i \tag{7.1}$$

where S_i is the area of influence of each of the 14 measurement positions indicated in Figure 7.2. The pressures on the upper and lower faces of the block were measured directly on the 8 positions shown in black in Figure 7.2, which correspond to the half of the block closer to the impinging jet. A procedure was developed to extrapolate the pressures to the "virtual" measurement stations on the left half of the block (in grey in Figure 7.2).

The time-averaged pressure distribution on the water-rock interface follows a Gaussian distribution as a function of the distance r from the jet centerline. Ervine et al. (1997) propose the following expression:

$$\frac{p_{mean}}{p_{mean\ cl}} = exp\left\{-K_2\left(\frac{r}{Y}\right)^2\right\} \tag{7.2}$$

where p_{mean} is the time-averaged pressure and p_{meancl} is the time-averaged pressure in the jet centerline. For the tests performed in this study, the values of the parameter K_2 varied between 25 for $Y/d_j = 4.2$ and 250 for $Y/d_j = 11.1$ (Chapter 5).

The time-averaged pressures computed with Eq. (7.2) are used as an estimate of the instantaneous pressure values in the virtual measurement points on the upper face of the block. The pressure values in these points are significantly smaller comparatively to the rest of the block, which will attenuate the extrapolation imprecision. It has been observed that the pressures at the position PB1 are very small due to the formation of a wall jet in this region. Consequently, pressures further away from this point represent little contribution to the resulting force acting on the block.

On the other hand, the pressures on the virtual measurement points on the lower face of the block are relevant for the balance of forces acting on the block. The evolution of the time-averaged pressure coefficient C_p along the fissure is shown in detail in Figure 7.5 for a shallow pool ($Y/d_j = 4.2$). The fissure distance l_f is defined as the unfolded length of the fissure with zero at the water-rock interface.

Fixed blocks have a nearly constant behavior in the vertical fissure, followed by a steep linear decay in the horizontal fissure. However, for free blocks, C_p decay seems to have a homogeneous linear trend in the entire fissure. A significant pressure release is observed for free blocks compared to fixed blocks, due to the block displacements, as pointed out in Chapter 6. The experimental data set is complemented with results from Federspiel (2011), who performed tests with the jet impinging on the left side of the block.

Nevertheless, it has been noticed that the use of an average value would generate important errors in the instantaneous forces estimates. The instantaneous pressures inside the fissures were found to also reduce linearly, which can be explained by a laminar flow in the fissure according to Darcy law (Hager and Schleiss, 2009). Therefore, a linear regression was performed for each time step to generate estimates of the instantaneous pressures on the virtual stations on the lower face of the block and obtain the respective uplift force.

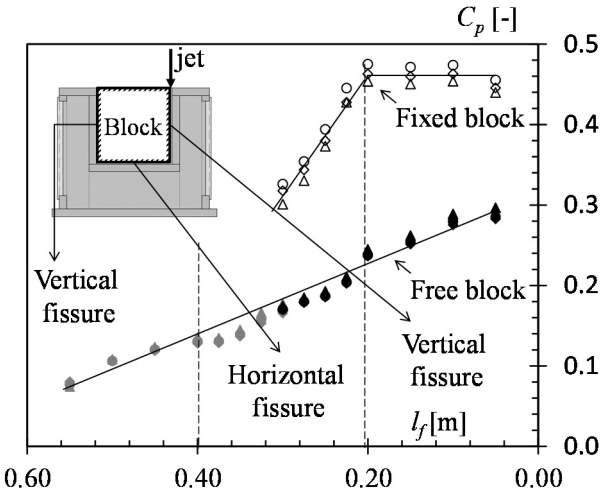

Figure 7.5. Mean pressure coefficient C_p *versus* fissure distance l_f non-aerated jets; $Y/d_j = 4.2$; (continuous lines) linear trends; fixed block: (◊) V_{aw} = 22.1 m/s; (○) V_{aw} = 19.6 m/s; (□) V_{aw} = 17.2 m/s; free block: (♦) V_{aw} = 22.1 m/s; (●) V_{aw} = 19.6 m/s; (■) V_{aw} = 17.2 m/s; and free block (Federspiel, 2011): (♦) V_{aw} = 22.1 m/s; (●) V_{aw} = 19.6 m/s; (■) V_{aw} = 17.2 m/s

7.3.2 Immerged weight of the block

The immerged weight considers the effects of gravity and buoyancy forces on the immerged block. The mass of the fully equipped block is m_b = 21.7 kg. The immerged weight is obtained using:

$$W_i = m_b g - \rho_w \forall_b g \tag{7.3}$$

where g is the acceleration of gravity, ρ_w is the water density and $\forall_b = s^3$ is the volume of the block. Note that the block was conceived to have an apparent density ρ_b close to the rock density; ρ_b = 2700 kg/m^3 approximately (Federspiel, 2011). Hence, the block immerged weight is a constant downward force of $W_i \sim$ 135 N.

7.3.3 Shear stresses in the vertical fissures

A laminar flow can be assumed inside the fissures due to its small opening (1 mm), as observed by the measurements. Indeed, only velocities above 1.2 m/s inside the fissures could produce turbulent flows if a limit of R_e = 1000 is taken into account. If an idealized one-degree-of-freedom vertical displacement of the block inside the cavity is considered, the hydraulic friction force F_{hf} integrated over the 4 vertical walls due to the plane couette flow (Kundu and Cohen, 2010) is given by

$$F_{hf} = -4s^2 \tau_f = -4s^2 \frac{\mu_{aw}}{t_h} V_b \tag{7.4}$$

where V_b is the displacement velocity of the block and μ_{aw} is the dynamic viscosity of the air-water mixture flow inside the fissures. The effect of the flow velocity inside the fissure can be neglected in the vertical direction as the sum of the upward and downward friction forces tends to compensate one another.

Furthermore, the influence of the hydraulic friction force is small compared to the other forces. Nevertheless, the block is submitted to a high net horizontal force that pulls the block away from the jet centerline. Horizontal translation and rotations are minimized by the lateral guides and a part of the friction forces come from the solid contact between the lateral guides and the fissure cavity. Each lateral guide has 8 contact points of reduced surface. Coulomb's law of friction stipulates that the friction forces between 2 solid bodies sliding one against the other are independent from the area of contact (Beatty, 2006). Complexity arises from the differences between static and dynamic friction coefficients. Hereby, only the dynamic friction is considered, as the block is constantly vibrating. The solid friction force F_{sf} is thus expressed as

$$F_{sf} = \upsilon F_h \tag{7.5}$$

and is always opposed to the block displacement. F_h is the sum of the horizontal forces applied on the block and υ is the dynamic friction coefficient. To simplify, and also because a precise instantaneous estimate of F_h was not possible as the pressures were not measured in both of the vertical fissures, a time-averaged value was obtained for each test run, considering a linear decay as illustrated in Figure 7.5. Federspiel (2011) performed tests to determine the value of the friction coefficients. The block was pulled from the cavity 20 times under dry and wet conditions. The obtained dynamic friction coefficient under wet condition is υ = 0.32.

7.3.4 Fluid resistance to a change in volume

The instantaneous volume of the fissure between the lower face of the block and the cavity plays a major role in the block dynamics. The resistance of the air-water mixture present in the fissure, regarding compression or decompression, is expressed by the bulk modulus of elasticity K_{aw}, given by:

$$K_{aw} = -\forall_f \frac{dp}{d\forall_f} \tag{7.6}$$

where $\forall_f = x \cdot s^2$ is the lower fissure volume. Using $F_u = p \cdot s^2$ to integrate the pressures applied by the block on the fluid in the lower fissure and solving Eq. (7.6) for F_u yields

$$F_u = -K_{aw} s^2 (\ln x + B) \tag{7.7}$$

where B is a constant of integration. However, the pressure variations caused by the block displacements also generates a fluid flow q inside the fissures (see Figure 7.4). In other words, a downward block movement results in fluid compression and a pressure rise in the lower fissure, which ejects the fluids into the vertical fissures, and vice-versa. This significantly dampens the fluid stiffness in the lower fissure. The analysis of the experimental results shows that the real fluid stiffness force responds according to the following expression:

$$F_u = -K_{aw} s^2 (x - x_0) \tag{7.8}$$

Eq. (7.8) is equivalent to Hooke's law of linear elasticity (Beatty, 2006) and represents the fluid compressibility as a spring with a stiffness $k = K_{aw}\, s^2$. The fluid stiffness generates a force that pulls or pushes the block to an origin position x_0 where the fluid density is at an equilibrium condition. One difficulty is that, while the block vibrates and moves, the equilibrium position changes with time as the flow q fills or empties the fissure. Moreover, unlike the shear stresses, the stiffness force is not always opposed to the displacement.

7.3.5 Virtual forces due to the added mass of the block

The added mass is commonly used in fluid dynamics to represent the inertia of the fluid mass that has to be accelerated by a moving solid body in contact with the fluid (see Figure 7.4). This may be done by adding a virtual mass to Newton's law of motion:

$$\sum F = (m_b + m_{add})\frac{d^2x}{dt^2} \tag{7.9}$$

where F represents external forces applied on the block and m_{add} is the added mass of the system. Federspiel (2011) performed computations of the block movement with and without consideration of the added mass and confirmed its importance to correct the inertia of the block which dampens its vibrations.

7.3.6 Model for block displacement

A model that integrates all the external forces into Eq. (7.9) yields the following ordinary differential equation:

$$(m_b + m_{add})\frac{d^2x}{dt^2} + s^2\frac{\mu_{aw}}{t_h}\frac{dx}{dt} + K_{aw}s^2(x - x_0) + vF_h = F_v - W_i \tag{7.10}$$

The model represents a damped spring-mass system with a forced vibration (Beatty, 2006). The active forces are in the right-hand side, whilst the passive forces, dependent on the block response, are represented in the left-hand side of Eq. (7.10). The theoretical model was solved using an explicit finite-differences scheme.

Spring models were also used by Federspiel (2011), Bollaert (2013) and Bollaert et al. (2013a) to simulate the block vibrations. The general mass-spring-dashpot model was solved for the added mass, as well as for a global stiffness coefficient k and a global damping coefficient c of the system. Bollaert et al. (2013a) analyzed a single test run with a plunging jet, not actively aerated, impinging on the side of the block in the same facility. The pool depth Y was 60 cm. They found good results by adding mass to the block up to 100 times the original block mass. The stiffness k of the system was 1.7×10^6 N/m and the damping coefficient c was 5×10^5 Ns/m.

However, Eq. (7.10) provides a more detailed understanding of the processes involved and the parameters have a physical meaning, which enables a better interpretation of the results.

7.4 Results and discussion

7.4.1 Observations regarding block vibrations

The tested jets produced relatively small block displacements. The block moves within a range of some millimeters. Some particular features of the measured block vibration signals are worth being discussed before addressing the results. Figure 7.6 presents position measurements of the 2 sensors for a test case with a relatively shallow pool ($Y/d_j = 4.2$), under a not previously aerated jet with issuance velocity $V_{aw} = 12.3$ m/s.

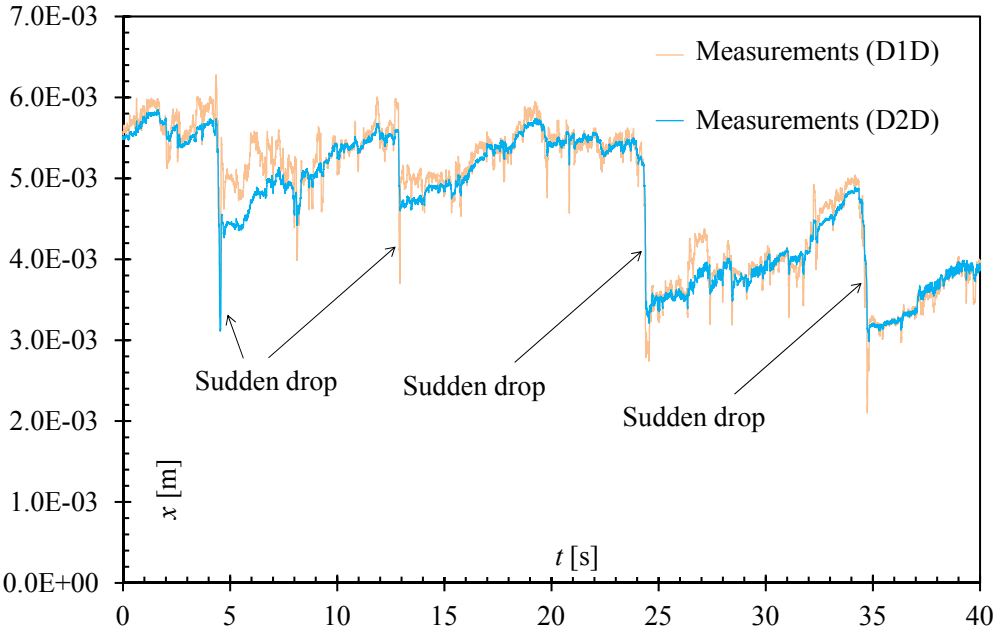

Figure 7.6. Measured block positions with time for the 2 sensors D1D (yellow) and D2D (blue). $Y/d_j = 4.2$; $V_{aw} = 12.3$ m/s; $\beta_l = 0$ %.

First, it can be noticed that the block frequently has sudden undamped drops. This was observed more clearly for low jet velocities and shallow pools, probably because the signal between two drops is steadier under these conditions. The sudden drops seem to take place after a slow rise of the block, but not systematically at the same height.

The theoretical model is not able to correctly reproduce this behavior. In certain cases, a measured reduction of the pressures under the block allowed the model to reproduce a drop, but smaller than observed (Figure 7.7). In other cases, the drops were barely reproduced by the model. After the drops, important differences between model and measurements indicate that there was a change in the parameters state.

A most probable explanation for these drops is the sudden release of air pockets from the lower fissure when the block has moved a certain distance upwards. This leads to an almost immediate change of the fissure volume, and also to subsequent change of the air-water mixture compressibility, which prevents the model to continue to correctly represent the block displacement.

For high-velocity jets, the air bubbles most probably enter and leave the lower fissure at a more regular pace. This is underlined by the fact that the model has a better agreement with the measured data for high-velocity jets, as shown in §7.4.3.

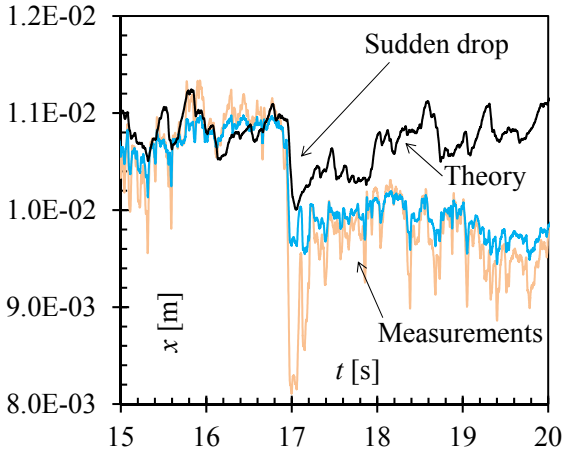

Figure 7.7. Example of model split after a sudden drop of the block; (yellow) D1D measurements; (blue) D2D measurements; (black) theoretical model; $Y/d_j = 4.2$; $V_{aw} = 17.2$ m/s; $\beta_l = 23$ %.

7.4.2 Frequency analysis of fixed and free blocks

Another important observation from Figure 7.6 is that measurements from sensor D1D fluctuate more than those of D2D. This is a consequence of block rotational vibrations, which are stronger for D1D due to the longer distance from the jet centerline. These rotations are minimized by the implementation of the lateral guides, but are unavoidable due to the strong rotational moments applied to the block. The lateral guides have a construction tolerance of ± 0.01 mm, which correspond to maximum rotations of ± 0.003° (Federspiel, 2011).

The Power Spectral Densities of pressure P_{xx} and position X_{xx} fluctuations were computed using a Welch periodogram-based Fast-Fourier-Transform algorithm (Figure 7.8). The signals of each test run, composed of 2^{16} samples per sensor, were divided into 64 segments with a Hamming window and 50 % of overlapping.

In Figure 7.8, PSD estimates of pressure and position signals for fixed and free blocks are compared for jets plunging into relatively shallow pools (Y/d_j = 4.2). In agreement with the results from Chapter 6, a free block generates lower resonance frequencies than a fixed block, due to the block vibrations (compare f_{res1} = 55 Hz for a fixed block in Figure 7.8a with f_{res1} = 35 Hz for the corresponding free block in Figure 7.8b).

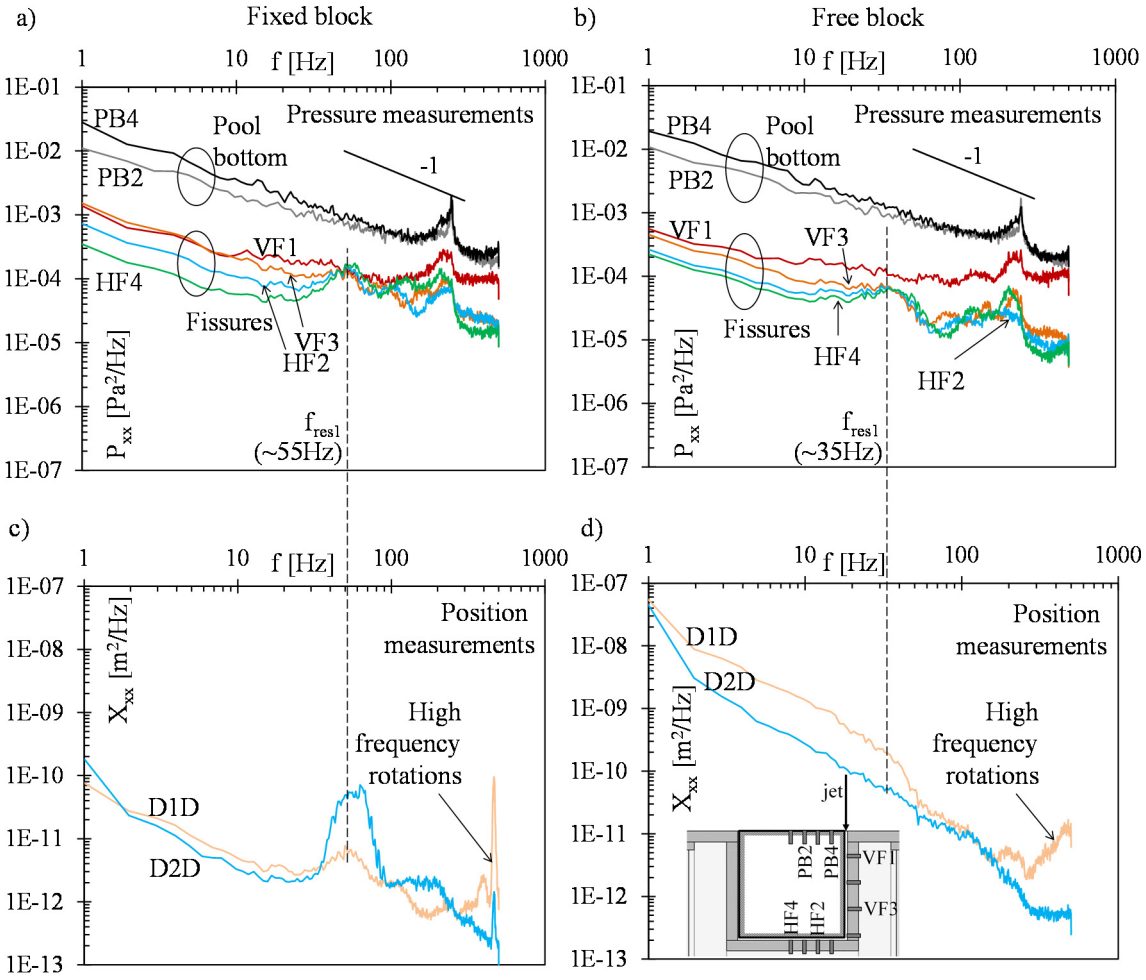

Figure 7.8. PSD of the pressure and position fluctuations around the block; Y/d_j = 4.2; V_{aw} = 22.1 m/s; β_l = 23 %; a) pressure signals for a fixed block; b) pressure signals for a free block; c) position signals for a fixed block; d) position signals for a free block.

The fixed blocks can also vibrate in the cavity and a displacement response to the pressure excitation is measurable (Figure 7.8c). This can be seen especially at the resonance frequency f_{res1} of the pressure waves inside the fissures, even if the whole spectral energy for the full range of frequencies is much lower than for the free block case. Very sharp peaks at high-frequencies (approximately 465 Hz for both fixed and free blocks) were registered, which are related with the block rotations.

Furthermore, it can be seen that the block displacements respond to the resonance effects of the pressure waves inside the fissures. The peak is more pronounced in the case of a fixed block (Figure 7.8c). Moreover, a small increase in the spectral energy of the block displacements is also observed at the resonance frequency for free blocks (Figure 7.8d). This shows that pressure waves amplifications influence block displacements. Although only minor block displacements were registered, this phenomenon may have an influence in prototype conditions, where relevant block uplift pressures are generated.

7.4.3 Modeling of block movement

Parameter x_0 in Eq. (7.10) is *a priori* unknown and changes with time, as mentioned before. Together with the added mass, it is the most important calibration parameter. Constant values were calibrated for each test run. The calibrated result is justified according to the observations for a certain time period. In certain cases, it is even constant for the whole test run.

The dynamic viscosity μ_{aw} and the bulk modulus of elasticity K_{aw} are, in principle, also unknown due to the impossibility to measure the instantaneous air content inside the fissures. The former plays an almost negligible role in the overall forces, but the latter is essential to correctly reproduce the water stiffness.

Therefore, the theoretical model (Eq. (7.10)), implemented with calibrated constant parameters, is in accordance with the measured block displacements for a certain period of time. This confirms that the theory developed for the one-degree-of-freedom block vibrations is valid.

Figure 7.9 compares the theoretical model with the experimental data for aerated high-velocity jets plunging into a shallow pool and a deep pool. The model appropriately reproduces the measured block displacements. The coefficients of determination R^2 found for these examples are 54 and 71 %, respectively.

The computations were performed with the dynamic viscosity μ_{aw} equal to the water viscosity, since the hydraulic friction has very little effect on the final result. The calibration process gave K_{aw} values varying roughly between 3.0×10^6 to 1.1×10^7 Pa. These are intermediate values between the bulk modulus of elasticity of air (1.0×10^5 Pa) and of water (2.2×10^9 Pa). The computed added mass varies approximately from 40 to 200 kg, which corresponds up to 10 times the block mass.

7.4.4 Influence of aeration on the block displacements

A straightforward analysis of the influence of the issued jet aeration was performed by computing the maximum displacement of each test run $d_{max} = \max(x) - \min(x)$. Figure 7.10 shows the results for the 3 runs of each test scenario as a function of the jet aeration β_I at issuance.

The general trends reveal a changing behavior with increasing relative pool depths. While, for a shallow pool, increasing jet aeration clearly reduces the maximum displacements of the block, a transition occurs for the intermediate pool depth and, finally, the maximum displacements tend to increase with jet aeration for deep pools.

These results are in agreement with the findings of Chapter 5, where the aerated jets were found to produce two distinct and opposed effects. One is a lower momentum of the jet due to its reduced apparent density, which generates lower pressures on the bottom of the pool. The other is a higher jet velocity due to lower dissipation rates throughout the pool depth, which in turn results in higher pressures on the water-rock interface. The

influence of the latter is higher for relatively deep pools, and this is the reason of the increasing block displacements with jet aeration found for $Y/d_j = 11.1$.

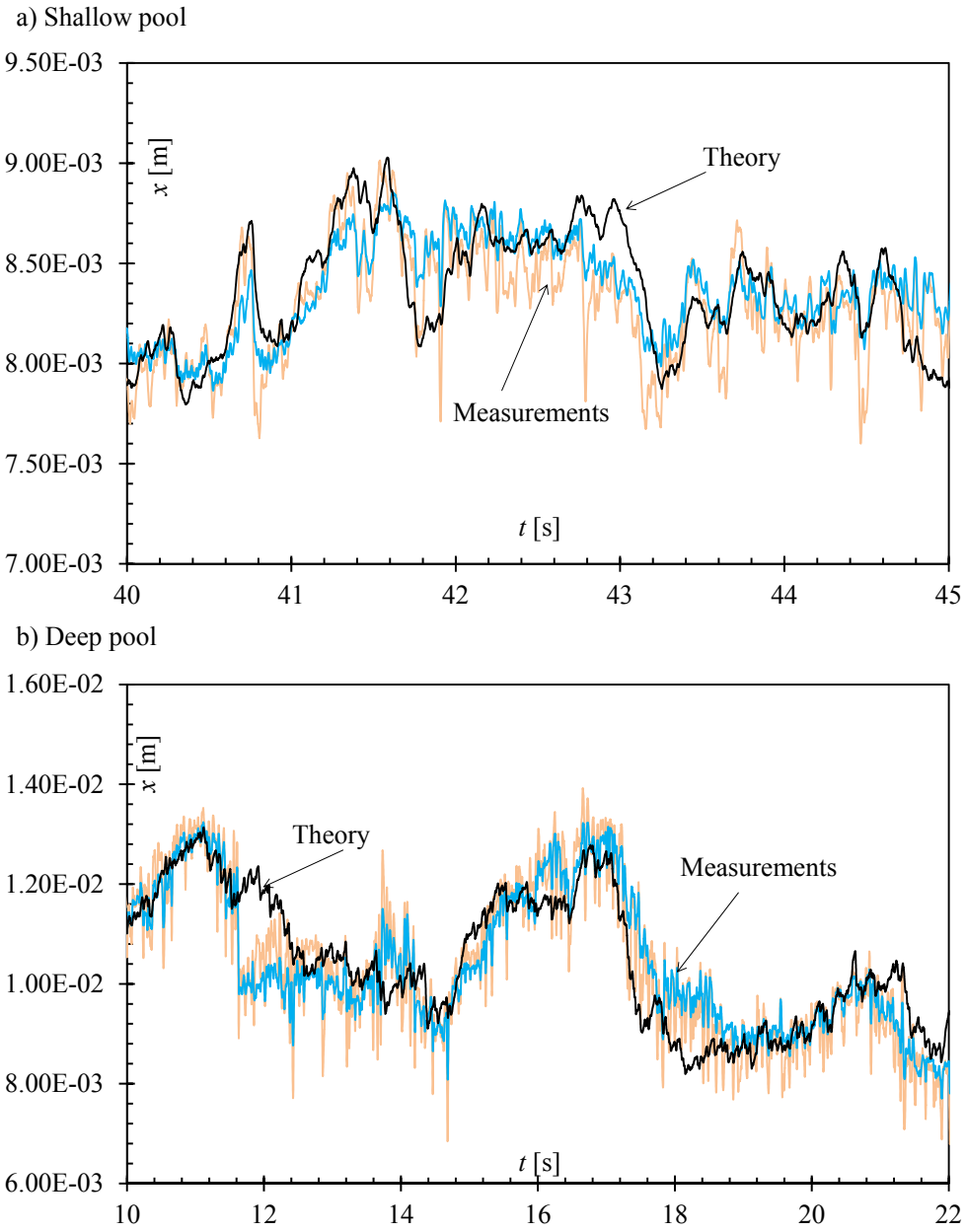

Figure 7.9. Comparison between the theoretical model and experimental data; (yellow) D1D measurements; (blue) D2D measurements; (black) theoretical model; V_{aw} = 22.1 m/s; β_l = 23 %; a) $Y/d_j = 4.2$; b) $Y/d_j = 11.1$.

Another important result is that higher displacements are observed for deep pools compared to shallow pools. While for shallow pools (Figure 7.10a) the different jet velocities are grouped in a narrow band, without a clear influence of the velocity of the jet in the maximum displacements, for deep pools (Figure 7.10c) the outer bounds of the results are much wider and it is clear that larger displacements were generated by the higher jet velocities. These results show that developed jet impact on the bottom of plunge pools produce larger block displacements.

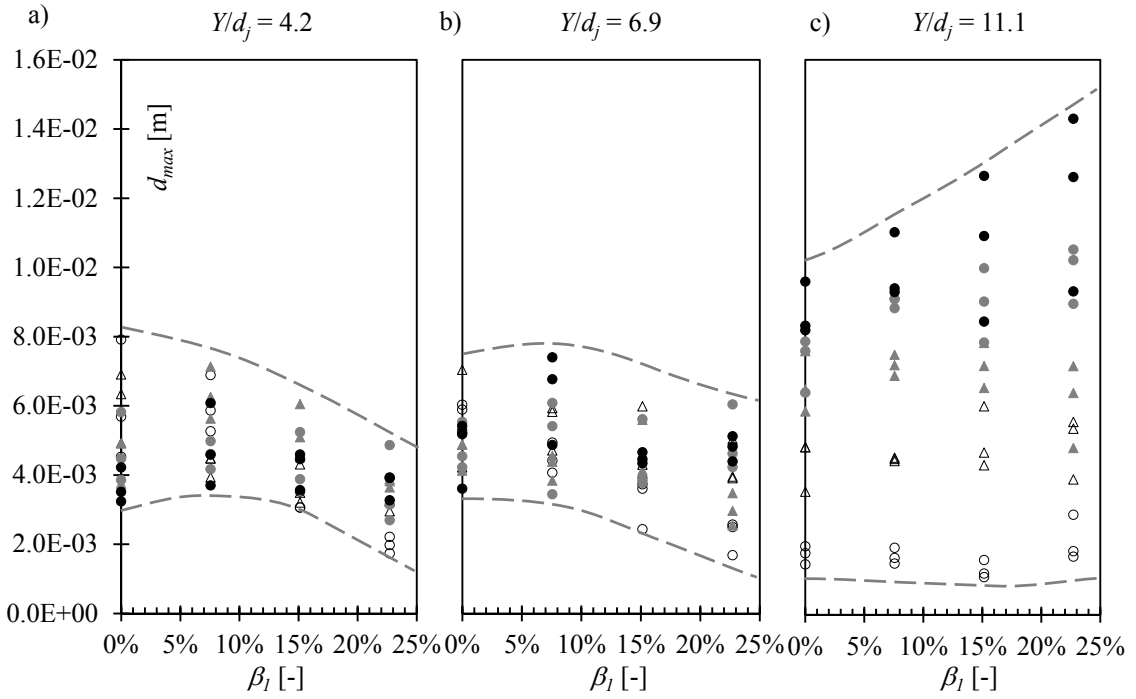

Figure 7.10. Maximum displacement of the block d_{max} at each test run *versus* issuance jet aeration β_I; (dashed lines) outer bounds; (○) V_{aw} = 12.3 m/s; (Δ) V_{aw} = 14.7 m/s; (▲) V_{aw} = 17.2 m/s; (●) V_{aw} = 19.6 m/s; (●) V_{aw} = 22.1 m/s; a) Y/d_j = 4.2; b) Y/d_j = 6.9; c) Y/d_j = 11.1.

7.5 Conclusions

The response of a block embedded at the bottom of a plunge pool and impacted by aerated high-velocity jets was assessed by a theoretical and experimental study. The block stability is dependent on active and passive forces. The active forces are independent from the block response. Conversely, passive forces consist on reactions to the block vibrations and hinder its displacements.

The active forces are the following:

- The pressure field around the block generated by the jet is the only force which results in block uplift.
- The block immerged weight, resulting from gravity and buoyancy forces on the block.

The passive forces are listed below:

- Friction forces along the vertical fissures, resulting either from hydraulic flow friction or from the solid contact between the cavity and the block lateral guides. The former is nearly negligible.
- Compressibility of the air-water mixture in the horizontal fissure between the block and the cavity, which plays a major role and works like a spring force that pulls or pushes the block to an equilibrium position varying with time.
- The virtual force due to the added mass, which considers the inertia of the water that must be accelerated together with the block during its displacements.

It was found that the block is subject to sudden undamped drops, especially in the case of lower jet velocities, which is probably due to the release of air pockets from the lower fissure. This feature changes the air-water mixture properties and avoids the model to correctly represent the block displacements.

Additionally, the spectral content of the block vibrations reveals that the block is submitted to small rotational movements inside the cavity at a high frequency, even if such rotations are kept to less than ± 0.003° by the lateral guides. Furthermore, a frequency analysis confirmed that the block displacements are influenced by the resonance phenomena of the pressure waves inside the fissures.

The physically-based theoretical model showed a good agreement with the experimental data, especially for high jet velocities. This is due to the more regular behavior of the air content inside the fissures, which results in steadier coefficients of the differential equation. The model contributes to a better understanding of the physical-mechanical processes involved in the dynamic block ejection from the bottom of plunge pools. However, for engineering practice, the model is difficult to implement due to its detailed representation of the forces. An engineering method for rock scour assessment taking into account block ejection is proposed in Chapter 8.

Block displacements are smaller for aerated jets in the case of shallow pools, but, inversely, they are higher for deep pools. This is in agreement with the findings of Chapter 5, where jet aeration generated two opposing effects on the pressures applied on the rock mass on the pool bottom. If, on the one hand, the lower apparent density of aerated jets reduces these pressures, on the other hand, lower velocity decay along the pool depth due to the presence of air bubbles in the dissipating jet results in a pressure rise. Overall, block displacements are higher for the deeper pool (Y/d_j = 11.1), indicating that developed jets generate more block uplift than core jets.

Finally, the measured block displacements have reduced amplitude, even for the near-prototype jets reproduced at the large facility. The displacements of the block are strongly damped by the reduced joint thickness. In other words, in the experimental facility, the 1 mm thin openings prevent the fluid from quickly filling or emptying the fissure. This leads to strong stabilizing forces from the fluid underneath the block to resist to a change in volume. This suggests that, in prototype conditions, block uplift is enhanced by a progressive joint break-up. This process will make rotations easier and progressively larger, which will expectedly contribute to the enlargement of the cavities and to facilitate the blocks total ejection.

8

Adaptations of a physically-based scour model in order to consider air entrainment

Based on systematic experiments of air entrainment influence on rock block stability in plunge pools impacted by high-velocity jets, this study recommends adaptations for a physically-based scour model. The modifications regarding jet aeration are implemented in the Comprehensive Scour Model (CSM), which allows it to reproduce the physical-mechanical processes involved in scour formation concerning the three phases, namely, air, water and rock. The enhanced method considers the reduction of momentum of an aerated jet as well as the decrease of energy dissipation in the jet diffusive shear layer, resulting from the entrainment of air bubbles. Block ejection from the rock mass depends on a combination of the aerated time-averaged pressure coefficient and on the modified maximum dynamic impulsion coefficient, which was found to be a constant value of 0.2 for high-velocity jets in deep pools. The modified model is applied to the case of the observed scour hole at Kariba dam with good agreement.

Keywords: Air entrainment, uplift, rock scour, dam safety, high-velocity jets, block stability, scour assessment

8.1 Introduction

Many empirical engineering methods are available to estimate scour formation downstream of plunging jets. Nevertheless, such empirical formulations are site-specific and not applicable to a wider range of cases (Bollaert and Schleiss, 2003a). As a matter of fact, the scouring process at plunge pool floors is a result of the interactions of the three phases involved: water, rock and air. Moreover, the highly turbulent nature of the flow and the resulting pressure fluctuations on the water-rock interface and inside rock fissures make appropriate scaling impossible in hydraulic modeling. Therefore, the applicability of Froude-based reduced-scale models is extremely limited.

The Comprehensive Scour Model (CSM) was first proposed by Bollaert (2002) and Bollaert and Schleiss (2005). It has the advantage of considering the physical phenomena involved in the scour of the rock impacted by plunging water jets. The model was developed as a result of experiments with plunging jets of near-prototype velocities impacting on closed-end and open-end fissures at the pool bottom. As such, the model reproduces the characteristics of the pressures signals of prototype jets, thus minimizing scale effects. Further, Manso (2006) and Manso et al. (2009) proposed adaptations to the CSM which took into account the influence of the pool bottom geometry and the resulting induced flow patterns.

This Chapter proposes adaptations to the CSM in order to consider the effect of jet air entrainment as obtained by a systematic experimental campaign. The investigation included the influence of the air bubbles on the jet dissipation in the plunge pool (Chapter 4), the resulting dynamic pressures acting on the water-rock interface and inside underlying fissures on pools with flat bottom (Chapter 5) and with confined bottom (Chapter 7), as well as the ejection of blocks from the rock mass (Chapter 7).

8.2 Proposed adaptations of the Comprehensive Scour Model for considering jet aeration

The Comprehensive Scour Model (CSM) was developed based on a theoretical and experimental study of rock scour created by plunging high-velocity jets. The scour process is the result of complex subsequent physical phenomena and can be divided into three parts, those being the falling jet, the plunge pool and the rock mass, each corresponding to a module of the CSM as shown in Figure 8.1.

In the following, the different modules of the CSM are presented. The developments refer to the proposed adaptations of the model unless it is specifically stated not so.

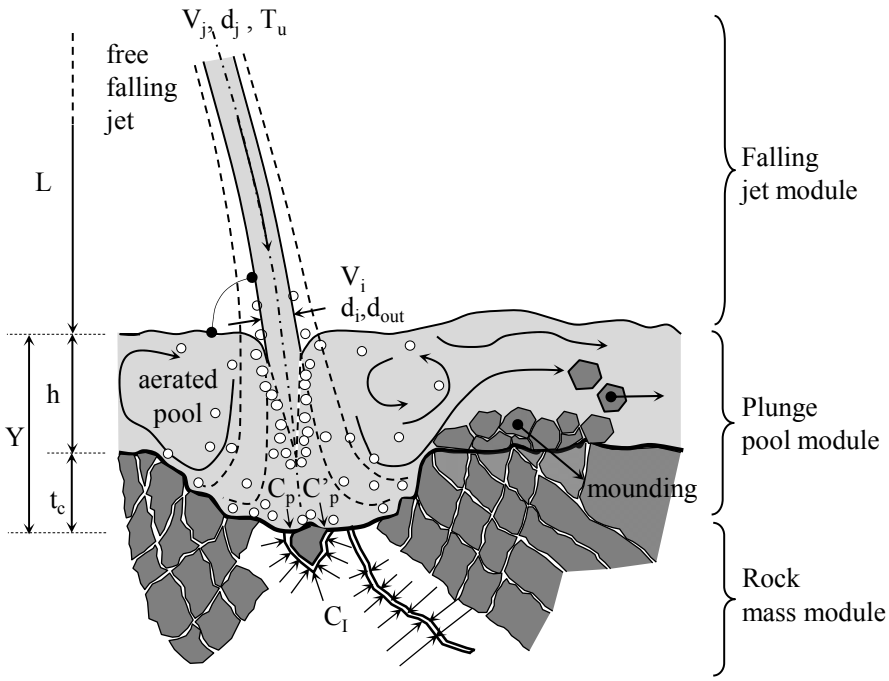

Figure 8.1. Physical processes responsible for scour formation and definition of the main parameters. From Bollaert (2002).

8.2.1 Falling jet module

The falling jet module reproduces the jet characteristics during its trajectory through the air. Ballistics theory governs the trajectory of the jet core. The jet develops an aerated outer layer as internal turbulence creates increasing disturbances on the jet's surface. The jet, issued with velocity V_j, diameter (or thickness in the case of plane jets) d_j and turbulence intensity T_u, is subjected to acceleration of gravity during the fall length L, impacting the pool at the plunge section with velocity V_i and diameter d_i. Providing enhancements to the representation of the falling jet considering aeration was not in the scope of this research project. The reader is referred to the original references for detailed information (Bollaert, 2002; Bollaert and Schleiss, 2005).

8.2.2 Plunge pool module

The plunge pool module represents the diffusion of the jet throughout the pool depth. This process dissipates a fraction of the energy of the jet. The jet entrains large quantities of air into the water pool at the plunge section, which strongly influences the diffusion properties. The jet aeration or air-to water ratio is defined as $\beta = Q_a/Q_w$, where Q_a and Q_w are respectively the air and water discharges. To compute β, the expression proposed by Ervine et al. (1997) is considered:

$$\beta = K_1 \left(1 - \frac{V_e}{V_i}\right) \sqrt{\frac{L}{d_i}} \tag{8.1}$$

where K_1 is a parameter that varies between 0.2 for smooth turbulent jets and 0.4 for very rough jets, and V_e is the onset velocity of the jet at the plunge section above which air entrainment begins, normally taken as ~1 m/s.

The mean density of the air-water jet inside the pool ρ_{aw} is given by

$$\rho_{aw} = \frac{1}{1+\beta}\rho_w + \frac{\beta}{1+\beta}\rho_a \tag{8.2}$$

in which ρ_a and ρ_w are the air and water densities. The input of energy to the process is determined by the kinetic energy per unit volume of the air-water jet at the plunge section:

$$E_k = \frac{1}{2}\rho_{aw} V_i^2 \tag{8.3}$$

After plunging into the pool with aeration β, mean density ρ_{aw} and kinetic energy E_k, the dissipation process of the jet begins. The inner core of the jet is progressively disintegrated from its borders towards the centerline, where the flow remains approximately at the same velocity as at the plunge section. The jet core vanishes according to the following expressions (see Chapter 4):

$$\begin{cases} \dfrac{y_c}{d_i} = 7.74 \times 10^{-6}\ \dfrac{V_i d_i}{\nu} & if \quad 7.74 \times 10^{-6}\ \dfrac{V_i d_i}{\nu} \leq A' \\ \dfrac{y_c}{d_i} = A' & if \quad 7.74 \times 10^{-6}\ \dfrac{V_i d_i}{\nu} > A' \end{cases} \tag{8.4}$$

where y_c is the core development length and ν is the kinematic viscosity of the fluid. The parameter A' is 3.5 for submerged jets and 7.8 for plunging jets (Chapter 4). The term $V_i d_i/\nu$ corresponds to the Reynolds number of the jet at the plunge section. Once the jet core is disintegrated, jet velocity decay follows a linear function of the pool depth for both submerged and plunging jets.

The remaining kinetic energy of the jet is converted into dynamic pressures acting on the plunge pool bottom. The time-averaged pressures p_{mean} are maximal at the intersection of the jet centerline with the water-rock interface, named stagnation. The time-averaged pressure coefficient is defined as $C_p = (p_{mean} - \rho_w g Y)/E_k$, where g is the gravitational acceleration. For the non-aerated jets at stagnation, C_p is reproduced by the following relationship (Chapter 5):

$$C_p = \psi\left(0.926 - 0.0779\frac{Y - y_c}{d_i}\right)^2 \quad if \quad Y > y_c \tag{8.5}$$

$$\psi = \frac{1}{1 + exp\left\{-5.37 \times 10^{-6}\left(\frac{V_i d_i}{\nu} - 6.63 \times 10^5\right)\right\}} \tag{8.6}$$

If $Y < y_c$, the core of the jet impacts directly on the rock bottom and $C_p = 0.86$. The parameter ψ reflects the loss of energy that takes place at the impingement region formed at the vicinity of the intersection of the jet centerline with the pool bottom (Beltaos and

Rajaratnam, 1977). Chapter 5 showed that ψ is a logistic function of the jet velocity that asymptotically reaches the value 1 for high jet velocities.

Aerated jets have a lower momentum compared to clear-water jets of the same discharge, due to a reduced mean density of the air-water mixture (Ervine and Falvey, 1987; Manso et al., 2004). However, as explained in Chapter 5, the air bubbles reduce the shear stresses with the surrounding water in the pool, resulting in lower velocity decay rates and higher C_p values for the aerated jets at the bottom.

The influence of the jet aeration β on the C_p values could be assessed precisely for the tests with submerged jets, as the full air entrainment discharge was provided at the nozzle. The time-averaged pressure coefficients for aerated jets $C_p{}^a$ divided by the corresponding C_p value for non-aerated jet are shown as a function of β in Figure 8.2. A linear increase can be observed, represented by the expression:

$$\frac{C_p^a}{C_p} = 1 + 0.4\beta \tag{8.7}$$

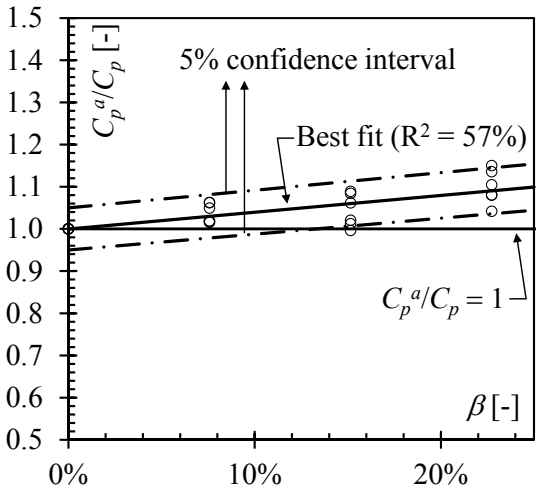

Figure 8.2. Time-averaged pressure coefficient of the aerated jets $C_p{}^a$ divided by the time-averaged pressure coefficient of the corresponding non-aerated jet C_p *versus* air-to-water ratio β. Test results for submerged jets at stagnation; Y/d_i = 9.7; jet velocities V_i ranging from 7.4 to 22.1 m/s.

8.2.3 Rock mass module

The rock mass module reproduces the physical processes occurring on the rock media. These processes are the progressive break-up of rock joints and subsequent ejection of the so formed blocks from the pool bottom. Two methods were developed to simulate each of these processes, respectively, the Comprehensive Fracture Mechanics method (CFM) and the Dynamic Impulsion method (DI) (Bollaert and Schleiss, 2005).

The current research enables improving the latter by including the experimental results of high-velocity jets of different air contents impinging on a completely open-ended 3D joint. This open-ended 3D joint is represented by a block inserted into a cavity where dynamic pressures and displacements were measured simultaneously. Fixed and mobile block responses were studied.

8.2.4 Dynamic Impulsion method

The Dynamic Impulsion method aims to evaluate the scour potential of plunging jets by means of their capacity to remove the mobilized rock blocks from the pool bottom (Bollaert, 2002; Bollaert and Schleiss, 2005). Differently from the CFM, the DI method does not consider the evolution in time of the scour hole, but instead computes the equilibrium or ultimate scour depth.

It uses a non-dimensional maximum dynamic impulsion coefficient C_I^{max}, defined as the non-dimensional uplift force acting on the rock block during a given time period. The impulse $I_{\Delta p}$ is defined as a time integration of the forces applied on the block

$$I_{\Delta p} = \int_0^{\Delta p} \left(F_v - F_u - W_i - F_{hf} - F_{sf}\right) dt = (m_b + m_{add}) \cdot V_b \tag{8.8}$$

where Δp is the pulse time, F_v is the sum of the vertical forces around the block due to the impinging jet, F_u is the resistance of the fluid inside the fissures to a change in volume, W_i is the immerged weight of the block, F_{hf} and F_{sf} are the hydraulic and solid friction forces on the vertical fissures, m_b is the block mass, m_{add} is the added mass of the block and V_b is the block displacement velocity.

Eq. (8.8) is a complete formulation of the impulse according to the detailed description of the forces developed in Chapter 7. For practical engineering applications, a simplified formulation will be used, discarding the stabilizing forces. This simplification is conservative in the way that it results in stronger destabilizing impulses. Furthermore, it is also realistic to neglect the fluid resistance to a change in the volume of the lower fissure in real cases. This effect was important when modeling block movements in the experimental facility in Chapter 7. However, in prototypes, with the progressive widening of the fissures caused by a simultaneous hydraulic fracturing, the fluid can rapidly fill the volume created by a positive block displacement, which was not the case in the facility. The resulting expression is equivalent to the formulation proposed by Bollaert and Schleiss (2005):

$$I_{\Delta p} = \int_0^{\Delta p} (F_v - W_i) dt = m_b \cdot V_b \tag{8.9}$$

The impulse $I_{\Delta p}$ is considered whenever net uplift forces exist. The maximum impulse of a test run is I^{max}. The time is made non-dimensional by dividing it by the period of the pressure waves inside the joints $T_p = 2L_f/c$, where L_f is the fissure length and c is

the wave celerity (Bollaert and Schleiss, 2005). For simplicity, the rock blocks are considered to have a square base of side x_b and height z. Hence, $L_f = 2z + x_b$. The forces are made non-dimensional by transforming them into a pressure acting on a block face (in this case the top or the bottom of the block with area x_b^2) and dividing the result by the kinetic energy per unit volume E_k. The maximum dynamic impulsion coefficient C_I^{max} can thus be computed with the following expression:

$$C_I^{max} = \frac{I^{max}c}{x_b^2 \rho_{aw} V_i^2 L_f} \tag{8.10}$$

The experimental results of C_I^{max} are presented in Figure 8.3 as a function of jet aeration at issuance β_I, in Figure 8.4 as a function of incoming jet velocity V_{aw} and in Figure 8.5 as a function of relative pool depth Y/d_j.

The maximum and minimum values of C_I^{max} range roughly between 0.35 and 0.15, respectively. The influence of the issued jet aeration β_I is relatively small and the values decrease for high β_I values towards approximately 0.20 (Figure 8.3). Analyzing the influence of the issued jet velocity (Figure 8.4), it can be seen that C_I^{max} decays smoothly towards 0.2 for high jet velocities. The convergence towards 0.2 can also be observed as a function of relative pool depth in Figure 8.5, where the results for the different jet aerations approach the average value for deeper pools. Hence, based on the experimental results, the use of $C_I^{max} = 0.2$ is proposed, which corresponds to the strongly aerated high-velocity jets found in prototype conditions.

Finally, the maximum dynamic impulsion on dislodged rock blocks on the plunge pool bottom is dependent on the dissipation of the kinetic energy of the jet in the water pool and on the maximum impulsion coefficient acting on a block. The former is represented by the time-averaged pressure coefficient C_p^a, which considers the effect of aeration. The maximum dynamic impulsion and the vertical displacement of the block are computed with the following expressions:

$$I^{max} = C_I^{max} C_p^a \frac{\rho_{aw} V_i^2}{2} x_b^2 \, \Delta p \tag{8.11}$$

$$h_{up} = \frac{V_b^2}{2g} \tag{8.12}$$

This adapted method differs from Bollaert (2002) and Bollaert and Schleiss (2005), who suggest a maximum impulsion dependent exclusively on C_I^{max}, instead of both C_I^{max} and C_p^a as in Eq. (8.11). They propose an empirical relationship of C_I^{max} as a decreasing function of the relative pool depth based on their experimental results

$$C_I^{max} = 0.0035 \left(\frac{Y}{d_i}\right)^2 - 0.119 \left(\frac{Y}{d_i}\right) + 1.22 \tag{8.13}$$

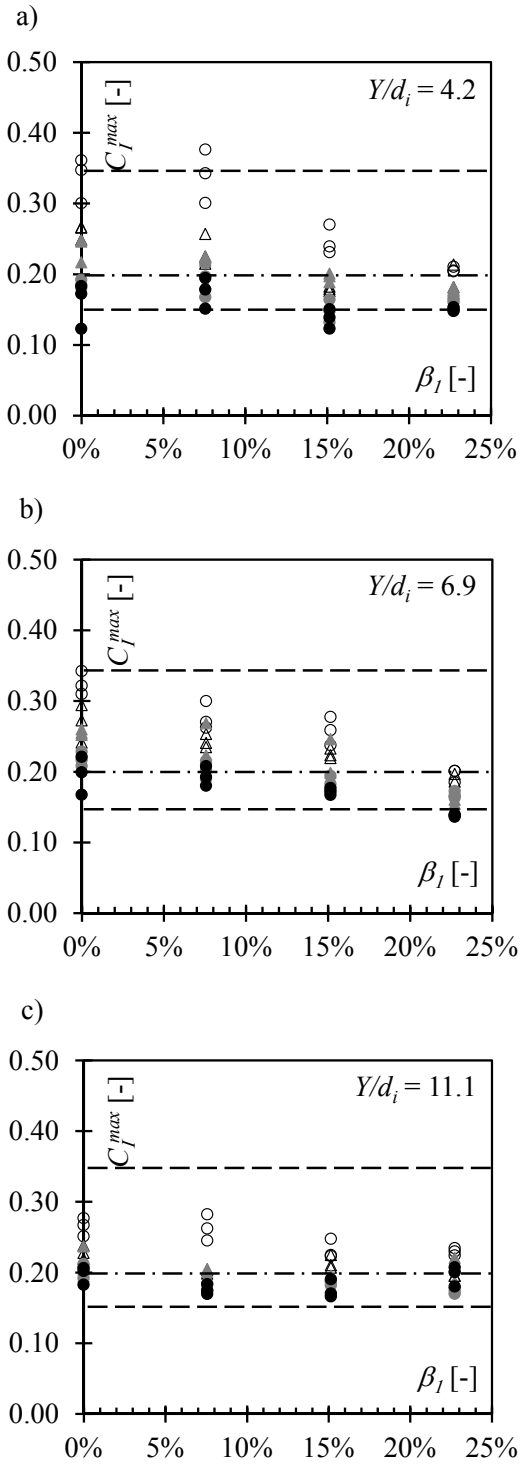

Figure 8.3. Experimental results of the maximum dynamic impulsion coefficient CI^{max} *versus* jet aeration at issuance β_I; (○) V_{aw} = 12.3 m/s; (Δ) V_{aw} = 14.7 m/s; (▲) V_{aw} = 17.2 m/s; (●) V_{aw} = 19.6 m/s; (♦) V_{aw} = 22.1 m/s; a) Y/d_j = 4.2; b) Y/d_j = 6.9; c) Y/d_j = 11.1. CI^{max} varies between 0.15 and 0.35 with an averaged at 0.20 (dashed lines).

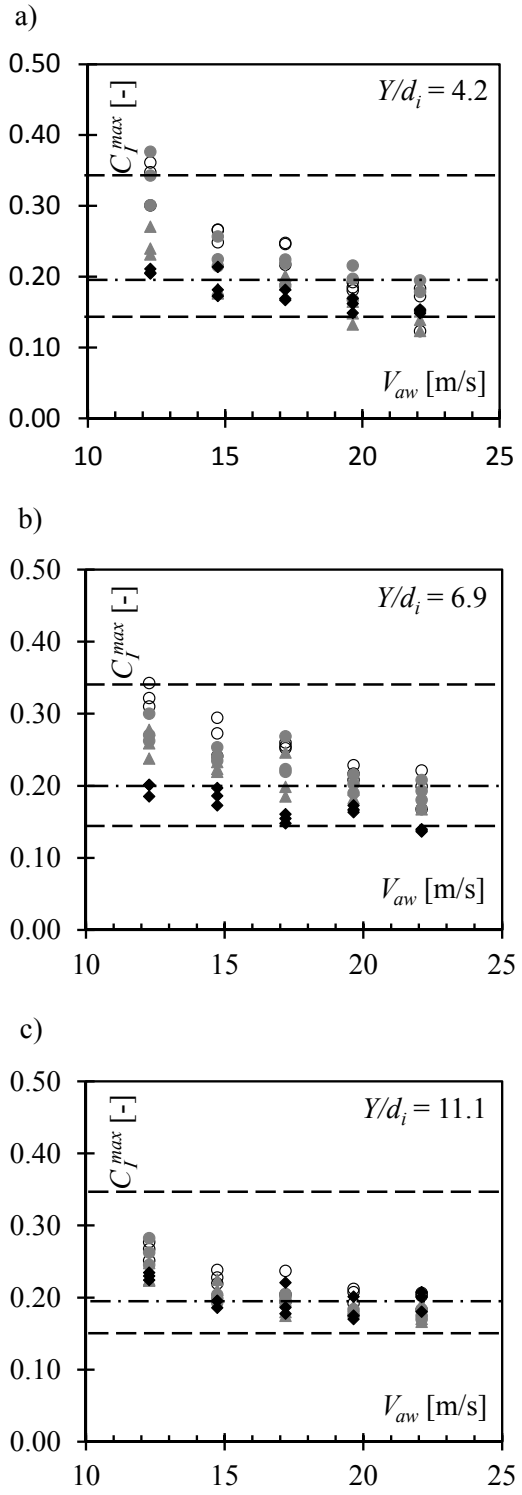

Figure 8.4. Experimental results of the maximum dynamic impulsion coefficient C_I^{max} *versus* jet velocity at issuance V_{aw}; (○) β_I = 0 %; (●) β_I = 8 %;(▲) β_I = 15 %; (♦) β_I = 23 %; a) Y/d_j = 4.2; b) Y/d_j = 6.9; c) Y/d_j = 11.1. C_I^{max} varies between 0.15 and 0.35 with an averaged at 0.20 (dashed lines).

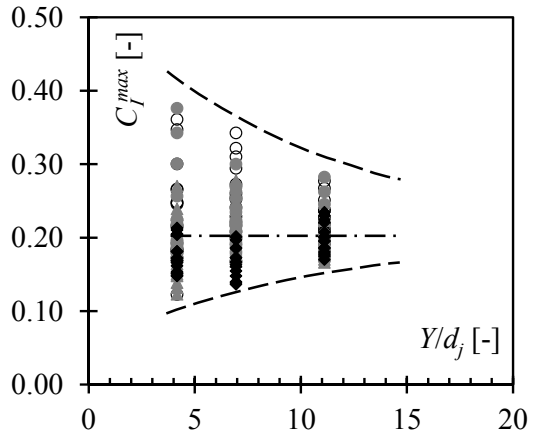

Figure 8.5. Experimental results of the maximum dynamic impulsion coefficient Cf^{max} *versus* relative pool depth Y/d_j; (○) β_I = 0 %; (●) β_I = 8 %;(▲) β_I = 15 %; (♦) β_I = 23 % (dashed lines) indicative outer bounds and average value.

In the method proposed in this Chapter, $C_p{}^a$ is a decreasing function of the relative pool depth, according to Eqs. (8.5) and (8.7). This reflects the jet dissipation along the pool. The pressure rise due to lower velocity decay caused by the entrainment of air bubbles is represented in the formulation of $C_p{}^a$ in Eq. (8.7). On the other hand, the pressure reduction due to a lower apparent density of aerated jets is reproduced by a lower kinetic energy of the jet in Eq. (8.11).

8.3 Case study: Kariba dam scour hole

8.3.1 Description of the hydraulic scheme

Kariba dam is located at the Zambezi River between Zambia and Zimbabwe, where it creates one of the largest man-made reservoirs in the world. The hydropower plant has a capacity of 1'266 MW with current refurbishment works to increase the total capacity to 1'450 MW (Noret et al., 2013; Tapfuma et al., 1994). The facility is operated by the Zambezi River Authority (ZRA). The flood release devices are 6 middle outlet gates with a discharge capacity of 1'500 m^3/s each. No additional structure is located outside the dam with the purpose of flood release (Figure 8.6).

As a result of long spilling periods since it started operating in 1959, a deep and steep-sided scour hole was formed at the bottom of the plunge pool downstream of the dam. Bathymetry campaigns indicate that the pool bottom was at the level of 306 m a.s.l. in 1981 (Figure 8.7), which also corresponds to the pool bottom level in 2001. This pool bottom is therefore approximately 80 m below the normal tailwater level and 70 m below the original riverbed.

Hybrid modeling, using a combination of hydraulic model tests and of CSM numerical modeling, was carried out to find a solution to stabilize the scour hole (Bollaert et al., 2012; Bollaert et al., 2013b). The main concern is to prevent further erosion towards

the dam toe. For such, excavation works are planned to reshape the plunge pool bottom, in order to reduce pressure fluctuations at the rock and guide the deflected jet downstream (Noret et al., 2013).

Figure 8.6. Downstream view of the Kariba dam during spillage through 3 non-adjacent gates on April 2010.

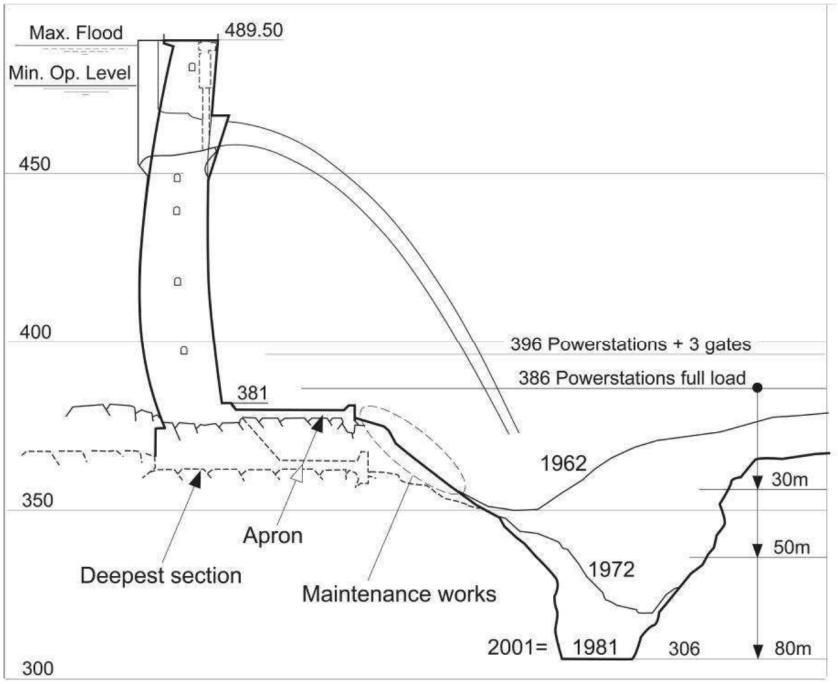

Figure 8.7. Longitudinal section of the Kariba plunge pool with time evolution of the scour hole (Noret et al., 2013).

8.3.2 Rock scour estimates with the adapted DI method

The main input parameters and intermediate results are shown in Table 8.1. The jet reaches the plunge pool surface with a velocity V_i = 41.4 m/s. The jet entrains very large air quantities into the plunge pool (C_a = 48 %). With a jet core length of 49.1 m, a developed jet reaches the pool bottom.

Table 8.1. Parameters used in the adapted DI method

Input parameters			
Max flood level		489.5	[m a.s.l.]
Tailwater level at impact		402	[m a.s.l.]
Sluice height		9.14	[m]
Sluice width		8.87	[m]
Sluice discharge		1'500	[m^3/s]
Sluice altitude		462.3	[m a.s.l.]
Jet fall length	L	60.3	[m]
Block width	x_b	1	[m]
Block length	x_b	1	[m]
Block height	Z	0.5	[m]
celerity	C	70	[m/s]
Block density		3'000	[kg/m^3]
water density	ρ_w	1000	[kg/m^3]
air density	ρ_a	1.2	[kg/m^3]
Intermediate results			
Jet velocity at issuance	V_j	18.5	[m/s]
Jet velocity at impact	V_i	41.4	[m/s]
Jet diameter at impact	d_i	6.3	[m]
Reynolds Nb. at impact	R_e	2.3E+08	[-]
Froude Nb. at impact	F_r	5.3	[-]
jet aeration	β	90%	[-]
jet air concentration	C_a	48%	[-]
jet mean density	ρ_{aw}	526	[kg/m^3]
Core development length	y_c	49.1	[m]

A pressure wave celerity inside the rock fissures of 70 m/s is chosen, in accordance with the results of Chapter 5 and Chapter 6 for a highly aerated high-velocity jet. It was found that pressure wave celerity is strongly reduced by the air content and by the block vibrations, which correspond to a pseudo-elastic behavior of the flow boundaries.

Indeed, the fissures around the blocks located at the water-rock interface are progressively widened by the hydraulic fracturing caused by the jet, allowing the blocks to vibrate more and more inside the cavity. As it was shown in Chapter 6, these vibrations

reduce the celerity of the pressure waves, together with the effect of aeration. Additionally, as discussed in Chapter 7, the opening of the joints facilitates the establishment of a flow that fills the fissures as the block rises, and vice-versa, thus reducing the resistance force of the fluid to a change in volume inside the fissures. This aspect partially supports the simplifying assumption of neglecting the stabilizing forces made in Eq. (8.9).

The geological surveys indicate that rock mass is a composition of fresh and altered gneiss of very good quality (150~200 MPa) with vertical and sub-horizontal joint sets at a dip angle of approximately 20 – 30° (Bollaert et al., 2013b).

Regarding block ejection from the rock mass, different criteria have been used in the past. The critical parameter is h_{up}/z, which determines the degree of displacement of the block inside the rock mass cavity. Bollaert (2002) used $h_{up}/z = 1$ to determine the threshold below which the rock bottom is stable. Later, Bollaert and Schleiss (2005) assumed that an intermediate region exists for $h_{up}/z > 0.2$, where the blocks are vibrating. A stable plunge pool is thus attained below this limit.

Recently, Asadollahi et al. (2011) investigated rock scour based on the ejection of rock blocks from a fractured rock media. They developed an iterative algorithm, the Block Stability in 3 Dimensions (BS3D), which was validated with experimental data from Federspiel (2011). Asadollahi et al. (2011) suggest that rock blocks are most likely removed from the pool bottom mass, if their displacements are higher than a quarter of the block height.

The results of the ultimate scour depth computed using the adapted Dynamic Impulsion method are shown in Table 8.2. The results are given for a failure criterion of $h_{up}/z = 1$ or 0.25. These results are shown graphically in Figure 8.8 and compared to the longitudinal profiles measured in 1972 and 1981.

The difference between the two failure criteria is small. Furthermore, the results for the ultimate scour depth are close to the deepest point of the pool bottom, as measured in 1981 and 2001. In fact, a failure criterion of $h_{up}/z = 0.25$ resulted in exactly the same pool bottom elevation of 306 m a.s.l. It indicates that the scour hole has attained its ultimate scour potential considering the capacity of the impinging jet to eject blocks from the rock mass.

For comparison, the original DI method with a failure criterion of $h_{up}/z = 0.25$ results in a bottom elevation at 289.5 m a.s.l. Moreover, if these results are compared to the Eq. (6.1) proposed by Mason and Arumugam (1985) with constant parameters, a bottom elevation is found at 338.8 m a.s.l., far above the current elevation. Additionally, if Eq. (6.1) is computed with variable parameters, as obtained by Mason and Arumugam (1985) with both model and prototype data, the results show a total pool depth of only 1.5 m, showing that the parameters are out of range in this case. This example shows that empirical formulas can seldom represent complex prototype situations, and only a physically-based representation can estimate the scour phenomenon with accuracy.

However, these statements have to be taken with precaution, since other aspects have to be analyzed. It must be noted that the DI method takes into account only the erosion capacity of the turbulent shear layer of the jet. In other words, it considers the effect of a direct jet impingement and does not include the influence of the rollers formed by the deflection of the jet against the scour hole.

Table 8.2. Numerical results of the ultimate scour depth based on the adapted DI method

Y [m]	Bottom [m a.s.l.]	Y/d_i [-]	ψ [-]	C_p [-]	C_p^a [-]	C_I [-]	I^{max} [Ns]	I^{net} [N/s]	h_{up} [m]	h_{up}/z [-]
56	346	8.9	1	0.71	0.96	0.20	43'388	38'483	33.55	67.09
58	344	9.2	1	0.67	0.91	0.20	40'869	35'964	29.30	58.60
60	342	9.5	1	0.63	0.85	0.20	38'425	33'520	25.45	50.90
62	340	9.9	1	0.59	0.80	0.20	36'057	31'152	21.98	43.97
64	338	10.2	1	0.55	0.75	0.20	33'764	28'859	18.87	37.73
66	336	10.5	1	0.51	0.70	0.20	31'546	26'641	16.08	32.15
68	334	10.8	1	0.48	0.65	0.20	29'404	24'499	13.60	27.19
70	332	11.1	1	0.44	0.61	0.20	27'336	22'431	11.40	22.80
72	330	11.4	1	0.41	0.56	0.20	25'345	20'440	9.46	18.93
74	328	11.8	1	0.38	0.52	0.20	23'428	18'523	7.77	15.54
76	326	12.1	1	0.35	0.48	0.20	21'587	16'682	6.30	12.61
78	324	12.4	1	0.32	0.44	0.20	19'822	14'917	5.04	10.08
80	322	12.7	1	0.30	0.40	0.20	18'131	13'226	3.96	7.93
82	320	13.0	1	0.27	0.37	0.20	16'516	11'611	3.05	6.11
84	318	13.3	1	0.24	0.33	0.20	14'976	10'071	2.30	4.60
86	316	13.7	1	0.22	0.30	0.20	13'512	8'607	1.68	3.36
88	314	14.0	1	0.20	0.27	0.20	12'123	7'218	1.18	2.36
90	312	14.3	1	0.18	0.24	0.20	10'809	5'904	0.79	1.58
91	311	14.5	1	0.17	0.23	0.20	10'180	5'275	0.63	1.26
92	310	14.6	1	0.16	0.21	0.20	9'571	4'666	0.49	0.99
93	309	14.8	1	0.15	0.20	0.20	8'980	4'075	0.38	0.75
94	308	14.9	1	0.14	0.19	0.20	8'408	3'503	0.28	0.56
95	307	15.1	1	0.13	0.17	0.20	7'854	2'949	0.20	0.39
96	306	15.3	1	0.12	0.16	0.20	7'320	2'415	0.13	0.26
97	305	15.4	1	0.11	0.15	0.20	6'804	1'899	0.08	0.16
98	304	15.6	1	0.10	0.14	0.20	6'307	1'402	0.04	0.09
99	303	15.7	1	0.09	0.13	0.20	5'829	924	0.02	0.04

The adapted DI method allows simulating changes in the jet air entrainment rates. Although purely hypothetical in the case of Kariba, the effects of adding air to the jets on the ultimate scour depth are estimated in Figure 8.9. The failure criterion used was h_{up}/z

= 0.25. Increasing entrained air concentrations were simulated, starting with the estimated value of 48% of the existing jets, up to approximately 65%.

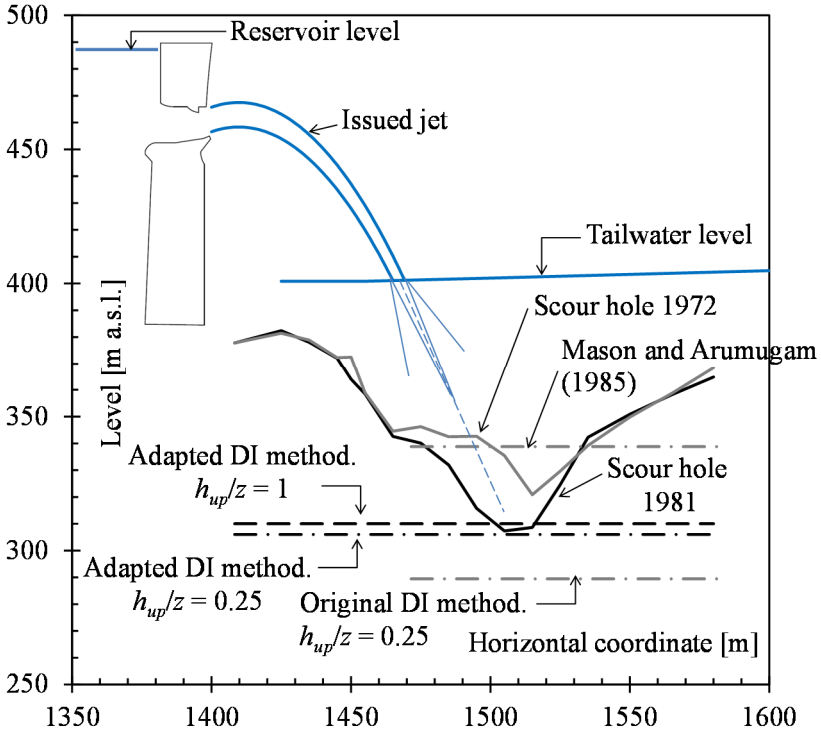

Figure 8.8. Results of the adapted Dynamic Impulsion (DI) method for the Kariba dam scour hole; (grey solid line) pool bottom measured in 1972; (black grey line) pool bottom measured in 1981, corresponding also to measurement in 2001; (dashed black lines) adapted DI method with either h_{up}/z = 1or h_{up}/z = 0.25; (dashed grey line) original DI method with h_{up}/z = 0.25.

Figure 8.9 shows that adding air to the jets reduces scour. The bottom elevation increases steadily with the entrained air concentration. Nevertheless, this level increase is small. The simulated increase of 17% of the air concentration resulted in an ultimate scour depth only 2.1 m smaller, rising the bottom from an elevation of 306 to 308.1 m a.s.l.

As highlighted by Manso et al. (2009), the geometry of the plunge pool bottom generates induced flow patterns and has a strong influence on the way the jet dissipates and is deflected at the pool bottom. Subsequently to jet impingement at the intersection of the jet centerline with the water-rock interface, the jet is deflected and forms a wall jet parallel to the bottom. Wall jets have a scour potential as well (Bellin and Fiorotto, 1995; Fiorotto and Rinaldo, 1992b), which is not represented in the DI method as stated before. In the case of Kariba, jet deflection towards upstream of the impingement point is a specific concern, which may cause erosion towards the dam foundations. The current reshaping efforts have the objective of leading the deflection of the impinging jet towards downstream, thus avoiding further erosion towards the dam (Noret et al., 2013).

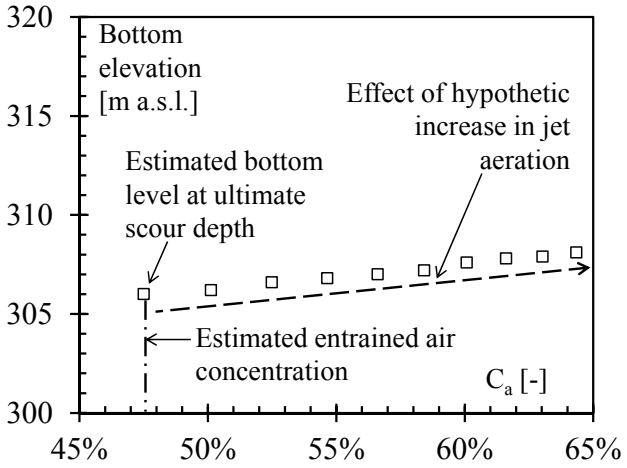

Figure 8.9. Bottom elevation of the Kariba dam scour hole at the ultimate scour depth *versus* entrained air concentration C_a, (□) model results; (black dashed arrow) tendency of the results; computational results with adapted DI method, $h_{up}/z = 0.25$.

Other uncertainties arise from the parameters used in the model. For example, it is highly dependent of the used wave celerity. Although the celerity used in this case is a robust result of the experimental campaign, the study can be extended in the future to assess the influence of the block geometry relatively to the jet and pool geometric scales and interlocking of the joints on the wave celerity. Moreover the dynamic impulse applied on a rock block was computed neglecting the stabilizing forces of the moving block as a simplifying assumption for the engineering practice.

8.4 Conclusions

The proposed enhancements to a physically-based scour model originally developed by Bollaert (2002) and Bollaert and Schleiss (2005) take into consideration the influence of jet air entrainment by the use of systematic experiments with near-prototype velocity jets. With the proposed modifications, the Comprehensive Scour Model is the only engineering method to evaluate erosion of rock downstream of jets issued from hydraulic schemes that is fully based on the physical-mechanical processes involving the three phases, namely, water, rock and air.

The adaptations involve the time-averaged pressures attaining the water-rock interface as a result of the dissipation in the pool, which is greatly influenced by air entrainment. These pressures are represented by the aerated time-averaged pressure coefficient, which considers the lower density of the air-water mixture and the lower dissipation of the aerated jet flow in the pool.

Moreover, adaptations were proposed to the representation of the dynamic impulse applied on a dislodged block at the pool bottom. This feature is represented by the maximum dynamic impulsion coefficient, which was found to be a value of approximately 0.2, especially for high-velocity jets impinging into deep pools. Finally, the impulsion acting on a rock block is the combined influence of the aerated time-averaged coefficient and of the maximum dynamic impulsion coefficient.

A case study of the Kariba dam scour hole was presented. The results are close to the bottom level indicated in the 1981 and 2001 surveys. Especially, if the failure criterion is that a block is ejected whenever one quarter of its height leaves the cavity, the computed ultimate scour depth coincides with the measured elevation of the scour hole bottom (306 m a.s.l.). However, it was pointed out that the Dynamic Impulsion (DI) method considers the erosion capacity of the impinging jet only, and does not account for other scour mechanisms, such as the wall jet created by the deflection of the impinging jet on the water-rock interface.

Furthermore, additional developments to the model may include the influence of the block dimensions relatively to the jet dimensions and their influence on parameters such as the wave celerity and the maximum dynamic impulsion. Additional case studies will help to validate the adapted model for engineering practice.

9

Conclusions and recommendations

9.1 General

This research study was conducted in the framework of a long-term research line studying rock scour since 1998. The goal is to study rock scour by a detailed representation of its physical processes and perform systematic experiments with near-prototype jet velocities to assess realistic data of dynamic pressures acting on the rock mass.

With the results of the present research project, a better understanding of the effect of air entrainment on the scour process could be acquired. Previous systematic experiments studied dynamic pressures on the water-rock interface, as well as inside different geometries of closed-end and open-end fissures (Bollaert, 2002). They also examined the influence of pool bottom geometry on these pressures (Manso, 2006) and the response of a block embedded in the pool bottom (Federspiel, 2011). These achievements are now completed with the influence of jet air entrainment, since the dissipation of air bubbles in the pool until block ejection from the rock mass. The scour process can now be reproduced by an engineering model which represents the physical-mechanical processes of water, rock and air considering in detail the effect of air entrainment.

The present research assessed the influence of jet air entrainment on block stability in plunge pools for rock scour estimation with five main focuses. The analyses address air bubbles dissipation in the jet shear layer in the pool, dynamic pressures on the water-

rock interface and underlying fissures around an embedded block either fixed or mobile, the influence of pool confinement, the response of the block impacted by the aerated high-velocity jets and adaptations of a physically-based engineering scour model. In the following, the conclusions of each focus are discussed in detail.

9.2 Air bubble parameters in the jet shear layer

The vertical components of the air bubbles velocity and the air concentrations were measured at 33 positions of the jet shear layer inside the 80 cm deep pool. For this, a phase-detection double-fiber optical probe was employed. Vertical cylindrical jets were tested, with different aerations added into the nozzle. Comparison is made between submerged and plunging jets. For submerged jets the entire air discharge is known, whilst plunging jets entrain additional air discharge at the plunge section with the pool. For the first time, the air bubble parameters could be assessed experimentally in the jet shear layer of aerated high-velocity jets. The study is based on careful dimensional analysis and scale effects are minimized by the use of high Weber and Reynolds numbers.

The air bubbles velocity in the jet centerline can be considered representative of the flow velocity, due to the strong turbulent drag which pulls the bubbles toward the bottom and, together with the reduced size of the bubbles in this region makes buoyancy forces negligible. The undermentioned conclusions can be drawn:

- The centerline velocity of the jet into the plunge pool is composed of a constant region in the jet core, followed by a linear decay in the *zone of established flow*.
- For submerged jets, the velocity in the jet core region is the same as in the impact section, which is also the issuance section.
- On the other hand, for plunging jets, the flow velocity in the jet core is approximately 0.83 times the jet impact velocity, due to energy losses at the plunge section.
- The dispersing jet velocity then decays linearly as a function of the normalized depth in the *zone of established flow* with a rate of 0.07, for both submerged and plunging jets.
- Hence, empirical expressions are derived for the jet core length and jet velocity decay for submerged and plunging jets.
- The air concentrations for plunging and submerged jets were analyzed by their centerline decay and radial distribution. Empirical expressions were proposed to describe the air concentration at any point of the jet shear layer.
- In the case of plunging jets, air entrainment at the plunge region takes place in the induction trumpet, which bends the water surface meniscus between the jet perimeter and the receiving pool. The measurements suggest that the induction trumpet varied between 10 cm for low jet velocities and 30 cm to high-velocity jets.
- The air concentration along the jet centerline for submerged jets is a function of the entrained air concentration and of the relative depth below jet impingement. For plunging jets, it is also a function of induction trumpet length, below which the air entrainment process is complete.

- The radial distribution of air concentration of the dispersing jet in the pool for submerged jets is a simple-Gaussian, similarly to the radial velocity distribution.
- On the other hand, the radial distribution of air concentration of the dispersing jet in the pool for plunging jets is a double-Gaussian. This reflects air entrainment on the induction trumpet between the jet perimeter and the pool surface.
- The proximity with the pool bottom influenced the parameters of the radial distributions, indicating the presence of the impingement region in the vicinity of stagnation. A pressure build-up takes place at the impingement region, which expels the bubbles from the jet centerline.

9.3 Effect of air entrainment on dynamic pressures around a block

On the bottom of plunge pools, the kinetic energy of impinging jets is transformed into dynamic pressures. The pressures act on the top of rock blocks embedded at the pool bottom surface, as well as they propagate inside underlying fissures as pressure waves. These pressures are at the origin of the rock scour phenomenon, which is a combination of progressive joint break-up by hydraulic jacking and block uplift.

The experiments reproduced aerated high-velocity jets impinging on an instrumented block on the bottom. Submerged and plunging jets are compared, as well as jet impingement on the center of the block or on a fissure on one of its sides. Additionally, different pools depths were tested. The dynamic pressures were measured at 12 positions uniformly distributed along one half of the symmetric cubic block. The main conclusions are listed below:

- At the water-rock interface, the non-dimensional coefficients representative of the time-averaged pressures, pressure fluctuations, maximum and minimum observed pressures show a Gaussian decay with the distance from the jet centerline, similarly to the velocity distribution of a transversal section of the impinging jet.
- The results of the jet centerline velocity decay were used to derive an expression for the time-averaged pressure coefficient of plunging jets at stagnation. The best fit of the experimental data is rather close to the theoretical expression.
- The time-averaged pressures of plunging jets at stagnation is a function of the kinetic energy of the jet at the plunge section, reduced of energy losses at the plunge region, energy losses due to jet dissipation along the pool, and energy losses in the impingement region.
- The air entrained by the jet influences dynamic pressures affecting the rock mass in two opposed ways.
    - ✓ On one hand, the entrained air discharge lowers the apparent density of the jet, which corresponds to a reduction of momentum. This effect reduces the pressures attaining the rock at the pool bottom.
    - ✓ On the other hand, the entrained air bubbles reduce the shear between the jet and the surrounding water, resulting in lower velocity decay along the pool. This effect increases the pressures at the pool bottom. Due to the

nature of this process, this effect is better observed close to stagnation and increases when pool depth increases.

- Inside the fissure, the pressure signals are excited by the dynamic pressures acting on its entrances at the water-rock interface and propagate as pressure waves on pressurized flows. Resonance effects take place, as a consequence of wave reflections on the fissure extremes and partial reflections on the fissure bends. Resonance depends thus on the fissure length and on the pressure wave celerity.
- The pressure wave celerity inside the fissures is directly affected by jet air entrainment. The resonance frequencies reduce with increasing air-to-water ratio of the jet, indicating that the air bubbles entered the fissures and changed the properties of the fluid such as mean density and bulk modulus of elasticity.
- Centered jets generate no flow inside the fissures due to the symmetric arrangement. The non-dimensional coefficients of centered jets increase slightly towards the center of the fissure. The increase is related to the pressure waves' amplifications taking place inside the fissures.
- Sided jets, however, produce linearly decreasing coefficients inside the fissures due to the energy differences between their extremes and a laminar flow inside the fissures.

9.4 Simultaneous effects of pool confinement and jet aeration

The effects of aeration alone were discussed before. However, jet dissipation in plunge pools is strongly influenced by the geometry of the pool bottom. If for the simpler case of a flat bottom, the impinging jet is deflected radially at the water-rock interface and produces a wall jet parallel to the bottom, in the case of a laterally confined bottom the jet is deflected back towards the pool surface. This results in shear between the downward current of the impinging jet and the upward current of the deflected jet, increasing energy dissipation. The following conclusions are drawn concerning the tests with simultaneous confinement and jet aeration effects:

- The combined influence of jet air entrainment and pool confinement on the dynamic pressures acting on the rock bottom is a superposition of the two opposed effects imposed by the entrained air bubbles with the increasing energy dissipation of confined jets.
- Nevertheless, it was mentioned that the pressure rises due to lower jet velocity decay for aerated jets. This effect increases as a function of the pool depth, which is also the case for the pressure reduction of confined jets. Indeed, the energy dissipation between the jet and the deflected upward currents takes place along the pool depth. Therefore, the pressure reduction for jets impinging on a confined bottom was maximal for deep pools, but barely noticed for shallow pools.
- At the intersection of the jet centerline with the water-rock interface, for a given pool depth, the time-averaged pressure coefficient grows as a function of the incoming jet velocity until a maximum is reached. This first region corresponds to a developed jet impact on the bottom.

- The maximum value of the time-averaged pressure coefficient is observed when the jet core development length is equal to the pool depth. It means that this is the situation at stagnation where the conversion of the energy of the jet into pressures is the most efficient.
- After the maximum value, the time-averaged pressure coefficient decreases slightly with the incoming jet velocity, following a convex curve. This region corresponds to a core jet impact on the bottom.
- A confined jet dissipation at the bottom also changes the structure of the turbulent flow by shifting spectral energy generation toward lower frequencies.

9.5 Differences between fixed and mobile blocks

The experimental tests compared blocks either fixed inside the cavity or free to move. The data show that, when the block is free to move, its vibrations cause a pressure release inside the fissures, in opposition to a fixed block. The main conclusions are listed below:

- The release of the time-averaged pressure coefficient inside the fissures for free blocks grows with the incoming jet velocity. This is because the block vibrates more with high-velocity jets.
- Very small differences were observed between the pressure fluctuation coefficients of fixed and free blocks.
- The resonance phenomena of the pressure fluctuations inside the fissures are deeply affected by the vibrations of free blocks. The resonance peaks are dramatically damped and the resonance frequencies are strongly reduced when compared to fixed blocks.
- In fact, the vibrations of a block as a response to the pressure waves that propagate inside the fissures around it are analog, to a certain point, to an elastic behavior of the boundaries of pressurized flows at the passing of a water-hammer. The pressure wave celerity is a function of the bulk modulus of elasticity of the fluid, of the fluid density and of the pseudo-elastic properties of the boundaries. However, the difference between the vibrating block in the rock mass and the water-hammer propagating inside conduits is that the former has displacements of the entire solid body, while the latter shows an actual elastic deformation of the flow boundaries.

9.6 Block response to aerated jet impact

The vertical displacements of the block impacted by aerated high-velocity plunging jets impinging on one of its lateral fissures were assessed. A theoretical and experimental study was carried on and resulted on the development of a numerical model of the block vibrations. The study allows the following conclusions:

- The block is submitted to active and passive forces. Active forces are independent from the block response, whereas passive forces are reactions to the block response and exist only during block displacements.

- The active forces are:
  - ✓ The pressure field around the block, the only which may result in an uplift force.
  - ✓ The block immerged weight, consequence of gravity and buoyancy forces around the block.
- The passive forces are:
  - ✓ The friction forces caused by either the hydraulic friction between two moving solid boundaries and the solid friction between the metallic lateral guides sliding against the cavity walls.
  - ✓ The resistance of the fluid in the fissure formed underneath the block to a change in volume.
  - ✓ The virtual force due to the added mass of the block.
- The spectral content of the pressure fluctuations show that the block has small rotations at high-frequencies. These rotations are minimized by the lateral guides but are unavoidable due to the high moment applied on the block by the sided jet and the small construction tolerance between the guides and the cavity walls.
- The results also show that the block had sudden undamped drops. This is observed more often for low velocity jets. These drops are probably caused by the release of air pockets from the fissure below the block after a certain block rise. They change the apparent fluid properties in the lower fissure.
- The proposed theoretical model represents correctly the block displacements. The agreement is better with the measurements for high-velocity jets.
- For high-velocity jets, the air bubbles enter and leave the fissure at a steadier pace, leading to more constant parameters of the differential equation.
- The theoretical model of block displacements has the objective of providing a better understanding of the phenomenon. It is not aimed for practical engineering applications.
- The influence of jet aeration on the block displacements differs with the relative pool depth, due to the influences of jet air entrainment on the pressures highlighted before.
- For shallow pools, block displacements decrease with jet air entrainment. This is due to the reduction of momentum of the jet being the predominant effect of aeration.
- For deep pools, block displacements increase with jet air entrainment. This is due to the decrease of jet velocity decay, which is a function of the pool depth, being the predominant aeration effect.

9.7 Adaptations of a physically-based scour model

Adaptations are proposed to the Comprehensive Scour Model (CSM) originally developed by Bollaert (2002) and Bollaert and Schleiss (2005) to account for jet air entrainment. The proposed adaptations are based on the findings of this research, including particularly the following features:

- The jet core development length.
- The aerated time-averaged pressure coefficient, which considers the opposed effects of jet aeration.
    - ✓ The lower momentum of aerated jets is reproduced by the apparent density of the air-water mixture in the formulation of the kinetic energy per unit volume of the jet.
    - ✓ The effect of the lower jet velocity decay on the pressures is reproduced in the expression relating aerated and non-aerated time-averaged pressure coefficients.
- The new proposed maximum impulsion coefficient at an average value of 0.2, based on the experimental results.

The adapted Dynamic Impulsion method (DI) combines the aerated time-averaged pressure coefficient, which takes into account the influence of aeration and the jet energy dissipation along the pool depth, with the maximum impulsion coefficient on the block.

A case study was performed with the adapted model. The ultimate scour depth of the Kariba plunge pool was simulated.

- The results of the model are close to the pool bottom elevations measured in 1981 and 2001. If the failure criterion is that the block is ejected from the rock mass whenever his displacement attains one quarter of the cavity height, the ultimate scour depth was 306 m a.s.l., exactly the same elevation of the geological surveys.
- The adapted DI method allows simulating different jet aerations. In the case of Kariba, a hypothetical increase of entrained air concentration results in a lower ultimate scour depth. Nevertheless, the reductions are very small.
- However, the DI method does not reproduce the scour potential of wall jets, which are the deflected jets flowing parallel to the pool bottom. Also, the DI method does not take into account scour development in time. These aspects are covered though by the QSI and CFM modules of the Comprehensive Scour Model (Bollaert et al., 2013b).

9.8 Recommendations for future research

The following topics could be addressed in future investigations to help improving rock scour understanding and modeling:

- As stated in Chapter 5, the experimental facility reproduces near-prototype jet velocities, but the geometry of the model may be subject to scale effects. Future developments should test the influence of the ratios between jet diameter and block dimensions and fissure thickness. The jet diameter can be easily modified in new nozzle designs. Other block and fissure dimensions require one or some new blocks to be built with different side lengths and compatible lateral guides. The block is expected to vibrate more with a thicker fissure, which allows the fluid to fill the volume created in the fissure underneath the block during an upward displacement, and vice-versa.

- Additionally, the representation of the rock mass can be modified to represent multiple blocks, thus approaching progressively to a real case scenario. This corresponds to a small network of joints, which will certainly have an influence on the resonance effects since a large number of partial pressure wave reflections will be observed.
- Moreover, the influence of the turbulence intensity of the issued jets should be quantified. The turbulence intensity is at the origin of the formation of jet surface disturbances, which was found in past research to have a fundamental role in air entrainment (Zhu et al., 2000). Furthermore, it is certainly important to account for the turbulence intensity in the jet dissipation process along the pool. Different values of turbulence intensities can be tested by adapting the nozzle design. For such, nozzle walls with different roughness could be built.
- Also plane jets could be tested for the first time in the frame of this research line. This would avoid the difficulties involved with cylindrical efforts acting on a cubic block.

Bibliography

Abramovich, G.N., 1963. The theory of turbulent jets. M.I.T. Press, Massachusetts Institute of Technology , Cambridge, Ma.

Albertson, M., Dai, Y., Jensen, R., Rouse, H., 1948. Diffusion of submerged jets. Transactions of the ASCE Paper N° 2409, 639-664.

Annandale, G.W., 1995. Erodibility. Journal of Hydraulic Research 33, 471-494.

Annandale, G.W., Schleiss, A.J., 2007a. Predicting rock scour - Part one. International Water Power & Dam Construction 9, 22-26.

Annandale, G.W., Schleiss, A.J., 2007b. Predicting rock scour - Part two. International Water Power & Dam Construction 10, 38-42.

Arndt, R.E.A., Ippen, A.T., 1970. Turbulence Measurements In Liquids Using An Improved Total Pressure Probe. Journal of Hydraulic Research 8, 131-158.

Asadollahi, P., Tonon, F., Federspiel, M.P.E.A., Schleiss, A., 2011. Prediction of rock block stability and scour depth in plunge pools. Journal of Hydraulic Research 49, 750-756.

Beatty, M.F., 2006. Principles of Engineering Mechanics. Springer US.

Bellin, A., Fiorotto, V., 1995. Direct dynamic force measurement on slabs in spillway stilling basins. Journal of Hydraulic Engineering 121, 686-693.

Beltaos, S., Rajaratnam, N., 1974. Impinging circular turbulent jets. Journal of the Hydraulics Division-Asce 100, 1313-1328.

Beltaos, S., Rajaratnam, N., 1977. Impingement of Axisymmetric Developing Jets. Journal of Hydraulic Research 15, 311-326.

Bin, A.K., 1993. Gas entrainment by plunging liquid jets. Chemical Engineering Science 48, 3585-3630.

Blevins, R.D., 1984. Applied fluid dynamics handbook. Van Nostrand Reinhold Company Inc., New York, USA.

Bollaert, E., 2002. Transient water pressures in joints and formation of rock scour due to high-velocity jet impact, in: Schleiss, A.J. (Ed.), Communication N° 13. Laboratory of Hydraulic Constructions (LCH), École Polytechnique Fédérale de Lausanne (EPFL), Switzerland.

Bollaert, E., 2013. One-degree-of-freedom rigid body dynamics of rock blocks in turbulent flows, 35th IAHR World Congress. TUP, Chengdu, China, pp. 1-11.

Bollaert, E., Duarte, R., Pfister, M., Schleiss, A., Mazvidza, D., 2012. Physical and numerical model study investigating plunge pool scour at Kariba Dam, 24th Congress of CIGB – ICOLD, kyoto, Japan, pp. 241-248.

Bollaert, E., Federspiel, M., Schleiss, A., 2013a. The influence of added mass on rock block uplift in plunge pools, 35th IAHR World Congress. TUP, Chengdu, Chine, pp. 1-10.

Bollaert, E., Schleiss, A., 2003a. Scour of rock due to the impact of plunging high velocity jets Part I: A state-of-the-art review. Journal of Hydraulic Research 41, 451-464.

Bollaert, E., Schleiss, A., 2003b. Scour of rock due to the impact of plunging high velocity jets Part II: Experimental results of dynamic pressures at pool bottoms and in one- and two-dimensional closed end rock joints. Journal of Hydraulic Research 41, 465-480.

Bollaert, E., Schleiss, A., 2005. Physically based model for evaluation of rock scour due to high-velocity jet impact. Journal of Hydraulic Engineering ASCE Vol. 131, 153-165.

Bollaert, E.F.R., Munodawafa, M.C., Mazvidza, D.Z., 2013b. Kariba Dam Plunge Pool Scour: quasi-3D Numerical Predictions. Houille Blanche-Revue Internationale De L Eau, 42-49.

Brattberg, T., Chanson, H., 1998. Air entrapment and air bubble dispersion at two-dimensional plunging water jets. Chemical Engineering Science 53, 4113-4127.

Canepa, S., Hager, W., 2003. Effect of jet air content on plunge pool scour. Journal of Hydraulic Engineering ASCE 129, 358-365.

Cartellier, A., Achard, J.L., 1991. Local phase detection probes in fluid/fluid two-phase flows. Review of Scientific Instruments 62, 279-303.

Chanson, H., 1997. Air Bubble Entrainment in Free-Surface Turbulent Shear Flows. Academic Press, London, UK.

Chanson, H., 2009. Turbulent air-water flows in hydraulic structures: Dynamic similarity and scale effects. Environmental Fluid Mechanics 9, 125-142.

Chanson, H., Aoki, S., Hoque, A., 2004. Physical modelling and similitude of air bubble entrainment at vertical circular plunging jets. Chemical Engineering Science 59, 747-758.

Chanson, H., Toombes, L., 2003. Strong interactions between free-surface aeration and turbulence in an open channel flow. Experimental Thermal and Fluid Science 27, 525-535.

Chassaing, P., 2000. Turbulence en mécanique des fluides: analyse du phénomène en vue de sa modélisation à l'usage de l'ingénieur. Cépaduès-Editions.

Cola, R., 1965. Energy dissipation of a high-velocity vertical jet entering a basin, Proceedings of 11th IAHR Congress. IAHR, Leningrad, pp. 1-13.

Cummings, P.D., Chanson, H., 1997a. Air entrainment in the developing flow region of plunging jets - Part 1: Theoretical development. Journal of Fluids Engineering, Transactions of the ASME 119, 597-602.

Cummings, P.D., Chanson, H., 1997b. Air entrainment in the developing flow region of plunging jets - Part 2: Experimental. Journal of Fluids Engineering, Transactions of the ASME 119, 603-608.

Davoust, L., Achard, J.L., El Hammoumi, M., 2002. Air entrainment by a plunging jet: the dynamical roughness concept and its estimation by a light absorption technique. International Journal of Multiphase Flow 28, 1541-1564.

Duarte, R., 2013. Air concentrations in plunge pools due to aerated plunging high-velocity jets and dynamic pressures in underlying fissures, Proceedings of 35th IAHR World Congress. TPI, Chengdu, China, pp. 1-10.

Duarte, R., Schleiss, A., Pinheiro, A., 2013. Dynamic pressure distribution around a fixed confined block impacted by plunging and aerated water jets, 35th IAHR World Congress. TUP, Chengdu, China, pp. 1-8.

Duarte, R., Schleiss, A.J., Pinheiro, A., 2014. Discussion on "CFD analysis of the effect of nozzle stand-off distance on turbulent impinging jets". Canadian Journal of Civil Engineering, 1-2.

Ervine, D.A., 1998. Air entrainment in hydraulic strucutures: a review. Proceedings of the Institution of Civil Engineers - Water Maritime and Energy 130, 12.

Ervine, D.A., Falvey, H.T., 1987. Behavior of turbulent jets in the atmosphere and in plunge pools. Proceedings of the Institution of Civil Engineers Part 2-Research and Theory 83, 295-314.

Ervine, D.A., Falvey, H.T., Withers, W., 1997. Pressure fluctuations on plunge pool floors. Journal of Hydraulic Research 35, 257-279.

Ervine, D.A., McKeogh, E., Elsawy, E.M., 1980. Effect of turbulence intensity on the rate of air entrainment by plunging water jets. Proceedings of the Institution of Civil Engineers Part 2-Research and Theory 69, 425-445.

Federspiel, M.P.E.A., 2011. Response of an embedded block impacted by high-velocity jets, in: Schleiss, A.J. (Ed.), Communication N° 47. Laboratory of Hydraulic Constructions (LCH), École Polytechnique Fédérale de Lausanne (EPFL), Switzerland.

Federspiel, M.P.E.A., Bollaert, E.F.R., Schleiss, A., 2009. Response of an intelligent block to symmetrical core jet impact, 33rd IAHR Congress. IAHR, Vancouver, Canada, pp. 3573-3580.

Federspiel, M.P.E.A., Bollaert, E.F.R., Schleiss, A., 2011. Dynamic response of a rock block in a plunge pool due to asymmetrical impact of a high-velocity jet, 34th IAHR World Congress, Brisbane, Australia, pp. 2404-2411.

Fiorotto, V., Rinaldo, A., 1992a. Fluctuating Uplift and Lining Design in Spillway Stilling Basins. Journal of Hydraulic Engineering 118, 578-596.

Fiorotto, V., Rinaldo, A., 1992b. Turbulent pressure fluctuations under hydraulic jumps. Journal of Hydraulic Research 30, 499-520.

Ghidaoui, M.S., McInnis, D.A., Axworthy, D.H., Zhao, M., 2005. A Review of Water Hammer Theory and Practice. Applied Mechanics Reviews 58, 49-76.

Giralt, F., Chia, C.J., Trass, O., 1977. Characterization of impingement region in an axisymmetric turbulent jet. Industrial & Engineering Chemistry Fundamentals 16, 21-28.

Hachem, F.E., Schleiss, A.J., 2011. A review of wave celerity in frictionless and axisymmetrical steel-lined pressure tunnels. Journal of Fluids and Structures 27, 311-328.

Hager, W., Schleiss, A.J., 2009. Constructions hydrauliques. PPUR, Lausanne, Switzerland.

Halliwell, A.R., 1963. Velocity of a waterhammer wave in an elastic pipe. ASCE Journal of the Hydraulics Division 89, 1-21.

Hartung, F., Häusler, E., 1973. Scours, stilling basins and downstream protection under free overfall jets at dams, 11th Congress on Large Dam. ICOLD, Madrid, pp. 39-56.

Heller, V., 2011. Scale effects in physical hydraulic engineering models. Journal of Hydraulic Research 49, 293-306.

Kiger, K.T., Duncan, J.H., 2012. Air-Entrainment Mechanisms in Plunging Jets and Breaking Waves. Annual Review of Fluid Mechanics 44, 563-596.

Kolmogoroff, A., 1941. The local structure of turbulence in incompressible viscous fluid for very large Reynolds numbers. C. R. Acad. Sci. URSS 30, 301-305.

Kundu, P.K., Cohen, I.M., 2010. Fluid Mechanics. Elsevier Science, San Diego.

Mahzari, M., Arefi, F., Schleiss, A.J., 2002. Dynamic response of the drainage system of a cracked plunge pool liner due to free falling jet impact, in: Schleiss, A.J., Bollaert, E. (Eds.), Rock Scour due to falling high-velocity jets. Swets & Zeitlinger, Netherlands, pp. 227-237.

Manso, P., Bollaert, E., Schleiss, A., 2007. Impact pressures of turbulent high-velocity jets plunging in pools with flat bottom. Experiments in Fluids 42, 49-60.

Manso, P., Fiorotto, V., Bollaert, E., Schleiss, A., 2004. Discussion of « Effect of jet air content on plunge pool scour » by Stefano Canepa and Willi H. Hager. Journal of Hydraulic Engineering 130, 1128-1130.

Manso, P.A., Bollaert, E.F.R., Schleiss, A., 2009. Influence of plunge pool geometry on high-velocity jet impact pressures and pressure propagation inside fissured rock media. Journal of Hydraulic Engineering 135, 783-792.

Manso, P.F.A., 2006. The influence of pool geometry and induced flow patterns in rock scour by high-velocity plunging jets, in: Schleiss, A.J. (Ed.), Communication N° 25. Laboratory of Hydraulic Constructions (LCH), École Polytechnique Fédérale de Lausanne (EPFL), Switzerland.

Manso, P.F.A., Bollaert, E.F.R., Schleiss, A.J., 2008. Evaluation of high-velocity plunging jet-issuing characteristics as a basis for plunge pool analysis. Journal of Hydraulic Research 46, 147-157.

Mason, P.J., 1989. Effects of air entrainment on plunge pool scour. Journal of Hydraulic Engineering-Asce 115, 385-399.

Mason, P.J., Arumugam, K., 1985. Free jet scour below dams and flip buckets. Journal of Hydraulic Engineering-ASCE 111, 220-235.

May, R.W.P., Willoughby, I.R., 1991. Impact pressures in plunge basins due to vertical falling jets, Report SR242, HR-Wallingford, UK.

McKeogh, E.J., Elsawy, E.M., 1980. Air retained in pool by plunging water jet. Journal of the Hydraulics Division-Asce 106, 1577-1593.

McKeogh, E.J., Ervine, D.A., 1981. Air entrainment rate and diffusion pattern of plunging liquid jets. Chemical Engineering Science 36, 1161-1172.

Melo, J.F., 2002. Reduction of plunge pool floor dynamic pressure due to jet air entrainment, in: Schleiss, A.J., Bollaert, E. (Eds.), Rock Scour due to falling high-velocity jets. Swets & Zeitlinger, Netherlands, pp. 125-136.

Melo, J.F., Pinheiro, A.N., Ramos, C.M., 2006. Forces on plunge pool slabs: Influence of joints location and width. Journal of Hydraulic Engineering-Asce 132, 49-60.

Mercier, F., Bonelli, S., Pinettes, P., Golay, F., Anselmet, F., Philippe, P., 2014. Comparison of Computational Fluid Dynamic Simulations with Experimental Jet Erosion Tests Results. Journal of Hydraulic Engineering 04014006, 1-11.

Noret, C., Girard, J.-C., Munodawafa, M.C., Mazvidza, D.Z., 2013. Kariba dam on Zambezi river: stabilizing the natural plunge pool. La Houille Blanche, 34-41.

Ohl, C.D., Oğuz, H.N., Prosperetti, A., 2000. Mechanism of air entrainment by a disturbed liquid jet. Physics of Fluids 12, 1710-1714.

Pagliara, S., Amidei, M., Hager, W., 2008a. Hydraulics of 3D Plunge Pool Scour. Journal of Hydraulic Engineering 134, 1275-1284.

Pagliara, S., Hager, W., Minor, H., 2006. Hydraulics of Plane Plunge Pool Scour. Journal of Hydraulic Engineering 132, 450-461.

Pagliara, S., Hager, W., Unger, J., 2008b. Temporal Evolution of Plunge Pool Scour. Journal of Hydraulic Engineering 134, 1630-1638.

Pfister, M., Hager, W.H., 2010. Chute Aerators. I: Air Transport Characteristics. Journal of Hydraulic Engineering-Asce 136, 352-359.

Pfister, M., Lucas, J., Hager, W.H., 2011. Chute Aerators: Preaerated Approach Flow. Journal of Hydraulic Engineering-Asce 137, 1452-1461.

Pinheiro, A.N., 1995. Acções hidrodinâmicas em soleiras de bacias de dissipação de energia por ressalto. . PhD Thesis. Instituto Superior Técnico, Lisbon, Portugal.

Pinheiro, A.N., Melo, J.F., 2008. Effect of jet aeration on hydrodynamic forces on plunge pool floors. Canadian Journal of Civil Engineering 35, 521-530.

Pope, S.B., 2000. Turbulent Flows. Cambridge University Press.

Qu, X., Goharzadeh, A., Khezzar, L., Molki, A., 2013. Experimental characterization of air-entrainment in a plunging jet. Experimental Thermal and Fluid Science 44, 51-61.

Qu, X.L., Khezzar, L., Danciu, D., Labois, M., Lakehal, D., 2011. Characterization of plunging liquid jets: A combined experimental and numerical investigation. International Journal of Multiphase Flow 37, 722-731.

Rajaratnam, N., 1976. Turbulent Jets. Elsevier Science.

Rajaratnam, N., Zhu, D.Z., Rai, S.P., 2010. Turbulence measurements in the impinging region of a circular jet. Canadian Journal of Civil Engineering 37, 782-785.

RBI, 2012. ISO Software. Two-phase flow study. User's guide, Meylan, France.

Schleiss, A., 2002. Scour evaluation in space and time – the challenge of dam designers, in: Schleiss, A.J., Bollaert, E. (Eds.), Rock Scour due to falling high-velocity jets. Swets & Zeitlinger, Netherlands, pp. 3-22.

Sene, K.J., 1988. Air entrainment by plunging jets. Chemical Engineering Science 43, 2615-2623.

Shademan, M., Balachandar, R., Barron, R.M., 2013. CFD analysis of the effect of nozzle stand-off distance on turbulent impinging jets. Canadian Journal of Civil Engineering 40, 603-612.

Spurr, K.J.W., 1985. Energy approach to estimating scour downstream of a large dam. Water Power and Dam Construction 37, 81-89.

Tapfuma, V., Mazvidza, D., Goguel, B., Molyneux, J.D., 1994. Kariba dam safety monitoring and resulting maintenance works, 18th ICOLD Congress, Durban, South Africa, pp. 1445-1464.

Tennekes, H., Lumley, J.L., 1972. A First Course in Turbulence. MIT press, USA.

Van de Donk, J.A.C., 1981. Water aeration with plunging jets. PhD Thesis. Technische Hogeschool Delft.

Van de Sande, E., Smith, J.M., 1973. Surface entrainment of air by high velocity water jets. Chemical Engineering Science 28, 1161-1168.

Van De Sande, E., Smith, J.M., 1975. Mass transfer from plunging water jets. The Chemical Engineering Journal 10, 225-233.

Van De Sande, E., Smith, J.M., 1976. Jet break-up and air entrainment by low velocity turbulent water jets. Chemical Engineering Science 31, 219-224.

Vejražka, J., Večeř, M., Orvalho, S., Sechet, P., Ruzicka, M.C., Cartellier, A., 2010. Measurement accuracy of a mono-fiber optical probe in a bubbly flow. International Journal of Multiphase Flow 36, 533-548.

Whittaker, J.G., Schleiss, A.J., 1984. Scour related to energy dissipators for high head structures, Mitteilungen der Versuchsanstalt fur Wasserbau, Hydrologie und Glaziologie Nr. 73 VAW-ETHZ, Zurich, Switzerland.

Yuditskii, G.A., 1963. Action of falling jet on joint blocks of a rock and conditions of its erosion. Izvestiya VNIIG 7, 35-60.

Zhu, Y., Oguz, H.N., Prosperetti, A., 2000. On the mechanism of air entrainment by liquid jets at a free surface. Journal of Fluid Mechanics 404, 151-177.

Acknowledgements

This PhD research was performed in the framework of the IST-EPFL Joint Doctoral Initiative, and co-financed by the Portuguese Foundation for Science and Technology (Grant No. SFPH/BD/51074/2010) and LCH-EPFL.

First of all, I would like to express my gratitude to Prof. Anton Schleiss, who trusted in my capacity to perform this research in such a defying and multidisciplinary topic and accepted to guide my work. I had previously worked with Prof. Schleiss, even if indirectly, during my previous stay for an internship at LCH-EPFL for the Master of Advanced Studies, and returning for the doctoral studies meant a lot to me. Prof. Schleiss combines perfectly engineering knowledge and management skills, and guides a team which I had to opportunity to see evolve with time. The atmosphere at LCH-EPFL is always healthy and positive, with motivated people who like to work together. There is something special going on at LCH-EPFL, and I have no doubt it comes from the way it is managed.

I have the same gratitude towards Prof. António Pinheiro, who accepted to lead my research on the "Portuguese side" of the thesis. All my gratefulness to the proximity and openness he showed to perform tests and "watch" the data together on the computer screen to, at a certain point, practically have brainstorms with me to interpret the results. Our discussions were a key element of the achievement of this thesis.

I would like to thank the members of the Jury for accepting to evaluate and discuss the contents of this research. Prof. Alain Nussbaumer, thank you so much for accepting to chair the PhD defense. Prof. António Bento Franco, thank you for agreeing to come from Lisbon to argue and discuss the research. Prof. Willi Hager, I hereby express all my gratitude and admiration for your work in the various fields of hydraulic engineering. Special thanks go to Dr. Erik Bollaert, who was the first to develop the concepts and experiments with which I have worked, and now joins the PhD thesis Jury. I had the pleasure to work directly with Dr. Bollaert during the first one year and a half of this PhD effort, where I learned a lot about scour assessment in a practical project.

In addition, many thanks to the other colleagues, now also my friends, who performed the researches on rock scour at LCH-EPFL before me, Dr. Pedro Manso, and Dr. Matteo Federspiel.

As mentioned before, I had the opportunity to witness 3 generations of motivated researchers at LCH-EPFL. The first was while I was enrolled in the Master of Advanced Studies. Special thanks to Dr. Jean-Louis Boillat, who advised me during this period with his peculiar wisdom and kindness. Thank you to Giovanni De Cesare, Martine Tiercy, Caroline Etter, Louis Schneiter, Frédéric Jordan, Philippe Heller, Burkhard Rosier, Azin Amini, Tobias Meile, Sameh Kantoush, Alexandre Duarte, Marcelo Leite-Ribeiro, Sabrina Pereira, Javier García, Jolanda Jenzer, Ramesh Khanal.

Also thanks to the “intermediate” team that I had the opportunity to join when coming back to the PhD, Dr. Micheal Pfister, Fadi Hachem, Martin Bieri, Michael Müller, Violaine Dugué, Tamara Ghilardi, Milad Daneshvari, Raphael “Xará” Sprenger, Ramona Receanu, Théodora Cohen Liechti, Cédric Bron; and to the amazing new crew that I leave formed by Mona Jafarnejad, Stéphane Terrier, Sebastian Schwindt, Alex Pachoud, Fränz “Chef” Zeimetz, Elena Battisacco, Sabine Chamoun, Davide Würthrich, Nicolas Adam, Mélanie Baehler, Felix Oberrauch, Jessica Zordan and Reyhaneh Sadat. Particularly, thanks to Mário Franca for his friendliness and his availability to discuss many technical aspects of the thesis. Thanks also to Michel Teuscher, Marc-Eric Pantillon and the particularly skilled people who really make a difference when working at LCH: Laurent Morier, David, Grégory, Virgile, Jean-Marc, Jonathan, Shawna.

Another group had the opportunity to share the particularity of a fully joint doctoral program between Lausanne and Lisbon. Ana Margarida Ricardo helped me enormously when I was in Lisbon. José Pedro Matos, Sebastian Guillén, David Ferràs, Irene Samora and Mohammad Ostad Mirza. I also met incredibly nice people who definitely made my life much easier in Portugal: Artur, Nuno, Isabel, Ana Bejinha, Helena, Ricardo, Maria João, Silvia, thank you so much.

Thanks to the group of friends who became my family in Lausanne, and never stops growing: Juliano, Maria, Alê, Reni and Lucas, Marcelo, Montse, Elisa and Juan, Pietro, Simona and Mattias, Mark, Joana, Pedro Camilo, Luis Borges, Pipo, Bruno, Didier, Camilo, Danilo, Laetitia; and those who already left Switzerland, Paulo, Sabrina e Bárbara, Alexandre, Henry, Leandro, Antônio “Conselheiro”, Luciana e Stella, Schubert, Milene e Artur.

Thanks to the professors and staff for Drhima and LHC-COPPE UFRJ, especially to the “cell team” Prof. Flávio Mascarenhas, Prof. Marcelo Miguez, Luiz Paulo Canedo, Guilherme, Rodrigo, Carlos and Aline. Thanks to the colleagues of the Brazilian National Water Agency (ANA), particularly to my dear friend Alexandre Lima and Joaquim Gondim. Also, thanks to the staff from Enel in Brazil and Alessandro Karlin, who always gave me full support and advice, even when I had to announce that I would start a PhD.

Mes remerciements les plus chaleureux sont pour la personne à qui cette thèse est dédiée. La personne qui a rendu ce travail possible avant toute autre chose avec son soutien, amour et douceur indescriptibles. Laurinha, eu tenho muita sorte de poder compartilhar a minha vida com você. Eu te amo muito! Muito obrigado!

Finalmente, gostaria de agradecer a toda a minha família, Felipe, Juliana, Felipe Jr, Gabriel e Gustavo, Tia Vânia, Davi, Viviane, Mário e Marinho, Nelson, Deli, Bruno e Guilherme, Fernanda, Isabela e Luiza, Fátima, Silvana, Antônio Carlos, Carlos José e suas famílias, bem como todos aqueles que eu não terei espaço para citar aqui mas que têm igualmente um espaço fundamental na minha vida. Um agradecimento especial para minha avó Penha. E essa tese também é dedicada às pessoas que formaram quem eu sou hoje. Minha mãe Liana, que tanto me apoiou na minha decisão de realisar esse trabalho de tese e em todos os momento da minha vida e pelo seu amor incondicional. E meu pai Paulo, meu maior exemplo de engenheiro e de homem, cujos ensinamentos moldaram minha forma de ver o mundo.

A1

Experimental results of air concentration

In this appendix, graphical representations of the air concentration results in the measurement region inside the pool are show for all tested jet configurations with a deep pool (Y = 0.80 m). This corresponds to the configurations shown in Table A1.1 below.

Table A1.1. Test configurations shown in A1

Jet impact	Jet discharge [l/s]	Nozzle aeration [%]	Pool depth [m]
Plunging jets	20; 30; 40; 50; 60;70;80;90	0; 8; 15; 23	0.8
Submerged jets			

Table A1.2. Air concentration results for plunging jets

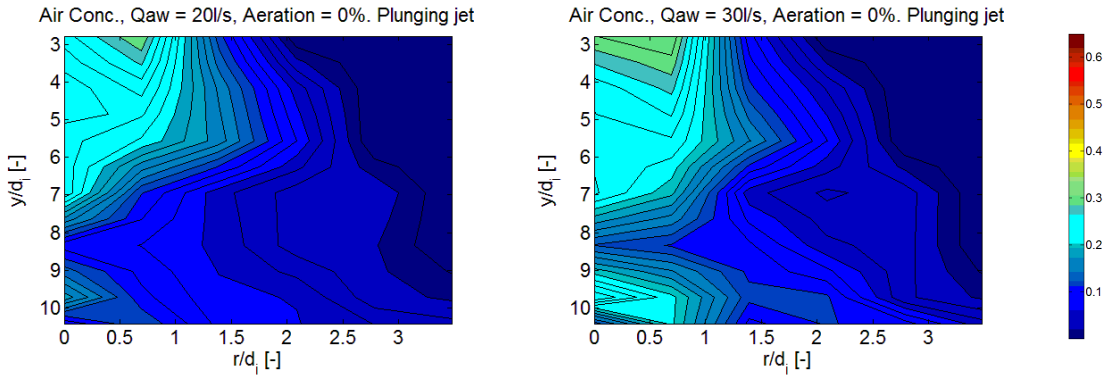

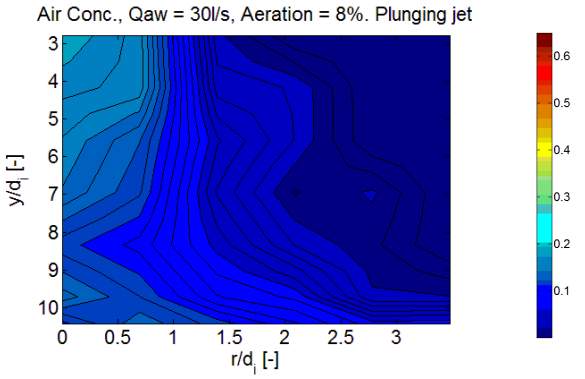

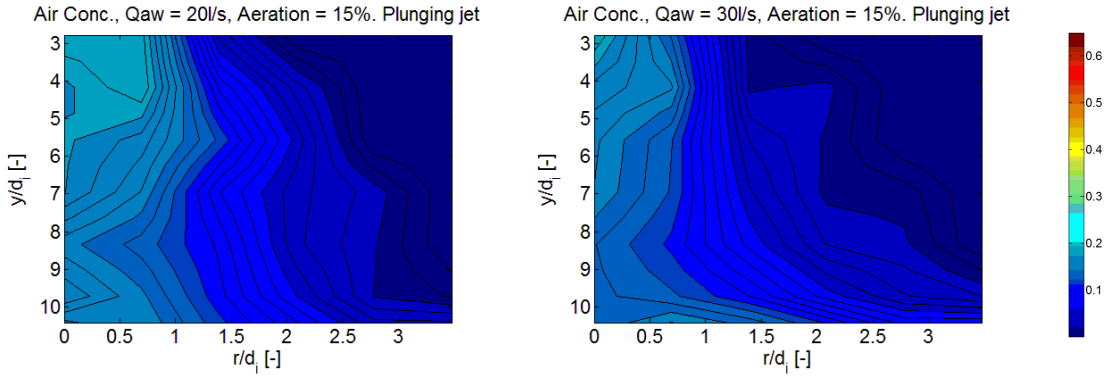

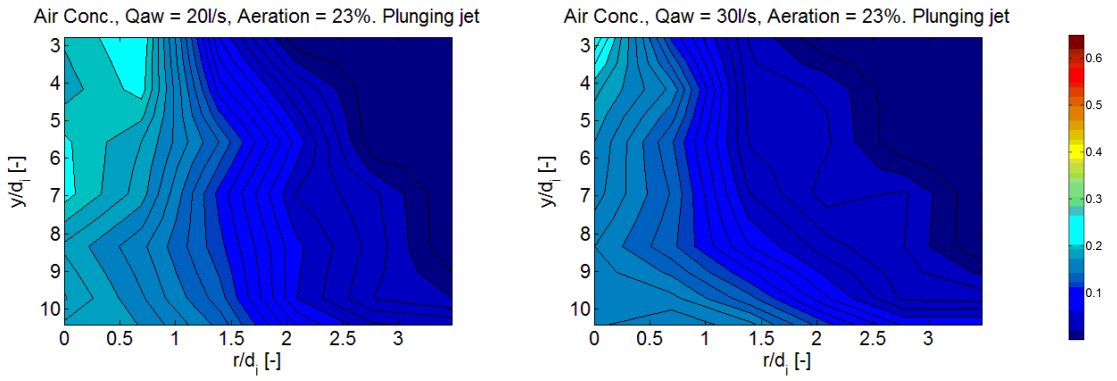

Table A1.2. Air concentration results for plunging jets (continued)

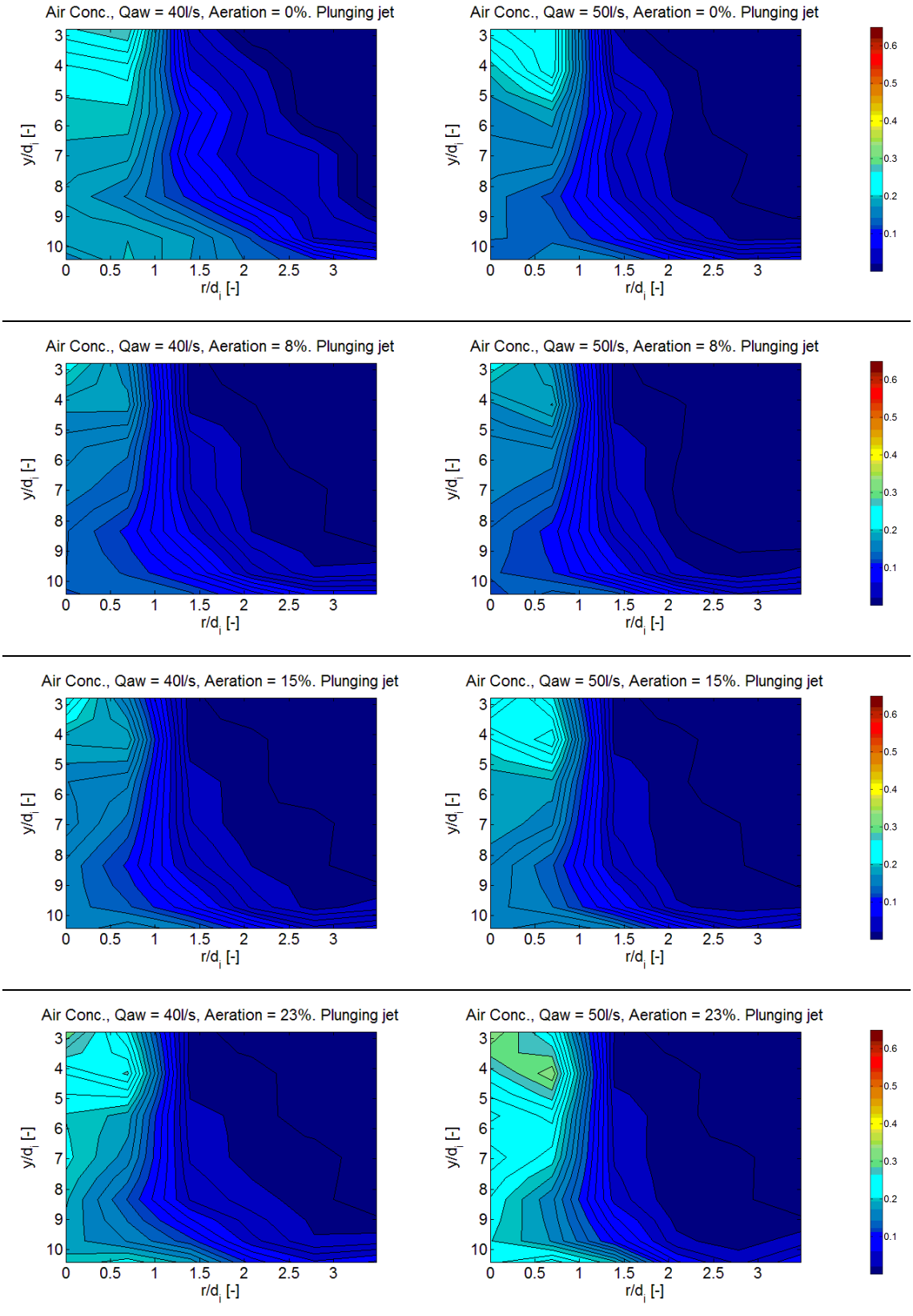

Table A1.2. Air concentration results for plunging jets (continued)

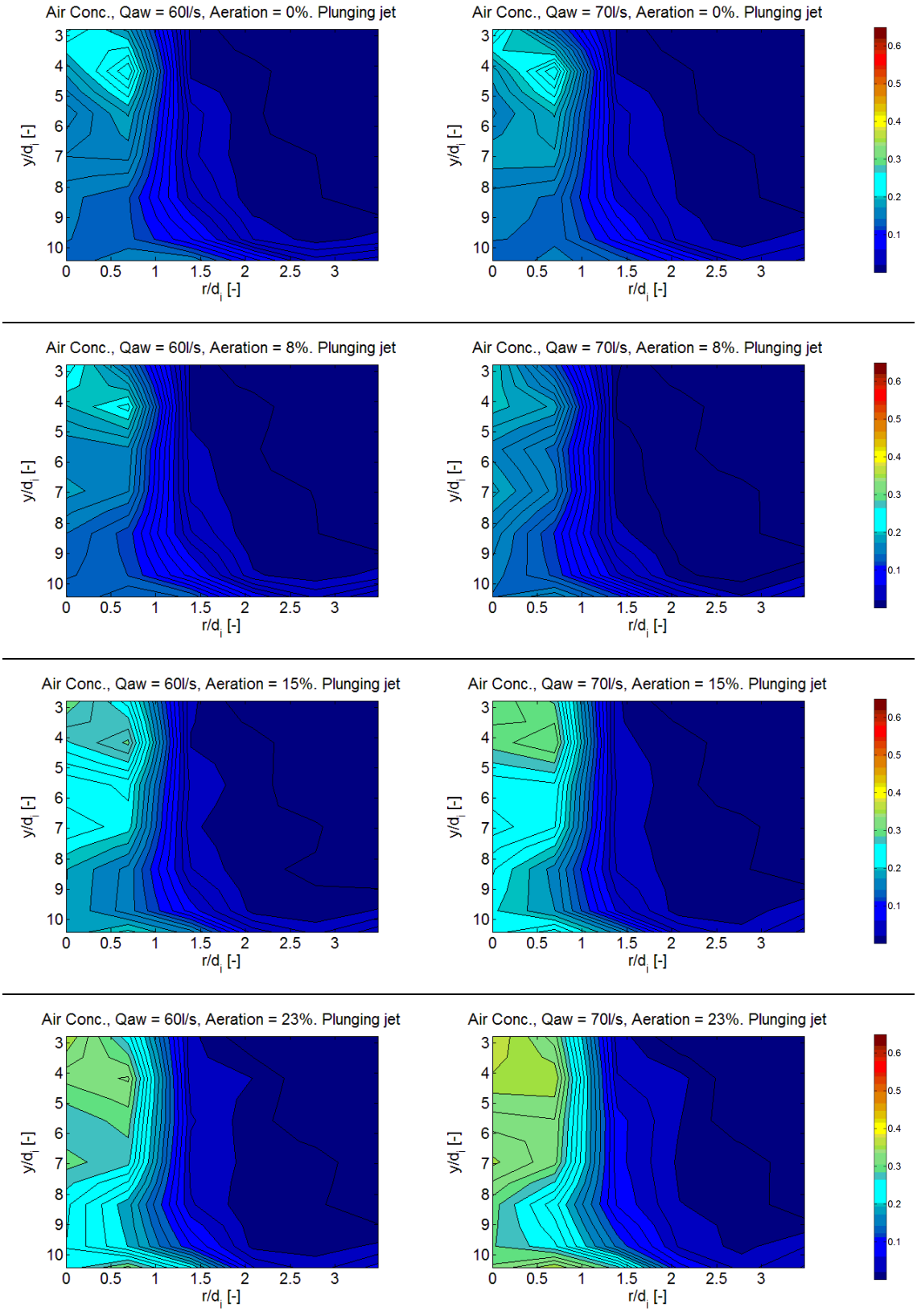

Table A1.2. Air concentration results for plunging jets (continued)

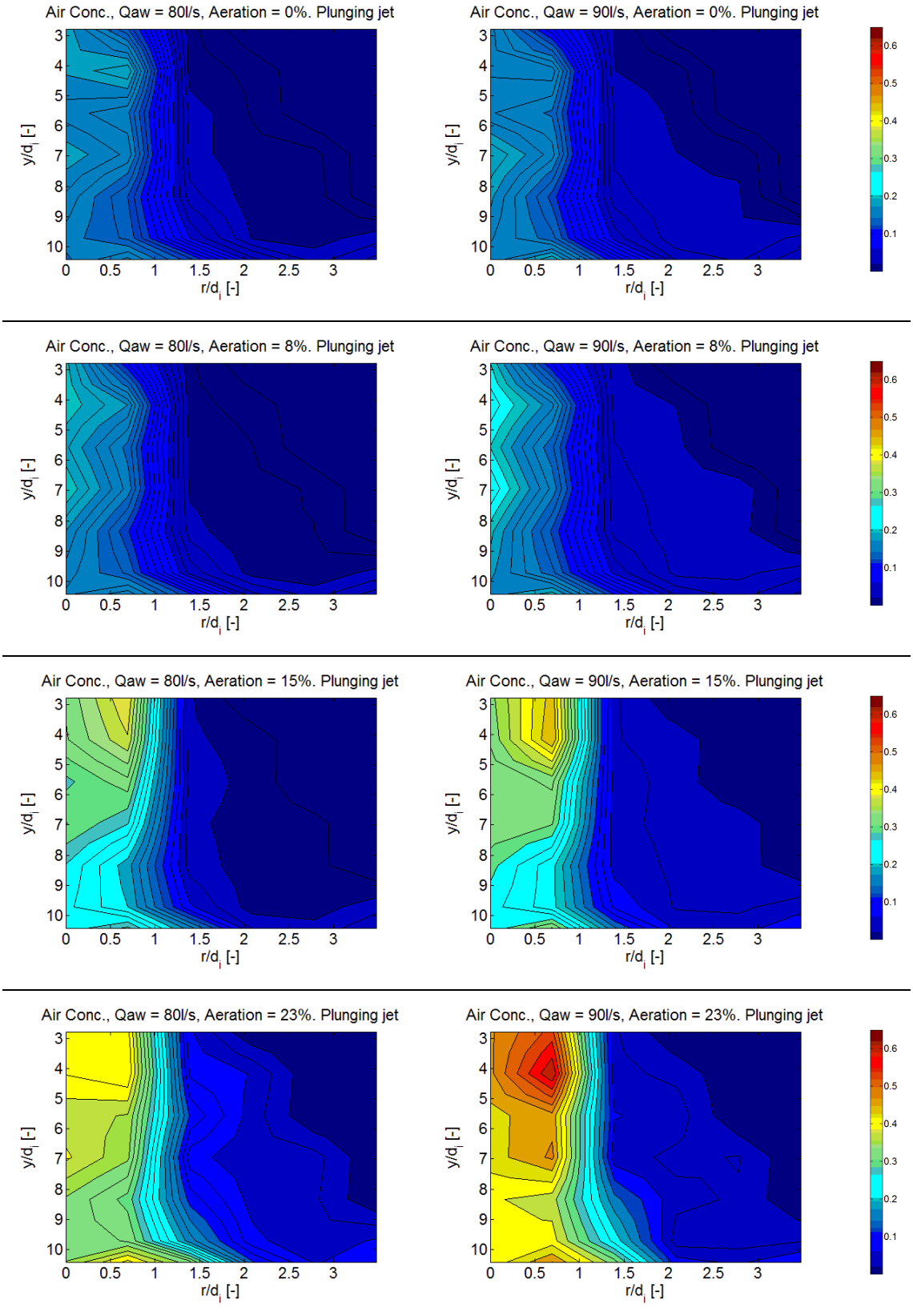

Table A1.3. Air concentration results for submerged jets

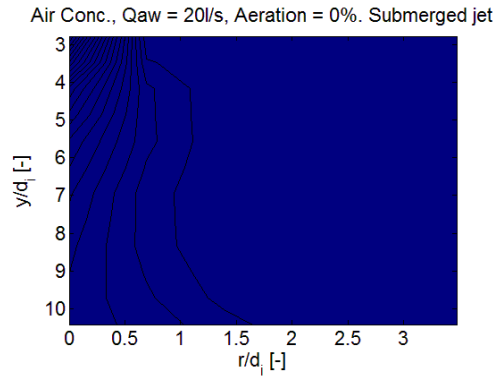

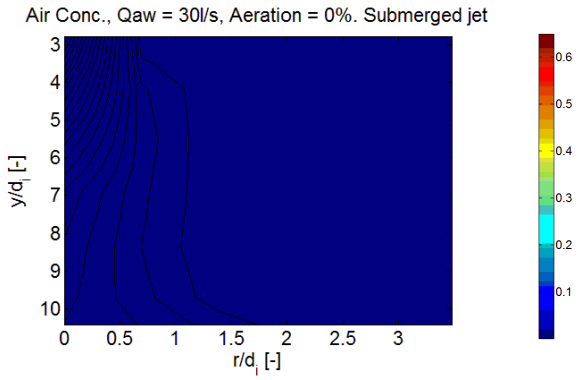

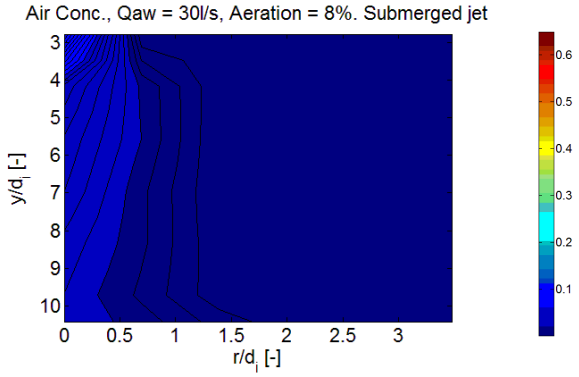

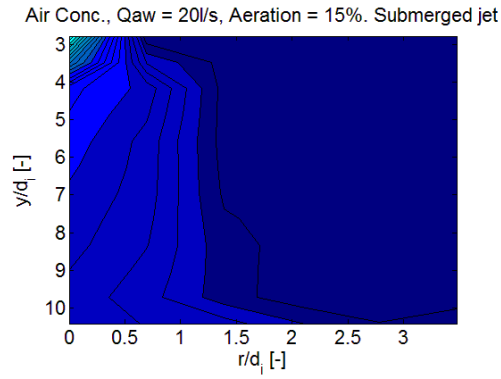

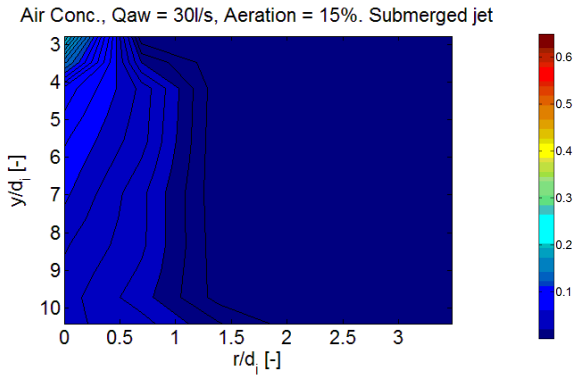

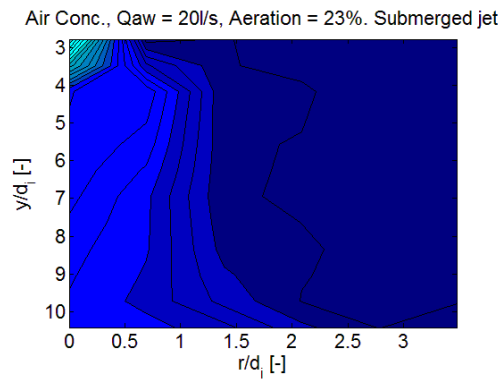

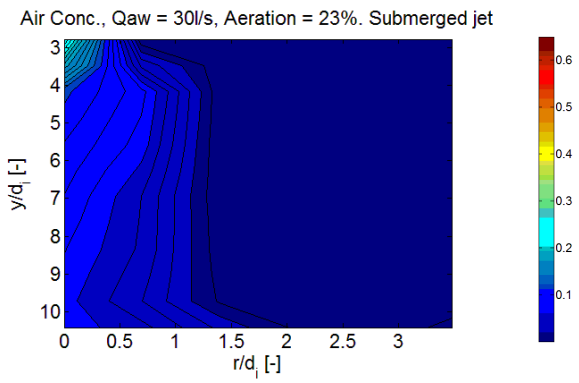

Table A1.3. Air concentration results for submerged jets (continued)

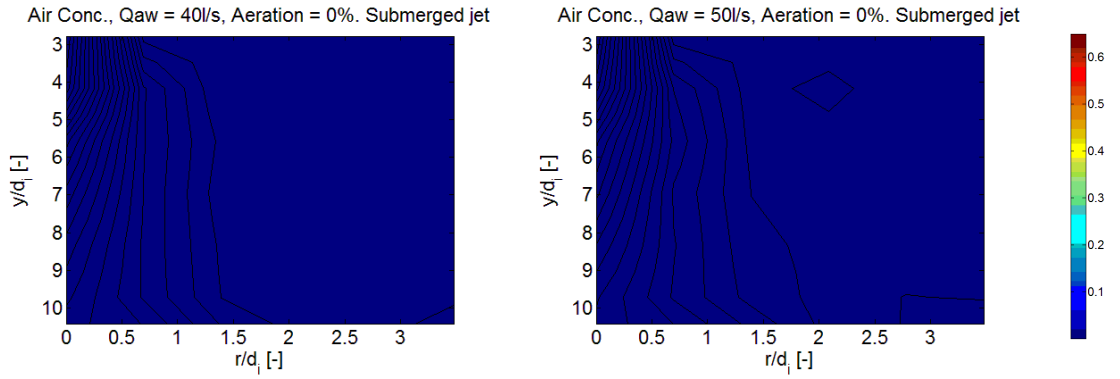

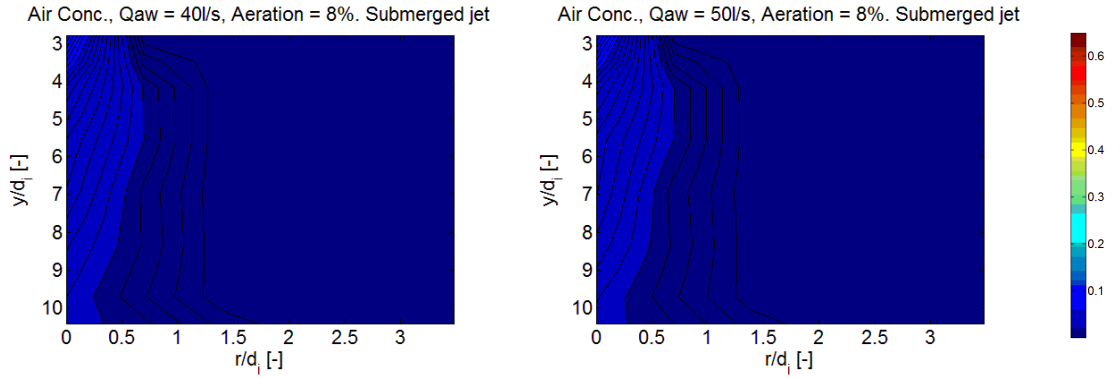

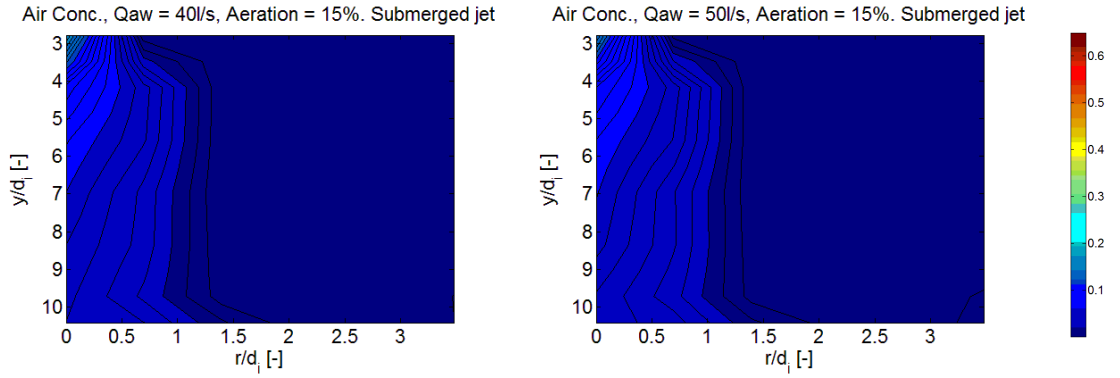

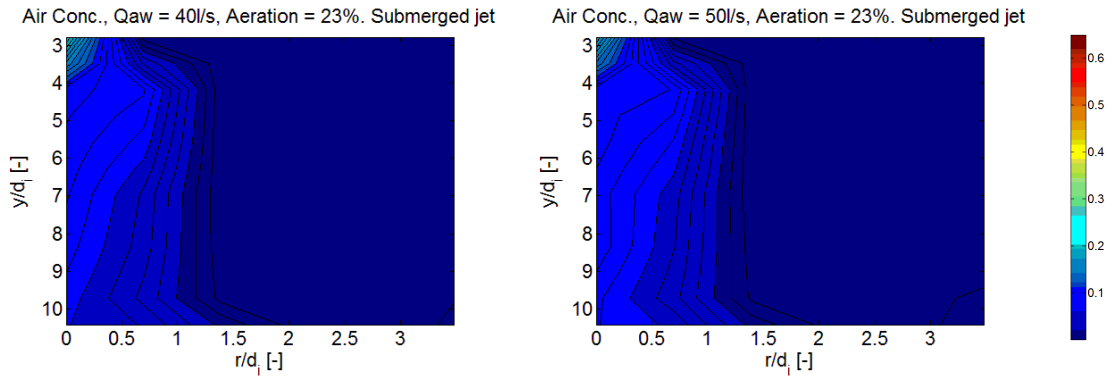

Table A1.3. Air concentration results for submerged jets (continued)

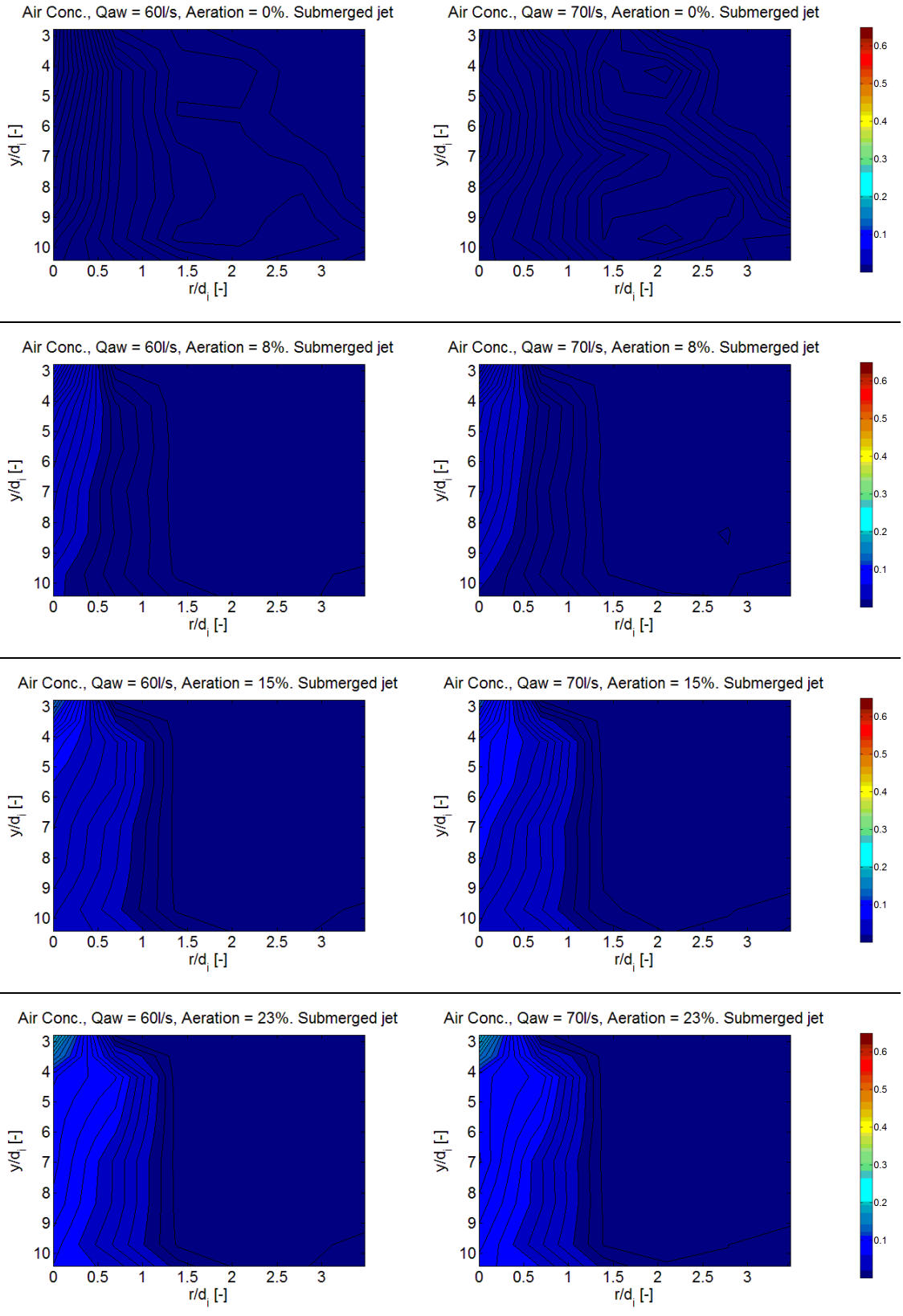

Table A1.3. Air concentration results for submerged jets (continued)

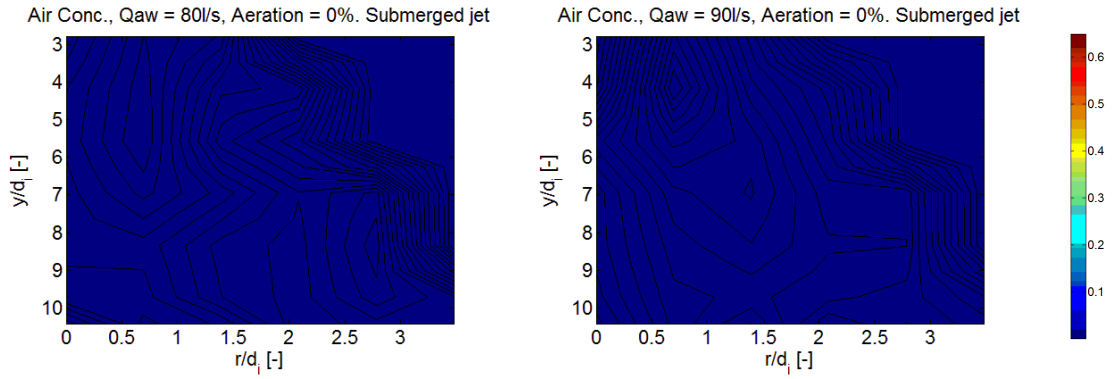

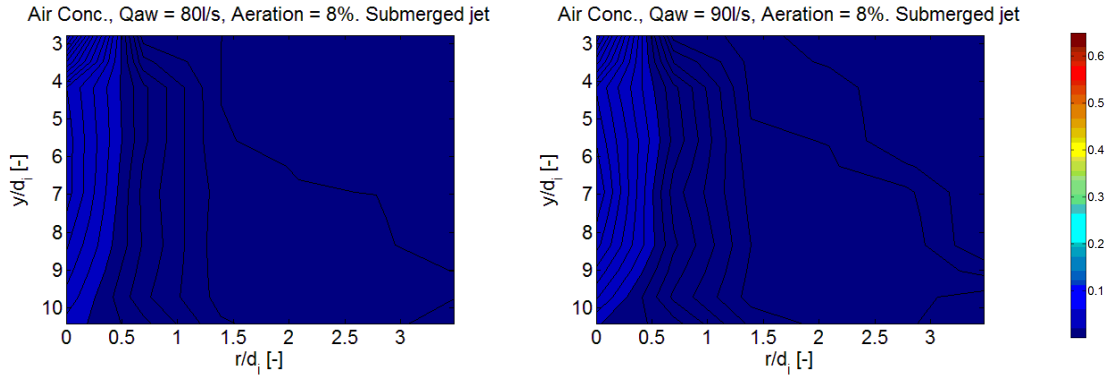

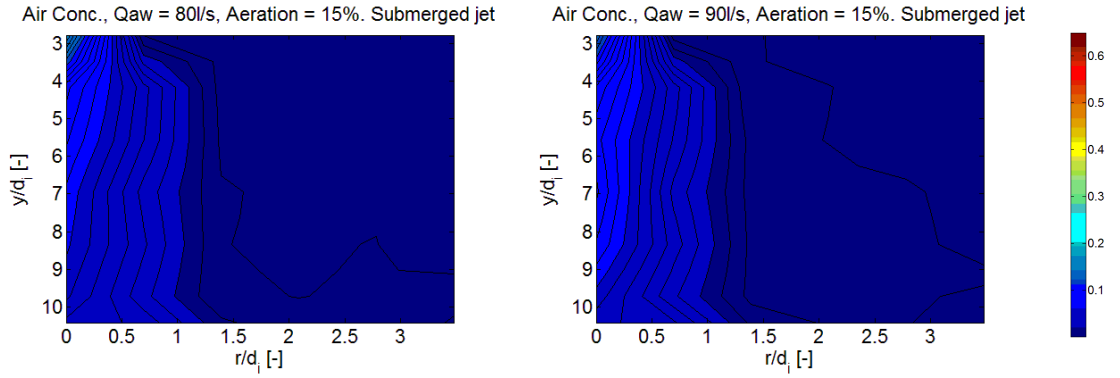

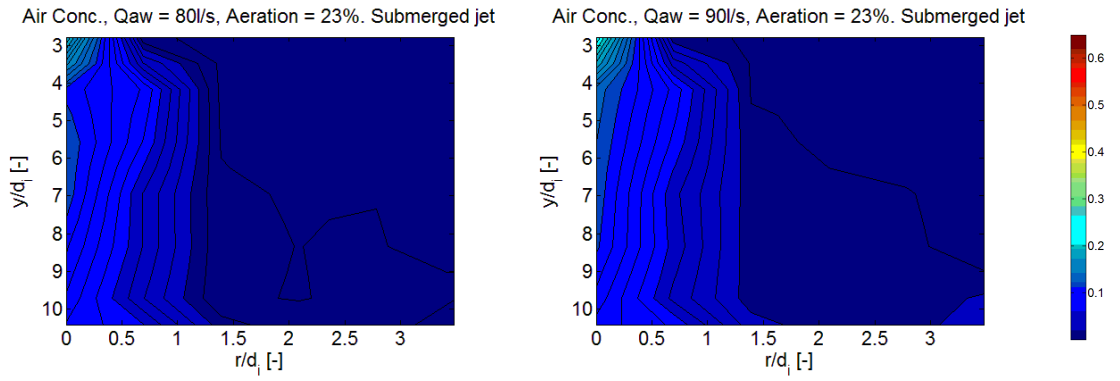

A2

Experimental results of centerline jet velocities

This appendix presents results for the jet centerline velocity in the plunge pools for all tested jet configurations with a deep pool ($Y = 0.80$ m). These configurations are shown in table A2.1.

Table A2.1. Test configurations shown in A2

Jet impact	Jet discharge [l/s]	Nozzle aeration [%]	Pool depth [m]
Plunging jets	20; 30; 40; 50; 60;70;80;90	0; 8; 15; 23	0.8
Submerged jets			

Table A2.2. Centerline velocity. (□) β_1 = 0%; (▲) β_1 = 8%: (●) β_1 = 15%; (♦) β_1 = 23%

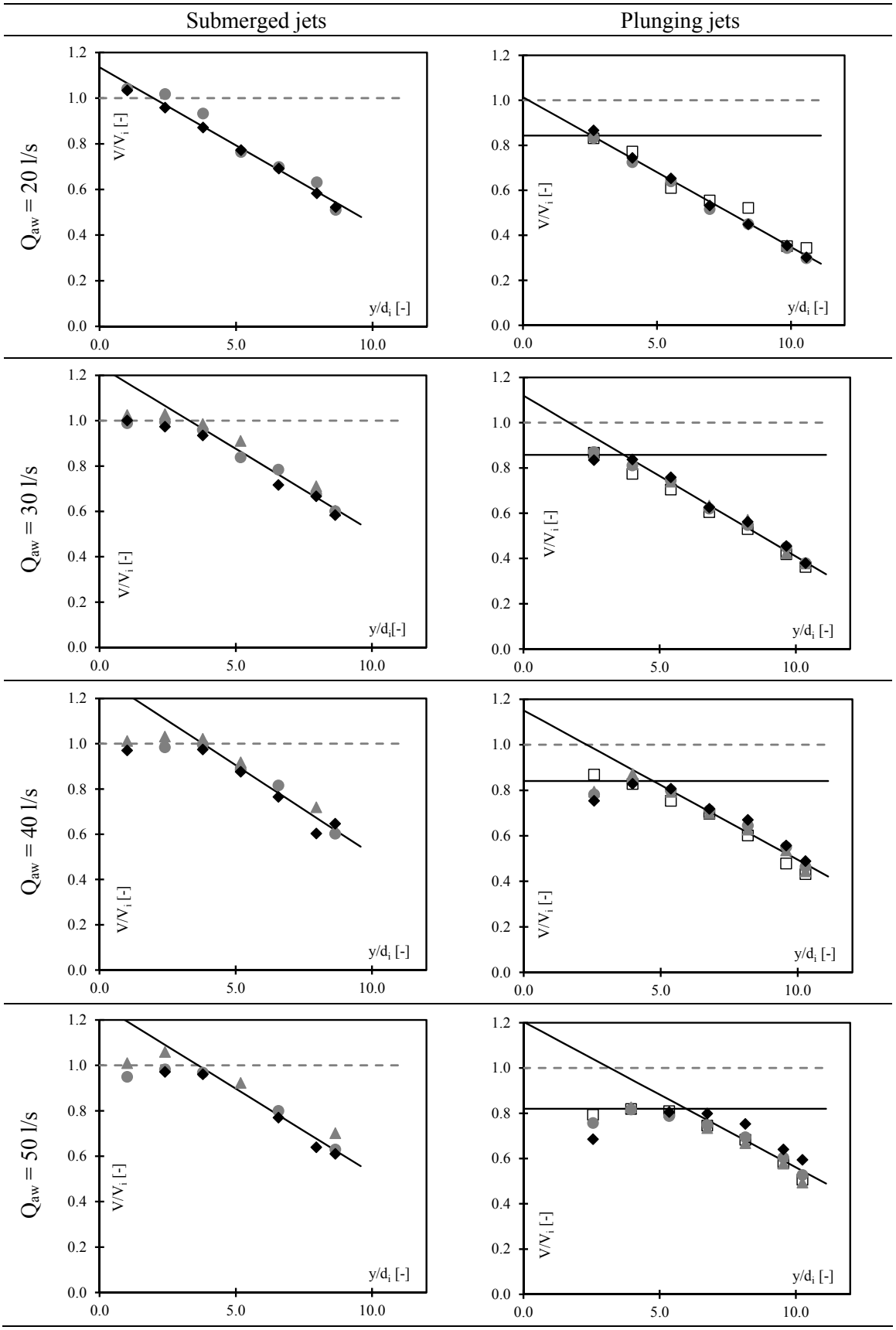

Table A2.2. Centerline velocity. (□) β_I = 0%; (▲) β_I = 8%: (●) β_I = 15%; (♦) β_I = 23% (continued)

	Submerged jets	Plunging jets
Q_{aw} = 60 l/s	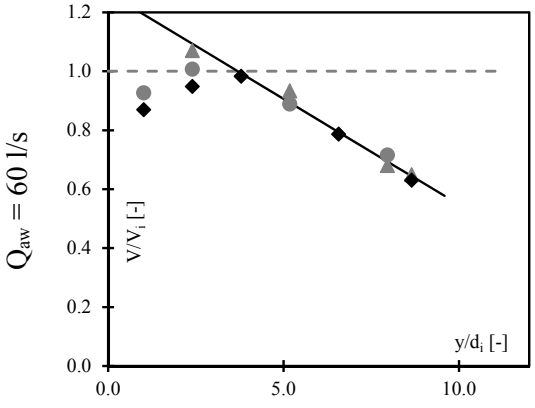	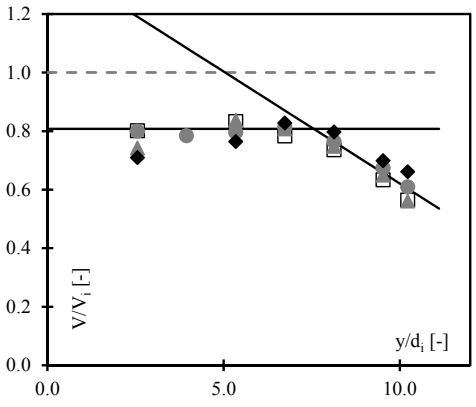
Q_{aw} = 70 l/s	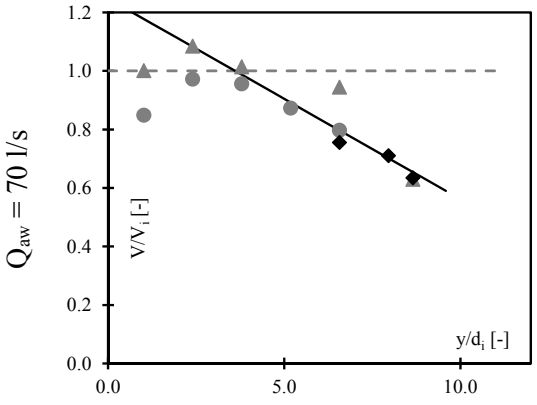	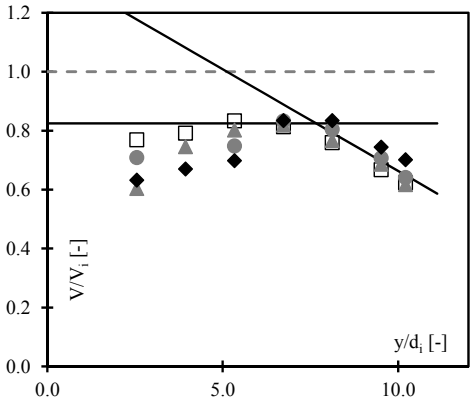
Q_{aw} = 80 l/s	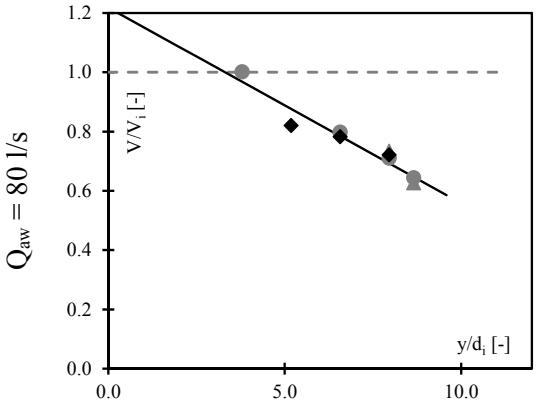	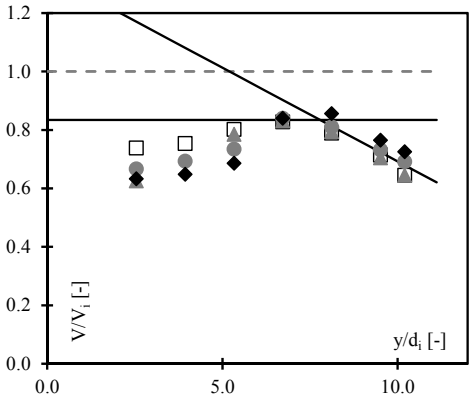
Q_{aw} = 90 l/s	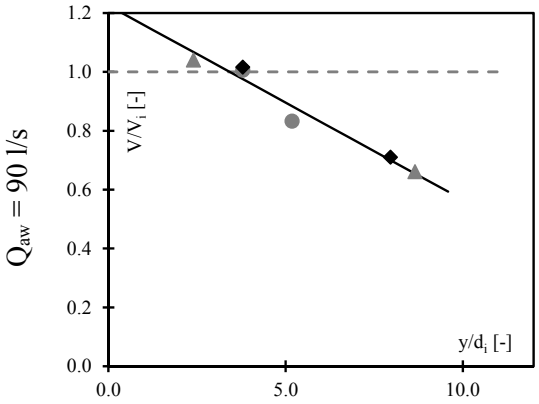	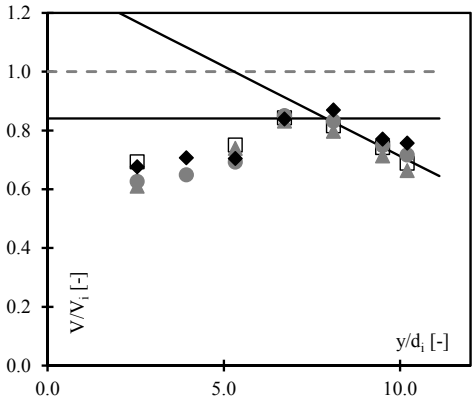

A3

Experimental results of time-averaged pressures

This appendix shows results of the absolute time-averaged pressures around the block for the configurations shown in table A3.1.

Table A3.1. Test configurations shown in A3

Jet impact	Jet discharge [l/s]	Nozzle aeration [%]	Pool depth [m]	Block movement
Plunging jets	40; 60; 80	0; 8; 15; 23	0.8; 0.3	fixed; free
Submerged jets			0.8	fixed

Table A3.2. Time-averaged pressures around the block for selected configurations

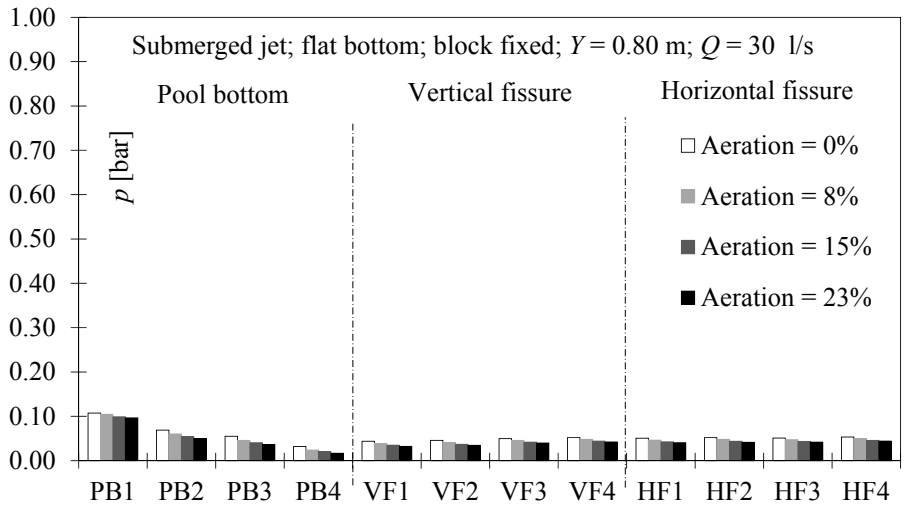

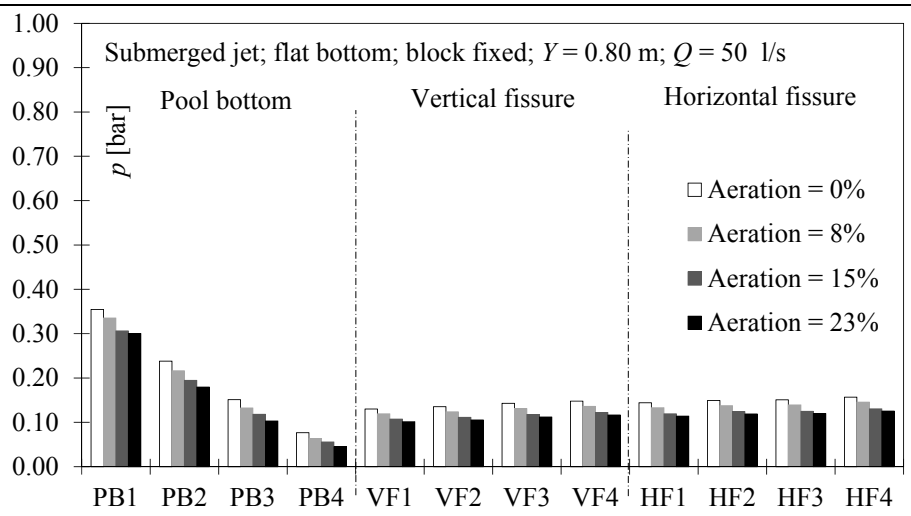

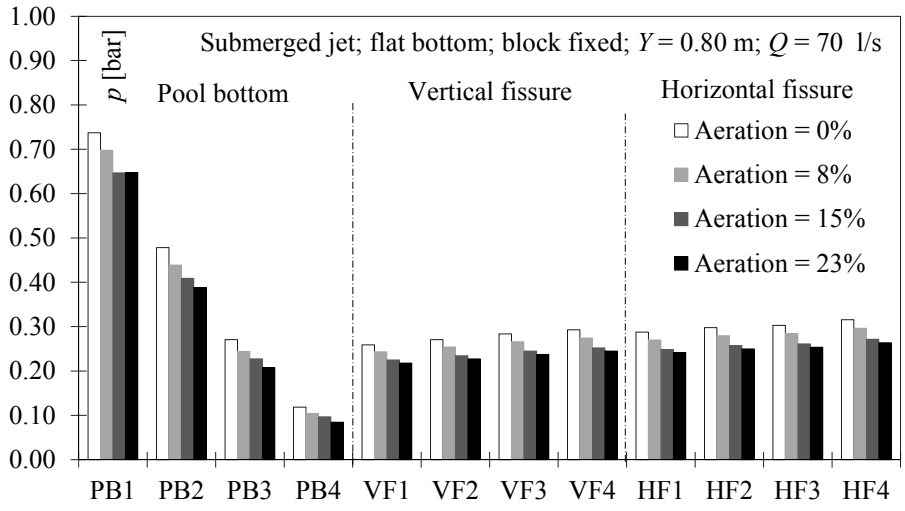

Table A3.2. Time-averaged pressures around the block for selected configurations (continued)

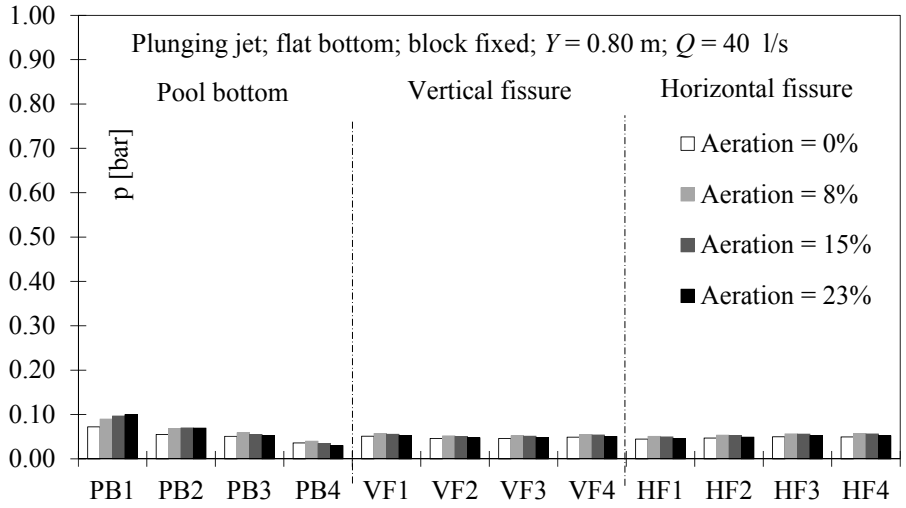

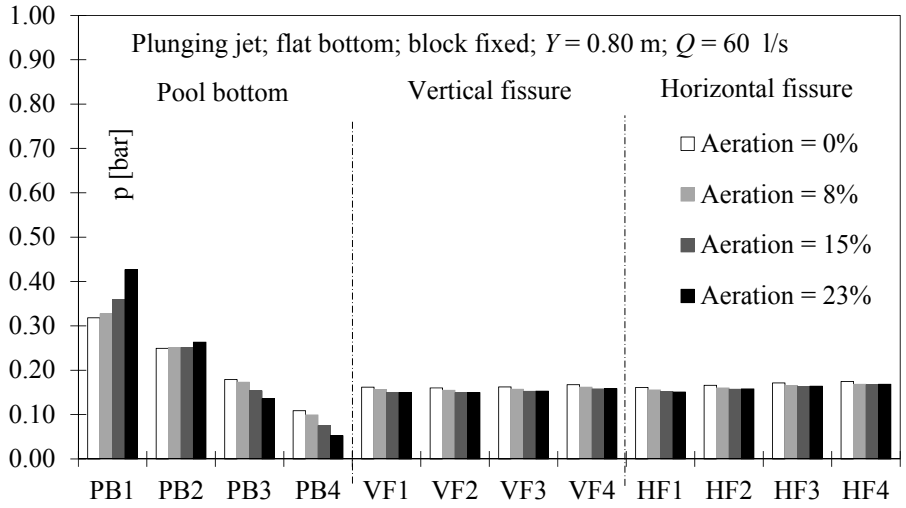

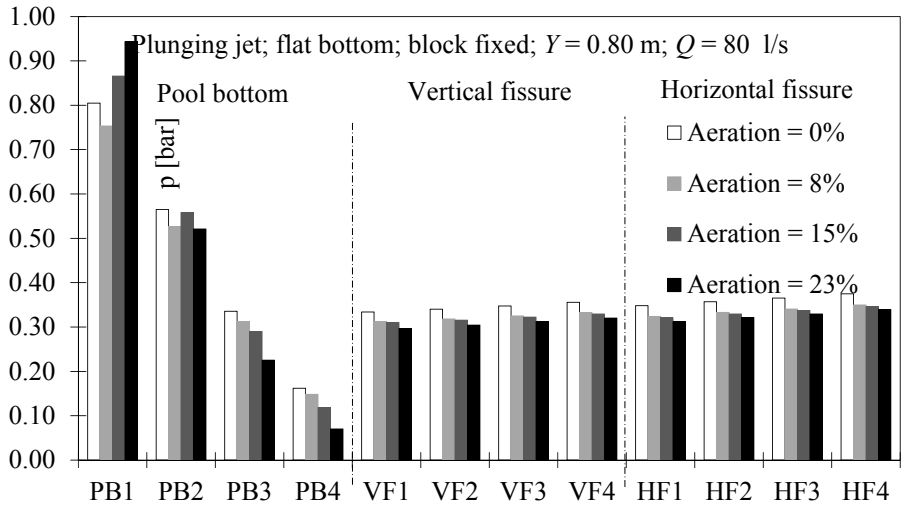

Table A3.2. Time-averaged pressures around the block for selected configurations (continued)

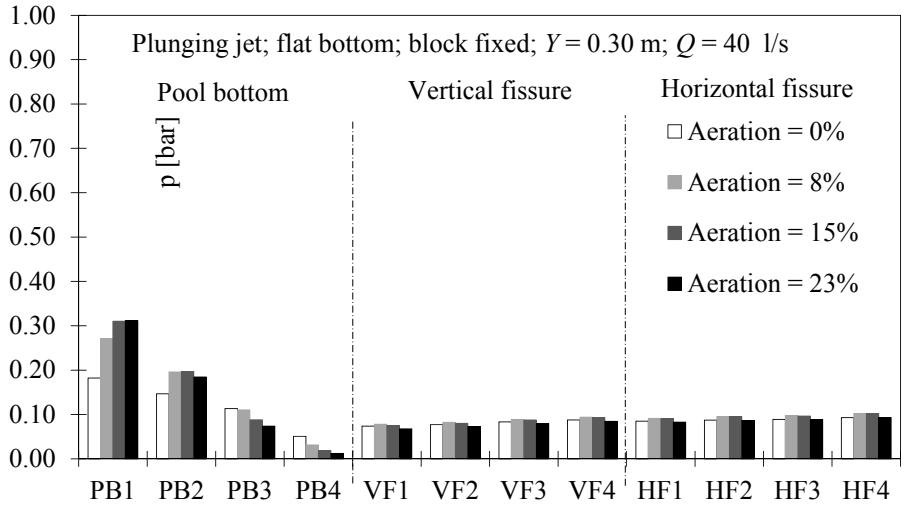

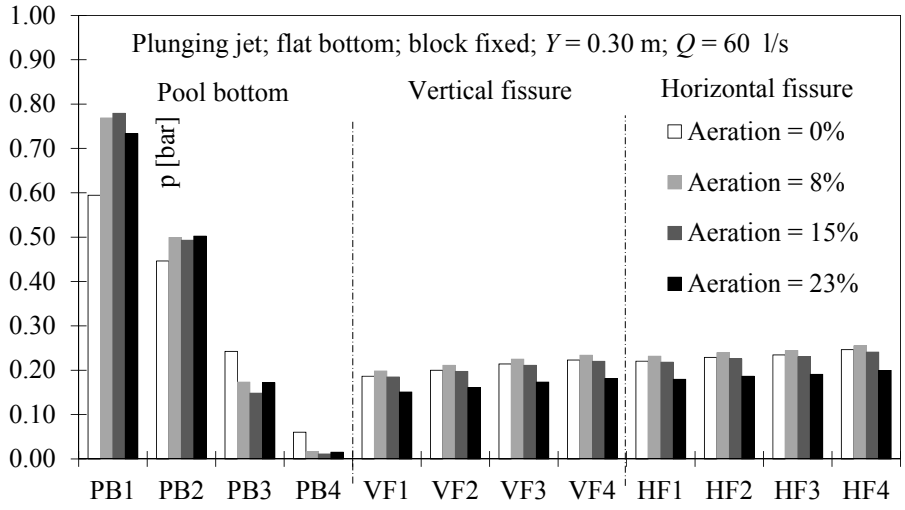

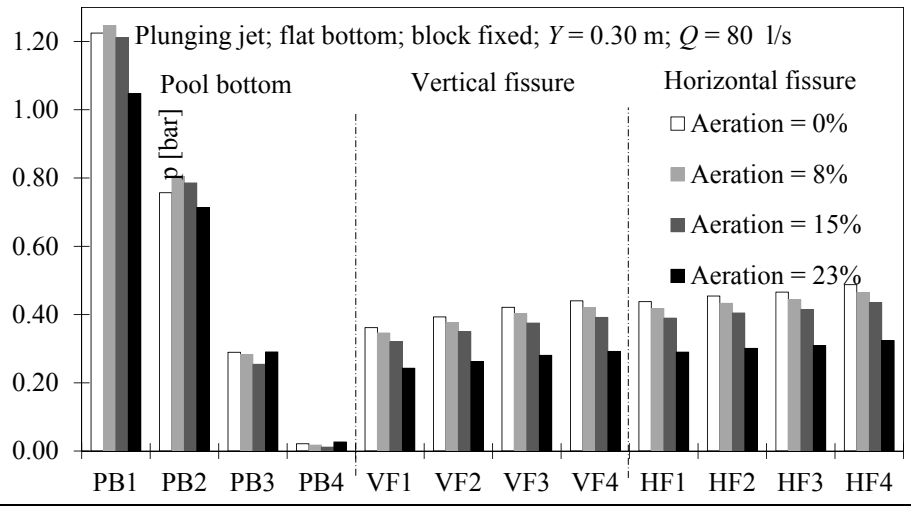

Table A3.2. Time-averaged pressures around the block for selected configurations (continued)

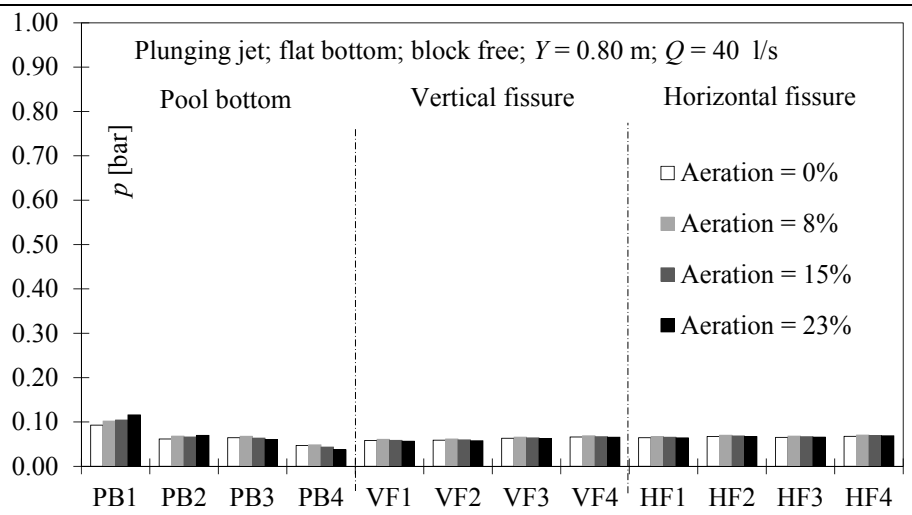

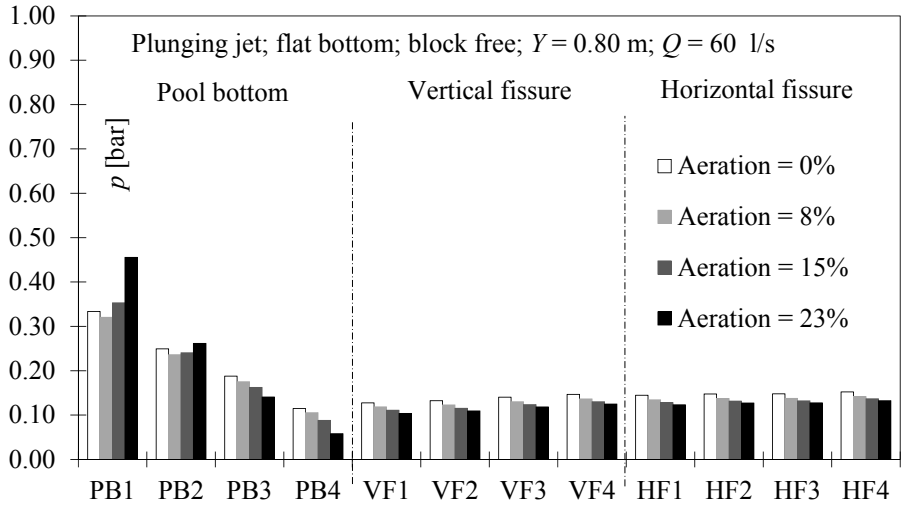

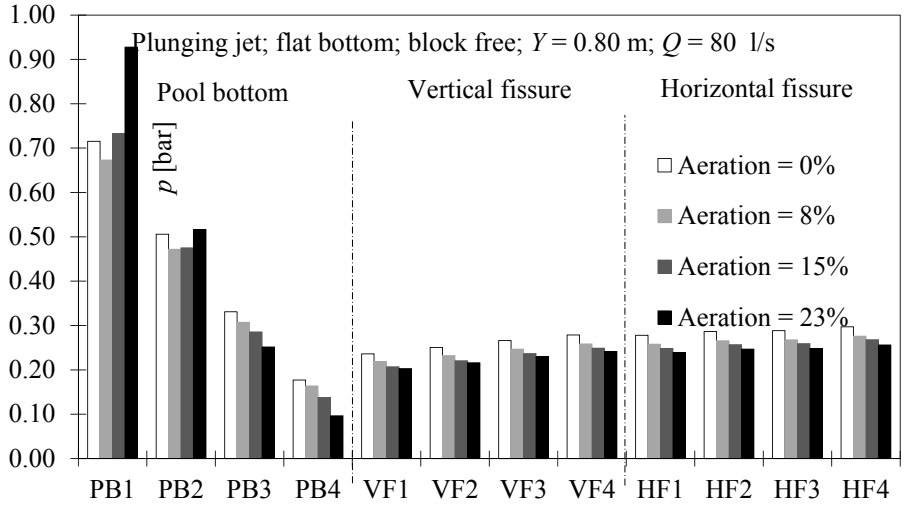

Table A3.2. Time-averaged pressures around the block for selected configurations (continued)

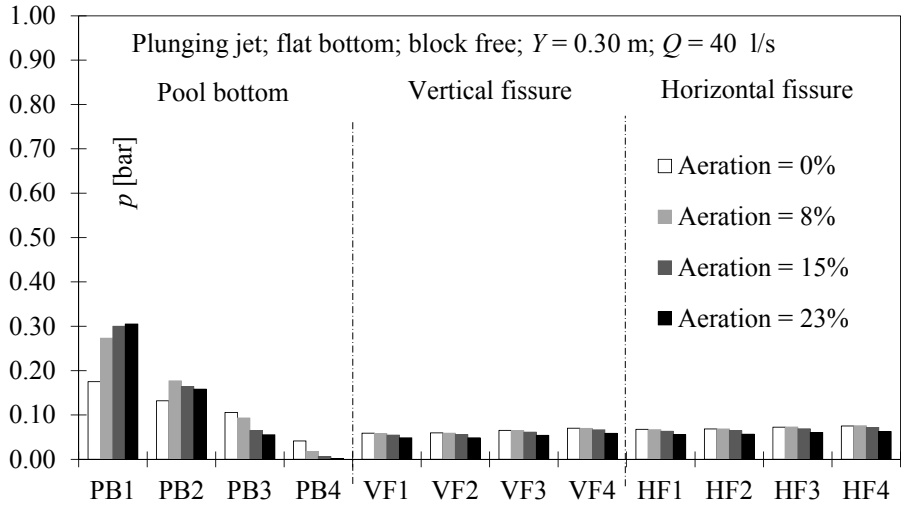

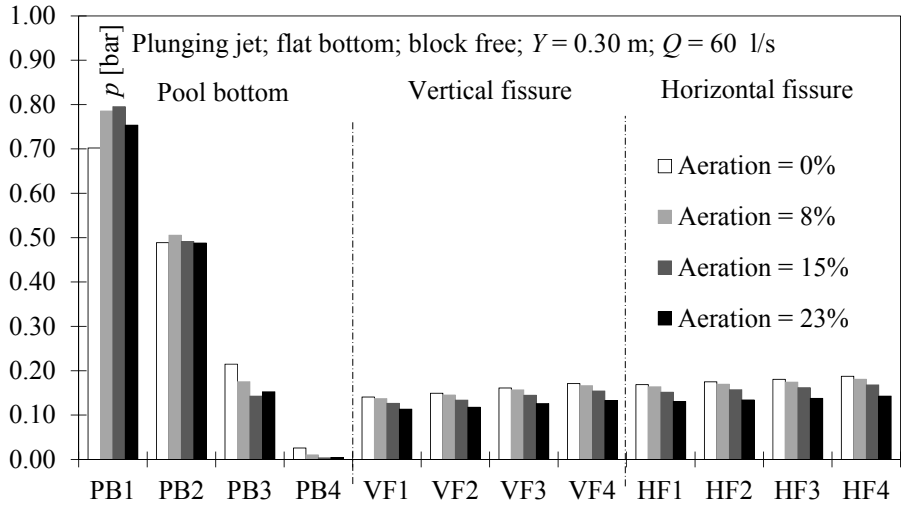

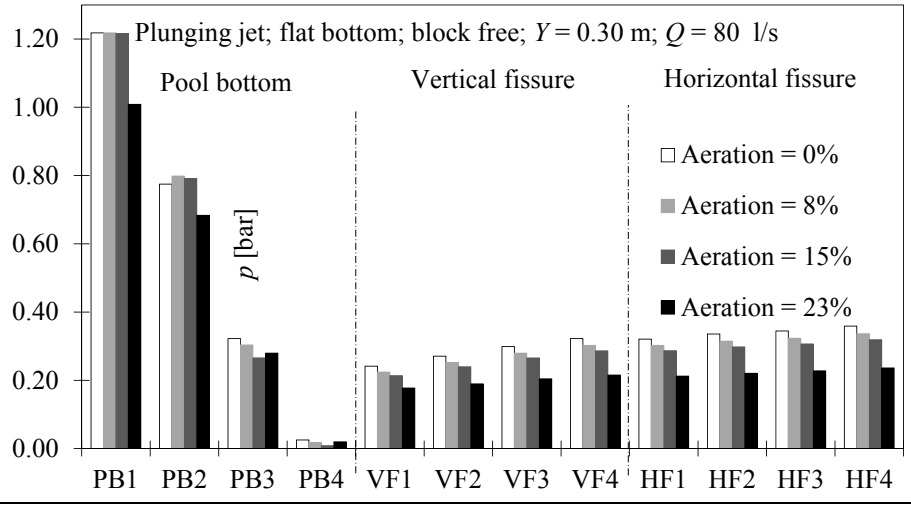

A4

Experimental results of pressure fluctuations

This appendix shows results of the absolute RMS value of the pressure fluctuations around the block for the configurations shown in table A4.1.

Table A4.1. Test configurations shown in A4

Jet impact	Jet discharge [l/s]	Nozzle aeration [%]	Pool depth [m]	Block movement
Plunging jets	40; 60; 80	0; 8; 15; 23	0.8; 0.3	fixed; free
Submerged jets			0.8	fixed

Table A4.2. Pressures fluctuations around the block for selected configurations

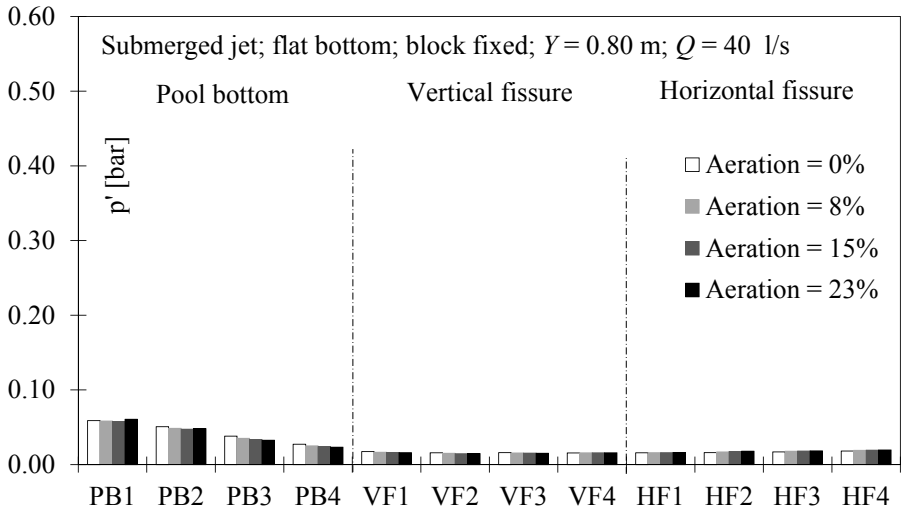

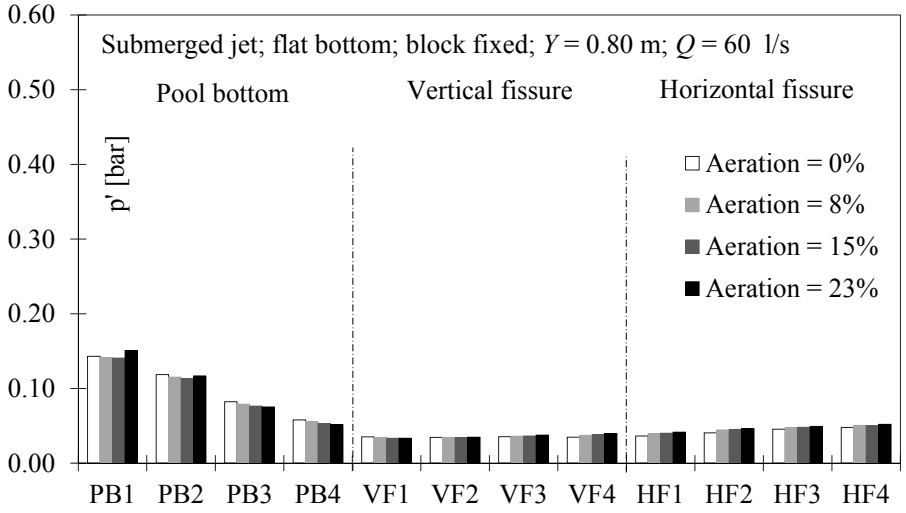

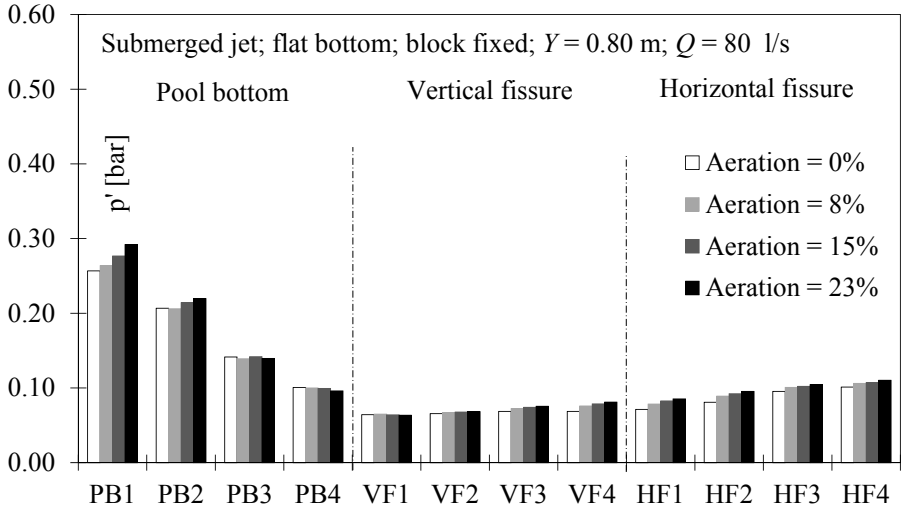

Table A4.2. Pressures fluctuations around the block for selected configurations (continued)

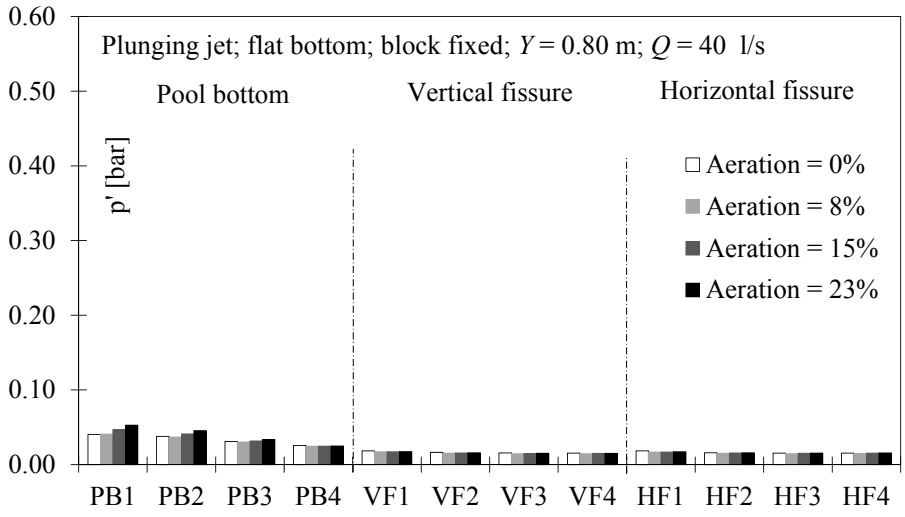

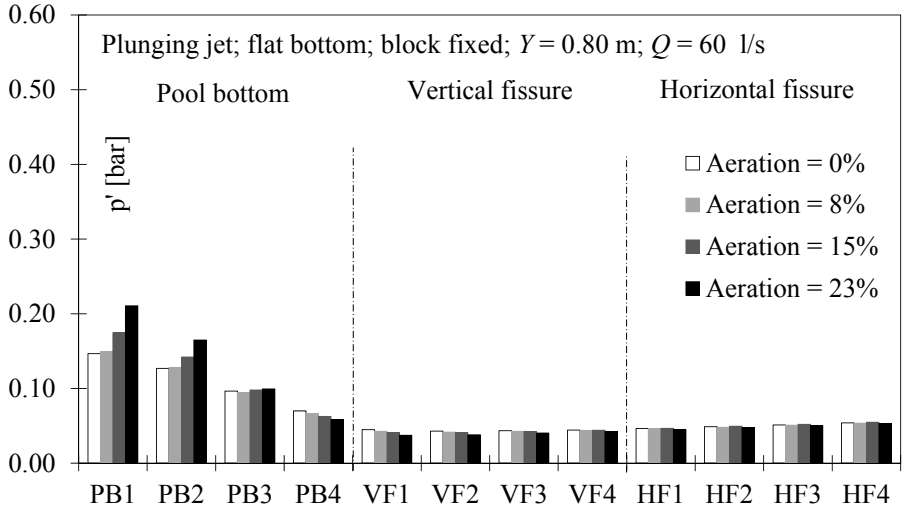

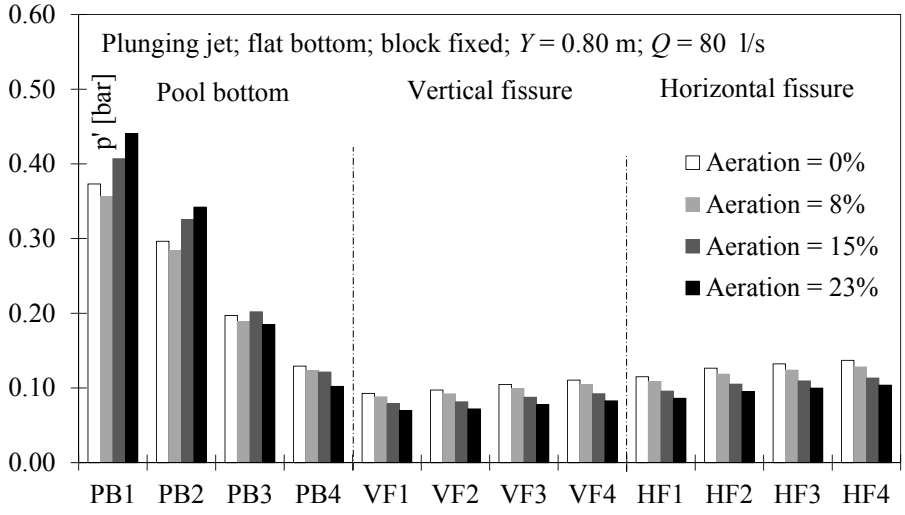

Table A4.2. Pressures fluctuations around the block for selected configurations (continued)

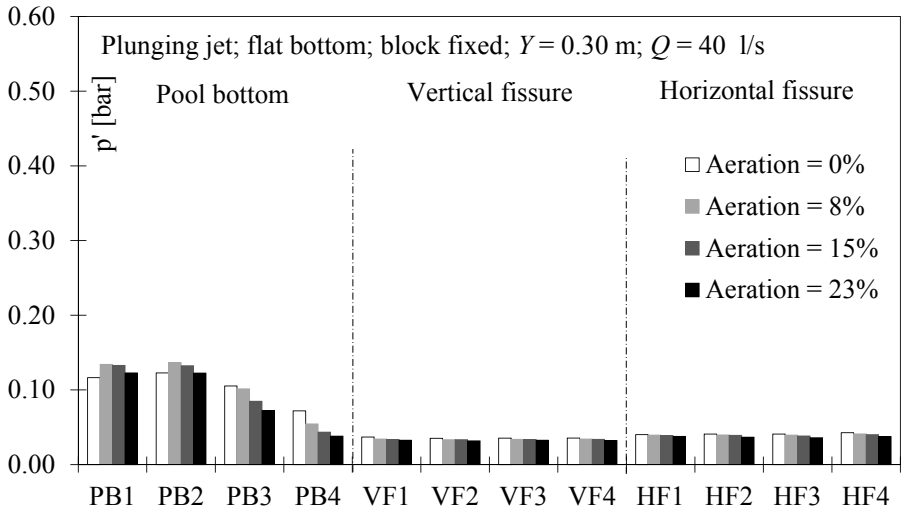

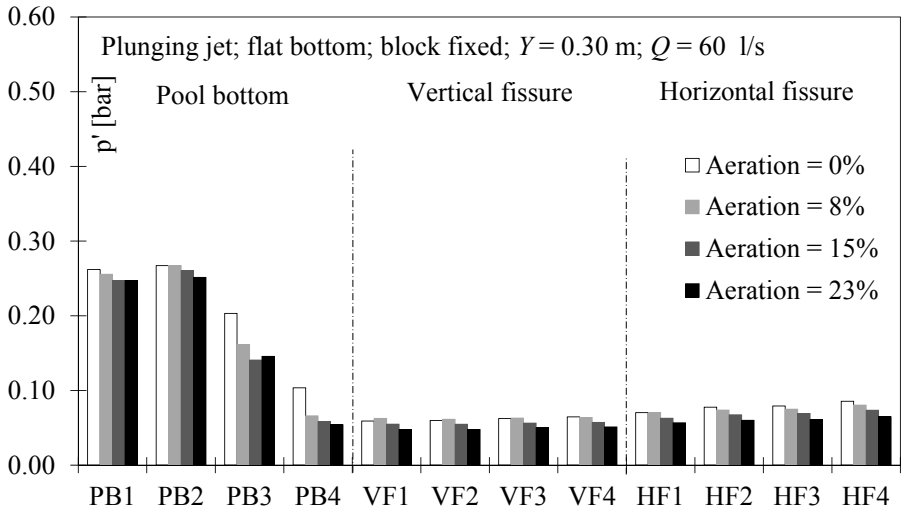

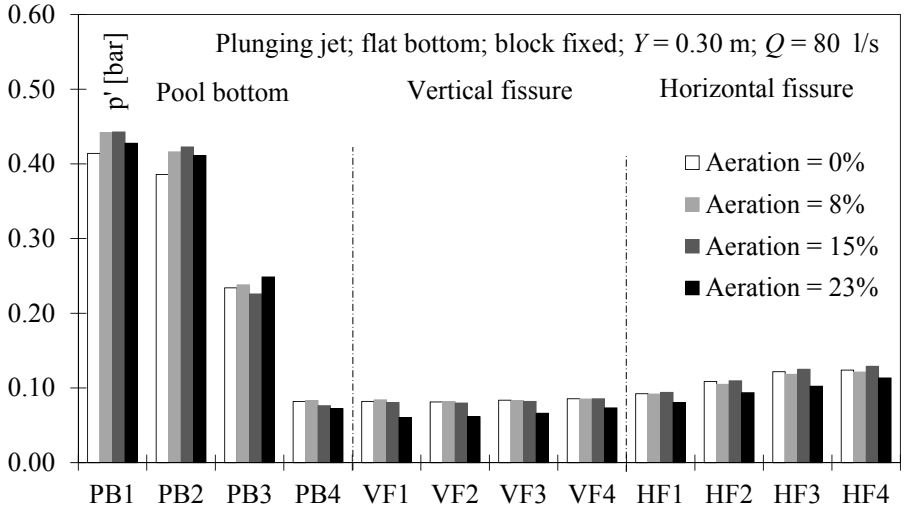

Table A4.2. Pressures fluctuations around the block for selected configurations (continued)

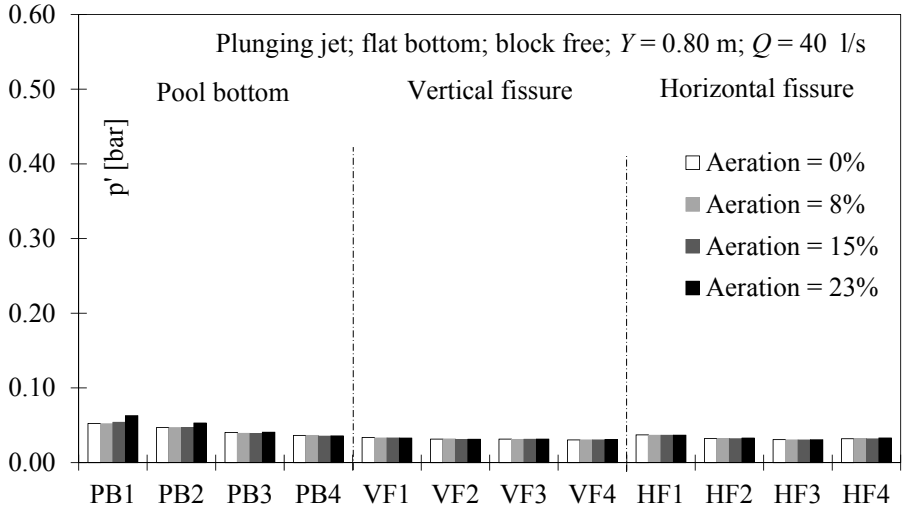

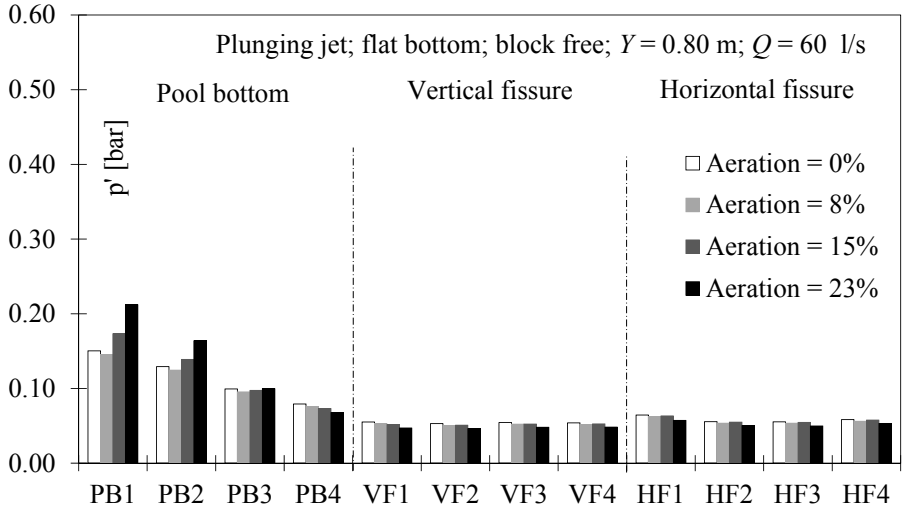

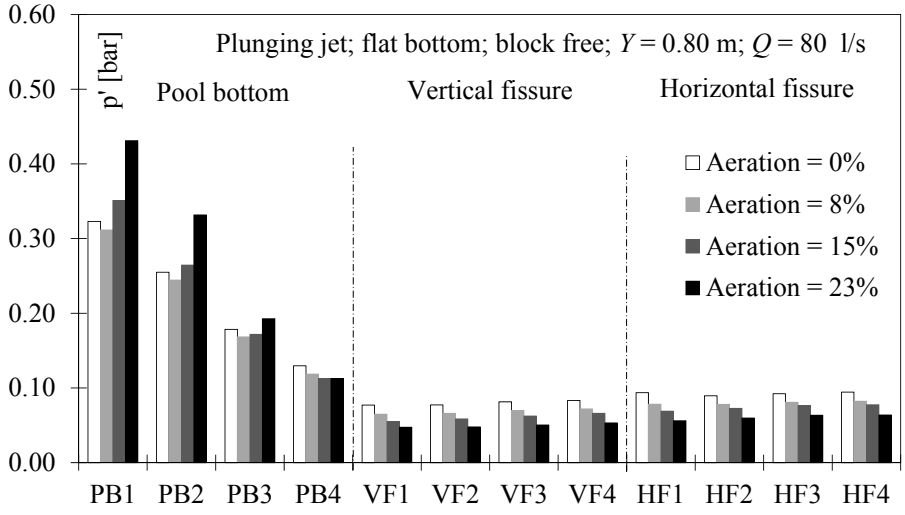

Table A4.2. Pressures fluctuations around the block for selected configurations (continued)

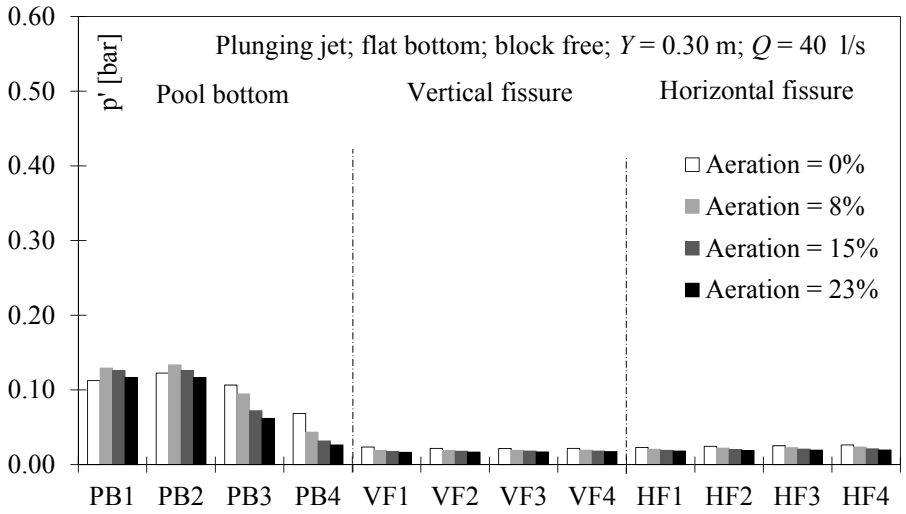

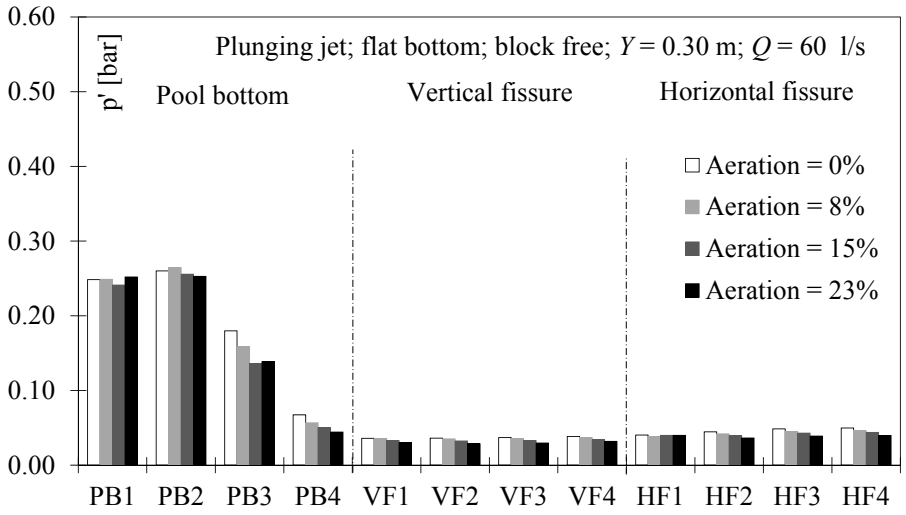

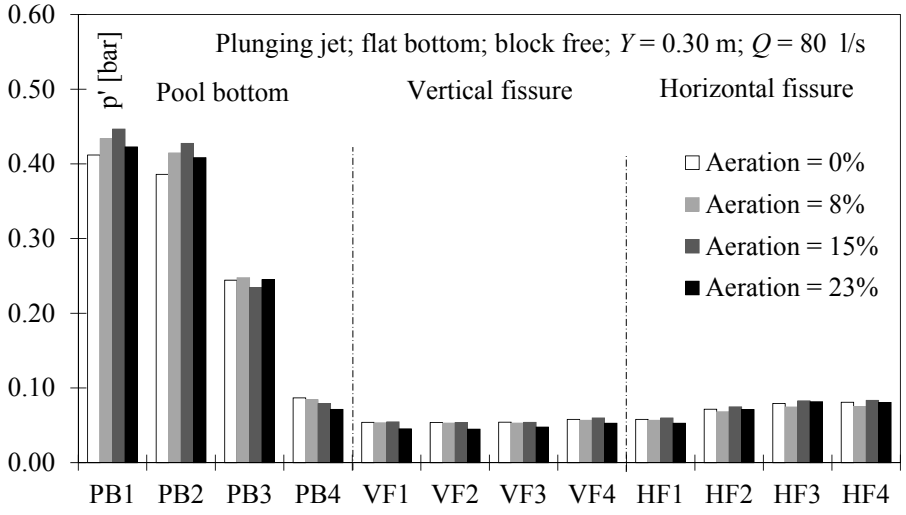

A5

Frequency analysis results

This appendix shows results of the Power Spectral Densities around the block for the configurations shown in table A5.1.

Table A5.1. Test configurations shown in A5

Jet impact	Jet discharge [l/s]	Nozzle aeration [%]	Pool depth [m]	Block movement
Plunging jets	40; 60; 80	0; 23	0.8	fixed; free
Submerged jets				fixed

Table A5.2. Power Spectral Densities around the block for selected configurations

Submerged jet; flat bottom; fixed block; Q = 40 l/s; Y = 0.80 m

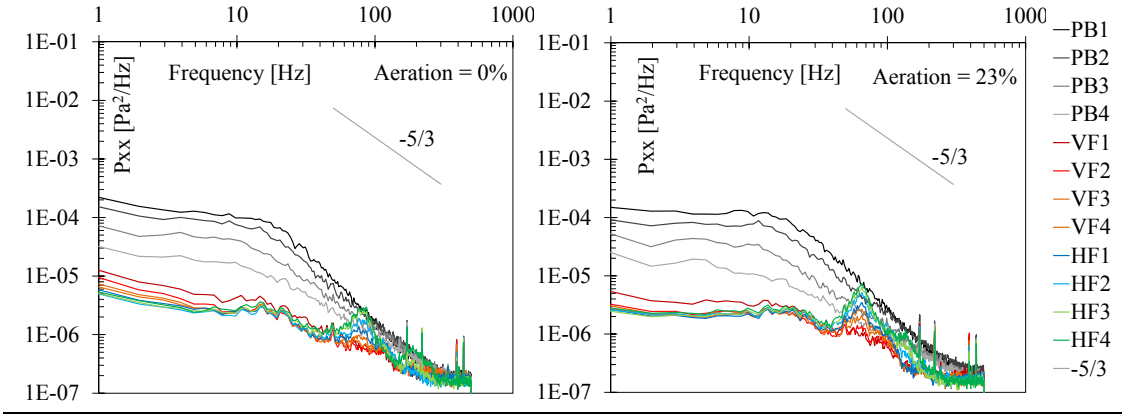

Submerged jet; flat bottom; fixed block; Q = 60 l/s; Y = 0.80 m

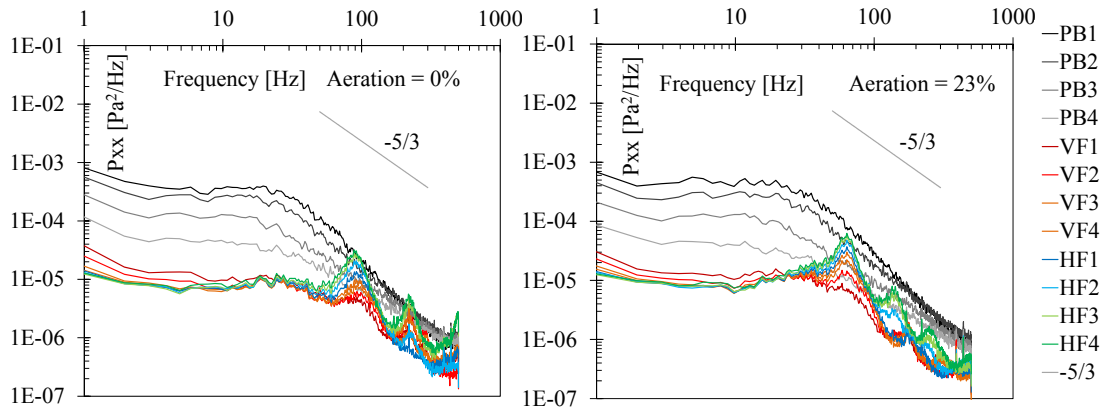

Submerged jet; flat bottom; fixed block; Q = 80 l/s; Y = 0.80 m

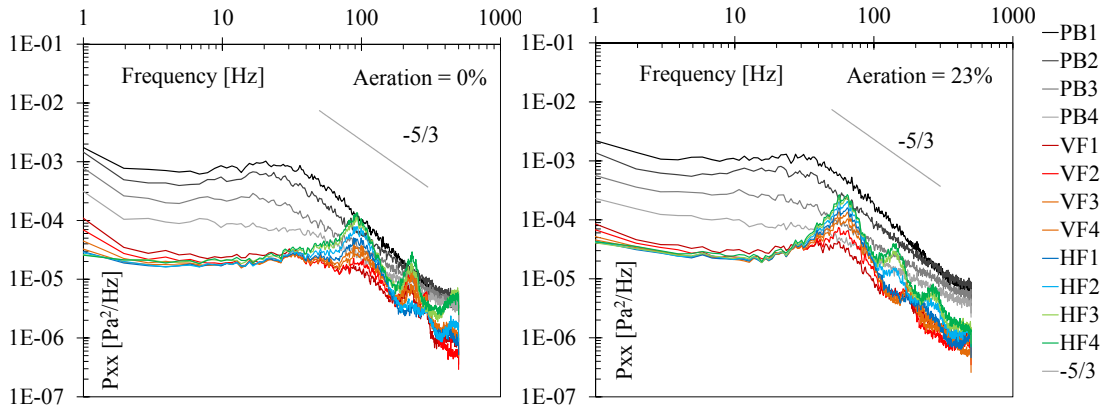

Table A5.2. Power Spectral Densities around the block for selected configurations (continued)

Plunging jet; flat bottom; fixed block; Q = 40 l/s; Y = 0.80 m

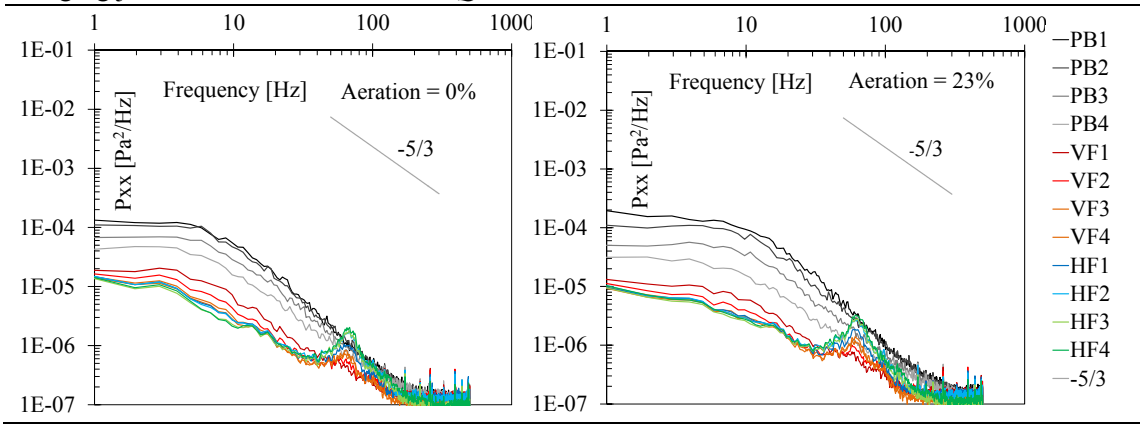

Plunging jet; flat bottom; fixed block; Q = 60 l/s; Y = 0.80 m

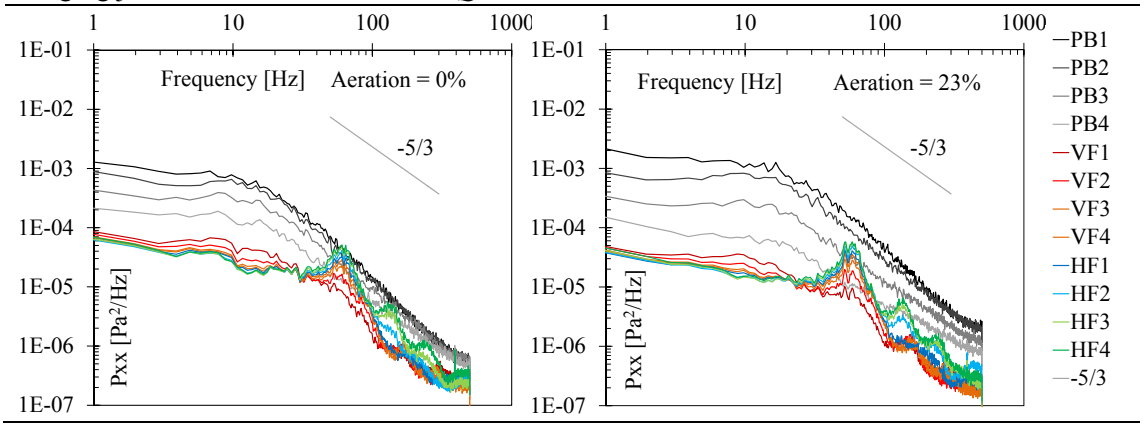

Plunging jet; flat bottom; fixed block; Q = 80 l/s; Y = 0.80 m

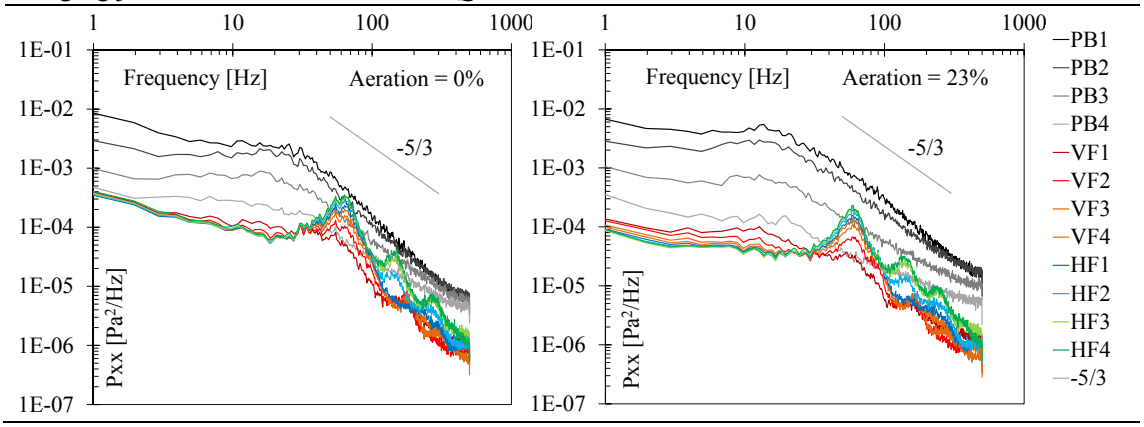

Table A5.2. Power Spectral Densities around the block for selected configurations (continued)

Plunging jet; flat bottom; free block; Q = 40 l/s; Y = 0.80 m

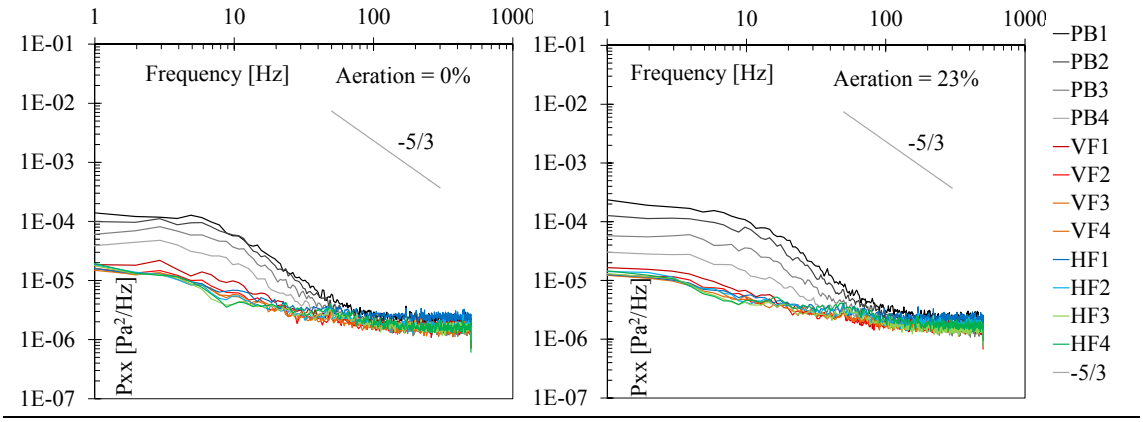

Plunging jet; flat bottom; free block; Q = 60 l/s; Y = 0.80 m

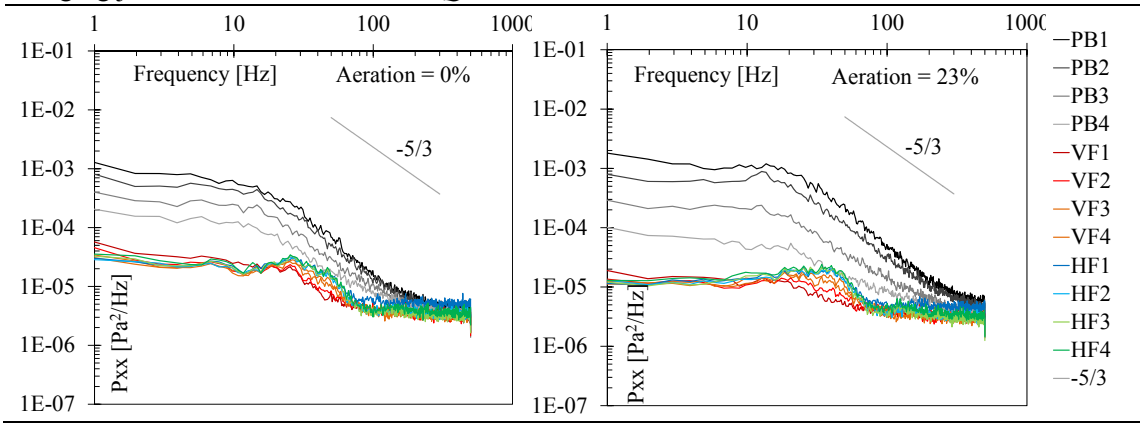

Plunging jet; flat bottom; free block; Q = 80 l/s; Y = 0.80 m

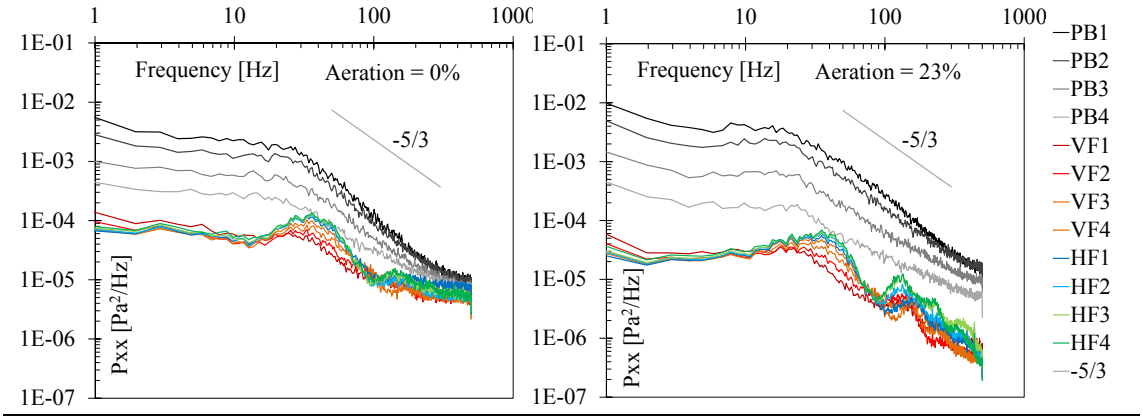

Communications du Laboratoire de Constructions Hydrauliques ISSN 1661-1179
Ecole Polytechnique Fédérale de Lausanne
Editeur: Prof. Dr A. Schleiss

N° 46 2011 M. Leite Ribeiro
Influence of tributary widening on confluence morphodynamics

N° 47 2011 M. Federspiel
Response of an embedded block impacted by high-velocity jets

N° 48 2011 J. García Hernández
Flood management in a complex river basin with a real-time decision support system based on hydrological forecasts

N° 49 2011 F. Hachem
Monitoring of steel-lined pressure shafts considering water-hammer wave signals and fluid-structure interaction

N° 50 2011 J.-M. Ribi
Etude expérimentale de refuges à poissons aménagés dans les berges de rivières soumises aux éclusées hydroélectriques

N° 51 2012 W. Gostner
The Hydro-Morphological Index of Diversity:
a planning tool for river restoration projects

N° 52 2012 M. Bieri
Operation of complex hydropower schemes and its impact on the flow regime in the downstream river system under changing scenarios

N° 53 2012 M. Müller
Influence of in- and outflow sequences on flow patterns and suspended sediment behavior in reservoirs

N° 54 2013 V. Dugué
Influencing river morphodynamics by means of a bubble screen: application to open-channel bends

N° 55 2013 E. Person
Impact of hydropeaking on fish and their habitat

N° 56 2013 T. Cohen Liechti
Influence of dam operation on water resources management under different scenarios in the Zambezi River Basin considering environmental objectives and hydropower

N° 57 2014 A. M. da Costa Ricardo
Hydrodynamics of turbulent flows within arrays of circular cylinders

N° 58 2014 T. Ghilardi
Sediment transport and flow conditions in steep rivers with large immobile boulders

N° 59 2014 R. Duarte
Influence of air entrainment on rock scour development and block stability in plunge pools

ISSN 1661-1179

DOI: 10.5075/epfl-lchcomm-59

Prof. Dr A. Schleiss
Laboratoire de constructions hydrauliques - LCH
EPFL, Bât. GC, Station 18, CH-1015 Lausanne
http://lch.epfl.ch
e-mail: secretariat.lch@epfl.ch